© 2021 Suya Gao

STUDY OF MULTI-COMPONENT SPRAY AND COMBUSTION AND THEIR OPTIMIZATION WITH MACHINE LEARNING IN INTERNAL COMBUSTION ENGINES

BY

SUYA GAO

DISSERTATION

Submitted in partial fulfillment of the requirements
for the degree of Doctor of Philosophy in Mechanical Engineering
in the Graduate College of the
University of Illinois Urbana-Champaign, 2021

Urbana, Illinois

Doctoral Committee:

Professor Chia-fon F. Lee, Chair
Associate Professor Kelly Stephani
Professor Xinlei Wang
Associate Professor Matthew West

ABSTRACT

As energy resources dry up and environmental pollution becomes severe, clean and highly efficient internal combustion engine operation has become the need of the hour. Understanding the physical process of the fuel spray evolution is imperative in predicting and improving the performance of applications of modern fuel injection systems. Once fuel is directly injected into the combustion chamber, the proceedings, such as liquid fuel vaporization and formation of the fuel-air mixture, would conspicuously influence the onset of combustion, combustion efficiency and thus the emissions. Studies in this dissertation focus on two phenomena in internal combustion engines: the liquid fuel spray evolution and fuel-air mixture preparation. The computational methodologies which specialized in physics-based and data-driven model development and simulations are utilized in order to predict the performances of internal combustion engines and to seek better solutions for clean energy, higher efficiency, and lower emission design.

In this dissertation, the objectives included are: 1) a comprehensive model considering preferential vaporization of a complex fuel mixture using discrete approach; 2) a unified model for spray atomization under the consideration of flash boiling; 3) a new approach of emission reduction in the compression-ignition engine is introduced. By controlling the fuel-air mixing process the burning sequence of the mixture is shifted from traditional ignition behavior; 4) applications of artificial intelligence techniques to help accelerating the model development and engine design processes.

Fuel droplet vaporization rates and corresponding flow evolutions are important because they directly influence the onset of combustion, the efficiency of combustion, thus emissions. Therefore, prediction of the real fuel vaporization is the first step of this research project. An

efficient and precise multi-component fuel droplet vaporization model has been developed in this work using a discrete approach. A quasi-1D frame for liquid droplet is constructed such that the evolution of the non-uniform mass and energy distribution for liquid droplets can be accurately described by the surface state and bulk mean state.

The second objective is to develop a comprehensive model for spray atomization under the consideration of flash boiling. To develop a comprehensive multi-component fuel flash boiling model, three main processes, bubble nucleation, bubble growth, and breakup, are considered. The effect of superheating on breakup is built into a classic aerodynamic breakup model such that the unified breakup model is feasible to be used over all possible engine operation conditions. The new vaporization and breakup model are integrated into a CFD program (KIVA-3V) to further conduct the evaluation of the spray superheating effects.

A new approach of NOx reduction in compression-ignition engines is introduced using a fuel that exhibits the "inverted ϕ-sensitivity" (IPS) behavior in this work. From 0-D calculations, ethanol, which is also a clean and renewable fuel, is selected as the test fuel for satisfying the criteria considered in this study. Engine conditions that cover from low to high load operations are tested with 3-D simulations. Characteristics of ethanol vapor/air mixture are analyzed to reveal the mechanism of inverted ϕ-sensitivity fuel in reducing emissions. Optimal operations for compression-ignition engines with IPS fuel are conducted using the genetic algorithm to exaggerate the superior effect of inverted ϕ-sensitivity on engine performance.

Advanced modeling methods utilizing machine learning are developed to substitute the high-fidelity CFD simulation and coupled with optimization algorithms to accelerate the design processes and increase predictive capability of models. The underlying patterns and relations between engine control parameters and performances (emissions and efficiency) are revealed by

data-driven models. Such compact information processes are assembled to construct a stacked machine learning model. Instead of using CFD models, this machine learning model is called as a function at the genetic algorithm interface for optimization procedures.

This work provides the fundamental understandings of liquid fuel spray and corresponding mixture evolutions and combustion processes in internal combustion engines. New technologies for better atomization process and engine emission reduction are provided. Applications of artificial intelligence demonstrate the possibilities of implementing the advanced computational knowledge and addressing the cross-disciplinary work to engine studies.

In memory of my dear father,
Who taught me to be brave and persist dreams

ACKNOWLEDGMENTS

Looking back now, it has been over six years since I started my graduate research life. Being a researcher and seeking for professionals are a long and hard journey, and so many memories are rewinding and come back clearly to me, some can even make me laugh or cry. For all these people that I have encountered, that I have worked with and that I love, they have supported, encouraged, guided, and inspired me. I am truly grateful to have you in my life and made who I am today.

First, I would like to sincerely thank my research advisor, Professor Chia-Fon Lee. Your inspirational mentorship and precious guidance provided me the knowledge and counsel I need to succeed in the PhD program. I was able to gain invaluable experience over years and to acquire the skills that I can benefit throughout in my future careers. I would like to thank Professor Kelly Stephani, Professor Xinlei Wang, and Professor Matthew West for their interest in this research and serving as members of my examination committee. Your careful reviews and valuable suggestions made it possible for me to improve my work from fresh and rigorous research perspective.

My most sincere and deepest gratitude is for my father, who gave me the greatest gift anyone could ever give another person. My dad believed in me. He knew that I could accomplish my dream someday in my life, to be an automotive engineer. When I was a little girl, I told my father that I really loved racing cars and dreamed I can take a career path in mechanical engineering that dominated by men. My dad encouraged me to harness my curiosity in science and nature, supported my ambitions, and was never absent from my childhood. I always remember that we spent time together on many easy experiments, exploring the unknown world and enlightening my

imaginations. His profound and endless love empowers me to take every challenge in the research and my life. I am the luckiest person to have had the best dad, and I wish my father was here to see me grow and to see what I've accomplished.

My deepest gratitude is also for my husband, Dr. Junhao Yan, who is my friend, my colleague, and most importantly my family. He supports me, backs me up through all the difficulties of research and life. His understanding and thoughtful suggestions in hard times mean more to me than I can ever express. He puts up with me, and loves me, and protects me. Throughout the ups and downs of the journey of life and research, he never left my side. Thank you for always being the most reliable and supportive people I could ever hope to know.

In addition to my family, I am grateful to all my colleagues and friends I have met. Their tremendous amount of friendship and encouragement are really my precious possession. I would like to thank my former colleague Dr. Mianzhi Wang for his kind and patient guidance on my research. He was my mentor and helped me a lot in modeling and simulation studies during my early years in Professor Lee's engine lab. Dr. Cai Shen helped me transiting smoothly into the work and life at U of I and gave me constructive suggestions during my job search. Dr. Wayne Chang gave me many cares and supports through difficult times, provided plentiful advice in my research. I would like to thank Dr. Karthik Nithyanandan and Robert Donahue for being friends and collogues, and I had great time to talk research, cars, and life with them. They also provided valuable experimental results that I could use for simulation validations. My great friends, Haiqin Zhou, Yuanxu Li, and Menghan Li, Jiaren Zhang, and Ying Lan, adds truckloads of joy and happiness in my life. You guys are really like sunshine to brighten up my day in my darkest time.

The accomplishments described in this dissertation are also based on my experiences obtained during my undergraduate research studies with Professor Abhijit Chandra and Professor

Daniel Attinger at Iowa State University. Without those experiences, it would be impossible for me to obtain insightful understandings about research. The rigorous attitude of my undergraduate professors reminded me that academic achievement requires years of hard work, which urged me to go further on the road to pursue professional knowledge.

I would like to acknowledge the Department of Energy, Office of Energy Efficiency and Renewable Energy and the Department of Defense, Tank and Automotive Research, Development, and Engineering Center for the financial sponsorship and CFD funding of the diverse research projects. I also want to truly thank U of I Mechanical Science and Engineering department for providing the teaching assistant position, fellowships, and sponsorships. The study could not be finished smoothly without the help of my department advisor Kathy Smith, who provided numerously patient assistances and supportive advice from the day one of my life in U of I.

Very special and heartfelt thanks go to my furry babies: two lovely golden retrievers, Bubble and Tiger; three fond kitties, Lucky, Kit Kat, and Lolly; and four adorable chinchillas, Qiuqiu, Lili, Dudu, Doudou. They are my precious, emotional supports, read my feelings, accompany me through every day. Without them, I could not have survived through this long and hard journey.

Last, but certainly not the least, I would like to thank my family. 我是幸运的有两个爱我的妈妈和爸爸，还有四个弟弟和妹妹。他们在我人生中，无论是开心还是艰难的时候，一直陪在我的身边。爸爸妈妈们在我无助之际给了我一个温暖的家，教会了做人，处事，面对人生的态度，以及对我学习和职业道路的选择提供了绝对的支持。弟弟妹妹们的陪伴，让我成长的道路上多了无尽的欢乐。打打闹闹的时光是如此的美好，姐姐很感激有你们在身边给我欢笑，让我在前进的道路上有了一份执着的温暖。

TABLE OF CONTENTS

LIST OF TABLES ..... **xi**

LIST OF FIGURES ..... **xii**

LIST OF ABBREVIATIONS ..... **xix**

LIST OF SYMBOLS ..... **xxiii**

CHAPTER 1: INTRODUCTION **1**

1.1 Motivations 1
1.2 Modeling of Multi-Component Droplet Vaporization 3
1.3 Modeling of Flash Boiling Sprays 6
1.4 Emission Reduction in Compression-Ignition Engine 10
1.5 Artificial Intelligence in Modeling and Computation for Engine Simulations 14
1.6 A Brief Introduction to KIVA 18
1.7 Objectives and Overview 19

CHAPTER 2: MODELING OF QUASI-1D MULTI-COMPONENT FUEL DROPLET VAPORIZATION USING DISCRETE APPROACH **23**

2.1 Experimental Setup 23
2.2 Liquid Phase Sub-Model 25
2.3 Gas Phase Sub-Model 29
2.4 Vapor-Liquid Equilibrium 31
2.5 Properties Evaluations 37
2.6 Single-Component Droplet Validations 43
2.7 Multi-Component Droplet Validations 49
2.8 Droplet Vaporization in Convective Environment 53
2.9 Droplet Vaporization Model Corrections 57

CHAPTER 3: ATOMIZATION OF MULTI-COMPONENT FUEL SPRAYS UNDER THE FLASH BOILING CONDITIONS **60**

3.1 Bubble Nucleation Model 61
3.2 Bubble Growth Model 62
3.3 Breakup Model 65
3.4 3-D Simulation Conditions 69
3.4.1 ECN Spray G 72
3.5 Flash-Boiling Sprays Simulation and Validation 75
3.5.1 Single-Component Sprays 79
3.5.2 Binary-Component Sprays 85
3.6 Characteristics of Spray Vaporization and Mixing 95
3.6.1 Exx Blends at Various Superheated Degrees 95
3.6.2 Hxx Blends at Various Superheated Degrees 106
3.6.3 Fuel Vapor Mixing and Distribution 107

CHAPTER 4: EMISSIONS REDUCTION IN COMPRESSION-IGNITION ENGINES BY INVERTED IGNITION PHI-SENSITIVITY **112**

4.1 Fuel Selection and 0-D Ignition Calculation 113

4.2 Computation Method and Simulation Conditions for 3-D Calculations 116
4.3 Impact of Inverted ϕ-Sensitivity on Engine-Out NOx Emissions 119
4.3.1 Influence of Inverted ϕ-Sensitivity on Ignition Events 119
4.3.2 Low and Medium Load Operations 121
4.3.3 High Load Operations 132

CHAPTER 5: MULTI-INJECTION CONTROL PARAMETERS OPTIMIZATIONS FOR HIGH-LOAD C.I. ENGINE WITH INVERTED PHI-SENSITIVITY FUEL 137
5.1 Genetic Algorithm Optimization 138
5.2 Optimal Strategy 142
5.2.1 Multiple Injection Optimization 142
5.2.2 Optimized Engine Performance 147
5.3 Realization of Inverted ϕ-Sensitivity Under High Load Condition 152

CHAPTER 6: APPLICATIONS OF MACHINE LEARNING IN ENGINE MODELING AND OPTIMIZATION 157
6.1 Supervised Machine Learning 158
6.2 Data Preparation 160
6.3 Machine Learning Algorithms 162
6.3.1 Linear Regression 163
6.3.2 Support Vector Regression 164
6.3.3 K-Nearest Neighbors 166
6.3.4 Tree-Based Algorithms 169
6.3.5 Artificial Neural Network 172
6.4 General Procedures for ML-GA Modeling 175
6.5 Bias and Variance Trade-offs 177
6.6 Hyperparameters Optimization 181
6.7 Optimization for Engine Control Parameters with Stacked ML Models 189

CHAPTER 7: SUMMARY AND FUTURE WORK 198
7.1 Development of Spray Models in IC Engines 198
7.2 Novel Investigations on Engine Emission Reduction 201
7.3 Applications of Advanced Techniques and Innovations 202
7.4 Recommendations for Future Works 204

REFERENCES 206

LIST OF TABLES

Table 2.1: Component distributions at the moment of start of F.C. for 50% C7-50% C10. 56

Table 2.2: Component distributions at the moment of start of F.C. for C7-C10 droplet..... 56

Table 3.1: Fuel properties for ethanol, hexane, and isooctane..... 71

Table 3.2: Spray G Nozzle Geometry..... 74

Table 3.3: Spray G Operating Conditions of ECN. 74

Table 4.1: Models used in the simulation. 118

Table 4.2: Key parameters of the derived and stock AVL 5402 single cylinder test engine..... 118

Table 4.3: Tested cases with E100 and PRF85..... 119

Table 4.4: Summary of the results for tested cases..... 121

Table 5.1: Independent control parameters and their prescribed ranges. 141

Table 5.2: Operation conditions for baseline and optimized cases..... 143

Table 5.3: Engine performance for baseline and optimized cases..... 150

Table 6.1: Comparisons for tree-based ML algorithms. 172

Table 6.2: Optimal hyperparameters for GBDT algorithm in double-injection scheme. 185

Table 6.3: Optimal hyperparameters for ANN algorithm in double-injection scheme. 185

Table 6.4: Optimal hyperparameters for SVM algorithm in double-injection scheme. 185

Table 6.5: Optimal hyperparameters for RF algorithm in double-injection scheme. 186

Table 6.6: Optimal control parameters obtained from CFD-GA and ML-GA. 191

Table 6.7: Computational cost comparisons between CFD-GA and ML-GA..... 197

Table 6.8: Optimal simulation results comparison for double injection scheme..... 197

Table 6.9: Optimal simulation results comparison for triple injection scheme. 197

LIST OF FIGURES

Figure 1.1: Fundamental processes of liquid fuel injection and vapor-air mixing. 20

Figure 2.1: (A) schematic of the experimental setup; (B) suspended droplets on a silica fiber. .. 24

Figure 2.2: Variation of fluid density versus temperature for n-heptane and ethanol. The measured data is from [115-117]. 33

Figure 2.3: Droplet surface temperature just before the end of the vaporization. The measured data is taken from Dubey *et al*. [118] 34

Figure 2.4: Temperature-phase phase diagram for n-pentane/n-heptane system. The experimental data are from Cummings *et al*. [120]. 36

Figure 2.5: Pressure-composition phase diagram for nitrogen-alkanes system. 36

Figure 2.6: N-heptane transport properties comparisons with measured data at atmospheric pressure. 40

Figure 2.7: Evolutions of viscosity prediction with the experimental data in binary systems. 41

Figure 2.8: Evolutions of thermal conductivity prediction with the experimental data in binary systems at various temperature. 41

Figure 2.9: Diffusion coefficients for binary mixtures at various temperature. 42

Figure 2.10: Latent heat of vaporization prediction at atmospheric pressure. 42

Figure 2.11: Measured and computed droplet temperature history for n-heptane fuel droplet at 1 atm. Note that the light-colored dashed lines in the averaged measured temperature curves indicate the strong ambient gas effect on thermocouple measurement. 44

Figure 2.12: Comparison of the diameter temporal history between experiment and computation for a n-heptane droplet at various ambient temperature. 45

Figure 2.13: Vaporization rate of n-heptane droplet at 1 atm, non-convective environment. The measured data are from authors' lab as well as from [42-44]. 47

Figure 2.14: Comparisons of final droplet temperatures between the current model and measured data obtained from [22]. The droplet of n-heptane has diameter of 1.8mm and under the non-convective environment. 48

Figure 2.15: Temporal history of droplet vaporization for n-heptane fuel droplet under different pressure and temperature conditions. 48

Figure 2.16: Temporal history of droplet vaporization for n-hexadecane fuel droplet at 10 bar ambient conditions. 49

Figure 2.17: Temporal history of multi-component droplet vaporization for ethanol/isooctane binary system under atmospheric pressure at 200°C environment. 51

Figure 2.18: Temporal history of multi-component droplet vaporization for n-heptane/decane binary system under atmospheric pressure at 297K environment..... 51

Figure 2.19: Temporal history of multi-component droplet vaporization for ternary mixture droplet under atmospheric pressure at 300°K environment (2005)..... 52

Figure 2.20: Evolutions of mass fraction during droplet vaporization for ternary mixture droplet under atmospheric pressure at 300°K environment..... 52

Figure 2.21: Measured and computed vaporization history for a n-heptane droplet and a decane droplet immersing in the convective flow at 1 atm. 54

Figure 2.22: Comparison of the diameter history between experiment and computation for a n-butanol droplet with different diameter of the supporting thermocouple. 54

Figure 2.23: Temporal variation of the vaporization of fuel mixture droplet with 50% of n-heptane and decane (volumetric composition). 56

Figure 2.24: Measured and computed droplet temperature history for binary fuel droplet at 1 atm. C7: n-heptane; C10: decane. 57

Figure 2.25: Temporal history of droplet vaporization for n-heptane fuel droplet with the weak FC modification at various temperature conditions. 58

Figure 2.26: Temporal history of droplet vaporization for n-heptane fuel droplet with the weak FC modification under different pressure and temperature conditions. 59

Figure 3.1: Schematic of the flash boiling phenomenon. 60

Figure 3.2: Bubble growing in a superheated liquid. 62

Figure 3.3: Droplet breakup mechanisms. Strong flash-boiling breakup is illustrated in Figure 3.1. 66

Figure 3.4: Vapor pressure validations for fuel blends. 71

Figure 3.5: ECN spray G configurations. Left: plume dimensions; Right: Front and top views of spray G plume orientation [151, 152]. 73

Figure 3.6: The synthetic droplet light blockage images for Ethanol-Isooctane sprays at EOI. .. 76

Figure 3.7: The synthetic droplet light blockage images for Hexane-Isooctane sprays at EOI.... 77

Figure 3.8: The synthetic droplet light blockage images for pure isooctane spray. 80

Figure 3.9: The synthetic droplet light blockage images for pure ethanol spray. 81

Figure 3.10: Liquid spray penetration for E0 at different ambient pressures. 81

Figure 3.11: Liquid spray penetration for E100 at different ambient pressures. 82

Figure 3.12: Comparisons of averaged SMD for single-component sprays. 84

Figure 3.13: Droplet size distribution along the radial direction at 15mm downstream of the injector tip fueling with E0 at different ambient pressures. 84

Figure 3.14: Droplet size distribution along the radial direction at 15mm downstream of the injector tip fueling with E100 at different ambient pressures. 85

Figure 3.15: The synthetic droplet light blockage images for E30 spray at different pressure. ... 86

Figure 3.16: The synthetic droplet light blockage images for Exx spray at $Pa = 50kPa$. 87

Figure 3.17: The synthetic droplet light blockage images for H30 spray at different pressure.... 89

Figure 3.18: Liquid spray penetration for E30 at different ambient pressures. 89

Figure 3.19: Liquid spray penetration for Exx at $Pa = 50kPa$. 90

Figure 3.20: Liquid spray penetration for H30 at different ambient pressures. 91

Figure 3.21: Comparisons of averaged SMD for binary-component sprays. 92

Figure 3.22: Droplet size distribution along the radial direction at 15mm downstream of the injector tip fueling with E30 at different ambient pressures. 93

Figure 3.23: Droplet size distribution along the radial direction at 15mm downstream of the injector tip fueling with H30 at different ambient pressures. 93

Figure 3.24: Droplet size distribution along the radial direction at 15mm downstream of the injector tip fueling with Exx at $Pa = 50kPa$. 94

Figure 3.25: 3D rendering visualization. 95

Figure 3.26: Gas/vapor and liquid phase distribution for Exx blends at the fix ambient pressure of $Pa = 50kPa$. DBI images (top) from experiments and corresponding rp value is marked on the top left of each image; simulation results at 0.25 ms after SOI (middle); simulation results at EOI (bottom). 97

Figure 3.27: Temperature distributions of gas-phase for sprays fueling with Exx at $Pa = 50kPa$. Distribution along the radial direction at 15mm downstream of the injector tip (top); distribution for entire testing domain (bottom). 99

Figure 3.28: Gas/vapor and liquid phase distribution for E30 sprays at different ambient pressures. 102

Figure 3.29: Mass fraction and temperature distributions of vapor-phase for E30 at different ambient pressures. Distributions along the radial direction are collected at 15 mm downstream of the injector. 104

Figure 3.30: Gas/vapor and liquid phase distribution for Hxx blends at the fixed ambient pressure of $Pa = 50\ kPa$. DBI images (top) from experiments and corresponding rp value is marked on the top left of each image; simulation results at 0.25 ms after SOI (middle); simulation results at EOI (bottom). 107

Figure 3.31: Evolutions of vapor phases for E30 at 30kPa and 50kPa ambient pressures during injection process. 109

Figure 3.32: Evolutions of vapor phases for E30 and H30 at 50kPa ambient pressure during injection process. 109

Figure 3.33: Local equivalence ratio comparisons for Exx sprays. 111

Figure 4.1: The result of 0-D calculation of ethanol ignition delay, ignition delay vs. equivalence ratio. Each curve is for a certain temperature and pressure..... 115

Figure 4.2: The result of 0-D calculation of ethanol ignition delay, ignition delay vs. temperature. ϕ increases from 0.2 to 2.0, and each curve is for a certain equivalence ratio. 115

Figure 4.3: AVL-5402 single cylinder diesel engine (a) derived engine and (b) stock AVL-5402 engine. 118

Figure 4.4: Onset of ignition of E100 and PRF85. The snapshot is taken at about 2° or 3° before CA10. Two sets of iso-surfaces, $\phi = 0.3$ and $\phi = 0.8$ (except the first at intake pressure of $1.0\ bar$ where the overall equivalence ratio of this case is small so the representative iso-surface of $\phi = 0.8$ does not exist) are used to represent the fuel-lean and near-stoichiometric regions. Iso-surfaces are colored by temperature. .. 120

Figure 4.5: Pressure history and HRR at $Pi = 1.0\ bar$ with default swirl ratio. 123

Figure 4.6: Average in-cylinder temperature and NOx emission in g/kWh at $Pi = 1.0\ bar$ with default swirl ratio. 124

Figure 4.7: Local equivalence ratio distribution before and after combustion for $Pi = 1.0\ bar$ with default swirl ratio. 124

Figure 4.8: Snapshot of the E100 and PRF85 emissions, and the mixture distribution after combustion. $Pi = 1.0\ bar$ with default swirl ratio. 125

Figure 4.9: Pressure history and HRR at $Pi = 1.2\ bar$ with swirl ratio of 3. 126

Figure 4.10: Average in-cylinder temperature and NOx emission in g/kWh at $Pi = 1.2\ bar$ with swirl ratio of 3. 126

Figure 4.11: Snapshot of the E100 and PRF85 emissions, and the mixture distribution after combustion. $Pi = 1.2\ bar$ with swirl ratio of 3. 127

Figure 4.12: Local equivalence ratio distribution before and after combustion for $Pi = 1.2\ bar$ with swirl ratio of 3. 128

Figure 4.13: Pressure history and HRR at $Pi = 2.0\ bar$ with default swirl ratio. 129

Figure 4.14: Average in-cylinder temperature and NOx emission in g/kWh at $Pi = 2.0\ bar$ with default swirl ratio. 130

Figure 4.15: Local equivalence ratio distribution before and after combustion for $Pi = 2.0\ bar$ with default swirl ratio. 130

Figure 4.16: Snapshot of the E100 and PRE85 emissions, and the mixture distribution after combustion. $Pi = 2.0\ bar$ with default swirl ratio. 131

Figure 4.17: Pressure history and HRR at $Pi = 2.0\ bar$ with swirl ratio of 3. 134

Figure 4.18: Average in-cylinder temperature and NOx emission in g/kWh at $Pi = 2.0\ bar$ with swirl ratio of 3. 134

Figure 4.19: Snapshot of the E100 and PRE85 emissions, and the mixture distribution after combustion. $Pi = 2.0\ bar$ with swirl ratio of 3. 135

Figure 4.20: The evolution of the E100 iso-surfaces, $\phi = 0.3$ and $\phi = 0.7$, during the combustion stage. 136

Figure 5.1: Main genetic operators for genetic algorithms. 139

Figure 5.2: Evolution of SOI through generations for double injection strategy. 144

Figure 5.3: Convergence of the injected fuel quantity in each injection through generations for double injection strategy. 144

Figure 5.4: Evolution of SOI through generations for triple injection strategy. 145

Figure 5.5: Convergence of the injected fuel quantity in each injection through generations for triple injection strategy. 145

Figure 5.6: Convergences of ignition delay and swirl ratio in 30 generations for double and triple injection schemes. 146

Figure 5.7: Variation of minimum target function values with generations. 147

Figure 5.8: Changes of combustion phasing through generations for double and triple injection strategy; CA XX represents the moment of XX% of heat released, and CA 10 usually refers to the timing that combustion just gets started. 148

Figure 5.9: Engine performance through generations for double and triple injection strategy. . 149

Figure 5.10: Improvements of NOx and CO emissions through generations. Values are in g/kWh, which are calculated from amount of emission of each species in PPM and indicated work, to eliminate the influence of incomplete combustion. 150

Figure 5.11: Correlation between the NOx formation and the post injection timing; the scatter plot is made by the results from all 1800 simulation cases. 151

Figure 5.12: Comparisons of pressure history and heat release rate for optimal multi-injection strategies and the baseline fueling with 50mg E100. 153

Figure 5.13: Comparisons of averaged in-cylinder temperature and engine-out NOx emissions for optimal multi-injection strategies and the baseline fueling with 50mg E100. 154

Figure 5.14: Local equivalence ratio distribution before CA10 (top) and at CA50 (bottom). The NOx region definition is from [173]. 154

Figure 5.15: Snapshot of mixture distribution and NOx emissions after combustion. 156

Figure 5.16: In-cylinder equivalence ratio distribution before CA10 for optimal multi-injection strategies and the baseline fueling with 50mg E100. 156

Figure 6.1: General procedures for ML model development. 159

Figure 6.2: k-fold ($k = 4$ in this example) cross validation process. 161

Figure 6.3: SVM for a simple 2D regression problem. 164

Figure 6.4: KNN learning for $k = 3$. Scatter plot of x versus y with predicted yi for an arbitrary value of xi based on 3 nearest neighbors. The prediction is represented as a red dot, and 3 nearest neighbors are black dots with pink filling. 167

Figure 6.5: Selection of k using elbow method. For demonstration purpose, two targets (NOx and IMEP) from double-injection scheme are plotted. The optimal values of k are 5 for NOx and 4 for IMEP. 168

Figure 6.6: Random Forest Regression structure. 171

Figure 6.7: Gradient Boosted Decision Tree in leaf-wise pattern [177]. 171

Figure 6.8: ANN with three layers of neurons. 173

Figure 6.9: ANN learning algorithm with an activation function. 174

Figure 6.10: Flow chart of the general procedure for ML-GA process. The dataset used in the generalized ML model is out-of-fold predictions from the base models. 177

Figure 6.11: Learning curves of different outputs (triple-injection scheme) with default hyperparameters for tree-based algorithm. 179

Figure 6.12: Hyperparameter optimization results for GBDT algorithm (double injections). ... 184

Figure 6.13: Number of leaves distribution for GBDT for NOx (double injections). 184

Figure 6.14: Learning curve comparisons between default and tuned tree-based ML algorithm for double injection scheme. 187

Figure 6.15: Learning curve comparisons between default and tuned tree-based ML algorithm for triple injection scheme. 187

Figure 6.16: ML scores for different algorithms (double-injection scheme)..... 188

Figure 6.17: ML scores for different algorithms (triple-injection scheme). 188

Figure 6.18: Schematic of stacked generalization. 189

Figure 6.19: Double-injection scheme ML-GA optimization history: variation of minimum target function values with generations for ten trails. 191

Figure 6.20: Triple-injection scheme ML-GA optimization history: variation of minimum target function values with generations for ten trails. 192

Figure 6.21: Optimal control parameters comparisons between ML-GA and CFD-GA methodologies in double-injection scheme. 192

Figure 6.22: Optimal control parameters comparisons between ML-GA and CFD-GA methodologies in triple injection scheme. 193

LIST OF ABBREVIATIONS

AI	artificial intelligence
AKI	anti-knock index
ALE	arbitrary Lagrangian-Eulerian
ANN	Artificial Neural Network
ATDC	after top dead center
BTDC	before top dead center
CA	crank angle
CAD	crank angle degree
CFD	computational fluid dynamics
CI	compression-ignition
CMC	continuous thermodynamic multi-component
CO	carbon monoxide
CO_2	carbon dioxide
CPU	central processing unit
CV	cross validation
DBI	Diffuse Backlight Imaging
DI	direct-injection
DMC	discrete multi-component
DT	decision tree
EI	expected improvement
ICE	internal combustion engine
IPC	inter-process communication

ECN	Engine Combustion Network
EDC	Eddy dissipation concept
EGR	exhaust gas recirculation
EM	Expectation Maximum
EOI	end of injection
EOS	equation of state
EVO	exhaust valve opening
FVM	finite volume method
GA	Genetic Algorithm
GBDT	gradient boost decision tree
GDCI	gasoline direct-injection compression-ignition
GDI	gasoline direct-injection
GHG	greenhouse gas
GP	Gaussian process
HCCI	homogeneous charge compression-ignition
HOV	heat of vaporization
HPC	high-performance computing
HRM	homogeneous relaxation model
HRR	heat release rate
IMEP	indicated mean effective pressure
IPS	inverted ϕ-sensitivity
IVC	Intake valve closing
KNN	K-Nearest Neighbor

LANL	Los Alamos National Laboratory
LISA	linearized instability sheet atomization
LR	linear regression
LTC	low-temperature combustion
MON	motor octane number
MPI	Message-Passing Interface
MSE	Mean Squared Error
NOx	oxides of nitrogen
NTC	Negative Temperature Coefficient
PCCI	partially premixed charge compression ignition
PDA	Phase Doppler Anemometry
PDF	probability distribution function
PI	probability of improvement
PRF	primary reference fuel
RF	Random Forest
RBF	Radial Basis Function
RMSE	Root Mean Square Errors
ROI	rate-of-injection
RSM	response surface method
SMBO	Sequential Model-Based Global Optimization
SMD	Sauter Mean Diameter
SI	spark-ignition
SOI	start of injection

SR	swirl ratio
SVR	Support Vector Regression
SVM	Support Vector Machine
TDC	top dead center
UCB	upper confidence bound
UHC	unburnt hydrocarbon
TAB	Taylor analogy breakup
TDC	top dead center
VLE	vapor-liquid equilibrium

LIST OF SYMBOLS

$\mathcal{B}_i$	the transfer number of component i
C_p	mass based constant pressure heat capacity
C_v	mass based constant volume heat capacity
	vaporization rate of droplet $[\frac{mm^2}{s}]$
D_i	mixture-averaged diffusivity of species i
E	factor of surface-mean difference due to non-zero Péclet number
	energy of the bubble-droplet system
f_i	fugacity of species i
ΔH_i	heat of vaporization
Ja	Jakob number
k	thermal conductivity
N	nucleation rate
Nu	Nusselt number
r_i	fuel split ratio for i^{th} injection
r_P	flash boiling intensity
R	radius of droplet; radius of microscopic voids
R_{32}	Sauter mean radius of droplets
$\hat{R}$	molar based ideal gas constant
Re	Reynolds number
P	pressure
P_v	vapor pressure

Pe	Péclet number
Pr	Prandtl number
Sc_i	Schmidt number of species i
Sh_i	Sherwood number of species i
T	temperature
ΔT	superheat
X	molar fraction of species i
y	deviation of the droplet equator from its equilibrium position
Y_i	mass fraction of component i
u	droplet speed relative to the gas
v	secondary droplet speed perpendicular to u; molar based specific volume
V	volume
We	Weber number
μ	dynamic viscosity; statistical mean
ρ	density
σ	surface tension, the Lannard-Jones parameter
θ_i	the fugacity coefficient of species i
ϵ	void fraction
η	viscosity
ϕ	equivalence ratio
ξ_i	correction factor for the effect of Stefan flow
ω	acentric factor
Ω	the collision integral

Δ	information gain
Σ	covariance matrix

Subscripts and superscripts:

$(\cdot)_0$	initial value of $(\cdot)$
$(\cdot)_a$	ambient condition
$(\cdot)_b$	$(\cdot)$ of bubble
$(\cdot)_c$	critical value of $(\cdot)$
$(\cdot)_d$	$(\cdot)$ of bubble-in-droplet system
$(\cdot)_g$	$(\cdot)$ of gas phase
$(\cdot)_i$	$(\cdot)$ of species i; $(\cdot)$ of the inner surface of the bubble-in-droplet system
$(\cdot)_l$	$(\cdot)$ of liquid phase
$(\cdot)_m$	the mean value of $(\cdot)$
$(\cdot)_o$	$(\cdot)$ of the outer surface of the bubble-in-droplet system
$(\cdot)_r$	reference value of $(\cdot)$
$(\cdot)_s$	$(\cdot)$ at surface
$(\cdot)_{sat}$	saturation value of $(\cdot)$
$(\cdot)_\infty$	$(\cdot)$ far out of the boundary layer

CHAPTER 1: INTRODUCTION

1.1 Motivations

The transport of goods and people is essential to modern society, and currently transport is almost entirely powered by internal combustion engines (ICE) using liquid fuels due to their plentiful supply, convenience, and affordability. There are around 1.2 billion light-duty vehicles and around 380 million heavy-duty vehicles in the world, and these numbers are growing. In addition, stationary combustion engines, for example generators, are ubiquitous in industries and in power generation facilities, which also promote the world's standard of living. Indeed, the demand for available and affordable energy is increasing with the increase in global population and prosperity, particularly in developing countries. The fact that the entire planet is linked by a massive transportation infrastructure that is largely based on ICEs and that would require decades and tremendous expense to replace. Many studies provide strong evidence that there are still no real alternatives can compete with the ICE over the entire range of applications even today [1-3].

Concerns on ICEs are from two aspects, shortage of fossil fuel and emissions. The actual global oil production and consumption continues to rise, a peak is expected in conventional world oil production as a result of resource constraints alone by 2025 or earlier [4, 5] and between 65 to 80 percent of current known fossil fuel reserves untouched [6]. ICEs operating on fossil fuel oil provide about 25% of the world's power from CO_2 and Greenhouse Gas Emissions report [7], and about 70% of fossil oil (i.e. about 3000 Mtoe) is consumed in ICEs. In doing so, ICEs produce only about 10% of the world's greenhouse gas (GHG) emissions. Many people believe that most of the world's GHG emissions come from cars and trucks, but that is a misconception. A worldwide

massive shift to electric vehicles could only result in a global (potential) reduction of about 10% of the equivalent tons of carbon dioxide (CO_2), under the assumption that all electric vehicles would charge their batteries from energy sources without CO_2 emissions (i.e., renewable/nuclear).

ICEs are undergoing continuous improvement, and exploring new and competing engine technologies, as well as new fuels, is important for a sustainable future. Efforts have been made to improve ICE performance, fuel economy and emissions; many technical innovations have been realized like advanced engine configurations [8-10], state-of-the-art fuel supply systems [11-13], effective fuel-air mixture preparation [14, 15], and latest combustion strategies [16, 17], not to mention the existing after-treatment systems [18-20].

The atomization process is a crucial step in achieving higher combustion efficiency and lower emissions. In spray atomization, fuel injection and the subsequent fuel/air mixing process, play an important role. Superior fuel atomization, producing fine droplets, will enhance the air/fuel mixing rate and reduce emissions from combustion whereas poor atomization could result in incomplete fuel vaporization and spray impingement on the cylinder walls, which cause high levels of unburned hydrocarbons and carbon monoxide emissions as well as fuel/oil dilution, and consequently deteriorate engine performance. In newer combustion concepts such as homogeneous charge compression ignition (HCCI) and premixed charge compression ignition (PCCI), where the pilot/main injection is much advanced, emphasis is placed on the impact of the charge mixture preparation, since it has been reported that excessive mixture stratification can lead to a non-negligible presence of overly rich ($\phi > 1.3$) or overly lean ($\phi < 0.4$) equivalence ratio (ϕ) zones, which undergo incomplete oxidation under highly dilute, low-temperature combustion (LTC) conditions, causing significant amounts of unburned hydrocarbons and carbon monoxide emissions. In this regard, air/fuel mixing is pivotal for both conventional and advanced combustion

technologies. In-cylinder oxides of nitrogen (NOx) reduction is one of the toughest tasks in the development of compression-ignition (CI) engines. Retarding the combustion timing or low-temperature combustion are effective methods to reduce the peak in-cylinder pressure and temperature, hence the NOx emission. However, the trade-offs between NOx and soot emissions are to remain unsolved. In the past, the development of CFD model usually takes years and limited computational power further impedes the simulation progress, making it more challenging to advance ICE designs.

1.2 Modeling of Multi-Component Droplet Vaporization

The combustion phenomenon has been widely applied in many areas, such as the internal combustion engines, rockets, and gas turbines. Among the stages of the combustion process, fuel droplet vaporization rates and corresponding flow evolutions are important because they directly influence the onset of combustion, the efficiency of combustion, and emissions such as NOx and soot [21]. Vaporization characteristics of single component droplets are now well understood under various conditions [22, 23]. A pure component is usually selected according to the requirement that its physical and chemical properties are close to those of the practice fuel. By using a single component model, the composition of the fuel remains unchanged during the vaporization process, cutting down the complexity of analysis. However, commercial fuel is typically composed of hundreds of complex compounds with different physical properties. The single-component model only utilizes the averaged thermo-physical properties and volatilities of practical fuel components [24]. As a result, the single component droplet representation is inefficient to describe the complex vaporization behavior. Furthermore, these potentially significant errors in vaporization model will affect the accuracy of combustion simulations and emission predictions.

The fuel vaporization process consists of several stages and is very complex. The highly volatile components within the petroleum fuel evaporate relatively fast at the liquid-vapor interface compared to their internal diffusion, leading to a non-uniform concentration distribution and a build-up of lighter components in the center of the fuel droplet. On the other hand, heavier components will vaporize later and affect the emissions formation process. Instead of using single-component models, the way to predict the vaporization behavior more accurately is to use the multi-component vaporization approaches to model the complex fuel composition and vaporization process [25]. One of the advantages of the multi-component vaporization model is the ability to account for the distributions of fuel components in the computational domain. Multi-component models have the potential to improve engine simulation accuracy by integrating with detailed chemical kinetics to simulate the combustion of individual fuel component. Therefore, it is important to develop an accurate and efficient multi-component fuel vaporization model.

Numerous theoretical and modeling studies have been carried out for describing the multi-component droplet vaporization, and these studies can be classified into two types: discrete multi-component (DMC) models [26-28] and continuous thermodynamic multi-component (CMC) models [29-31]. In the CMC approach, the fuel composition is characterized by a probability distribution function (PDF) with respect to an appropriate parameter such as molecular weight or boiling point. Tamim and Hallett [29] first developed a CMC model for analyzing the vaporization of isolated multi-component fuel droplets. This method features a reduction of computational load while maintaining the predictability of the complex behavior of the vaporization of multi-component fuels. However, a major deficiency with this approach is lack of an accurate calculation for each fuel species in most combustion numerical simulations. As an alternative, in the DMC approach, the droplet is assumed to be composed of a finite number of components that have

different properties. Each individual component of the fuel is tracked, and its temporal and spatial evolutions are solved using the transport equations. Although the DMC approach yields a high computational cost due to additional transport equations that must be solved, the advancement in computational capabilities makes the massive calculations feasible. Recently, new methods built on CMC and DMC have been conducted to extract and combine the salient features of CMC and DMC, such as the hybrid multi-component model [32] and the quasi-discrete model [33, 34]. Compared to conventional approaches, latter ones can satisfactorily predict the realistic multi-component fuel droplet behavior and lower the computational cost.

Droplet vaporization process can be envisioned as a multi-phase flow analysis. It is governed by both the mass and energy transports phenomena in both liquid phase and gaseous phase. A previous observation [35] suggests gas-phase transport rates are much faster than liquid-phase transport rates. The states at the droplet surface can be considered to be frozen during the characteristic time of gas-phase transport, hence quasi-steady assumption can be made for the vapor phase. In practical engine applications, the relatively high velocity between droplets and ambient gas implies a large Reynolds number in the gas phase. Under such circumstances, the shear stress at the droplet surface induced by the gas stream would generate the circulation motion within the droplet [36]. At least a 2-D model characterization is needed for liquid-phase, which adds another layer of complexity. Therefore, it is important to develop an accurate and efficient multi-component fuel vaporization model.

In addition to the computational study, extensive investigations on droplet vaporization have been conducted experimentally. The free-falling [37-39] method has been adopting to study the characteristics of fuel droplet under high pressure or high temperature conditions, providing the understanding of vaporization behaviors when combustion is desired. To minimize the natural

convection and distortion of the evaporating droplet, microgravity technology [40, 41] has gained attention in the recent decades. Special techniques are always needed to make the velocity of a free droplet zero relative to the freely falling chamber when employing microgravity approach. The suspended droplet technique [22, 42-44] can be easily set up and performed with little experimental difficulties, and the output includes droplet interior temperature and high-resolution images. The droplet is suspended either from a bead born at the tip of a thin cylindrical filament [45, 46] or from the intersection of two filaments. However, the heat conduction through the support fiber is inevitable, especially when a bead is used. Chauveau *et al.* [43] experimentally tested the droplet evaporation using fibers with different diameters. The results imply that the conduction heat flux into the droplet increases with the cross-sectional area of the fibers. Such correlation offers the possibility of lessening the influence of the fiber in the suspending droplet system. There is a reasonable agreement in the literature that for fiber diameter is less than 100 μm.

1.3 Modeling of Flash Boiling Sprays

Understanding the physical process of the fuel spray evolution are imperative in predicting and improving the performance of applications with the modern fuel injection systems. In direct injection engines, the fuel is introduced into the cylinder through a nozzle with injection pressures ranging from of 50 to 3000 bar, depending on the engine size and type of combustion [47]. A large pressure differential across the nozzle orifice is created thereby the injected liquid fuel will enter the combustion chamber at sufficiently high velocity to spread out. The liquid jet leaving the nozzle disintegrates and atomizes into droplets with sizes less than the diameter of the nozzle exit to enable rapid evaporation. This type of behavior is classified as atomization which consists of the breakup of the continuous liquid jet and the breakup of the discrete droplets.

Plenty of studies have been conducted to understand the fundamental mechanisms of atomization in direct-injection (DI) engines [48-51], yet the complexity has been strongly increased due to comprised multiphase flow and interaction with turbulence. Spray model development is a key for engine simulations as spray characteristics directly impact the formation of fuel-air mixture and therefore the combustion mode in cylinders. In gasoline direct injection (GDI) engines, the time available for mixture preparation after the injection is limited but the requirement of forming the homogeneous charge in GDI is desired under high load conditions [52]. For small diesel engines that operate at higher engine speeds than larger diesel engines, the fuel-injection and combustion system must achieve faster fuel-air mixing rates [47]. Therefore, a well-atomized and evenly dispersed fuel spray is expected. If the environment pressure is lower than the saturation pressure of the fuel, rapid phase transition from liquid to vapor occurs when a liquid spray is discharged, and such phenomenon is known as flash boiling.

Increased fuel temperature or lowered in-cylinder ambient pressure leads fuel to be superheated and enters a metastable state; and the latent heat is consumed for bubble nucleation within the liquid. If the initial bubble radius is greater than the critical value, a small fluctuation of the pressure on the bubble surface will result in either collapsing or bubble growth [53] depending on the local fuel conditions surrounding each bubble. As evaporation proceeds these bubbles continue to grow/burst until the point at which the liquid fuel breaks up, promoting disintegration of bulk liquid into smaller droplets. Though the flash boiling phenomenon is more common in gasoline engines, possible applications with flash boiling can also be adopted in diesel engines. In an indirect-injection type of small diesel engine, fuel is injected into a pre-combustion chamber which is separated from the main combustion chamber above the piston by a flow restriction or nozzle. Traditionally, liquid fuel is injected and heated in this pre-chamber during the later stages

of the compression process and mixed with air forced into the pre-chamber through the nozzle [47]. It is feasible to inject liquid fuel into the pre-chamber at the early stage of engine cycles to promote the spray atomization due to the presence of flash boiling in the liquid fuel, resulting in faster vaporization rate thus high mixing rate. Therefore, a rigorous model to evaluate flash boiling effects on atomization needs to be developed.

Neroorkar *et al*. [54] modeled the transient process of flash boiling with the concept of a finite relaxation time to equilibrium. The mixture quality is advanced with a finite rate toward the equilibrium value, i.e., an approximation for the flash boiling process. An empirical model was used to evaluate the relaxation time. The resulting model is called the homogeneous relaxation model (HRM). The model is implemented in a CFD application to simulate an n-hexane spray coming out of a pressure-swirl injector. Chapman-Jouguet point analysis upon Rayleigh-Hugoniot curves were conducted instead of vaporization rate analysis for droplets outside the nozzle. The fluid properties were evaluated using volume translated Peng-Robinson equation of state. The model is defined to be an engineering approach to evaluate inflow boundary conditions for 3-D CFD applications. Again, due to its homogeneous nature, the model provides limited information about multi-phase spray behavior. Due to the homogeneous nature of this model, the complex yet important behavior of the phase interface of the spray is neglected. Saha *et al*. [55] numerically analyzed the internal and near-nozzle flow of fuel injectors under the flash boiling conditions. The study was focused on the single-component fuel and the flash boiling model was based on the HRM which is capable for predicting phase changes from liquid to vapor and vice versa. However, the model failed to predict the spray behavior under flare flash boiling conditions in which the plume interaction and collapse are violent.

Another path of modeling flash boiling is the direct analysis of the multiphase system. Zuo *et al.* [56] constructed a vaporization model for both a conical liquid sheet and a liquid droplet from a swirl injector under superheated conditions. For the conical liquid sheet, the vaporization rate was solved by coupling with the heat transfer problem in the liquid sheet. The linearized instability sheet atomization (LISA) breakup model was modified to account for the vapor nucleation in the liquid. For the subsequent droplet, a surface vaporization model and flash boiling correlations were used for surface vaporizing and bubble growing cases, respectively. A flash boiling spray model for zero-dimensional boundary conditions has been developed by Price *et al.* [57] in STAR-CD over a wide range of injection systems. The model includes three major processes: bubble nucleation, bubble growth, and bubble departure frequency. Though the model is capable to quantify in-nozzle phase change effects and automatically predict important global spray characteristics such as spray collapse, droplet recirculation and plume merging within a Lagrangian particle tracking framework, the coupling between the flash boiling model and other models, e.g., droplet collision model and breakup model, is not well established. Furthermore, the zero-dimensional conditions for in-nozzle wall nucleation process are not adequate to represent the physical processes occurs for the flash boiling conditions.

Chang and Lee [58] constructed a vapor bubble growth model for flash boiling droplets. The growth of the vapor bubble was modeled by Rayleigh bubble equation. The 1-D problem in spherical coordinates was reduced to a 0-D problem by assuming the form of the spatial distribution of state variables. The simplified model was implemented in engine CFD codes to simulate a conical spray under superheated conditions. Wang [59] developed a combined model for flashing and aerodynamic droplet breakup was constructed based on the work done by Zeng and Lee [60] but with an approximate analytical solution for the problem of bubble growth. In this

research, the flashing breakup was formulated within the framework of the TAB model, such that the aerodynamic and superheating effect interact appropriately with each other for all the possible cases. Compared to experiments, this model fairly predicted the hollow spray behavior under different flash boiling conditions. Nevertheless, the prediction on GDI behavior failed as the individual jet evolution and the plume-plume interactions during the spray development were not fully resolved. The coupling mechanism needs to be reinvestigated for this combined model to widely apply to different spray applications.

Khan *et al*. [61] utilized a droplet distribution, known as Rosin Rammler profile, to artificially describe the droplet size distribution close to the injector nozzle under both flash boiling and non-flash boiling conditions. However, for each flash boiling condition, corresponding experimental data may be required to estimate parameters used in this distribution function. Furthermore, it is true that one of the significant influences of the flash boiling phenomenon is the size change of the fuel droplets, but other prominent outcomes, for example the droplets dispersion, brought by the flash boiling cannot be neglected. Detailed physical descriptions for the flash boiling process are imperative to develop a convincing model. To complete the tool kit for flash boiling simulations, improvements in the modeling of nucleation kinetics, vaporization rate calculation, secondary droplet prediction are necessary.

1.4 Emission Reduction in Compression-Ignition Engine

In-cylinder NOx and particulate emissions reduction is one of the toughest tasks in the advancement of CI engine design. Applying exhaust gas recirculation (EGR) is one of the most effective methods to reduce the in-cylinder NOx formation [15, 62, 63]. With EGR, the in-cylinder mixture is diluted by inert gas, and the temperature rises due to the combustion is reduced. The

lower the combustion temperature is, the less active the NOx formation reactions become. However, applying high EGR poses some challenges on the operation of the engine system. One grievous disadvantage is the increase in sooting tendency due to the reduction of the oxygen by the EGR gas. Soot absorption by the lubricant oil can significantly shorten the maintenance cycle of the engine, thus increase the down time of the vehicle or the machinery. In the cases where heavy EGR is applied to meet NOx emission regulations, a throttle is often needed in the exhaust to increase the pressure drop that drives the high EGR flow rate. The effectiveness of EGR is reduced with the lowering of the overall equivalence ratio. With less fuel and leaner overall equivalence ratio, the inert composition in the EGR gas is reduced, while the EGR becomes less effective considering the increased residual oxygen in the EGR.

In traditional CI engines (ϕ around 0.7), the temperature and equivalence ratio that favor NOx formation are different for soot formation, precluding the possibility of reduction of both NOx and soot at the same time. With the lean-burn (ϕ<0.7) technology [64-66], NOx and soot can be reduced simultaneously. The lean-burn technology not only reduces the overall equivalence ratio, but it also reduces the local equivalence ratio by alternative mixture preparation methods. Instead of relying on only near-TDC (top dead center) direct fuel injections, fuel is also injected at an earlier timing to create partially a premixed in-cylinder environment. When using volatile fuels such as gasoline and natural gas, the fuel can also be injected/induced in the upstream of the combustion chamber, resulting in a charge that is almost homogeneous. With the fuel vapor distributed more evenly compared to the traditional compression-ignition operation, the local equivalence ratio where most of the fuel resides is reduced. The low energy density of the lean mixture results in low combustion temperature, thus reducing the NOx and particulate formation synchronously. Unfortunately, the lean mixture combustion also results in high UHC and CO

emissions due to the reduced in-cylinder temperature that freezes the post-combustion oxidation processes.

The combustion temperature can also be reduced by lowering the charge temperature thus produces lower NOx emissions [67]. Besides using an inter-cooler to cool the boosted/diluted charge, water injection is another method to reduce the charge temperature. Water can be injected either into the intake manifold [68] or directly into the combustion chamber [69, 70]. After being injected, the water droplets evaporate and absorb heat from the surrounding gas, lowering the charge temperature. Apart from the strong charge cooling effect, water injection also dilutes the mixture. The combined effects of charge cooling and dilution make the water injection an effective approach to reduce NOx emissions.

For the sake of reducing pollutant emissions, controlling the combustion mode is an alternative approach. It is commonly achieved by retarding the combustion timing or incorporating new mixture preparation strategies. Kook *et al.* [71] studied the NOx emissions on a small-bore single cylinder diesel test engine. It was found that NOx and soot emissions dropped with retarded start of injection (SOI) timing, which delayed the conventional compression-ignition combustion. The CO emissions, on the other hand, increased with delayed SOI. Low temperature combustion mode exhibits high CO emissions. Strong correlation between the NOx emission and the maximum instantaneous gas temperature was demonstrated using extensive experimental data, indicating that the NOx reduction is due to the lowered combustion temperature with retarding the combustion timing. Unlike other methods to reduce the NOx emissions, retarding the combustion timing requires minimal changes in the hardware configuration of the engine, and can be applied on-the-fly, allowing maximum flexibility. However, retarded combustion timing reduced the performance and efficiency of the engine; the operation robustness is also compromised because of increased

cycle-to-cycle variation. To address these issues, further efforts on reducing CI engine emission are still needed.

Extensive studies on splitting injections illustrate that manipulating the fuel distribution inside the chamber can strongly affect combustion quality and emissions in a CI engine [72-75]. With a single injection, especially under high load conditions, the liquid fuel can penetrate into the low temperature region where a high risk of wall wetting tends to occur. As the result, the fuel vaporization rate is inhibited, a local fuel-rich region is formed, and the combustion is mixing-control dominated. The consequent higher pressure rising rate favors the formation of NOx, and the fuel-rich region produces plenty of soot. With splitting injections, a better fuel-air mixture can be obtained when the fuel split ratio and injection dwells are carefully selected, leading to a remarkable reduction in soot formation. In the work of Tow *et al*. [74], experiments of various injection strategies were carried out in a heavy duty diesel engine. It was found that for high load conditions, longer dwell and retarded rejection timing effectively suppressed the particulate emissions. The particulate formation hit the minimum with 10° CA dwell in double injection cases. Furthermore, no apparent increase in NOx emissions under high load conditions and up to 16% reduction in NOx emissions were attained from the mitigated peak heat release rate. When exploring triple injection strategies, the operating flexibility and the control authority of the injection processes enabled low temperature combustion (LTC) and pushed the engine load to a higher level without the penalty of increasing emissions [75].

Though multiple injection strategies under high load conditions have the potential to reduce the NOx and soot emissions in CI engines, an obstacle in its practical use is the increased number of engine operation parameters, thus a high degree of engine control is required [76]. It is inefficient to experimentally calibrate these parameters such that the optimal engine operating

conditions can be realized in terms of fuel economy, engine efficiency, and emissions. To reduce the experimental cost in finding the optimum values, Mallamo *et al.* [77] employed the Design of Experiments (DoE) techniques in conjunction with the objective function optimization. The full factorial experimental design was constructed based on a prescribed target function. The parameters that had insignificant effect on the engine response were excluded from model formulation, and a model of the target function was generated in the following engine test matrix. The optimum injection configuration was highly dependent on the formulation of the objective function. Montgomery and Reitz [78] experimentally tested a heavy-duty diesel engine operating with multiple injections and EGR. To optimize the engine performance and reduce the cost budget, a hyperspace defined by the response surface was introduced to predict the testing parameters in each highly fractionated two-level factorial experiment set. Unlike traditional optimization strategies, the response surface method (RSMs) was used to depict the implicit relation of an engine process, extending the engine design to a statistically level. Yet, the trade-off between the accuracy and the efficiency of the optimization process limited the resolution of the factorial experiment.

1.5 Artificial Intelligence in Modeling and Computation for Engine Simulations

With the increasing computational power of inexpensive computers and numerical optimizations routines, rigorous simulation and optimization techniques have been commonly applied to large scale problems such as those associated with the design, optimization and control of integrated chemical processes and energy systems [79]. Computational research has been a boon for scientific exploration, providing the ability to analyze more data, leverage more statistical algorithms, and explore theoretical models. Modern internal combustion engine research would be

impossible to conduct without rapid development of computers and advances in computational fluid dynamics (CFD) tools. Instead of generating the data from a real engine experiment that is expensive or very difficult to control, engine simulation can provide a good proxy.

Tremendous efforts have been made to develop accurate and effective models and methodologies for IC engines. Parallel computing schemes, such as Message-Passing Interface (MPI) [80, 81] and OpenMPI [82, 83] , have been utilized [84-86] to accelerate the process of solving combustion reaction kinetics, which allow to distribute the calculation on fast interconnected nodes of a computational ecosystem. This approach, using high-performance computing (HPC), is offering the possibility to accelerate chemical reaction calculations in combustion chamber or engine design processes by orders of magnitude. To obtain robust approach for design optimization, genetic algorithms (GAs), developed in the 1960s and 1970s [87, 88] to model or abstract biological evolution based on Charles Darwin's theory of natural selection [89], have been coupled with engine CFD simulations to evaluate the optimal engine control parameters given the prescribed conditions [90-94]. GA's are among the most popular evolutionary algorithms in terms of the diversity of their applications. In addition, genetic algorithms are population-based, and many modern evolutionary algorithms are directly based on GA or have some strong similarities. A vast majority of well-known optimization problems have been tried by GAs. Liu and Reitz [95] and Kim *et al.* [91] applied micro-genetic algorithms (μGA) to computationally optimize diesel engine operations using high-pressure multiple injections. Because of the reduced size of the population of designs made possible by μGA, the optimum engine operating parameters can be located effectively, saving considerable computation resources. Because of the self-convergence of μGA, the optimum engine parameters tend to diverge from the traditional operating range. The practical importance of the engine optimization problem is that there always exist

multiple conflicting objectives, such as the concern of fuel consumption and emissions in an engine design [96]. To deal with a set of optimal solutions, multi-objective *GA*s (MOGAs), coupled with the concept of the Pareto optimum solution, were introduced [90, 97]. However, to promote the optimization performance, values for certain merit functions have to be degraded, otherwise none of the merit functions can be improved. Apart from the guidance of elite engine designs that can be provided by this methodology, the preference-based single optimum solution can be obtained as well if a higher-level information is available.

Though superiority of the GA-CFD approach is obvious upon its ability to deal with complex problems and parallelism, a GA-CFD methodology may take a considerable amount of time (over 2 or 3 months) for a problem with a moderate design features (5-10) to optimize for even with a sophisticated cluster (100-1000 processors) [98], attributing to the fact that physics-based CFD simulations tend to be very expensive. Any inappropriate choice of initial setup for a GA-CFD will make it difficult for the algorithm to converge or it will simply produce meaningless results. Consequently, the dilemma that arises now is how to maintain accuracy of engine models without increasing the cost of central processing unit (CPU) time.

During the last few decades, AI techniques have been applied with great success to many scientific and engineering to tackle complex and ill-defined problems because of their remarkable capabilities of performing cognitive tasks with human-like characteristics [99]. As a major subset of AI, machine learning (ML) aims to give computers the ability to autonomously complete tasks by detecting patterns and improving performance based on data and empirical information, and subsequently to make future predictions using new data. ML has recently promoted research work on internal combustion engines to a novel era.

In the past, an abundance of data has been collected/generated both experimentally and computationally at the cost of significant time and money; experimental data helped to validate physical theories that planted in models, and outcomes of a simulation as a hypothesis provided a way of starting the experimental process. However, not enough information from data has been extracted and exploited sufficiently. Nevertheless, ML can be applied to existing data analysis processes to enhance pattern recognition and support more sophisticated data analysis. By developing data-driven ML models, programs learn from data rather than following hard-coded rules, capture input-output relationships, and finally provide an accurate and faster-running surrogate model for CFD. Attempts have been made in understanding and solving combustion problems [100-103] with the state-of-the-art ML methodology, and it has been reported that these cost-effective ML-based model can successfully be used for real engine control applications. Recent studies [98, 104, 105] combined GA and ML to predict and optimize CI engine performances. Instead of evaluating the CFD models in sequentially large batches to perform the optimization, GA runs over the search space created from the ML models trained from a lower number of CFD simulations in a parallel fashion.

However, the application of data-driven ML models in IC engine research is rather limited, and investigations and evaluations on these novel modeling approaches for other phenomena occurring over the engine operations are not well conducted. Furthermore, ML is stochastic, not deterministic, and there are no available constraints to the algorithms, occasionally leading to the unrealistic outcomes from the models. Applications akin to AI are not able to understand the situations that occur inside an engine cylinder and derive the right meaning from it. This barrier of meaning makes current ML give rise to potentially catastrophic errors and remain vulnerable in

engineering fields. Therefore, it is important to add physical constrains or interpretations to ML models, incorporating the law of nature of with ML methodologies.

1.6 A Brief Introduction to KIVA

The CFD platform used in this work is a customized version of KIVA-3V release 2 program [106]. The KIVA-3V computer code is a version of the KIVA-family CFD open-source codes developed by the Los Alamos National Laboratory (LANL) and is in use world-wide among the engine research communities. KIVA has ability to calculate complex physical and chemical processes in engine cylinders, including the turbulence flow, evolutions of evaporating fuels, transient three-dimensional dynamics of sprays, fuel-air mixing, ignition, ignition and combustion, chemical reactions, and heat transfer.

KIVA-3V is based on a block-structured, staggered grid, which allows complex geometries to be modeled as discrete blocks of zones can be coupled together to build the required structure. The Arbitrary Lagrangian Eulerian (ALE) finite volume method is applied to simulate flow fields with both continuous and discrete phases. Gas phase (continuous) is modeled in Eulerian coordinates and described by Navier-Stokes equation combined with continuity, energy and k-ε turbulence equations. Liquid fuel spray is considered as a large number of discrete parcels, and each parcel is a cluster of droplets with identical properties. Each parcel undergoes subsequent processes of breakup, collision and coalescence, and evaporation. For the liquid core near the injector nozzle, it is represented by these parcels as "blobs" of liquid [107]. A separate set of transport equations are utilized to describe the behavior of these Lagrangian parcels. Coupling of these two phases is accomplished with two source terms charactering the liquid-gas interactions and chemical reactions.

Within each computational cycle, three-phases solution procedure is adopted. Spray dynamics and source terms are solved with no convection across cell boundaries. Next, diffusion terms, as well as the pressure gradient and velocity changes, are computed semi-implicitly. Note that above two phases are performed with Lagrangian approach. The last step is the rezone phase to account for the effect of remapping onto the mesh because of valve and piston movement, and the convective transport is calculated explicitly. Consequently, thermodynamic quantities and vectors are updated that the former is stored at the center of cells and the latter is on the cell vertex and used immediately in next cycle.

In this study, recently developed droplet vaporization model and flash-boiling spray model are implemented into KIVA-3V to improve the accuracy of the spray calculations under various engine operations conditions. A novel concept of improving CI engine performance is tested in KIVA-3V and optimization on engine parameter is carried out to finalize the proposed method. The state-of-the-art modeling approach makes use of ML methodology is presented, and the results from previous KIVA-3V CFD simulations are utilized as the database to train and test these data-driven models.

1.7 Objectives and Overview

The works presented in this dissertation primarily focus on two objectives, first is the liquid fuel atomization and vaporization modeling, and second portion is the computational investigation of mixture preparation with renewable fuel. Two research methodologies are presented: high-fidelity CFD simulations and artificial intelligence techniques.

In an engine operation cycle, the liquid fuel injection process and air-fuel mixture preparation can greatly impact engine performance. A schematic of liquid fuel injection and fuel

vapor mixing process is given in Figure 1.1. Each liquid jet atomizes into droplets and ligaments at the exit from the nozzle orifice. As the fuel spray entrains air, it spreads out and slows down as the mass flow in the spray increases. The droplets on the outer edge of the spray evaporate first, creating a fuel vapor-air mixture sheath around the liquid-containing core, and the tip of spray penetrates further into the combustion chamber as injection proceeds. At a point, fuel vapor and air mix properly and the environment temperature is high enough then combustion occurs, producing energy as well as emissions products. How well the air and fuel vapor mix will determine the onset of combustion thus the engine efficiency

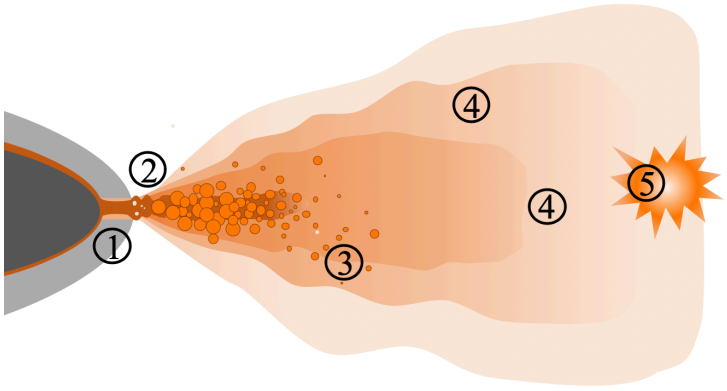


Figure 1.1: Fundamental processes of liquid fuel injection and vapor-air mixing.

An efficient multi-component fuel droplet vaporization model has been developed in this work using discrete approach. The precise modeling of droplet vaporization process is divided into two parts: vapor-phase and liquid-phase sub-models. Temporal evolution of flow inside the droplet is considered to describe the transient behavior introduced by the slow diffusion process. To account for the internal circulation motion, surface regression and finite diffusion without actually resolving the spatial governing equations within the liquid phase, a set of ordinary differential

equations is applied to describe the evolution of the non-uniform distributions of universal diffusional variables, i.e., temperature and species mass fraction. The differences between the droplet surface and bulk mean states are modeled by constructing a quasi-1D frame; the effect of the internal circulations is taken into consideration by using the effective diffusivity rather than physical diffusivity. Such quasi-1D droplet vaporization model can be applied into engine simulations without increasing the computational cost.

The second objective is to develop a comprehensive model for spray atomization under the consideration of flash boiling which includes nucleation, bubble growth, and droplet breakup. Although flash boiling has been studied previously, there is still no well-established analytical and numerical model of their mechanisms, or general guidelines on the implementation of this atomization strategy. This study is motivated by its close relation to spray atomization and fuel vaporization and its potential to improve air-fuel mixing in engines. The presented flash boiling model can be used to understand atomization mechanisms under different environment conditions and to estimate the SMD of the secondary droplets after breakup.

Next, the study of engine combustion and emissions are presented. A new approach of NOx reduction in the CI engine is introduced in this work. The previous research has shown that during the combustion stage, the high temperature ignition tends to occur early at the near-stoichiometric region where the combustion temperature is high and majority of NOx is formed; therefore, it is desirable to burn the leaner region first and then the near-stoichiometric region, which inhibits the temperature rise of the near-stoichiometric region and consequently suppresses the formation of NOx. Such inverted ignition sequence requires a mixture with inverted ϕ-sensitivity. Combustion with single-injection strategy is analyzed first under various engine load conditions using the fuel exhibits the such inverted ϕ-sensitivity, and possible improvements are discussed. To complete the

design processes, multi-injection strategies are presented next. Optimal engine operation parameters are exploited using GA methodology for the sake of reducing engine-out emission while keep a high engine efficiency.

For the rest of this work, the advanced technique, ML, for model development is presented. Unlike the CFD models to directly solve the complex thermodynamic, chemical kinetic, and fluid dynamic process that go on in an engine, ML models aim to give computers the ability to autonomously complete tasks by detecting patterns and improving performance based on data and empirical information, and subsequently to make future predictions using new data. Sample CFD simulation datasets are generated as "synthetic" training data to teach a fast-running, compact ML model the key relationships between the design features, and the engine outcomes (for example the fuel efficiency of an engine). The ML model then is coupled with GA methodology to accelerate the optimization process and shorten the engine design period to meet the industrial interests. By addressing the ML techniques, modeling, optimizing, and controlling for ICEs tend to be more competing and productive.

CHAPTER 2: MODELING OF QUASI-1D MULTI-COMPONENT FUEL DROPLET VAPORIZATION USING DISCRETE APPROACH

An efficient multi-component fuel droplet vaporization model has been developed in this work using discrete approach. The precise modeling of droplet vaporization process is divided into two parts: vapor-phase and liquid-phase sub-models. Temporal evolution of the flow inside the droplet is considered to describe the transient behavior introduced by the slow diffusion process. To consider the internal circulation motion, surface regression and finite diffusion without indeed resolving the spatial governing equations within the liquid phase, a set of ordinary differential equations is applied to describe the evolution of the non-uniform distributions of universal diffusional variables, i.e., temperature and species mass fraction. The differences between the droplet surface and bulk mean states are modeled by constructing a quasi-1D frame; the effect of the internal circulations is taken into consideration by using the effective diffusivity rather than physical diffusivity. Peng-Robinson (PR) Equation of State (EOS) is utilized to deliberate the non-ideal behavior in a high-pressure environment and to compute the vapor-liquid equilibrium (VLE) at droplet surface. The quasi-steady assumption is made for the gaseous flow in determining vaporization rate and heat flux to the droplet. The model is verified and validated with the experimental data measured from a non-combusting droplet chamber and with other extensive data from the literature prior to implementing into engine CFD platform.

2.1 Experimental Setup

A schematic of the experimental setup is presented in Figure 2.1. The droplet is suspended on a 100 μm diameter silica fiber (as indicated in Figure 2.1 (B)) and placed inside a constant

volume chamber. The size of the suspension filament is carefully selected to minimize the conduction effect [44, 108, 109]. The support fiber is bent for the purpose of guiding the droplet to slide away from the droplet generation system, eliminating the effect of the residual fuel on the tip of the droplet-generating needle. A thermocouple with a diameter of 50 µm is inserted into the droplet to measure the temperature inside the droplet. Multiple measurements for one sample fuel blend are taken to acquire droplet temperature observations.

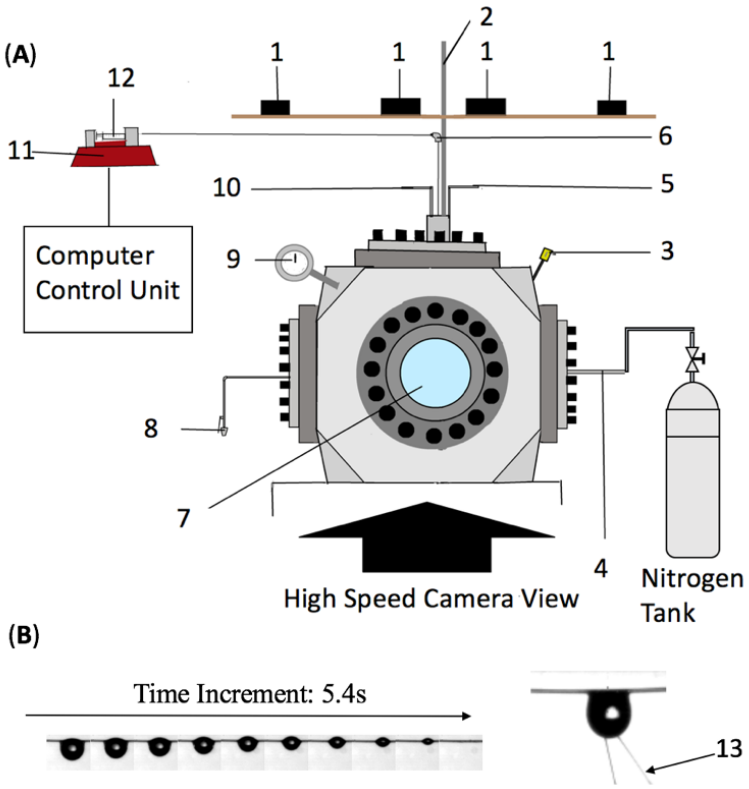


Figure 2.1: (A) schematic of the experimental setup; (B) suspended droplets on a silica fiber. (1) PID temperature control system, (2) droplet detachment system, (3) thermocouple, (4) nitrogen intake, (5) coolant intake, (6) fuel intake, (7) observation window, (8) nitrogen outlet, (9) pressure gauge, (10) coolant outlet, (11) syringe pump, (12) fuel injecting syringe, and (13) thermocouple used to measure droplet. interior temperature.

Six tubular heaters are embedded on each side of the chamber to heat up nitrogen (N_2), the ambient gas, to a desired temperature. Heaters are controlled by individual PID controllers to maintain the ambient temperature variations within ±0.5°C range for all testing cases. The ambient

temperature is measured by a K-type thermocouple placed inside the suspended droplet. A precise pressure gauge is installed on the top of the chamber to measure the ambient chamber pressure. Two cylindrical quartz windows are mounted on the front and the back side of the chamber to provide optical access. A liquid nitrogen tank is connected to supply nitrogen gas to the chamber. After each test, the chamber is flushed for 10 minutes with nitrogen to remove all the residues. A 600W halogen light and a light diffuser are used to create uniform illumination for the droplet. A high-speed camera (Phantom V7.1) with a 105-mm focal length lens (Nikkor) is placed at the opposite side of the light source to record the histories of droplet evaporation process. After comparing evaporation coefficient of several test cases, no significant difference is found for 100, 200, 300 frames per second. Therefore, 100 frames per second is used for experiments with relatively low ambient temperature conditions, and 300 frames per second is used for experiment with relatively high ambient temperature conditions. All images are taken with a resolution of 80 × 60 pixels. Droplets are generated by a drop-on-demand system which contains a precise syringe pump and a syringe with a 33-gauge needle. A cooling jacket is carefully designed to provide continuously cooling until the droplet separated from the needle. Heavy insulation is applied around the cooling jacket to minimize the effect on ambient temperature.

2.2 Liquid Phase Sub-Model

One of the major tasks of developing the droplet vaporization model is to accurately describe the unsteady flow inside the droplet. Previously, the liquid mixture of the simplified quasi-steady model was presented as an ideal mixture, i.e. the states of the droplet are spatially uniform but temporally varying. However, real fuel droplet contains components with different vaporization rates. As a result, there are concentration gradients in the liquid phase. The light

components preferentially vaporize more quickly at the droplet surface. Due to the finite mass diffusional rate, the light component deep inside the droplet is inhibited to reach the surface quickly. The droplet heating process is complex because it depends on the relative magnitude between the liquid-heating time scale and the droplet lifetime, which is then further complicated by the droplet internal circulation. A quasi-1D liquid model is developed in this section to account for the preferential vaporization of the fuel droplet and to describe the enhanced diffusional effect within the droplet. The formation of the liquid-phase sub-model is developed based on the work by authors' laboratory [110]. Instead of calculating the temperature and mass fraction within the droplet, the diffusion variables such as temperature and mass fraction differences between the droplet surface value and the bulk average values, ϕ, are solved in the transport equations for computational efficiency.

By assuming the droplet has spherical symmetry with uniform pressure, the governing equations for mass and energy can be written in the following forms:

$$\frac{\partial \rho_l Y_{li}}{\partial t} + \frac{\partial \rho_l Y_{li} r^2 V}{r^2 \partial r} = \frac{\partial}{r^2 \partial r}\left(D_{li}^e \rho_l r^2 \frac{\partial Y_{li}}{\partial r}\right) \tag{2.1}$$

$$\frac{\partial \rho_l C p_l T_l}{\partial t} + \frac{\partial \rho_l C p_l T_l r^2 V}{r^2 \partial r} = \frac{\partial}{r^2 \partial r}\left(k_l^e r^2 \frac{\partial T_l}{\partial r}\right) \tag{2.2}$$

where t is time and r is the radial spherical coordinate. ρ_l, Y_i $(i = 1, \dots, n)$, Cp_l and T are the density, the mass fraction of species i, specific heat, and temperature of the liquid droplet, respectively. The effective coefficients of the mass diffusivities D_{li}^e and the thermal conductivity, k_l^e, first developed by Jin and Bormann [111], are used to account for the enhancement of the transport by the internal circulation within the droplet:

$$\frac{D_{li}^e}{D_{li}} = 1.86 + 0.86 \cdot \tanh\left[2.245 \cdot log_{10}\left(\frac{Re_l \cdot Sc_l}{30}\right)\right] \tag{2.3}$$

$$\frac{k_l^e}{k_l} = 1.86 + 0.86 \cdot \tanh\left[2.245 \cdot log_{10}\left(\frac{Re_l \cdot Pr_l}{30}\right)\right] \tag{2.4}$$

Sc_l is the Schmidt number, Pr_l is the Prandtl number, and Re_l is the droplet Reynolds number in terms of the droplet radius, the nominal velocity u for the internal circulation, and the liquid viscosity,

$$Re_l = \frac{2\rho_l u R}{\mu_l} \qquad\qquad u = \frac{1}{32}\frac{\mu_g}{\mu_l}\frac{12.69Re^{1/3}}{1+\mathcal{B}}\,U$$

where U is relative velocity between the droplet and ambient gas, and $\mathcal{B}$ is the transfer number. With the enlarged diffusivities included in the diffusion transport terms in the right-hand side of Eq. (2.1) and (2.2), the mass fraction and temperature profiles can be determined first. The convective terms in Eq. (2.1) and (2.2), become less important since the density for hydrocarbons is also very similar. Therefore, to simplify the derivation, the convective term can be neglected, and the governing equations for mass and temperature can be expressed in the following generalized form,

$$\frac{\partial \Phi}{\partial t} = \frac{\partial}{r^2 \partial r}\left(\Gamma_\Phi^e r^2 \frac{\partial \Phi}{\partial r}\right) \tag{2.5}$$

The diffusional variables Φ represents either the mass fraction Y_{li} or temperature T, and Γ_Φ^e is either the mass diffusion coefficient D_{li}^e or the thermal diffusion coefficient $k_l^e/(\rho_l Cp_l)$. With the spherical symmetry assumption, the boundary condition at the droplet center is $\frac{\partial \Phi}{\partial r}|_{r=0} = 0$. The boundary at the interface, i.e., $r = R(t)$, can be determined by the vaporization rate and heat flux into the droplet. At the droplet surface, the mass flux for each species, by continuity, is

$$\omega_i = Y_{li,s}\omega - \rho_l D_{li}^e \left.\frac{\partial Y_{li}}{\partial r}\right|_{r=R} \tag{2.6}$$

ω is the total vaporization rate. The heat flux from the ambient gas to the droplet q, i.e. the sensible energy in Eq. (2.7), equals the energy difference in conductive fluxes to the energy required for

vaporizing the liquid at the droplet surface from Eq. (2.8), where h_l is heat transfer coefficient from the ambient gas to the droplet, T_∞ and T_s are the ambient temperature and droplet surface temperature, respectively, and $H_{v,i}$ is the latent heat of vaporization of species i.

$$q = h_l(T_\infty - T_s) - \sum \omega_i H_{v,i} \tag{2.7}$$

$$q = k_l^e \left.\frac{\partial T}{\partial r}\right|_{r=R} \tag{2.8}$$

Thus, the generalized form for boundary conditions is,

$$\left.\frac{\partial \Phi}{\partial r}\right|_{r=0} = 0 \qquad\qquad \left.\frac{\partial \Phi}{\partial r}\right|_{r=R} = \psi$$

ψ is determined from Eq. (2.6) for mass fraction and from Eq. (2.7) and (2.8) for heat flux at droplet surface. To initialize the problem, it is assumed that the initial distributions of mass fraction and temperature are inside the droplet; that is $\Phi|_{t=0} = \Phi_0$.

Strategies to solve the non-linear, second order equation Eq. (2.5) are to capitalize on the normalized form of the governing equations with $t = \tau R^2/\Gamma_\Phi^e$ and $r = \zeta R$. Non-dimensional equation through the coordinate transformations, suggested by Zeng and Lee [110] and Wang [28], equations are obtained and given by

$$(1 + 2\tau Pe)\frac{\partial \phi}{\partial \tau} + \left(\zeta\, Pe - \frac{2}{\zeta}\right)\frac{\partial \phi}{\partial \zeta} - \frac{\partial^2 \phi}{\partial \zeta^2} = 0 \tag{2.9}$$

$$\left.\frac{\partial \phi}{\partial \zeta}\right|_{\zeta=0} = 0 \qquad \left.\frac{\partial \phi}{\partial \zeta}\right|_{\zeta=1} = \beta \qquad Pe_i = -\frac{RdR/dt}{D_i^e} \qquad Pe_T = -\frac{RdR/dt}{k^e/(\rho_l C_p)}$$

Pe represents the Peclet number and subscript i and T denote for mass and energy transport, respectively. The approximated analytical solution after solving Eq. (2.9) is shown below, and μ_1 is a constant which is came forth from the procedure of separation of variables.

$$\phi(\tau, \zeta) \approx \phi_0 + 3\beta\tau + \frac{\beta\zeta^2}{2}\left(1 - e^{-\mu_1^2 \tau}\right) \tag{2.10}$$

By differentiating Eq. (2.10), the following expression is obtained:

$$\frac{d(\phi_s - \bar{\phi})}{d\tau} \approx \mu_1^2[\gamma\beta - (\phi_s - \bar{\phi})] \tag{2.11}$$

The preferential vaporization process is controlled by parameter γ, which is a constant coming from the mathematical derivation of $\phi(\tau, 1) - \bar{\phi}(\tau, \zeta)$. For the infinite diffusion model, $\gamma = 0$; and for preferential vaporization, $\gamma = 0.2$. If using the physical time and space, Eq. (2.11) can be expressed as,

$$\frac{d(\phi_s - \bar{\phi})}{dt} \approx \frac{\mu_1^2\left[\gamma E(Pe)\left.\frac{\partial\phi}{\partial r}\right|_{r=R} R - (\phi_s - \bar{\phi})\right]}{E(Pe)R^2/\Gamma_\Phi^e} \tag{2.12}$$

where ϕ represents either mass fraction, Y_i, of component i, or temperature T. With Eq. (2.12), the rate of the difference between the surface ϕ_s and mean $\bar{\phi}$ values can be predicated. It should be noted that $\left.\frac{\partial\phi}{\partial r}\right|_{r=R} R$ on the right-hand side indicates the equilibrium value of $\phi_s - \bar{\phi}$, and R^2/Γ_Φ^e is the time scale for the transient process. The time rate of change of the transport variables is proportional to the deviation from the equilibrium values. $E(Pe)$ is the normalized difference between the surface value and average value. The tabulated data of $E(Pe)$ for different Peclet numbers are implemented into the code to save computational time. It has been observed that with increasing Pe, the normalized difference decreases in a linearly manner initially, suggesting that the transport process tends to be enhanced by the surface regression.

2.3 Gas Phase Sub-Model

To completely solve the droplet vaporization process, the mass and energy balance at the droplet interface are needed. In this study, the gas phase heat and mass transfers are considered as quasi-steady, the pressure change is negligible in the ambient, and the gas phase properties are

evaluated at the reference conditions using the "1/3 rule". Furthermore, to accurately describe the gas phase sub-model, the correction factor for Stefan flow is applied to properly amend the effect of surface blowing. To completely solve the droplet vaporization process, the mass and energy balance at the droplet interface are needed. the evaporation rate of component i is given in Eq. (2.13), and $\overline{D}_{g_i}$ is the gas mass diffusivity at reference state. $\mathcal{B}_i$ is the transfer number of component i, and ξ_i is the correction factor for the effect of Stefan flow. Sh_i is the Sherwood number of component i and is given by [111].

$$\omega_i = \frac{\bar{\rho}_g \overline{D}_{g_i}}{2R} \mathcal{B}_i \xi_i Sh_i \tag{2.13}$$

$$Sh_i = 2 + \frac{0.552 Re^{1/2} \overline{Sc}^{1/3}}{[1 + 1.232/(Re\overline{Sc}^{4/3})]^{1/2}} \qquad \mathcal{B}_i = \frac{Y_{gis} - Y_{i\infty}}{1 - Y_{gis}}$$

$Y_{i\infty}$ is the gas-phase mass fraction of component i in the ambient; Y_{gis} is the gas-phase mass fraction of component i at the droplet surface, and it is determined by the thermodynamic phase equilibrium at the droplet surface. The correction factor ξ_i [111], shown in Eq. (2.14), is greater than unity. When a droplet is vaporizing, the equimodal rates of diffusion under the fixed pressure condition is not valid since in most cases it is assumed that the diffusion of fuel species from the vaporizing droplet surface is unidirectional; while the diffusion rate of the ambient gas, nitrogen for example, towards the droplet is assumed to be zero. For this reason, the mass transfer coefficient is corrected to account for the effect of vaporization.

$$\xi_i = \frac{z_i}{e^{z_i} - 1} \qquad z_i = \frac{\omega}{Sh_i \bar{\rho}_g \overline{D}_{g_i}/2R} \tag{2.14}$$

The heat flux to the droplet is calculated from Eq. (2.15). Again, h_l is the heat transfer coefficient from the ambient gas to the droplet, which is the function of Nu, Nusselt number. k_g is the gas conductivity evaluated at the reference state, and ξ_T is the Stefan flow correction factor

on heat transfer [111], representing the fraction of the total heat transfer from the environment supplies to the liquid droplet as the latent heat of vaporization and the sensible heat,

$$q = h_l(T_\infty - T_s) - \sum \omega_i H_{v,i} \tag{2.15}$$

$$h_l = Nu\frac{k_g}{2R}\xi_T \qquad Nu_i = 2 + \frac{0.552Re^{1/2}\overline{Pr}^{1/3}}{[1 + 1.232/(Re\overline{Pr}^{4/3})]^{1/2}}$$

$$\xi_T = \frac{z_T}{e^{z_T} - 1} \qquad z_T = \frac{\sum \omega_i \overline{Cp}_{gi}}{Nuk_g/2R}$$

$\overline{Cp}_{gi}$ is the gas-phase heat capability of component i. To solve the gas-phase mass fraction at the droplet surface, equilibrium at the gas-liquid interface is needed. The evaluation of droplet surface temperature, T_s, is also definitive because the gas-phase property predictions and heat transfer relations are on the premise of realizing precise prediction of the droplet surface temperature.

To account the effect of convective ambient flow on the vaporization rate, an empirical relation [112] is adopted as shown in Eq. (2.16). It describes that the droplet vaporization rate (C_v) in a convective flow is proportional to that in a free convection flow condition. Therefore, instead of explicitly calculating the drag effect due to the gas flow on the droplet vaporization process, the evolution of droplet size in convective flow can be corrected with the gas phase Reynolds number.

$$\frac{C_v(Re_g)}{C_v(0)} = 1 + 0.276\mathrm{Sc}_g^{1/3}Re_g^{1/3} \approx 1 + 0.25Re_g^{1/2} \tag{2.16}$$

2.4 Vapor-Liquid Equilibrium

The gas effect of VLE calculation during the droplet vaporization process is examined in this sub-section. Previously a simple and common method for solving VLE was to conduct Raoult's law coupled with the Clausius–Clapeyron relation. However, the prerequisite of applying this method is to assume ideal mixture behavior. Under most practical circumstances in engine

application, the ambient pressure is relatively high, thus the assumption of ideal gas law is no longer applicable.

To account for the effect of non-ideal behavior under the high-pressure environment, Peng-Robinson (PR) equation of state (EOS) [113] can be used, and its pressure-explicit form is,

$$P = \frac{\hat{R}T}{\hat{v} - b} - \frac{a}{\hat{v}^2 + 2b\hat{v} - b^2} \tag{2.17}$$

$\hat{v}$ is the molar based specific volume, coefficients a and b are made functions of the critical properties by imposing the criticality conditions, which yields:

$$a = \sum_{i}^{n_{sp}} \sum_{j}^{n_{sp}} X_i X_j a_{ij} \qquad b = \sum_{i}^{n_{sp}} X_i b_i$$

$$a_{ij} = (1 - \delta_{ij})\sqrt{a_i a_j} \qquad b_i = 0.077796\hat{R}T_{ci}/P_{ci}$$

$$a_i = 0.457235\frac{\hat{R}^2 T_{ci}^2}{P_{ci}}\left[1 + \kappa_i\left(1 - \sqrt{\frac{T}{T_{ci}}}\right)\right]^2 \qquad \delta_{ij} = 1 - \left(\frac{2\sqrt{v_{ci}^{1/3} v_{cj}^{1/3}}}{v_{ci}^{1/3} + v_{cj}^{1/3}}\right)^6$$

$$\kappa_i = 0.37464 + 1.5422\omega_i - 0.26692\omega_i^2$$

where P_{ci} is the critical pressure, T_{ci} is the critical temperature, ω_i is the eccentric factor, and $\hat{R}$ is the universal gas constant. δ_{ij} is an empirically determined binary interaction coefficient characterizing by component i and component j, and v_c is the critical molar volume of liquid species. In this study the semi-theoretical relation [114], developed for nonpolar mixture, is adopted. Due to this fact, the expression for δ_{ij} is prominent for paraffin-paraffin system, so for other system, it may have large errors. To find the roots of Eq. (2.17), following polynomial format in Eq. (2.18) is used. A and B are dependent on pressure, temperature, and composition, and Z is the compressibility factor

$$PZ^3 - (1 - B)Z^2 + (A - 3B^2 - 2B)Z - (AB - B^2 - B^3) = 0 \tag{2.18}$$

$$A = \frac{aP}{\hat{R}^2 T^2} \qquad B = \frac{bP}{\hat{R}T} \qquad Z = \frac{P}{\rho_l \hat{R}T}$$

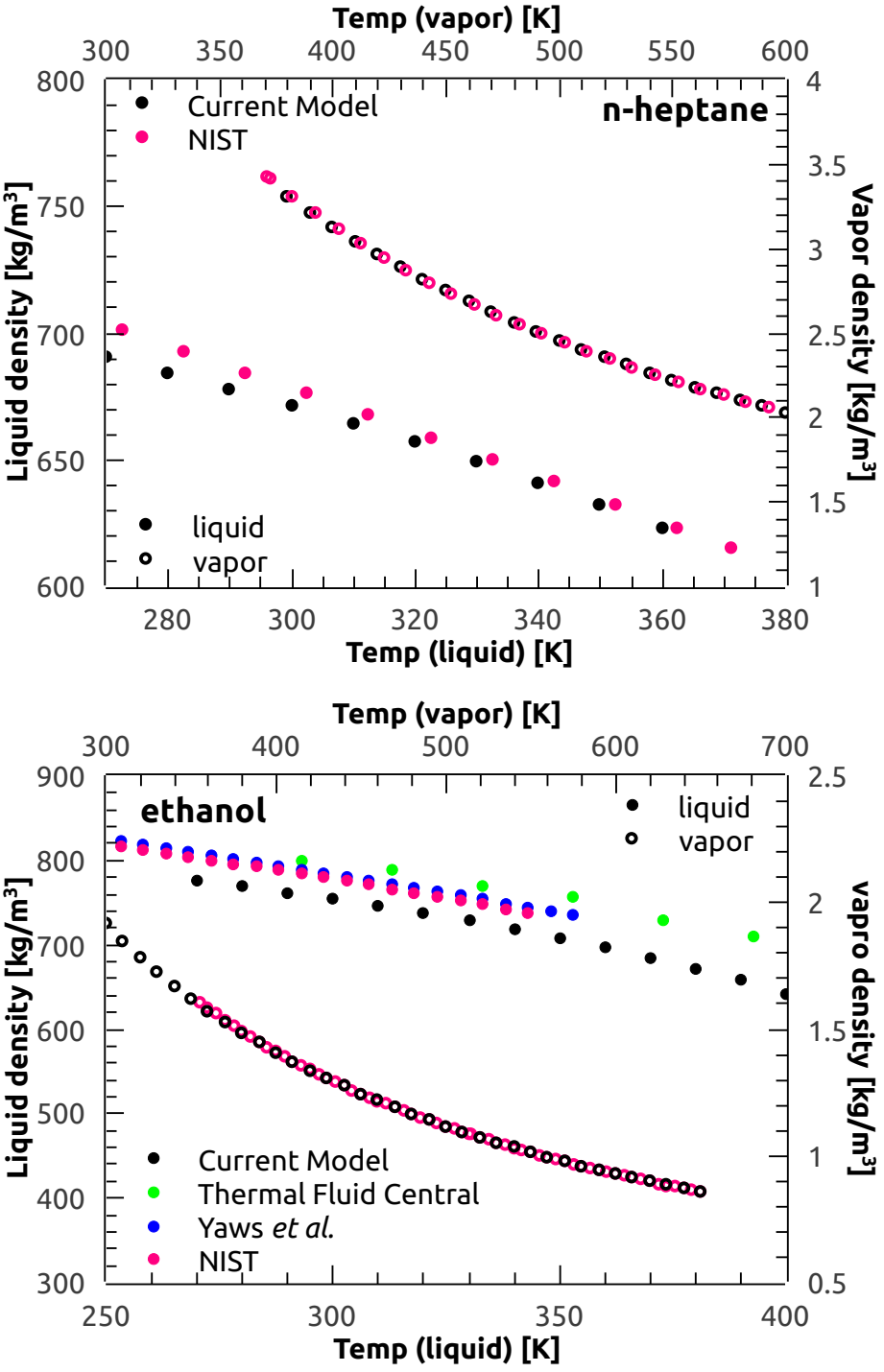


Figure 2.2: Variation of fluid density versus temperature for n-heptane and ethanol. The measured data is from [115-117].

One or three real roots can be obtained for Z for a given state. The largest real root corresponds to the gas phase, and the smallest real root corresponds to the liquid phase. Predictions of density for pure n-heptane and pure ethanol, representing the kind of alkanes and oxygenated fuels respectively, are tested first and shown in Figure 2.2. Both liquid phase and gaseous phase density predictions are consistent with the measured data over the wide range of temperatures under atmospheric pressure. Modeled PR EOS then is applied to calculate binary liquid mixtures of n-butanol/hexane and n-butanol/octane system. The results in Figure 2.3 show the reasonable accuracy compared with the measurements [118].

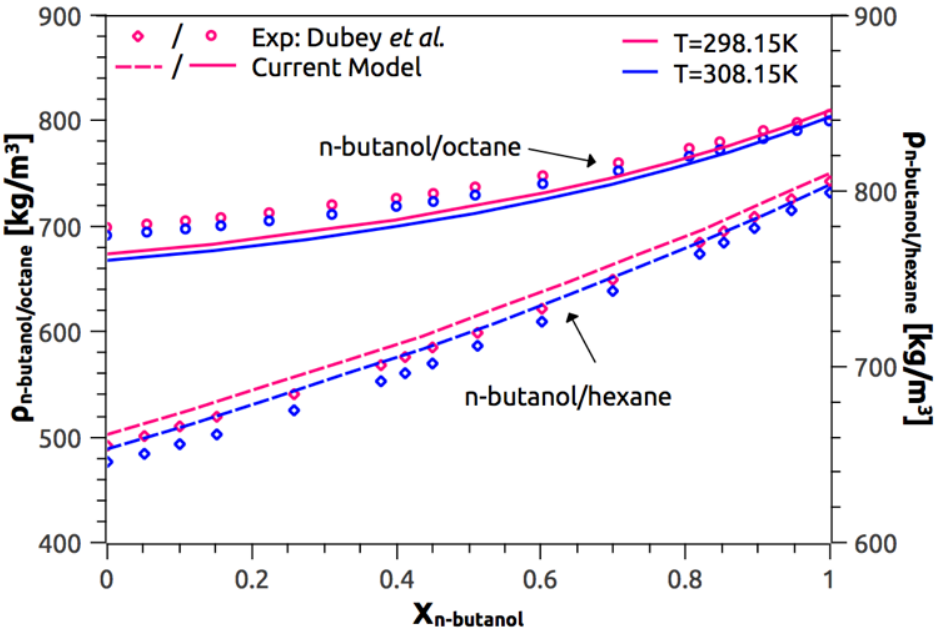


Figure 2.3: Droplet surface temperature just before the end of the vaporization. The measured data is taken from Dubey *et al*. [118]

To determine the phase-equilibrium relation at the interface, $r = R(t)$, the species fugacities of liquid and gas are set to be equal, and temperature is assumed to be continuous across the interface,

$$T_{ls} = T_{gs} \qquad\qquad \theta_{lis} X_{lis} = \theta_{gis} X_{gis}$$

θ_i is the fugacity coefficient of species i in the local fluid mixture, $\theta_i = f_i/PX_i$, and can be calculated using PR EOS [119],

$$ln\theta_i = \frac{b_i}{b}(Z-1) - ln(Z-B) + \frac{A}{2\sqrt{2}B}\left(\frac{b_i}{b} - \frac{2}{a}\sum_j^{n_{sp}} X_j a_{ij}\right) \cdot ln\left(\frac{Z+\left(1+\sqrt{2}\right)B}{Z+\left(1-\sqrt{2}\right)B}\right) \quad (2.19)$$

The phase equilibrium solver is tested and verified by comparing the calculated results with the measured data from literature. In Figure 2.4, the vapor-liquid equilibrium for the binary system composed of n-pentane and n-heptane are calculated at three different pressures. The predictions of bubble point and dew point for multi-component mixtures at low pressures, for example $P = 10\ atm$, match appropriately with the measurement. The consistency between model and experiment deteriorates with increasing pressure as it approaches the critical pressures of the species; especially at $P = 30.02\ atm$, bubble point and dew point both collapsed. Isothermal VLE tests for different n-alkanes/nitrogen combinations are carried out to verify the capability of the model to predict the phase equilibrium for various fuels. As indicated in Figure 2.5, calculations agree well with the experimental data found in literature. Despite of small discrepancy appears at very high-pressure conditions; it is acceptable since the typical engine operation range is below $200\ atm$.

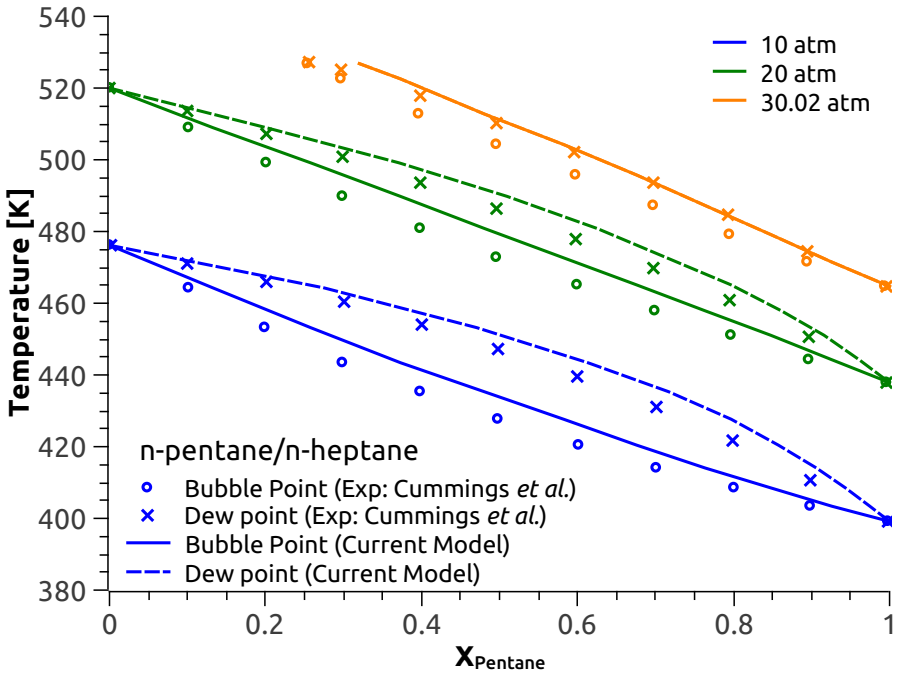


Figure 2.4: Temperature-phase phase diagram for n-pentane/n-heptane system. The experimental data are from Cummings *et al*. [120].

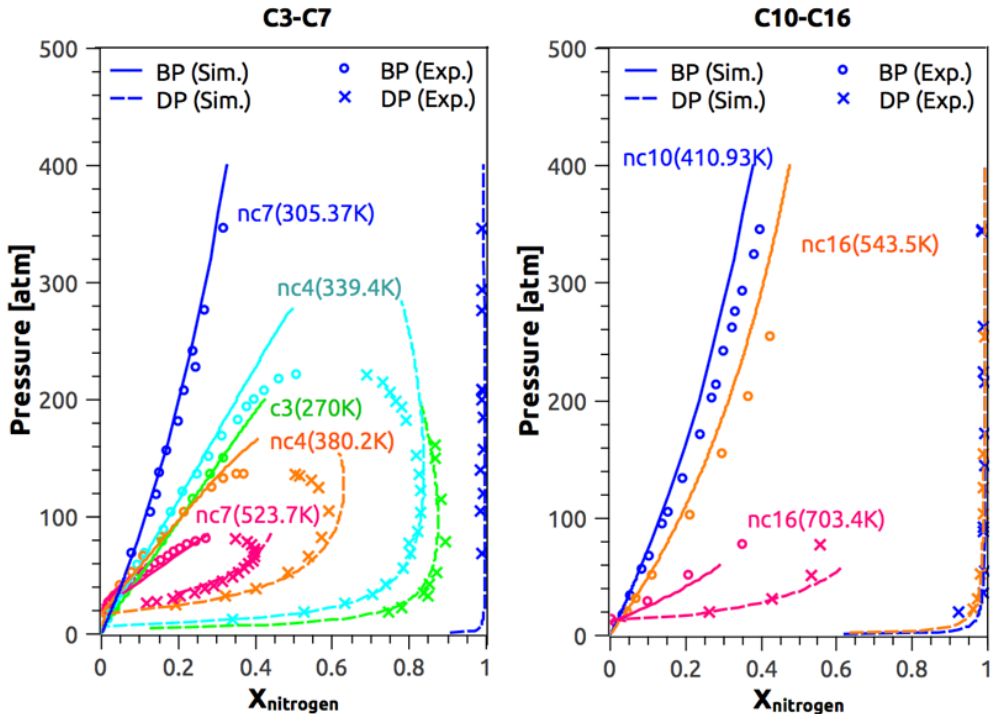


Figure 2.5: Pressure-composition phase diagram for nitrogen-alkanes system. The corresponding experimental data are from [121-125]. BP: bubble point; DP: dew point. c3: pentane, nc4: n-butane, nc7: n-heptane, nc10: n-decane, nc16: n-hexadecane.

2.5 Properties Evaluations

Accurate property evaluation is crucial for multi-component fuel vaporization predictions. To finalize the droplet vaporization model, properties such as the thermal conductivity, viscosity, physical diffusivity, and latent heat of vaporization, mentioned in previous sections need to be evaluated. Viscosity and thermal conductivity are estimated using the method originally derived from the rigorous kinetic theory of Chapman and Enskog to determine the transport properties of low-pressure multi-component mixtures. Chung *et al*. [126, 127] extended the technique to account for the fluid that has a high density and verified the theory for high pressure and condensed fluid. In addition, a factor is used to correct the hydrogen bonding effect. Hence the viscosity and conductivity of a mixture can be estimated with the following equations for viscosity η and thermal conductivity λ, respectively,

$$\eta = \eta^* \frac{36.344(M_m T_{cm})^{1/2}}{V_{cm}^{2/3}} \tag{2.20}$$

$$\lambda = \frac{31.2\eta^o \Psi}{0.001 M_m} \mathcal{H}_1 + \mathcal{H}_2 T_r^{1/2} \tag{2.21}$$

Subscript m refers to the mean value, η^o represents a low-pressure gas viscosity, Ψ is a function of $C_{v,m}$, the mean constant-volume ideal gas thermal capacity, acentric factor ω, and T_r, η^*, $\mathcal{H}_1$, and $\mathcal{H}_2$ are functions of the acentric factor ω, reduced dipole moment, and the association factor.

To precisely estimate the diffusion coefficients, the technique proposed by Riazi and Whiston [128] is applied to calculate the diffusion coefficients for binary systems. The correlation in Eq. (2.22) can be used for both gases and liquids over a large range of pressure. In Eq. (2.23), Ω_{di}, the collision integral, is an empirical function of temperature, and σ is the Lannard-Jones parameter. The detailed derivation of Eq. (2.20) to (2.23), can be found in [28].

$$\frac{\rho D_{im}}{(\rho D_{im})^o} = (1.0664 - 0.1228\rho_{ri} - 0.1118\rho_{ri}^2 + 001983\rho_{ri}^3) \tag{2.22}$$

$$(\rho D_{im})^o = \frac{0.0266[T(M_i^{-1} + M_m^{-1})/2]^{1/2}}{R(\frac{\sigma_i + \sigma_m}{2})^{1/2}\, \Omega_{di}} \tag{2.23}$$

To validate the predication of the fluid properties, the calculated results are compared with the database found in [115, 117, 129]. For model validation purposes, the single component substance is test first, and the predicated viscosity and thermal conductivity for pure n-heptane are shown in Figure 2.6. The calculations for the implemented transport property solver show a reasonable degree of accuracy for single component system. Then the transport property solver is evaluated with the experimental data for binary systems, and results are given in Figure 2.7 to Figure 2.9.

For the condensed binary systems, the estimation of the kinematic viscosity is comparable with the measured data. It is noticed that adding octane lowers the predicted viscosity thus increases the inaccuracy of the model. The thermal conductivity predictions for low-pressure gases binary system in Figure 2.8 indicate the superiority of transport property solver with a maximum derivation of 6%. The calculated and measured [130] diffusion coefficients are plotted in Figure 2.9 for different solute/solvent systems. A relatively large percent deviation about 40% on average, can be observed for n-heptane/n-octane system, but it is acceptable with the suggested accuracy of diffusivity correlations [130]. The preliminary evaluations show that the present transport property solver is satisfactory for modeling purposes.

In this work, the latent heat of vaporization (HOV) is derived from the Watson relation [131]. In Eq. (2.24), subscript r refers to the reduced temperature characterized by the critical temperature of each species, subscript b represents the normal boiling state, and subscript i refers to the target state of species i. A common choice for n is 0.38 [119]. The technique employed to

find the normal boiling point HOV is based on Riedel method [132]. The HOV of each evaporating species obtained from Eq. (2.24) is plugged into Eq. (2.7) which implicitly calculates the total energy required to vaporize the droplet.

$$\Delta H_{v,i} = \Delta H_{v,ib}\left(\frac{1-T_{r,i}}{1-T_{r,ib}}\right)^{n}$$
$$\Delta H_{v,ib} = 1.093RT_cT_{r,ib}\frac{lnP_c - 1.013}{0.93 - T_{r,ib}} \tag{2.24}$$

The HOV of each evaporating species obtained from Eq. (2.24) is plugged into Eq. (2.7) which implicitly calculates the total energy required to vaporize the droplet. Figure 2.10 shows a comparison between experimental results and those calculated by Eq. (2.24). The value of ΔH_v in Figure 2.10 agrees reasonably with that measured data [116]. Good agreement over nearly the entire liquid temperature range can be observed for n-heptane; For ethanol, maximum error of 11% comes at temperature around 400K. Therefore, Watson relation for HOV predictions is more reliable for alkanes. The above demonstration as well as the phase equilibrium calculation indicates that the elementary level of the droplet vaporization modeling structure satisfies the necessary requirement for core modeling processes, i.e. liquid-phase and gas-phase sub-models. In the following section, the elaboration of the droplet vaporization process will be presented.

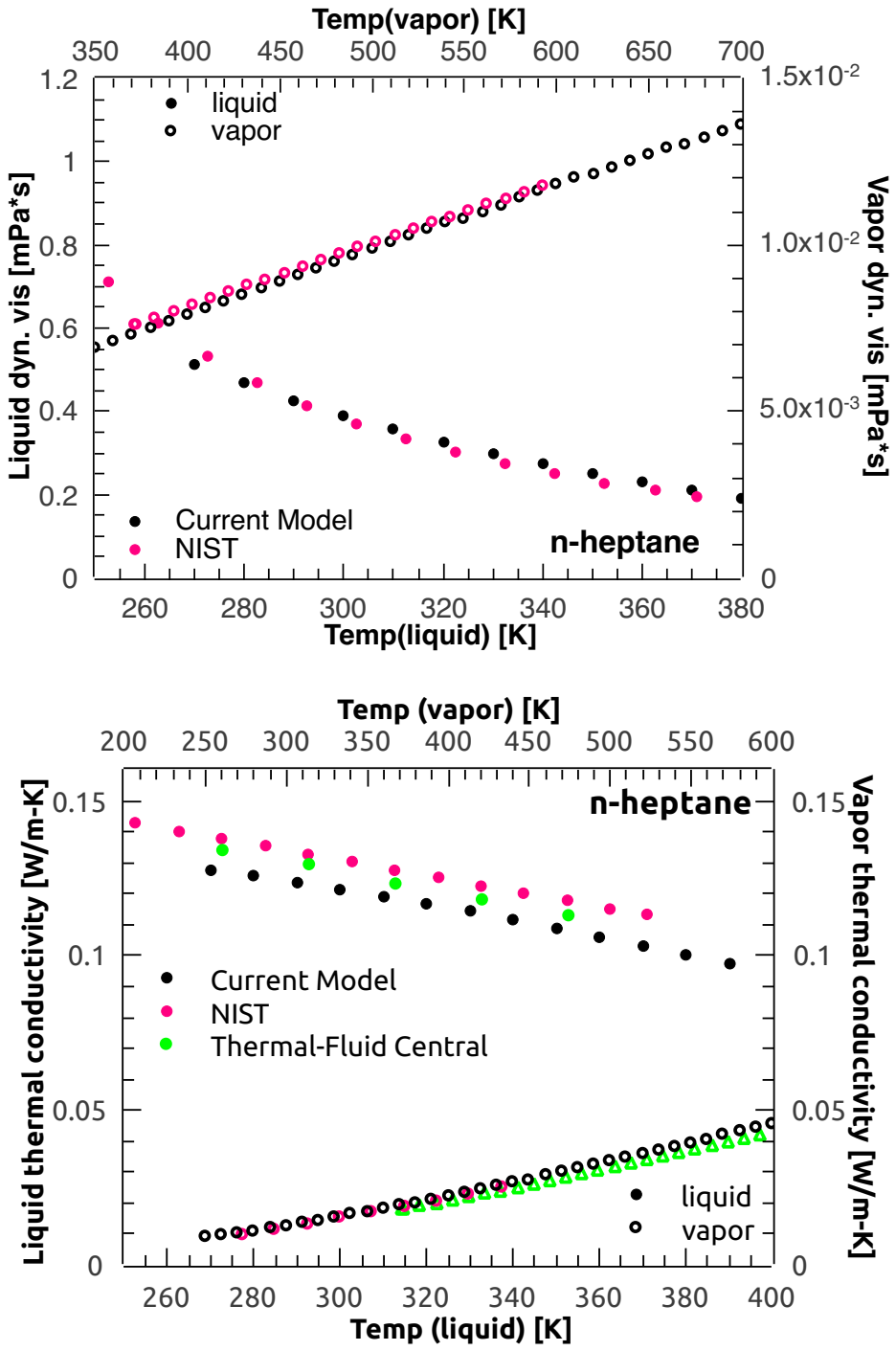


Figure 2.6: N-heptane transport properties comparisons with measured data at atmospheric pressure.

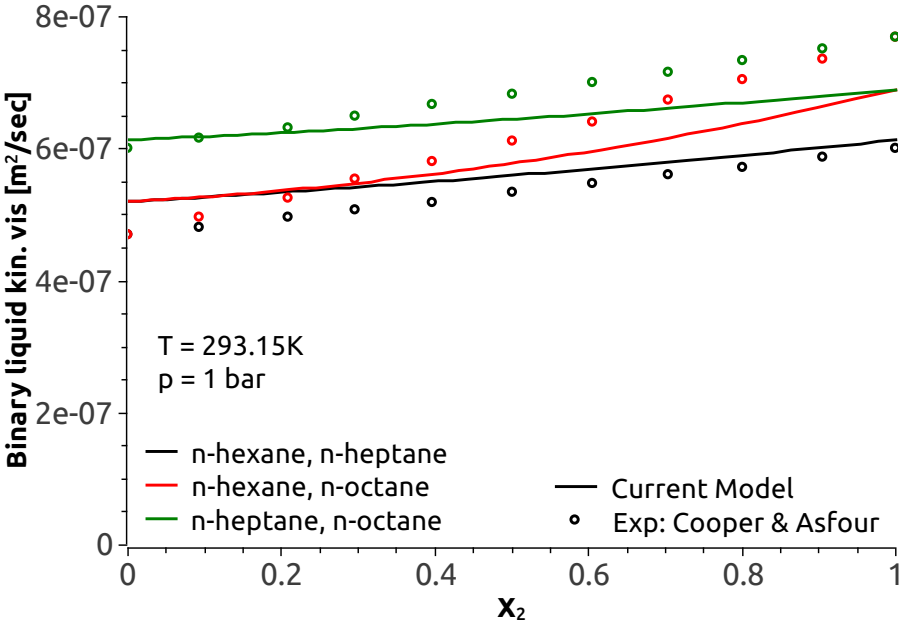


Figure 2.7: Evolutions of viscosity prediction with the experimental data in binary systems.

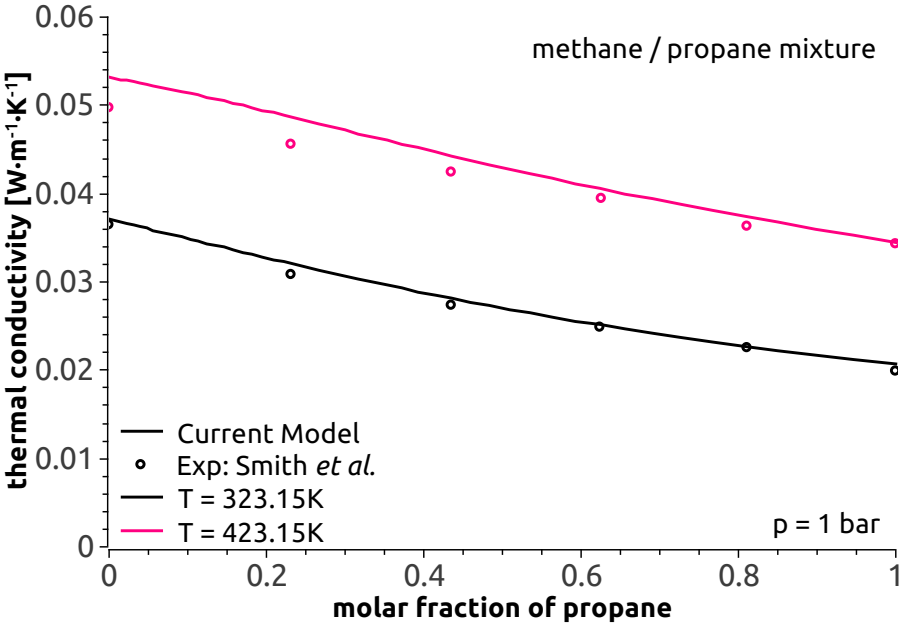


Figure 2.8: Evolutions of thermal conductivity prediction with the experimental data in binary systems at various temperature.

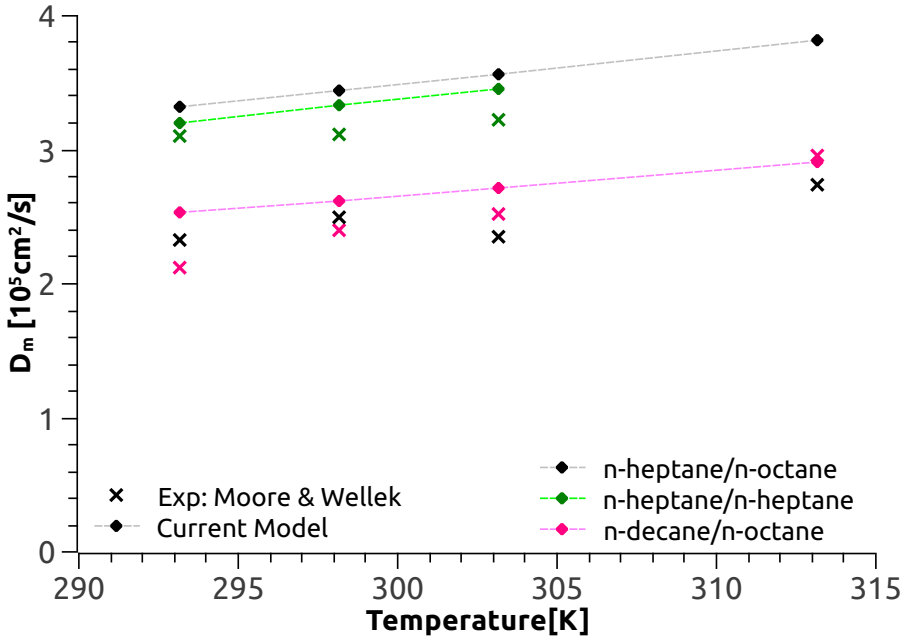


Figure 2.9: Diffusion coefficients for binary mixtures at various temperature.

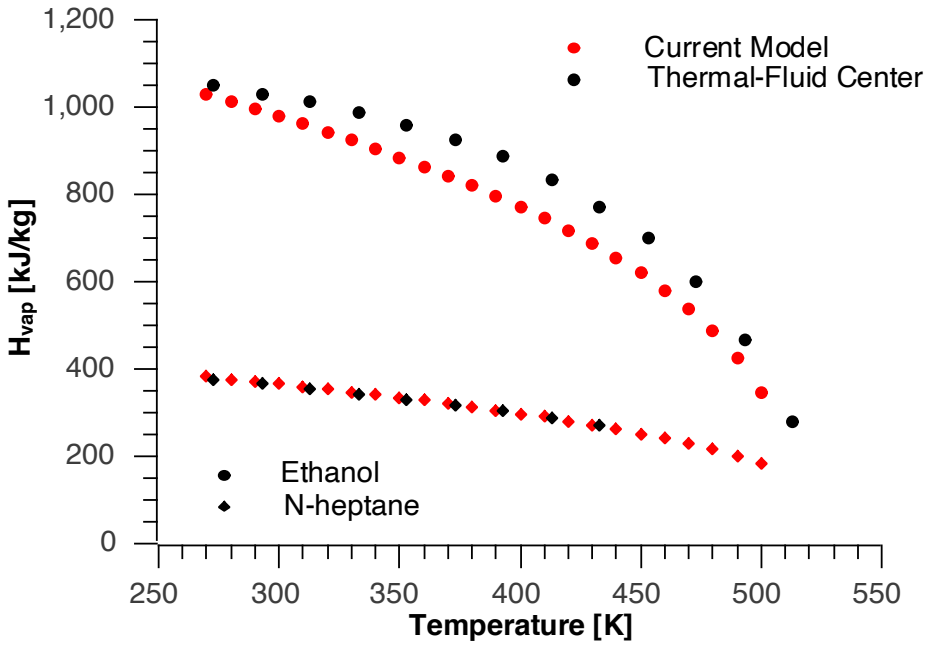


Figure 2.10: Latent heat of vaporization prediction at atmospheric pressure.

2.6 Single-Component Droplet Validations

The single-component droplet vaporization is validated against the results obtained from experimental test using the bended single-filament droplet suspension technique developed in authors' lab. The experiment of droplet vaporization evolution and the droplet interior temperature acquisition were carried out separately due to the significant heat conduction through the thermocouple to the droplet, especially at low ambient temperature conditions.

N-heptane droplet in a quiescent environment of T=100℃ is tested with initial droplet diameters of 1.35±0.5mm and temperature around 30°C. Multiple droplets are tested to validate stability of the temperature measurement. It should be pointed out that the constant volume chamber is flushed by compressed nitrogen gas after three droplets completely evaporated, eliminating the fuel vapor effect on droplet evaporating process. In Figure 2.11, eight samples of measured temperature are plotted (top), confirming the consistency in data acquisition. Also noted is that the relative location of the thermocouple used to measure the droplet temperature varies imperceptibly in each measurement due to the variation in droplet size, thus the recorded droplet temperature in Figure 2.11 (top) can be assumed to be the bulk mean temperature of a droplet in this study. The average temperature data from all sample tests is then used to compared with the calculated droplet temperature; results are given in Figure 2.11 (bottom). The predicted droplet temperatures from the current model agree very well with the measured temperatures at both ambient temperatures of 100℃ and 200°C, as well as at quasi-steady state droplet temperatures. The temperature variations at the beginning of the droplet evaporation process are due to the initial cooling of the thermocouple from ambient temperature by the droplet. At the end of the temperature temporal trends, the significant increase is due to the direct exposure of the thermocouple to the hot ambient gas in the chamber without the droplet.

Droplet experiments are also conducted without the temperature measurement, and a set of representative results of n-heptane size evolution is shown in Figure 2.12. Overall, the present model agrees well with the experimental tests, and the droplet lifetimes are similar. However, the model estimates lower vaporization rates at the initial stage (before around 1.5 *sec.*) and relatively higher vaporization rates after that for all three test conditions. Such discrepancy is possibly caused by the imperative droplet oscillating motion at the initial experimental stage. The oscillation, resulting from the droplet inertia, increases the uncertainty of choosing the onset of evaporation process, and consequently the evaporating behavior at the very early stage is not precisely captured. As seen in Figure 2.12, the violent fluctuation in droplet size evolution can be observed within 0.5s after the starting the test. With the lapse of time, the droplet deformation becomes conspicuous due to the presence of the support filament, leading to the inaccuracy in measuring the droplet size.

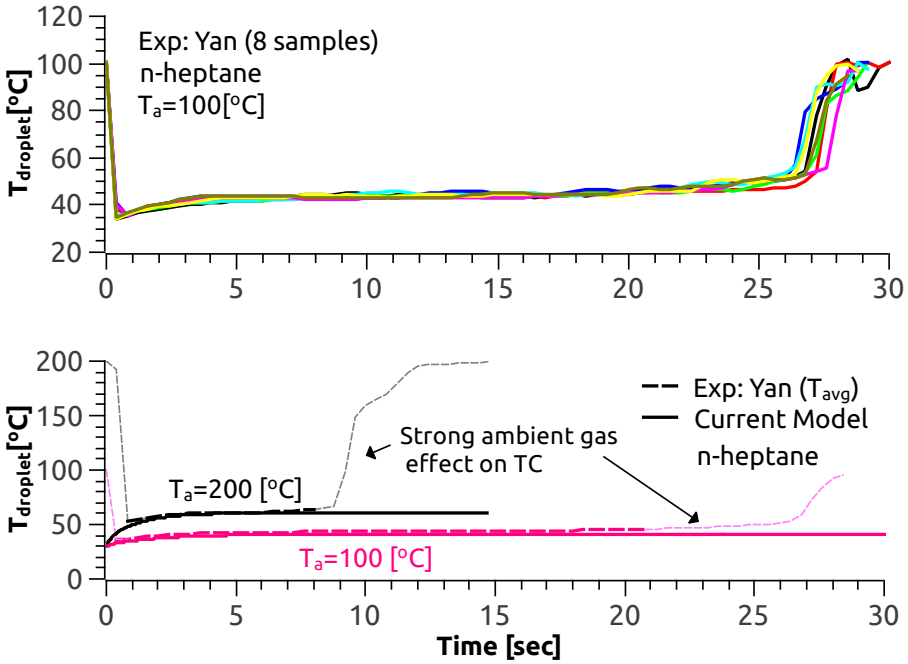


Figure 2.11: Measured and computed droplet temperature history for n-heptane fuel droplet at 1 atm. Note that the light-colored dashed lines in the averaged measured temperature curves indicate the strong ambient gas effect on thermocouple measurement.

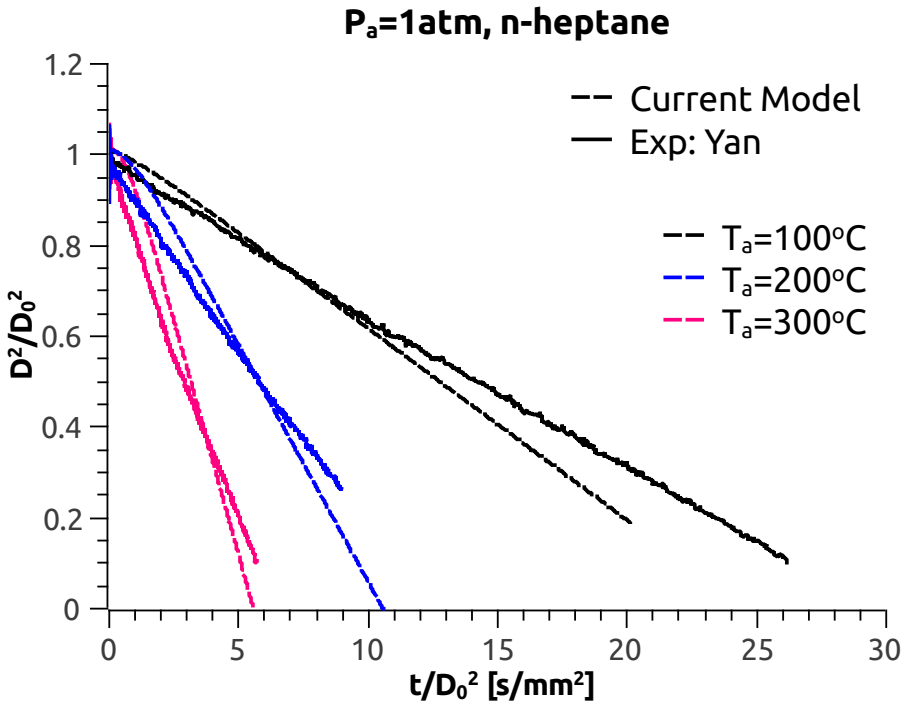


Figure 2.12: Comparison of the diameter temporal history between experiment and computation for a n-heptane droplet at various ambient temperature.

Next, the developed model is tested and compared with extensive experimental data found in literatures. Figure 2.13 shows the comparisons between the computed and measured droplet vaporization rates over a wide temperature range. Both predicted and measured vaporization rates lie within the range found in literatures. It is noteworthy that the vaporization rate obtained in literature are different due to: (1) higher vaporization rate can be procured for the experiment in which the large diameter fiber is used, for example 125 μm for Ghassemi *et al.* [42], 150 μm for Nomura *et al.* [41], and 14 μm for Chauveau *et al.* [43], thus the more pronounced heat conduction effect through the fiber is introduced; (2) natural convection has considerable influence on the evaporating process. In this study, the test is carried in terrestrial gravity with a fiber diameter of 100 μm, the measured data, therefore, are close to the high vaporization rate side. Apart from the measured data, present model also gives the higher vaporization rate mainly due to the effective diffusivity coefficients that enhanced the transport process.

To validate the present model performance in different pressure environments, the model is tested and compared with the high-pressure data acquired from literatures. Figure 2.14 shows the computed and experimental final droplet temperature at high pressure conditions. The present model can accurately estimate the droplet temperature at 1 atm and 11 atm ambient pressure. When further increasing the ambient pressure, the accuracy of the model becomes evanescent. The critical pressure of n-heptane is about 27.4 bar, higher ambient pressures, i.e. 31 atm and 51 atm, will degrade the accuracy of VLE solver (detailed discussion is presented in previous section) thus the core modeling results.

Figure 2.15 shows the temporal history of the normalized n-heptane droplet diameter. The present model is tested and compared with the high pressure experimental data [41]. The estimated results under high temperature conditions show a satisfactory agreement with the experiment for atmospheric ambient. Slight vaporization rate differences, also indicated in Figure 2.13, confirms the current model underestimates the vaporization rate when thermal conduction through the fiber is presented. When raising the ambient pressure from 1 bar to 5 bar, the effect of the heat conduction through the support fiber becomes less significant, where the vaporization rates are almost the same when comparing the measured data with the predicted data, for example C_v at 5 bar are about 0.384 mm^2/s and 0.194 mm^2/s for T_a around $749K$ and $556K$, respectively (Figure 2.15). However, it is noted that the initial heating process is elongated by 33.3% for $T_a = 749K$ and 20% for $T_a = 556K$, confirming the conclusion found in [133], and correspondingly a longer droplet lifetime is estimated by the model when elevating the pressure. Figure 2.16 shows the variation of the normalized droplet diameter for different environment temperatures at 10 bar for n-hexadecane. The overall vaporization profile matches well with the measured data found in [42] except at temperature of $400K$. The present model fails to replicate the initial droplet

expansion caused by the initial heating stage, particularly at higher ambient temperature conditions. The heating-up rate at the initial stage is slower compared with the measured data, thus the maximum percentage increase in droplet initial heating-up is about 16.4% when $T_a = 700K$. Model corrections will be discussed in the following sections to account the initial vibration effects on vaporization process. Nevertheless, the results show the capability of the current quasi-1D model in predicting the evaporation of the general single-component droplet system. Therefore, the test can proceed to the multi-component droplet system.

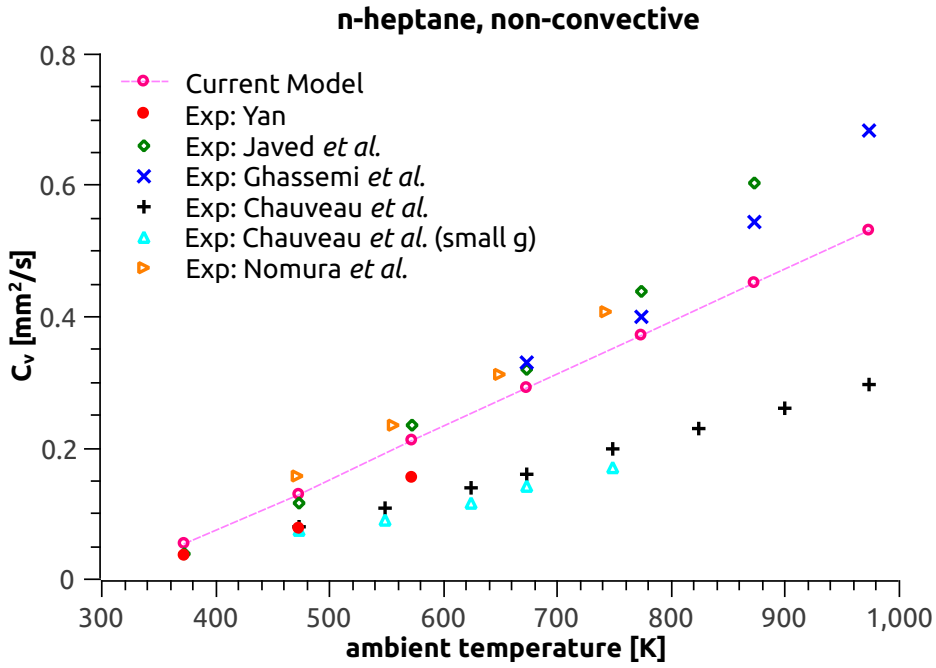


Figure 2.13: Vaporization rate of n-heptane droplet at 1 atm, non-convective environment. The measured data are from authors' lab as well as from [42-44].

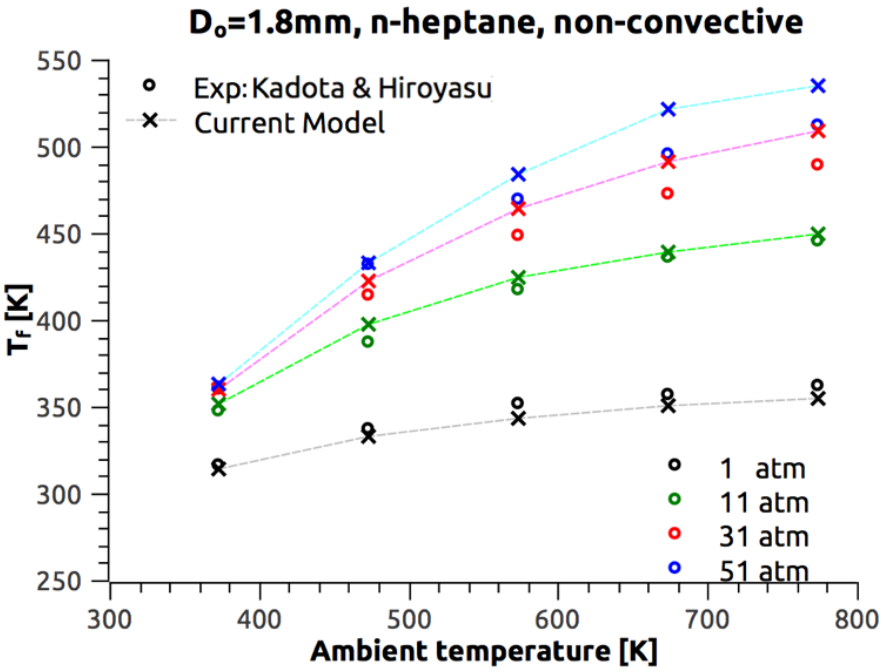


Figure 2.14: Comparisons of final droplet temperatures between the current model and measured data obtained from [22]. The droplet of n-heptane has diameter of 1.8mm and under the non-convective environment.

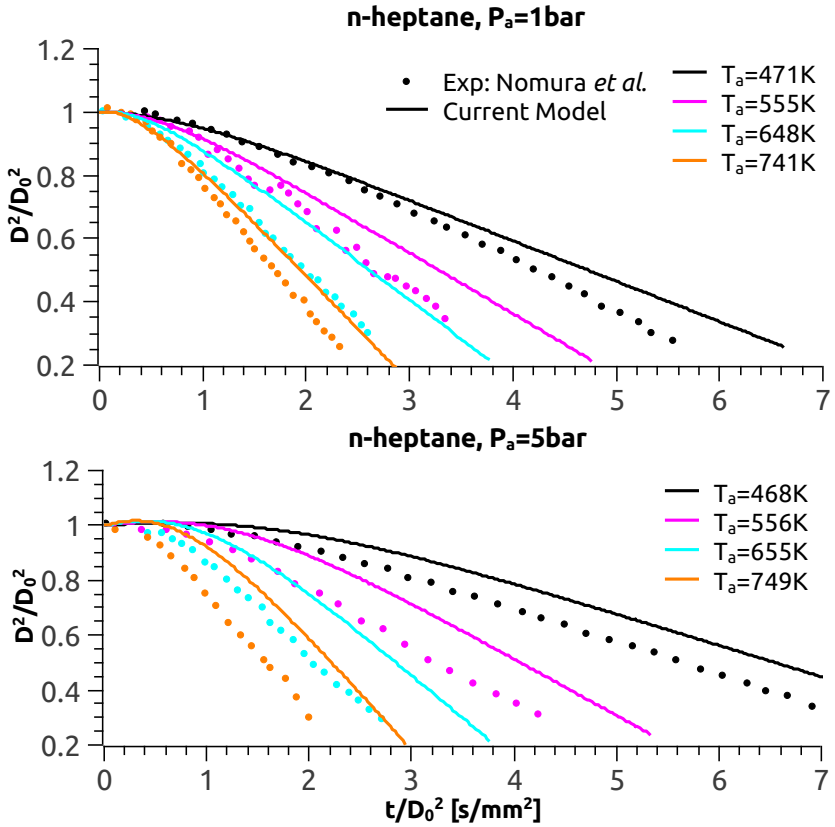


Figure 2.15: Temporal history of droplet vaporization for n-heptane fuel droplet under different pressure and temperature conditions.

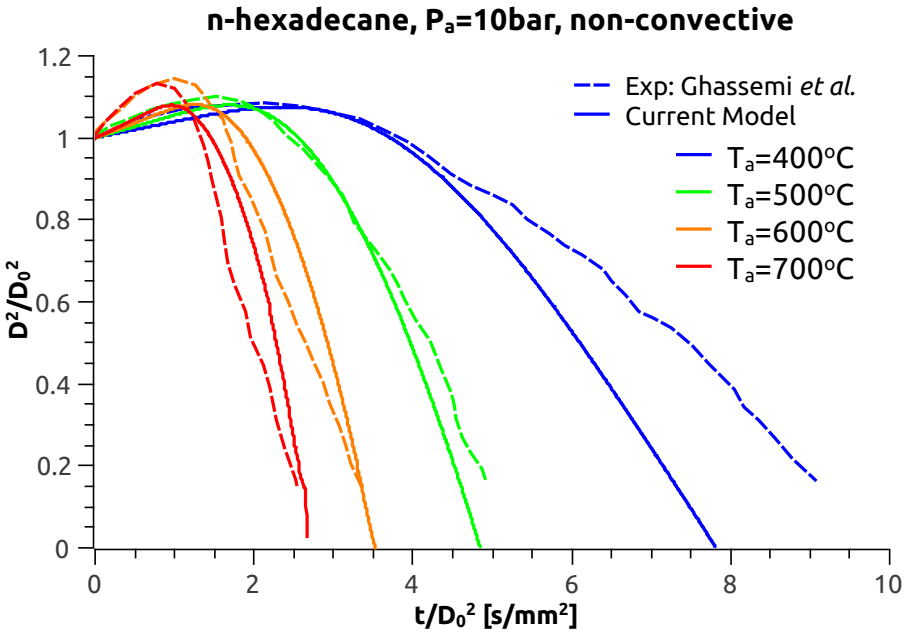


Figure 2.16: Temporal history of droplet vaporization for n-hexadecane fuel droplet at 10 bar ambient conditions.

2.7 Multi-Component Droplet Validations

In this sub-section, preliminary results for multi-component droplet system are presented. Figure 2.17 shows the variation of the normalized time history of diameter squared of droplet consisting of ethanol and isooctane. The evolution of droplet size predicted by the model agrees well with the experiment. For all four test conditions, the predicted and measured lifetimes are comparative. Increasing the ethanol content increases the droplet lifetime dramatically. The large HOV of ethanol (921 kJ/kg) is responsible for such lengthened lifetime. For E0, pure isooctane droplet, the estimated droplet vaporization rate is similar to the measurement. One of the significant differences between the measured and simulated data is a two-stage vaporization that can be observed for the E30, E50, and E85 cases. Isooctane molecular is heavier (114 kg/kmol) compared to ethanol, but it has a relatively small HOV (272 kJ/kg). There exists a strong competition between thermal-controlled and diffusion-controlled vaporizations. In addition, the

non-ideal behavior of the ethanol/isooctane mixture considerably brings about the different evaporation rates of individual components, and thus the evaporation history of the liquid mixture. However, such preferential vaporization behavior is not obvious in the experimental tests. The droplet inner core is heated by the filament, weakening the thermal-controlled vaporization.

When using a droplet consisting of two distinguished components, as shown in Figure 2.18, the effect of preferential vaporization is more pronounced. In Figure 2.18, the results for an evaporating droplet consisting of n-heptane and decane are plotted. The predicted trends of the current model are close to the experimental data [134]. The initial vaporization rate of the bi-component droplet is similar to that of the pure n-heptane, indicating that the light component, n-heptane, preferentially vaporizes more quickly at the droplet surface initially than decane. At later times, the vaporization of the bi-component droplet slows down as the mass diffusional resistance prohibits the n-heptane deep inside the droplet to reach the surface faster enough. Once all the n-heptane is vaporized, the bi-component droplet tends to behave like the pure decane droplet.

Vaporization behaviors of ternary mixture droplets are shown in Figure 2.19 and Figure 2.20. Normalized droplet diameters calculated with current model are compared with the measured data [135] with reference to the Figure 2.19. The comparisons show satisfactory agreements between the model and the experiments under the condition without relative motion between the droplet and the ambient gas. As depicted in Figure 2.20, for droplets consisting of multiple components of different volatility, the species of higher volatility is depleted from the droplet faster comparing to the less volatile species initially. However, the vaporization of more volatile components is weakened because the mass diffusion from the bulk to the surface limits the transport of more volatile component near the completion of the evaporation.

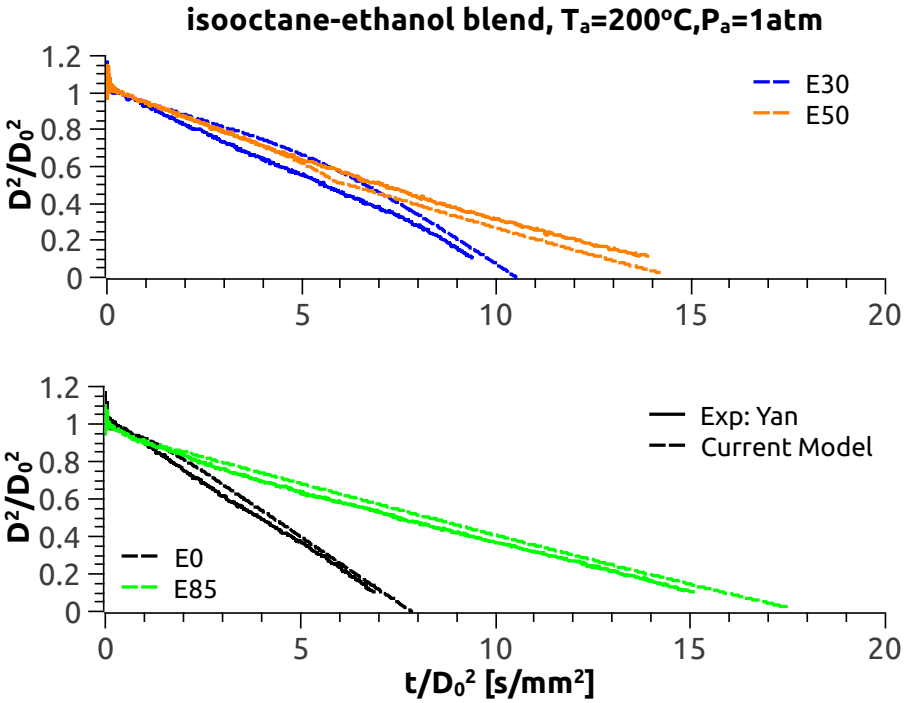


Figure 2.17: Temporal history of multi-component droplet vaporization for ethanol/isooctane binary system under atmospheric pressure at 200°C environment.

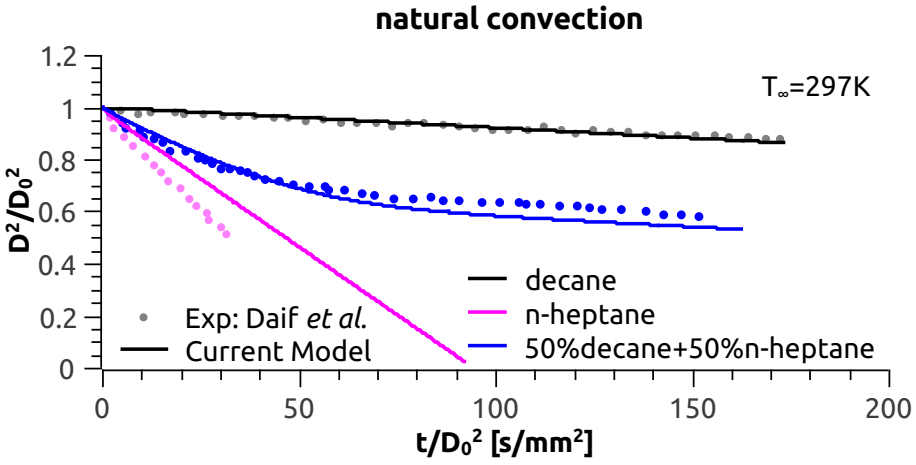


Figure 2.18: Temporal history of multi-component droplet vaporization for n-heptane/decane binary system under atmospheric pressure at 297K environment.

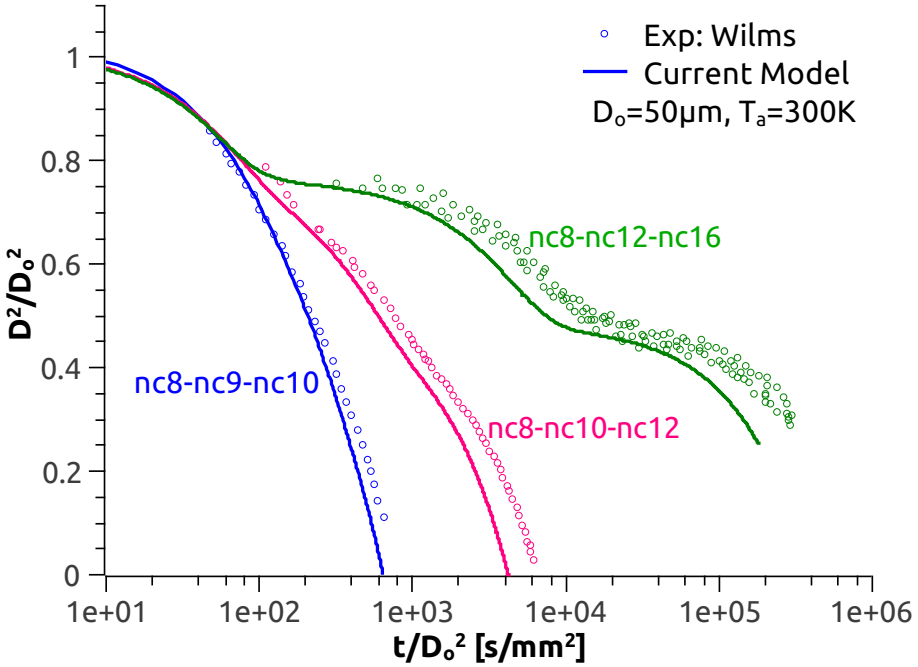


Figure 2.19: Temporal history of multi-component droplet vaporization for ternary mixture droplet under atmospheric pressure at 300°K environment (2005).

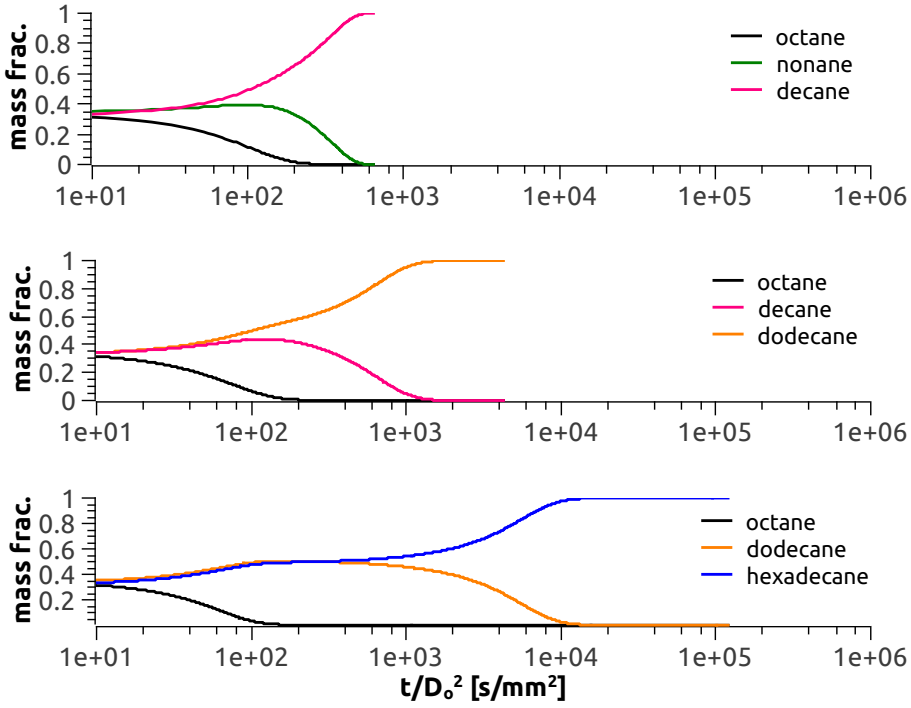


Figure 2.20: Evolutions of mass fraction during droplet vaporization for ternary mixture droplet under atmospheric pressure at 300°K environment.

2.8 Droplet Vaporization in Convective Environment

The current model using discrete method is tested under the convective ambient conditions, and it is validated for both single-component and multi-component fuel droplets against the measured data found in literatures. In Figure 2.21 and Figure 2.22, the evaporation of single-component liquid droplets in forced convection (F.C.) is first conducted. In the work done by Daif *et al*. [134], the droplet is suspended on the extremity of a glass capillary positioned perpendicularly to the flow, and the diameter of the capillary is $200\ \mu m$. As can be seen from Figure 2.21, the predications of the droplet size for both pure n-heptane droplet and pure decane droplet match well with the experimental measurement.

The steady state droplet surface temperature for the pure decane droplet is predicted to be about 1.8% higher than the measured one using the thermographic infer-red system, which is acceptable since the overall trend of the droplet heating process agrees satisfactorily and the droplet steady state temperatures both reach around $t/D_o^2 \approx 2\ s/mm^2$. In the work of Rehman *et al*. [136], a pure n-butanol droplet was suspended on the thermocouple directly. Counterintuitively, the droplet evaporation behaviors were not affected by changing the size of thermocouples (T.C.) as can be seen in Figure 2.22, and furthermore the measurements are nearly consistent with the prediction in the absence of the thermocouple. The droplet heating process is prominently enhanced by the internal circulation owing to the convective flow, which in turns mitigates the heat conduction effect from the thermocouple.

The vaporization history of fuel mixture droplets in forced convection is shown in Figure 2.23 and Figure 2.24. It should be noted that the initial ambient condition was set to be the natural convection and the droplets were immersed in the convective flow only after several seconds during the experiment. From Figure 2.23 and Figure 2.24, models in both the natural convection

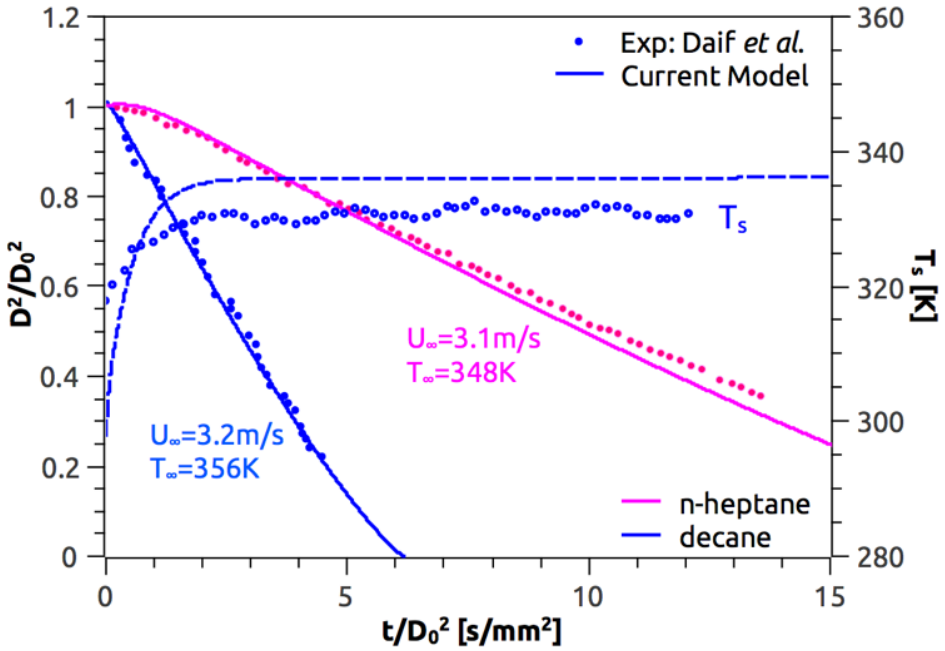


Figure 2.21: Measured and computed vaporization history for a n-heptane droplet and a decane droplet immersing in the convective flow at 1 atm.

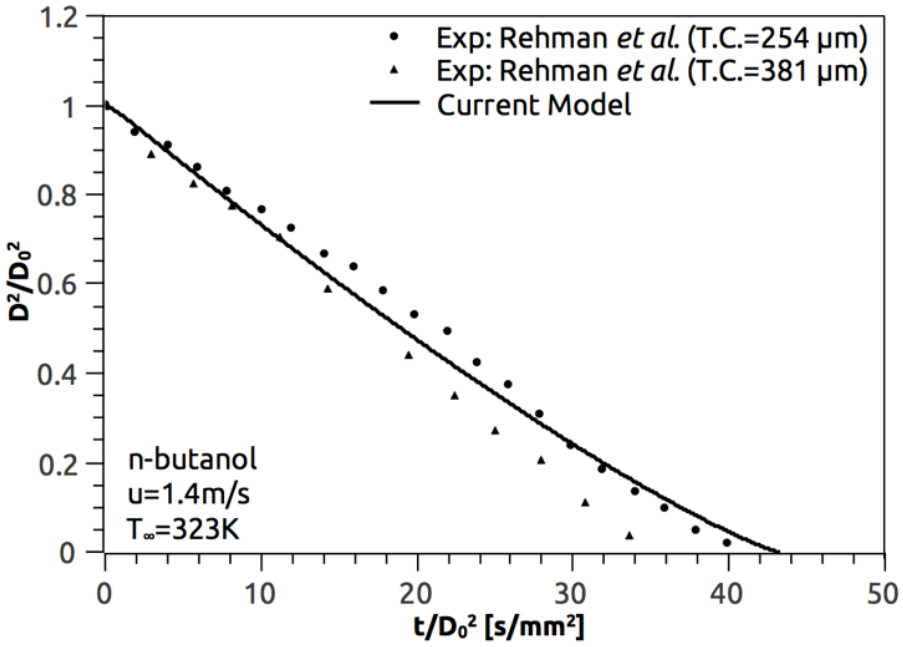


Figure 2.22: Comparison of the diameter history between experiment and computation for a n-butanol droplet with different diameter of the supporting thermocouple.

and forced convection confirm the experiment. It is clear that the vaporization rate of the droplet in the convective flow is faster than that in a natural convection flow when comparing the slope of the plot before and after the presence of the convective conditions. The surface temperature history from Figure 2.24 shows that in the convective flow, heat transfer from the ambient to the droplet is elevated, consequently leading to the higher vaporization rate. By comparing case 3 and case 2 in Figure 2.24, with the same compositions, the droplet lifetime decreases drastically from above 40 sec. to around 20 sec. if it is introduced to the convective flow at the early evaporation stage as the convective environment has a superior influence on the mass and heat transfer processes.

The distribution of the vol. fraction of the two components at the onset of the convective flow is indicated in Table 2.1 and Table 2.2. The current model can predict the volume percentage of the species within a droplet at the given timing, and the maximum difference is only 3%. It can be seen that when evaporating the bi-component droplets (for example see Table 2.1), the preferential vaporization occurs since the volume fraction of the light component (n-heptane) drops by 10% at the moment of the start of the forced convection, and in comparison, the average composition of the droplet evolved from 50% decane to about 60%. From the temporal variation of the droplet size in Figure 2.23 and Figure 2.24, the vaporization rate alternated apparently after the droplet is immersed in the convective ambient conditions. Unlike the preferential vaporization of multi-component droplets in convective free flows where the evaporation of more volatile species is controlled by the mass diffusion from bulk to droplet surface, in the convective flow the relative velocity between the ambient and droplet accelerates the transport processes within the droplet due to the presence of internal circulation. The mass or temperature gradient in droplets is reduced and the high volatility difference remains at the droplet surface. The preferential evaporation behavior proceeds until the depletion of the more volatile species.

Table 2.1: Component distributions at the moment of start of F.C. for 50% C7-50% C10.

moment of start of F.C.	***experiment***				***current model***			
9.5 sec.	43.0%	C7	57%	C10	40.0%	C7	60%	C10
10.8 sec.	42.3%	C7	57.7%	C10	41.0%	C7	59%	C10

Table 2.2: Component distributions at the moment of start of F.C. for C7-C10 droplet.

moment of start of F.C.		***experiment***				***current model***			
Case 1	22.1 sec.	63.5%	C7	36.5%	C10	64.7%	C7	35.5%	C10
Case 2	2.0 sec.	74.0%	C7	26.0%	C10	73.7%	C7	26.3%	C10
Case 3	12.0 sec.	21.3%	C7	78.7%	C10	19.0%	C7	81.0%	C10

** the initial composition for case 1 is 75% C7 and 25% C10; 25% C7 and 75% C10; for case 2 & 3*

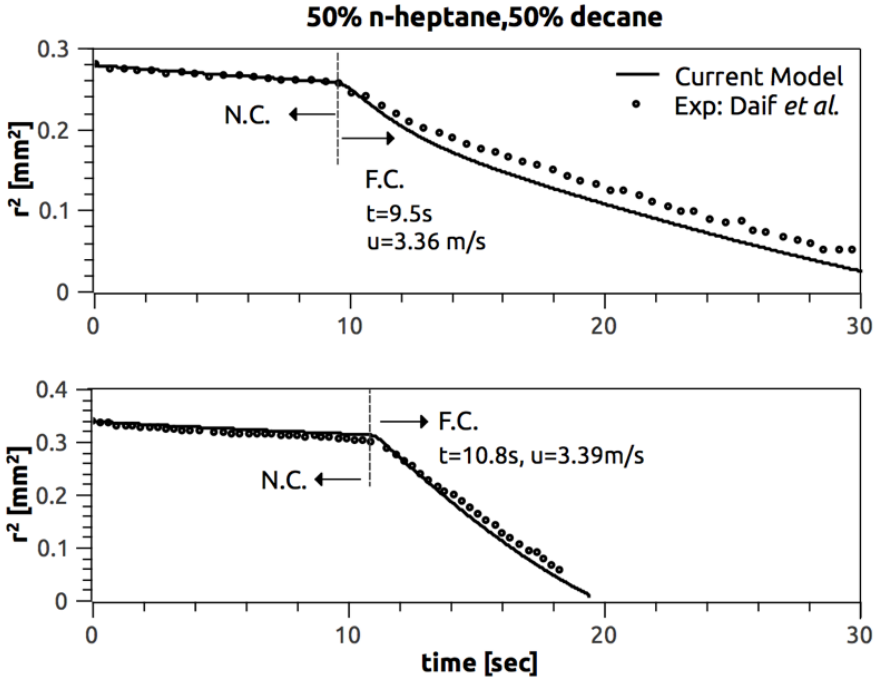


Figure 2.23: Temporal variation of the vaporization of fuel mixture droplet with 50% of n-heptane and decane (volumetric composition).

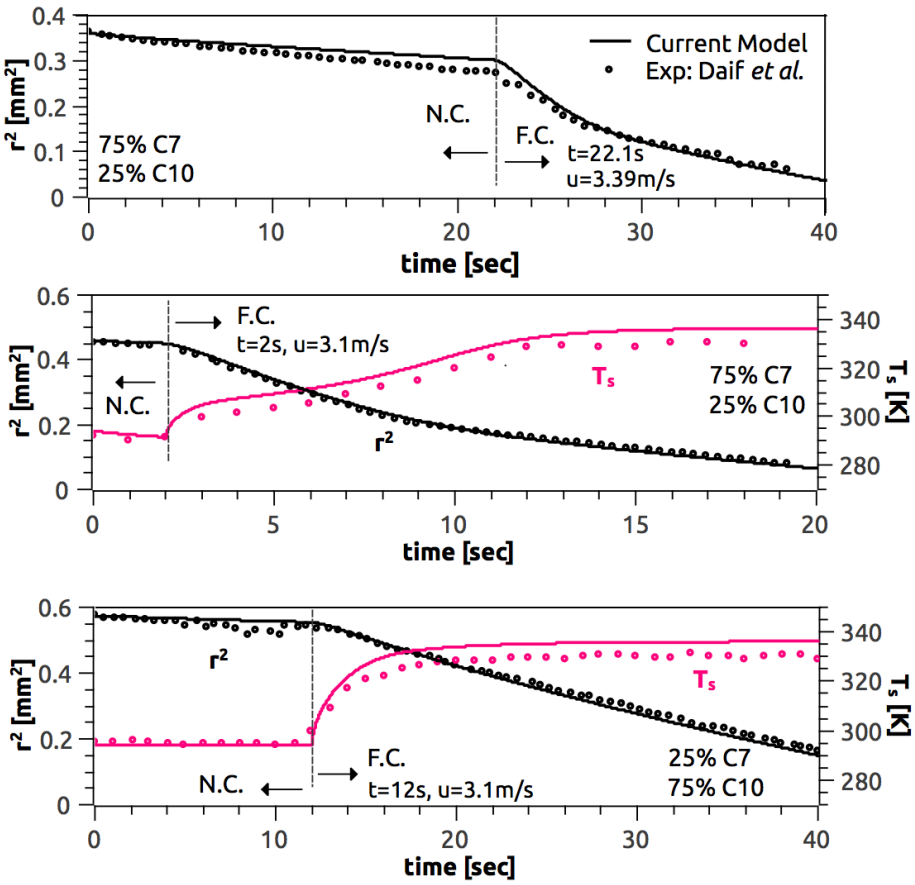


Figure 2.24: Measured and computed droplet temperature history for binary fuel droplet at 1 atm. C7: n-heptane; C10: decane.

2.9 Droplet Vaporization Model Corrections

The initial stage of droplet vaporization is modified by creating a weak forced convection to mimic the droplet vibration motion. When performing the experiment, oscillation motions have been observed at the initial stage of the droplet vaporization process. This is due to that the needle tip of the droplet generation system is not attached to the support fiber perfectly, and there is a very short distance between them. When droplet reaches the fiber, it can have certain small velocity. Also, as mentioned in the experimental setup, the support fiber is bent to guide the droplet to slide away from the generation system and to approach the test location. Consequently, droplets gain the velocity from the sliding motion and then experience the inertia at the beginning stage due to

the initial droplet velocity. The effect of the vibration on the droplet vaporization can be mimicked by considering the initial droplet velocity. Calculations have been done for cases with the initial relative velocity (the weak forced convection is imposed during the initial stage of 0.1~0.4s with ambient flow velocity of 0.2~0.4 m/s) between the ambient gas and droplet to create a weak convective environment, and the initial transport process can be enhanced and the droplet vaporization history, as shown in Figure 2.25 and Figure 2.26, matches well with experimental data [41, 44]. This modification can also be found in the literature [137]. Improvements can be found after employing the corrections by comparing results from Figure 2.15 and Figure 2.26.

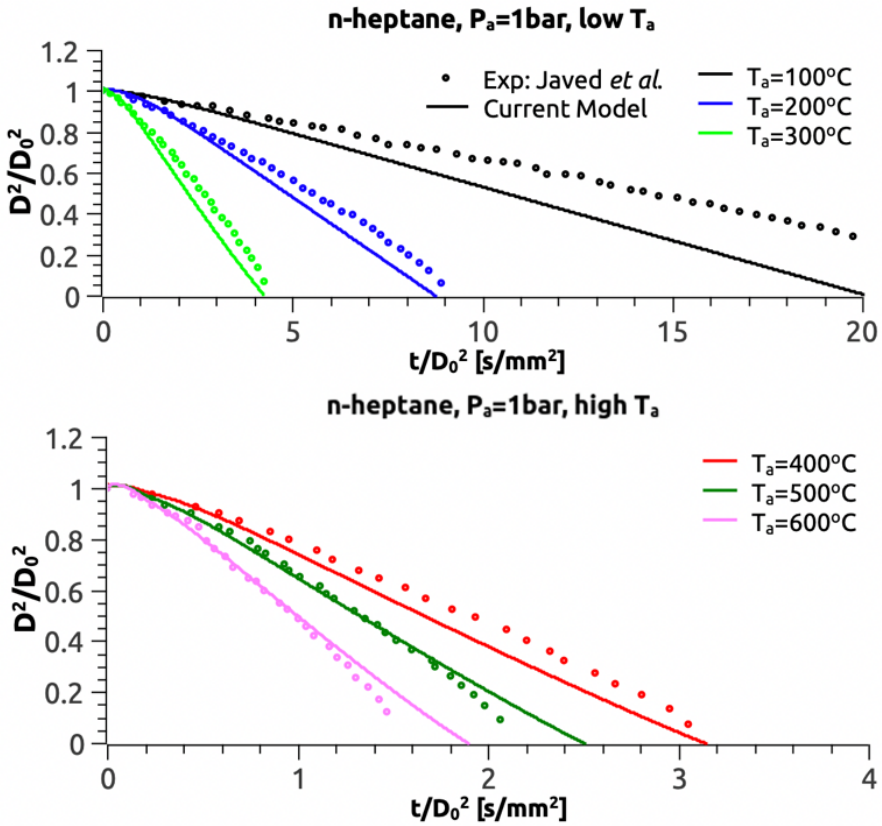


Figure 2.25: Temporal history of droplet vaporization for n-heptane fuel droplet with the weak FC modification at various temperature conditions.

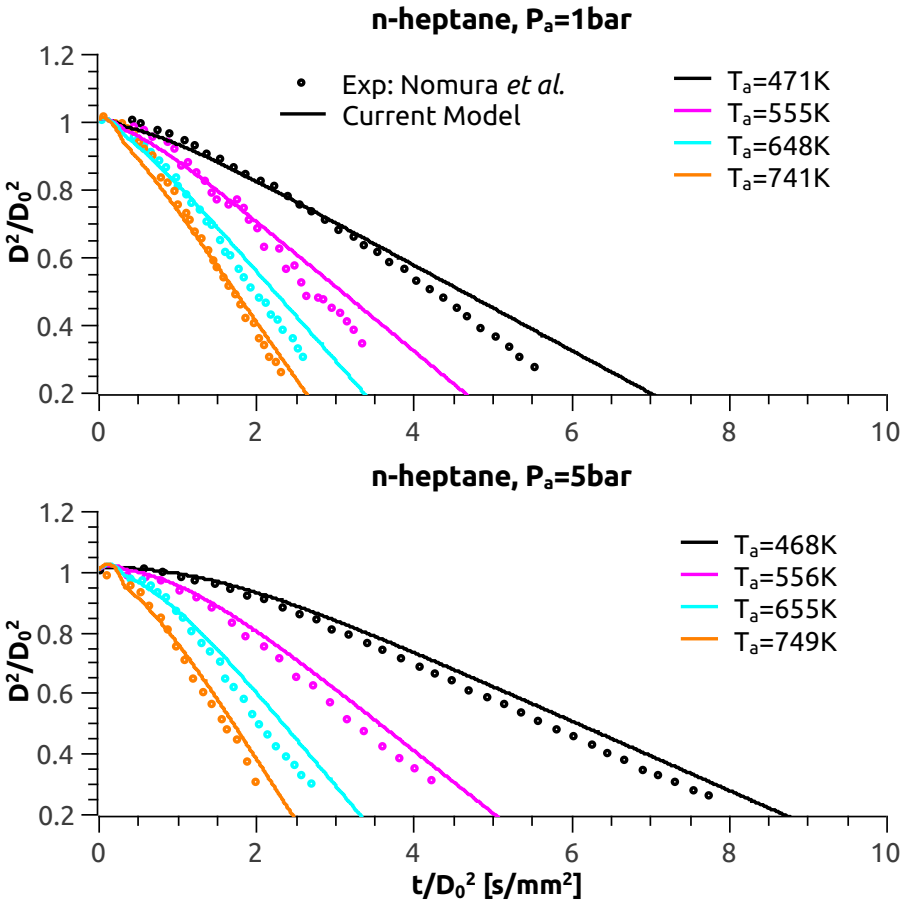


Figure 2.26: Temporal history of droplet vaporization for n-heptane fuel droplet with the weak FC modification under different pressure and temperature conditions.

CHAPTER 3: ATOMIZATION OF MULTI-COMPONENT FUEL SPRAYS UNDER THE FLASH BOILING CONDITIONS

Flash-boiling phenomenon is very complex, involving complicated analysis of thermodynamics, instabilities, dynamics, etc. To develop a comprehensive multi-component fuel flash boiling model, three main processes (see Figure 3.1), bubble nucleation, bubble growth, and breakup, are considered in this study. Each process will be elaborately discussed, and corresponding formulations are conducted. Model will be tested and implemented into KIVA for fuel spray simulations. All fluid properties and equilibrium calculations appear in this chapter will be evaluated using the solver developed in Chapter 2. In practical CFDs of the IC engine, the rate-of-injection (ROI) model with the spray representation of computational particles, Lagrangian parcels, that follow drop characteristic paths is commonly used under the consideration of the cost-effective simulations. Therefore, flash-boiling occurring inside the nozzle is not investigated in the present study.

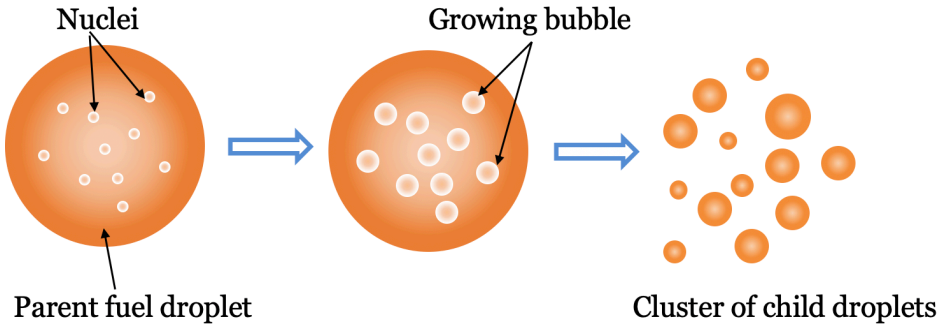


Figure 3.1: Schematic of the flash boiling phenomenon.

3.1 Bubble Nucleation Model

When liquid fuel is superheated and injected into the depressurized chamber nucleation may occur. There are two types of nucleation: homogeneous and heterogeneous. While the liquid fuel is put into a non-equilibrium metastable state with a local minimum of free energy, it is stable to small fluctuations in the thermodynamic variables but shortly will evolve to a state where free energy reaches its global minimum (bulk vapor) [138]. During this transformation, a fluctuation is required to overcome an energy barrier at a local maximum of the free energy. A small cluster of the new phase is formed due to this fluctuation and is called homogeneous nucleus. However, this process becomes predominant when the liquid pressure is greatly reduced corresponding to a tensile force opposed to the molecular force of the liquid [139, 140]. In practical CFD simulations, the decompression is much weaker than the tensile force, thus homogeneous nucleation is not considered in this study. Under high injection pressure conditions, small amount of air can dissolve into the liquid fuel and later become nucleation sites during the injection process. It has been reported that the number density of bubble nuclei exponentially increased with the increase in the superheating degree for the superheated flash boiling process. An empirical relation, developed by Senda *et al.* [139], is adopted to describe the steady-state rate of formation of bubble nuclei at different superheated degree, ΔT, for heterogeneous nucleation caused by the dissolved gas.

$$N = C \exp[-\frac{\Delta A}{k_B \Delta T}] \tag{3.1}$$

$$\Delta A = \frac{4}{3}\pi R^2 \sigma \qquad \Delta T = T - T_s$$

The nucleation rate, N, is defined as the number of the nucleation events occurring in a unit volume per unit time. C is a constant depending on fuels and injector configuration, R is the radius of microscopic voids, and σ is the surface tension at bubble-liquid interface.

3.2 Bubble Growth Model

Once a stable nucleus is formed in the superheated liquid fuel droplet, it grows appreciably during the injection to the desired bubble size. The bubble growth in this study can be idealized as spherically symmetric bubble expansion in an extensive uniformly superheated large liquid pool, and the physical circumstance of interest is shown in Figure 3.2.

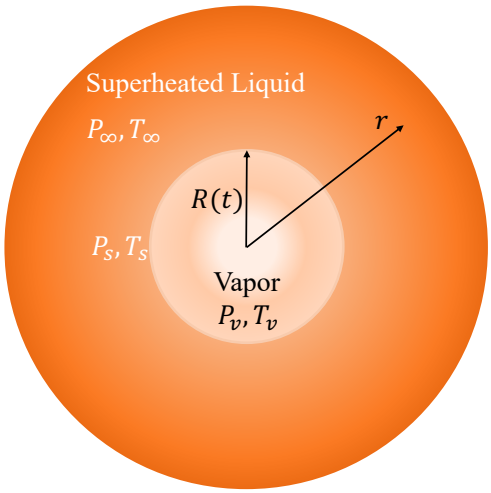


Figure 3.2: Bubble growing in a superheated liquid.

The vapor-liquid interface is located at $r = R$, and during the growth process it expands with a velocity dR/dt relative to the laboratory reference frame. It is assumed that the interface temperature is the same as the surrounding liquid, and the pressure of vapor generated at the interface is nearly equal the saturation pressure at the given temperature T_∞. Excessive energy of the superheated liquid at the interface is consumed to provide the latent heat of vaporization, and subsequently the radius of bubble increases and the interface temperature asymptotically drops to the saturation temperature $T_{sat}(P_\infty)$. Meanwhile, because of the increased bubble radius, capillary pressure difference across the interface decreases, bringing the vapor pressure toward to the surrounding liquid pressure P_∞.

Therefore, at the initial stage of bubble growth, the growth rate is controlled by the momentum interaction between the bubble and liquid fuel, a.k.a. inertia-controlled growth. The effect of fast heat transfer crossing the interface to the bubble size is minor at this stage. From the mass conservation at the interface, radial outward velocity, $u(R,t)$, can be found

$$\frac{dm_v}{dt} = \rho_v V = 4\pi\rho_v R^2 \frac{dR}{dt} \qquad \frac{dm_l}{dt} = \rho_l u_l A = 4\pi\rho_l R^2 u_l$$

$$u(R,t) = \frac{dR}{dt} - u_l = (1 - \frac{\rho_v}{\rho_l})\frac{dR}{dt}$$

Applying a kinematic boundary condition at the bubble surface $R(t)$ satisfying $u(R,t) = \frac{F(t)}{R^2}$, then the radial outward velocity at an arbitrary location r is

$$u(r,t) = \left(1 - \frac{\rho_v}{\rho_l}\right)\frac{R^2}{r^2}\frac{dR}{dt} = \frac{R^2}{r^2}\frac{dR}{dt} \text{ (for } \rho_v \ll \rho_l) \tag{3.2}$$

Momentum conservation in spherical coordinates for incompressible Newtonian fluids if only considering the radial direction yields

$$\rho_l\left(\frac{\partial u}{\partial t} + u\frac{\partial u}{\partial r}\right) = -\frac{\partial p}{\partial r} + \left[\frac{1}{r^2}\frac{\partial}{\partial r}(r^2\tau_{rr}) - \frac{\tau_{\theta\theta} + \tau_{\phi\phi}}{r}\right]$$

$$\tau_{rr} = \mu\frac{\partial u}{\partial r},\ \tau_{\theta\theta} = \tau_{\phi\phi} = \frac{u}{r}$$

Plugging in shear stress tensor and $u(r,t)$ from Eq. (3.2) and separating variables, after integrating from the bubble boundary $r = R$ to $r \to \infty$ gives

$$\frac{P_l(R) - P_\infty}{\rho_l} = R\frac{d^2R}{dt^2} + \frac{3}{2}\left(\frac{dR}{dt}\right)^2 \tag{3.3}$$

In Eq. (3.3), $P_l(R)$ can be replaced by P_v and surface tension σ of the interface by utilizing the Young-Laplace equation. Furthermore, under the inertia-controlled growth regime, the term $2\sigma/R$ is much smaller than the pressure difference across the interface thus can be removed from the analysis. Pressure difference $P_v - P_\infty$ can be evaluated with the linearized Clapeyron equation at

the cost of the inaccuracy at high superheated degree. Then Eq. (3.3) can be formulated as Eq. (3.4), and T_v equals T_∞ for inertia-controlled growth. The analytical solution to Eq. (3.4) for the bubble size change during the initial stage is indicated in Eq. (3.5). It is explicitly illustrated that the radius increases linearly with the time during the initial inertia-controlled stage.

$$R\frac{d^2R}{dt^2}+\frac{3}{2}\left(\frac{dR}{dt}\right)^2=\frac{\rho_v}{\rho_l}\left[\frac{\Delta H_v\left(T_v-T_{sat}(P_\infty)\right)}{T_{sat}(P_\infty)}\right] \tag{3.4}$$

$$R(t)=\left[\frac{2}{3}\left(\frac{T_v-T_{sat}(P_\infty)}{T_{sat}(P_\infty)}\right)\frac{\Delta H_v\rho_v}{\rho_l}\right]^{1/2}\cdot t \tag{3.5}$$

As the bubble grows, the dominant mechanism switches from inertia to heat transfer. The vapor temperature drops nearly to its minimum and the bubble growth rate is slow due to the fact that the superheat in the liquid has been dramatically depleted during the later stages of the bubble growth. The governing equation for heat transfer from surrounding liquid to the bubble in the heat transfer-controlled regime has been studied by Plesset and Zwick [141], and an approximate relation for long-time bubble growth rate is given in Eq. (3.6). By solving Eq. (3.6), the bubble radius can be attained, and it implies that the bubble radius grows proportional to the square root of time near the end of the bubble growth.

$$\frac{dR}{dt}=\frac{1}{2}\frac{B}{\sqrt{t}}\left(1-\frac{T_v-T_{sat}(P_\infty)}{\Delta T}\right)$$
$$B=\left(\frac{12}{\pi}\alpha_l\right)^{1/2}Ja \qquad \Delta T=T_\infty-T_{sat}(P_\infty) \qquad Ja=\frac{C_{pl}\rho_l(T_\infty-T_{sat}(P_\infty))}{\Delta H_v\rho_v} \tag{3.6}$$

At the intermediate times, the mixing effect of the inertia and heat transfer on bubble growth makes the analysis more complicated, and yet the transition between these two stages is required to completely describe the evolution process of bubbles growing in liquid fuels. Based on the procedures done by Mikic *et al.* [142], the unified bubble growth rate can be established by

replacing the term $(T_v - T_{sat})$ in Eq. (3.4) after solving for it form Eq. (3.6). Following relation for the bubble growth rate at any arbitrary time is derived,

$$\frac{3}{2}\frac{\rho_l T_{sat}(P_\infty)}{\Delta H_v \rho_v \Delta T}\left(\frac{dR}{dt}\right)^2 + \frac{2\sqrt{t}}{B}\frac{dR}{dt} - 1 = 0$$

The above equation can be expressed in a dimensionless form shown in Eq. (3.7). Solving for $\mathcal{R}$, the bubble radius in a uniformly superheated liquid can be estimated.

$$\frac{d\mathcal{R}}{d\tau} = (\tau+1)^{1/2} - (\tau)^{1/2}$$

$$\mathcal{R} = \frac{RA}{B} \qquad \tau = \frac{tA^2}{B^2} \qquad A = \left[\frac{2}{3}\frac{\Delta H_v \rho_v \Delta T}{\rho_l T_{sat}(P_\infty)}\right]^{1/2} \tag{3.7}$$

$$\mathcal{R}(\tau) = \frac{2}{3}[(\tau+1)^{3/2} - (\tau)^{3/2} - 1] \tag{3.8}$$

The relation in Eq. (3.8) well represents the aforementioned asymptotic limiting behaviors of the bubbles. In Eq. (3.8), it can be seen that $\mathcal{R}$ varies monotonically with τ, i.e. when $\tau \ll 1$, the bubble growth characteristics approach to the inertia-controlled regime as $\mathcal{R} \ll 1$; and similarly, in the cases of $\tau \gg 1$, the heat transfer-controlled bubble growth is more pronounced for $\mathcal{R} \gg 1$ and eventually the growing bubble will cause droplet breakup.

3.3 Breakup Model

The phenomena of deformation and breakup of a droplet are of utmost importance in the injection period and are often the rate-controlling process within dense sprays [143]. The breakup of liquid fuel drops into even smaller droplets is primarily driven by aerodynamic forces employed on the drops by the surrounding gas phase under most engine operating conditions where the liquid fuel is introduced into the chamber during the compression stoke. These forces cause a distortion of the initially spherical droplet and lead to breakup once they exceed surface tension that

counteracts the deformation droplet. However, for injections with superheated fuels, influence of flash boiling should be considered as the presence of bubbles inside the liquid droplets will significantly alter the breakup behaviors (see Figure 3.3). In this study, the effect of superheating on breakup is built into a classic aerodynamic breakup model such that the unified breakup model is feasible to be used over all possible engine operation conditions.

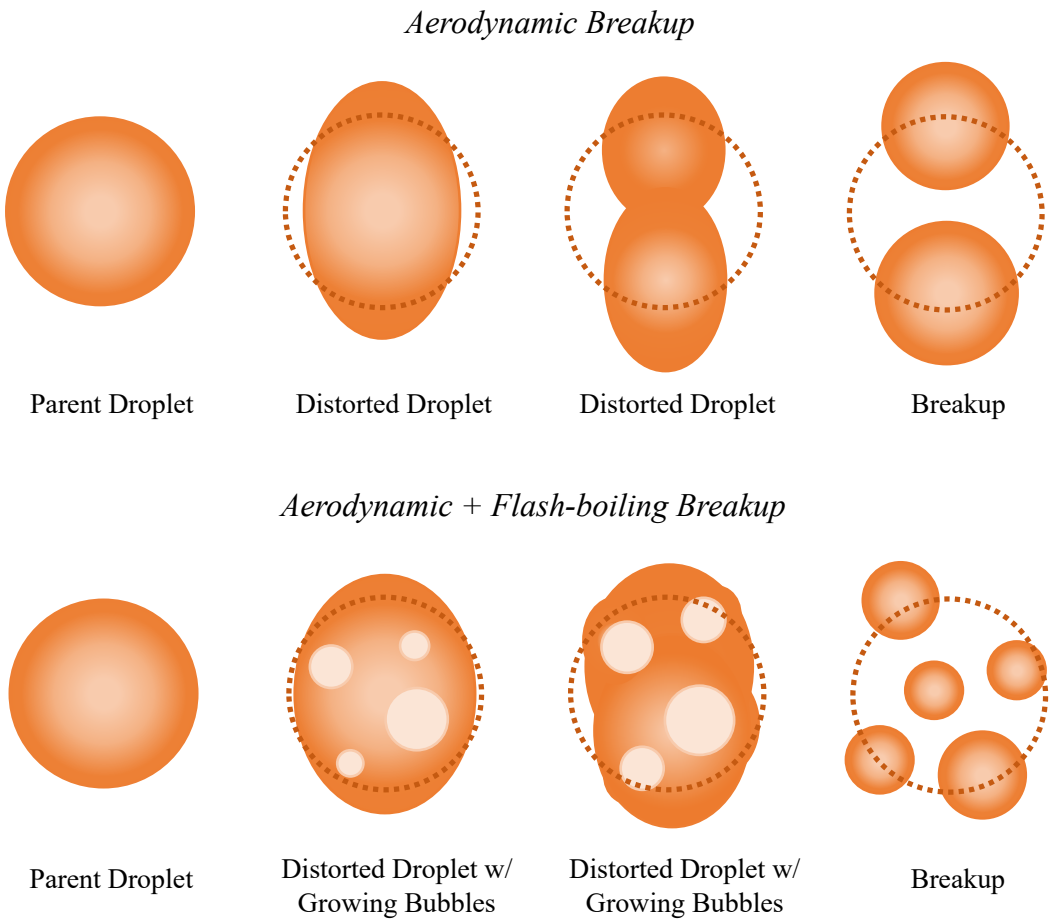


Figure 3.3: Droplet breakup mechanisms. Strong flash-boiling breakup is illustrated in Figure 3.1.

Droplet breakup induced by aerodynamic force has been studied by O'Rourke and Amsden [144] and a model based on an analogy [145] between an oscillating and distorting droplet and a spring-mass system was proposed which is known as the TAB (Taylor Analogy Breakup) model.

If assuming the aerodynamic force acting on the droplet is the driving force for deformation, the surface tension force acts as the restoring force, and the viscous force plays as the damping element, the equation of motion can be expressed as

$$\rho_l R_d^3 y'' = C_F \rho_g v_{rel}^2 R_d^2 - C_k \sigma y - C_d \mu_l R_d y' \tag{3.9}$$

In Eq. (3.9), y describes the deviation of the droplet equator from its equilibrium position and R_d is the radius of the droplet. C_F, C_d, and C_k are constants and determined from theoretical analysis [144]. After the presence of bubbles inside the droplet, the overall droplet density changes from ρ_l to ρ^* and the inertia force, as well as the viscous force, changes significantly, but the aerodynamic force and surface tension force remain the same.

$$\rho^* = \epsilon \rho_b + (1-\epsilon)\rho_l \qquad \mu^* = \epsilon \mu_b + (1-\epsilon)\mu_l \tag{3.10}$$

$$\epsilon = \frac{V_b}{V_b + V_l} \tag{3.11}$$

Void fraction ϵ is defined as ratio of the volume occupied by the bubble over the entire droplet volume. The modified equation of motion for the bubble-in-droplet system is written as

$$\rho^* R_{d,o}^3 y'' = C_F \rho_g v_{rel}^2 R_{d,o}^2 - C_k \sigma y - C_d \mu^* R_{d,o} y' \tag{3.12}$$

and $R_{d,o}$ is the outer radius of the bubble-in-droplet system. The breakup occurs in TAB model if and only if $y > C_b R_d$, and such criterion is unchanged in the bubble-in-droplet system for the effect of aerodynamics with $R_{d,o}$ instead. Criterion of the breakup by bubble growth will be given shortly. To solve Eq. (3.12), y is normalized by $C_b R_d$ first, given $Y = y/C_b R_{d,o}$, then the nondimensional form of Eq. (3.12) is

$$Y'' = \frac{C_F}{C_b}\frac{\rho_g}{\rho^*}\frac{v_{rel}^2}{R_{d,o}^2} - \frac{C_k}{\rho^*}\frac{\sigma}{R_{d,o}^3} Y - \frac{C_d}{R_{d,o}^2}\frac{\mu^*}{\rho^*} Y' \tag{3.13}$$

$$C_F = 1/3 \qquad C_d = 5 \qquad C_k = 8 \qquad C_b = 0.5$$

The breakup criterion due to the bubble growth has been investigated previously in author's lab. Zeng and Lee [60] the performed a linear stability analysis for impacts of void fraction ϵ on the disturbance growth rate of the bubble. It is reported that the growth rate of the disturbance increases with the bubble growth rate, and there exists a transition point where the bubble-in-droplet system becomes unstable, leading to the protentional breakup. The study shows that this critical void fraction is around 0.55. Accordingly, two competing breakup criteria stand for bubble-in-droplet system: aerodynamic criterion is $Y > 1$, and flash boiling breakup criterion is $\epsilon > 0.55$.

Secondary droplets are produced after breakup, and it is vital to accurately compute sizes and relative velocities of these droplet such that the successive spray evolution can be predicted. In TAB model, the outward velocity of the droplets after aerodynamic breakup approximately equals $C_b R_{d,o} Y'$. However, additional effect of droplet expansion on the momentum also needs to be included for the system. The resulting secondary droplets velocity due to expansion can be solved from the conservation laws coupled with the statistical analysis before and after the breakup [27] under the assumption the secondary droplets only have radial velocity relative to the velocity of the parent droplets. The completed outward velocity of droplets after breakup is given in Eq. (3.14) where $R_{d,i}$ is the bubble radius and $dR_{d,i}/dt$ can be calculated from Eq. (3.7).

$$v_d = C_b R_{d,o} \frac{dY}{dt} + \frac{3R_{d,i}^2\left(R_{d,o} - R_{d,i}\right)}{R_{d,o}^3 - R_{d,i}^3} \frac{dR_{d,i}}{dt} \tag{3.14}$$

Secondary droplet size can be determined from the conservation of energy. Total energy of the bubble-in-droplet system before breakup include surface energy at the liquid-gas interface and at the liquid-vapor interface, the energy in oscillation and distortion, as well as the kinetic energy due to the expansion of the bubble-in-droplet system,

$$E_o = 4\pi R_{d,o}^2\sigma + K\frac{\pi}{5}R_{d,o}^5(1-\epsilon)\rho_l\left(Y'^2 + \frac{C_k\sigma}{(1-\epsilon)\rho_l R_{d,o}^3}Y^2\right) + 4\pi R_{d,i}^2\sigma\, n + \int_{R_{d,i}}^{R_{d,o}} 4\pi r^2\rho_l\frac{1}{2}\left(n\frac{R_{d,i}^2}{r^2}\frac{dR_{d,i}}{dt}\right)^2 dr \tag{3.15}$$

where n is number density of the nucleation cluster in a droplet and calculated from Eq. (3.1), $K = 10/3$ is the ratio of the total energy in distortion and oscillation to the energy in the fundamental mode and determined from the experimental measurements on secondary droplets Sauter mean radius, R_{32}, for breakup at Weber number, a characteristic measure of the aerodynamic breakup behavior of liquid droplets, less than 10 ambient conditions [144]. After breakup, the total energy of the system is from the surface energy of the secondary droplets and the kinetic energy of these outward moving droplets,

$$E_1 = 4\pi R_{d,o}^2\sigma\frac{R_{d,o}}{R_{32}}(1-\epsilon) + \frac{1}{2}\cdot\frac{4\pi}{3}\left(R_{d,o}^3 - R_{d,i}^3\right)\rho_l v_d^2 \tag{3.16}$$

The Sauter mean radius, R_{32}, of the droplets after breakup can be solved by equating Eq. (3.15) and Eq. (3.16).

$$R_{32}^{-1} = \frac{1}{(1-\epsilon)R_{d,o}} + \frac{nR_{d,i}^2}{(1-\epsilon)R_{d,o}^3} + \frac{KR_{d,o}^2\rho_l}{20\sigma}Y'^2 + \frac{KC_k}{20\sigma(1-\epsilon)R_{d,o}}Y^2 + \frac{\rho_l n^2 R_{d,i}^3(R_{d,o}-R_{d,i})}{2\sigma(1-\epsilon)R_{d,o}^4}\left(\frac{dR_{d,i}}{dt}\right)^2 - \frac{\rho_l v_d^2}{6\sigma} \tag{3.17}$$

3.4 3-D Simulation Conditions

The vaporization model and flash boiling breakup model are implemented into KIVA and 3-D simulations are performed for model validations. Simulation results are first compared with the experimental measurement conducted using two methodologies, DBI (Diffuse Backlight Imaging) system for spray images captured by a high-speed camera, and PDA (Phase Doppler

Anemometry) system for droplet size measurement during the spray injection process. Elaborated experimental setups and measurements can be found in previous publications [146-148]. Two fuel blends are tested: ethanol-isooctane indicated with Exx, and hexane-isooctane denoted as Hxx; and each binary fuel mixture is produced by volume fraction, for example E30 refers ethanol-isooctane blends containing 30% vol. fraction of ethanol and 70% vol. fraction of isooctane, and H30 refers 30% vol. fraction of hexane and 70% vol. fraction of isooctane fuel mixture. For each blend, 5 different blend ratios are tested at various ambient pressure conditions. The flash boiling intensity is characterized by a quantity $r_P = P_a/P_s$, and it indicates the superheated degree, where P_a is the ambient pressure and P_s is the saturated pressure of the fuel.

Fuel properties for each individual species are listed in Table 3.1. The properties of mixtures can be calculated using the solver developed in Chapter 2. Vapor pressure calculations for Exx at liquid temperature of 35°C are compared with data found in literatures [149, 150] and plotted in Figure 3.4. After validations, calculation for vapor pressures of Exx and Hxx at 90°C are provided as well in Figure 3.4. As an oxygenate fuel additive, it has reported that adding ethanol to gasoline can enhance the engine efficiency and simultaneously reduce the emissions. However, due to the high HOV of ethanol, the vaporization of liquid spray for GDI operations deteriorates for Exx fuels. Investigations on the ethanol-isooctane blend under flash boiling conditions can provide an alternative approach to potentially enhance the atomization of liquid fuel spray, reduce the droplet size, and eventually improve the vaporization of Exx fuels. For comparisons, hexane-isooctane blends are testes as well. From Table 3.1, ethanol and hexane have similar properties except the HOV of hexane is much lower than ethanol. Both ethanol and hexane have similar vapor pressure, the primary effect of HOV can be revealed by analyzing Exx and Hxx spray behaviors under different conditions.

Table 3.1: Fuel properties for ethanol, hexane, and isooctane.

	Ethanol	**Hexane**	**Isooctane**
Density $[kg/m^3]$	725	591	631
Viscosity $[\mu Pa \cdot s]$	373.4	164.6	241.9
Surface tension $[mN/m]$	15.7	11.3	12.8
Specific heat $[kJ/kg \cdot K]$	3.24	2.51	2.40
Heat of vaporization $[kJ/kg]$	870.4	327.2	274.1
Vapor pressure $[kPa]$	157.4	186.9	77.2
Boiling point $[K$ at 50 $kPa]$	333.7	321.0	349.2

** all properties are calculated/obtained at 363K (90°C)*

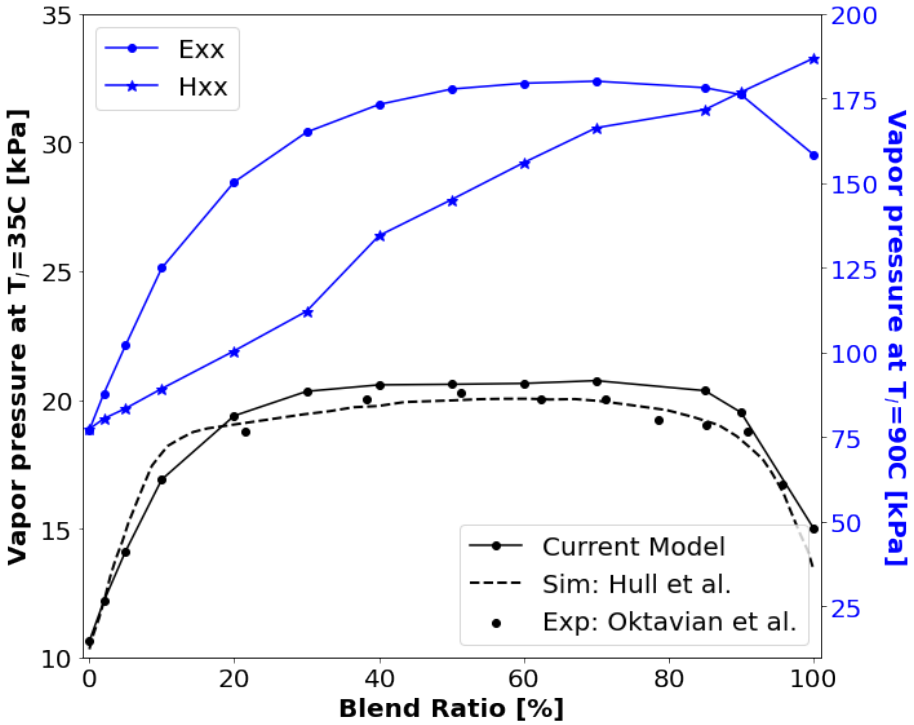


Figure 3.4: Vapor pressure validations for fuel blends.

3.4.1 ECN Spray G

In this work, a standard GDI spray injector using a Delphi multi-hole GDI nozzle, commonly referred to as Spray G and provided by Engine Combustion Network (ECN) [151], is used for experimental testing. Spray G configurations and injector specifications are provided in Figure 3.5 and Table 3.2. The standard operation condition for Spray G is listed in Table 3.3. To investigate the behaviors under different flash boiling intensities, the ambient gas pressure is varied from 15 kPa to 100 kPa. The fuel temperature is fixed at 90^oC, and ambient temperature is kept at 60^oC. DBI system captures the spray structure under all operation conditions, and the liquid penetrations or spray angles can be obtained after post-processing of spray images. For some selected cases, PDA system is used to measure the droplet velocity and size at fixed vertical testing position (15mm downstream from the injector tip), and droplet data is collected with a radial sweep with 1mm increment from the injector axis through the spray. At each testing location, minimum 10000 droplets are captured to ensure the statistically significance. Since the measurement location of PDA is relatively close to nozzle exit, the liquid dense region, not all droplets are considered by the equipment to calculate SMD. The accuracy and spherical accuracy are maintained at reasonable level for the measurement.

Simulations for spray G are performed accordingly using KIVA. Due to the axial-symmetry of the jet simulation, spray simulation only performed using 1/8 sector mesh with periodic boundary condition on the two radial cut planes to save the computational time. The direction of spray jet is centralized and has 22.5^o apart from either of the two radial cut planes in the azimuthal direction. Spray simulation is performed from SOI to 1 ms after SOI. For cases that selected for post-injection mixture analysis, simulation is terminated after 3 ms of SOI. In KIVA platform, liquid phase is computed as an extended series of Lagrangian parcels. Therefore, to mimic the DBI

vision, the parcels from one single jet simulation are copied and revolved every 45° to form 8 jets configuration for the GDI injector, and then all parcels are projected onto a vertical observation plane in the primary "Spray G" plume orientation (see front view in Figure 3.5). For each of the original and copied parcels, its location is disturbed within a small cubical volume to account for the fact that each parcel represents numbers of droplets distributed in the vicinity of the parcel. The light blockage of each pixel on the observation plane is proportional to the summation of the radius cubed of all droplets projected in such pixel divided by the physical area of the pixel.

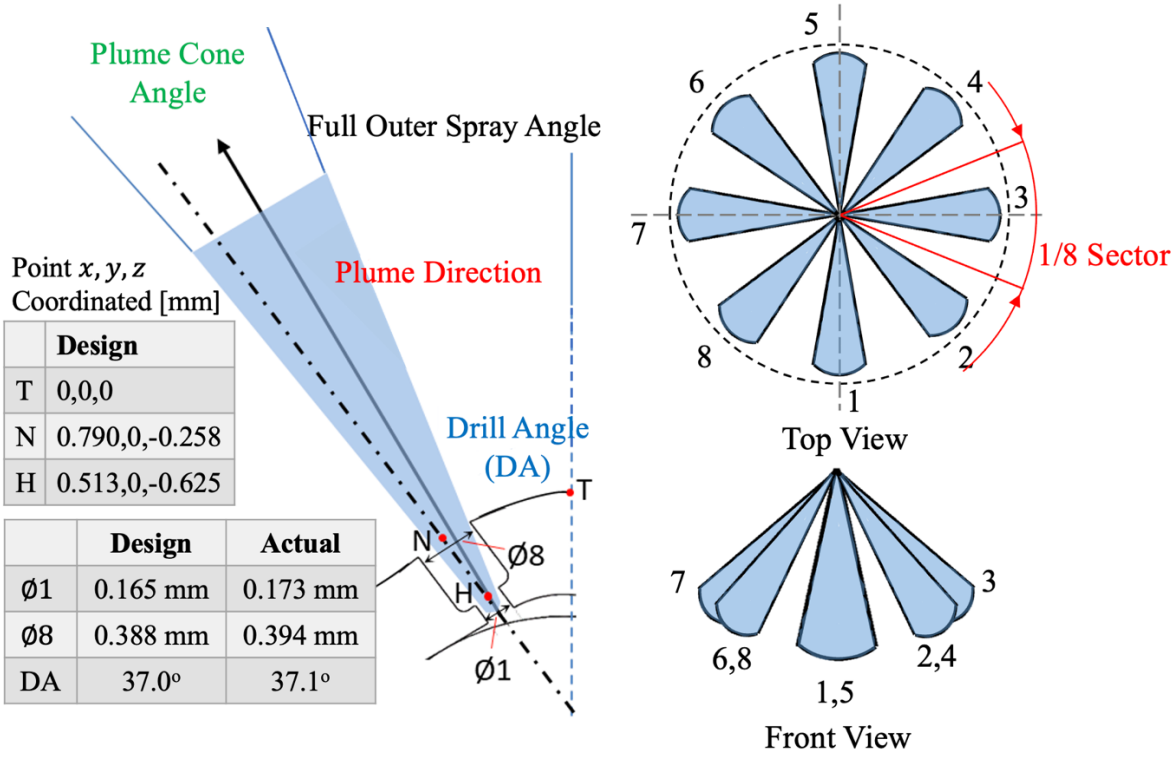


Figure 3.5: ECN spray G configurations. Left: plume dimensions; Right: Front and top views of spray G plume orientation [151, 152].

Table 3.2: Spray G Nozzle Geometry.

Number of holes	8
Spray Shape	circular
Bend Angle	0°
L/D ratio	1.4
Hole shape	straight
Manufacturing	EDM
Flow rate	15 cc/s @10 MPa
Fuel injector	Delphi solenoid-activated
Nozzle type	Valve-covered orifice (VCO)
Nozzle shape	Step hole
Orifice diameter	0.165 mm specification
Orifice length	0.16-0.18 mm
Step diameter	0.388 mm specification
Orifice drill angle	37° relative to nozzle axis
Full outer spray angle	80°

Table 3.3: Spray G Operating Conditions of ECN.

Ambient gas temperature	300 °C (573 K)
Ambient gas pressure	near 6.0 bar (600 kPa)
Ambient gas density	3.5 kg/m^3
Ambient gas oxygen (by volume)	0% O_2 (non-reacting)
Ambient gas velocity	Near-quiescent, less than 1 m/s
Fuel injector	Delphi solenoid-activated
Nozzle	8-hole
Fuel injection pressure	20 MPa (200 bar), prior to start of the injection
Fuel	Iso-octane
Fuel temperature at nozzle	363 K (90 °C)
Injection mass	10 mg
Electronic injection duration	680 µs
Actual injection duration	780 µs

3.5 Flash-Boiling Sprays Simulation and Validation

Figure 3.6 and Figure 3.7 show synthetic droplet light blockage images for all the spray simulations with Exx and Hxx under various ambient pressure conditions. Overall, the current model well predicts the characteristics of spray behavior, for example, jet collapsing and tip recirculating at different superheated degrees. Due to the strong plume-plume interaction and collapsing with the increase of the superheated degree (decrease of r_P), liquid tip penetration increases. Compared to isooctane, flash boiling characteristics, such as jet widening and diminished gaps between spray jets, are more pronounced for pure ethanol and hexane, and the near-field cone angle increases. This is mainly attributed to ethanol and hexane's higher superheated degree which led to stronger flash boiling. With the increase of hexane and ethanol contents, the vapor pressure of mixture increases. Thus, at the same r_P conditions the ambient pressure is higher for fuels containing higher ethanol or hexane content, and liquid penetration, therefore, decreases generally because of the higher resistance or drags presented by the surrounding gases.

Under non-flashing condition in which the r_P value is greater than 1, spray structures look comparable for all fuel blends except the liquid penetration length. There are numbers of factors to affect liquid penetration, such as aerodynamic drag, plume trajectory, and vaporization rate. There is a clear gap between two jet plumes, and the interaction between the adjacent jets is inconspicuous. The control mechanism for atominzation of liquid fuel is governed by the aerodynamic breakup. As r_P value drops, flash boiling intensity raises and makes contributions to the phase change and breakup processes. The plume starts to swell and widen, and the gaps between plumes gradually fade away. The individual plume of Exx sprays appears wider than that of Hxx spray because of the poor liquid vaporization of ethanol spray caused by its high latent heat

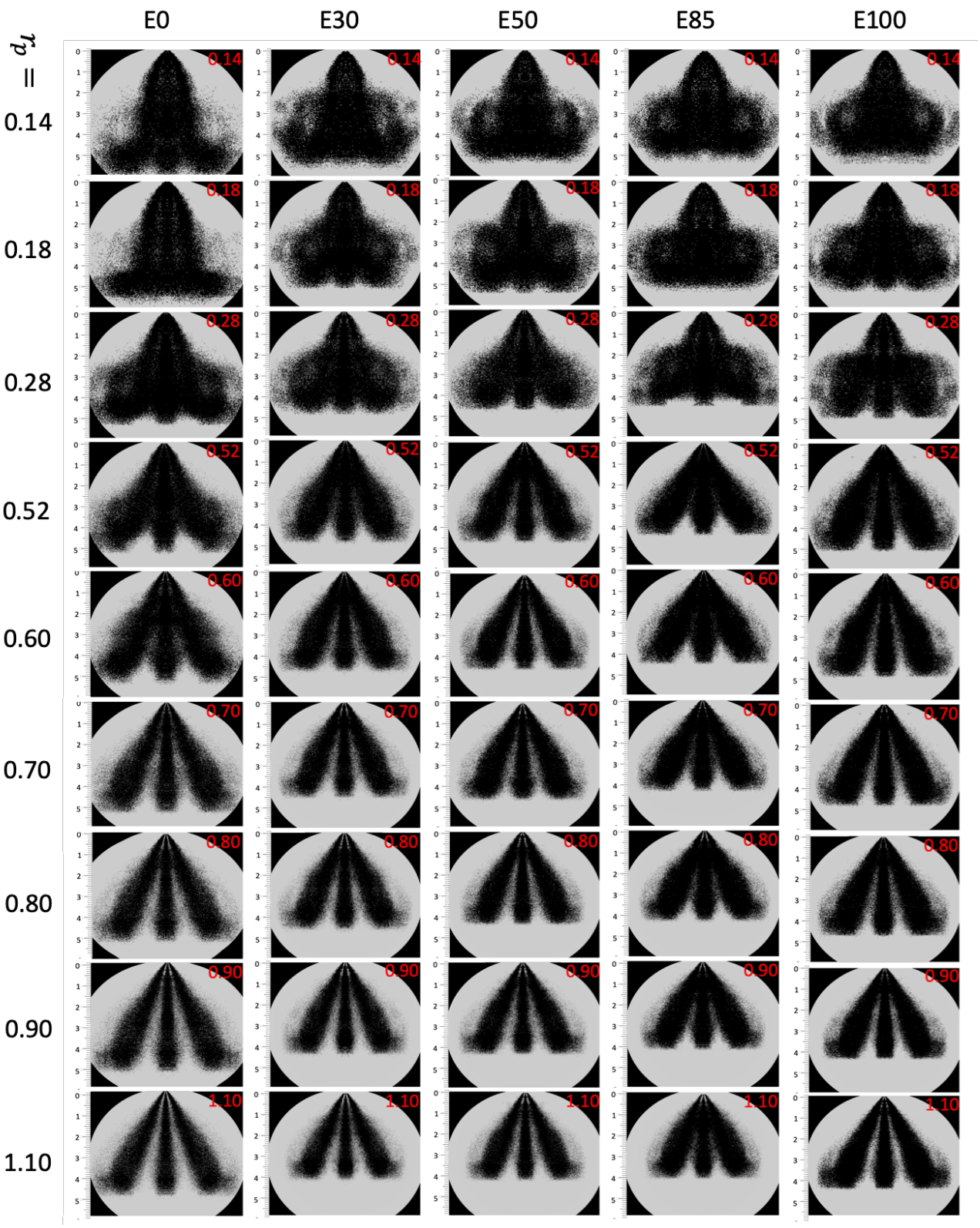


Figure 3.6: The synthetic droplet light blockage images for Ethanol-Isooctane sprays at EOI.

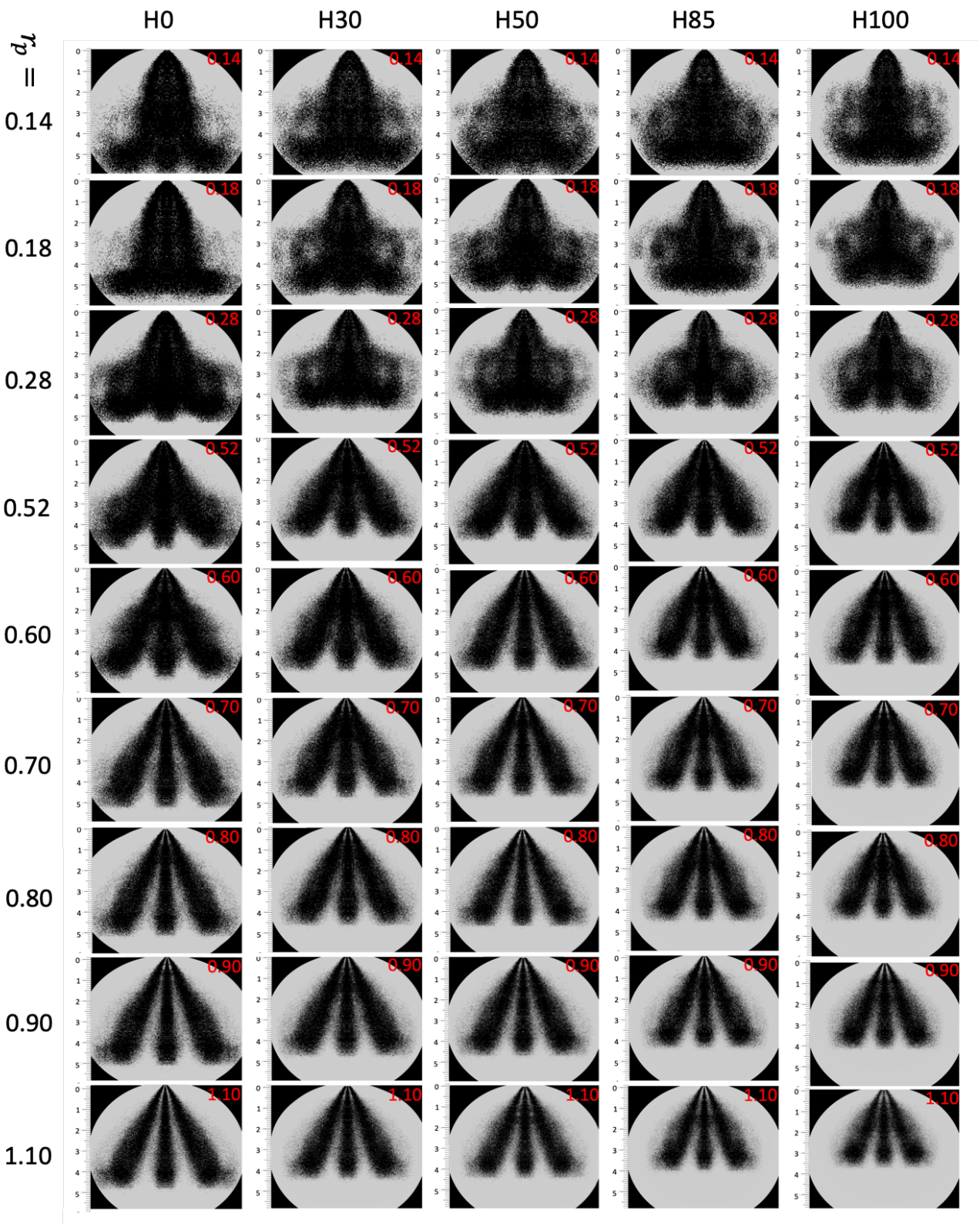


Figure 3.7: The synthetic droplet light blockage images for Hexane-Isooctane sprays at EOI.

of vaporization. Plume trajectory of Exx or Hxx sprays merges toward the centerline with decreasing r_P, while plumes of ethanol are least affected. Pressure differences between the spray center and the ambient environment induced by condensation [153] results in plume merging. Due to the poor vaporization of ethanol, the local vapor concentration is low, and the droplet size is larger comparing to Hxx spray, which can lead to small changes in plume trajectory. Changes of plume trajectory can affact the downstream spray angle, a.k.a. far-field angle, to a great extent. As ethanol spray is most resistant to jet merging, ethanol sprays therefor have the largest far-field angle. Strong merging phenomenon is observed in hexane sprays, and consequently the smallest far-field angle is expected. As indicated in Figure 3.6 and Figure 3.7 when r_P is lower than 0.3, the simulation predicts fully collapse for all the fuel blends, and such behavior is consistent with experimental observations not only performed in this study but from other literatures [154-156].

Comparisons are made between the simulations and experimental results. In the following sections, selected cases will be presented for validation purposes. Spray structures from high-speed images and synthetic droplet light blockage images are compared first. In each figure, images of sprays at EOI captured in experiments are displayed at the top, and corresponding simulations at the same time frame are given at the bottom. Liquid penetration history from experimental measurements and simulations for these selected cases at three flash boiling intensities are plotted next. The liquid penetration in simulation is defined by the vertical location of the farthest Lagrangian parcel. There is a minor difference between predicted and measured liquid penetration length due to the imaging processes filtered out the noise points based on the pixel threshold setup. For microscopic characteristics, SMD comparisons between experiments and simulations for selected cases are presented. Due to the limitations of the PDA experiment, i.e., the measurement of droplet size in the dense liquid region cannot be obtained, the SMD of droplets at 15 mm

downstream of the injector tip along the center of the spray plume are averaged and used for general droplet size trend analysis. Supplemental curves for droplet at radial location from center to outer edge of spray are provided as well to prove the model's ability to predict the droplet sizes at different spray locations.

3.5.1 Single-Component Sprays

Spray morphologies of pure isooctane (E0) and ethanol (E100) are given in Figure 3.8 and Figure 3.9. Liquid penetrations during entire injection process for E0 and E100 are given in Figure 3.10 and Figure 3.11, respectively. Figure 3.12 provides the averaged SMD for E0 and E100 at different superheated degrees. Both macroscopic and microscopic features of spray from simulations match reasonably well with experiments. As for the macroscopic characteristics, current spray model can depict spray patterns that observed in experiments and calculated liquid penetrations in the vertical direction are comparable with the measured ones. For microscopic features, averaged droplet SMD increases with the increase of ambient pressure as can be seen from experiment. Such behavior is well captured by the model for E0 and E100, and errors between the calculated and measured data are within 10% for all cases.

For pure isooctane spray at $P_a = 100\ kPa$ and $80\ kPa$, the r_p values are about 1.3 and 1.1, respectively. Sprays are under non-flashing conditions, and there are no obvious changes in spray structure. As the ambient pressure reduces, the plume cone angle opens up and becomes a wide-spreading mist. This could result from the velocity deviation of secondary droplet due to the flash boiling breakup. Besides, the flash boiling enhances phase transition from liquid to vapor, resulting in a fast momentum exchange between the two phases. The gas phase gains speed rapidly due to the momentum carried by the vapor generated at the droplet surface and, in turn, alters the stability

of liquid jets. Eventually, eight jets form a nearly hollow cone spray at $r_{p,E0} = 0.28$. The trajectory of spray plume is pushed inward, and the increased momentum of the droplet in the vertical direction causes longer liquid penetration (see Figure 3.10). Experimental measurements also confirm that at the spray center high vertical droplet velocity has been observed [148].

Similar changes can be discovered for pure ethanol spray with increased superheated degree. Spray collapsing fully developed once the r_p value drops below 0.3, and strong recirculation occurs at the tip of spray jets and vortices can be detected. Such strong recirculation prevents liquid jet penetrating further downstream. Droplet breakup is significantly enhanced by flash boiling, thus producing smaller droplets (refer Figure 3.12) which can be easily carried by the recirculation gases. Vortices are generated at the jet tip for E0 at $r_p = 0.28$, but not as distinct as that in E100 cases. The vaporization rate for isooctane is faster because of the lower HOV, thus isooctane droplets vaporize quickly as they enter the recirculation ambient. At the same superheated degree ($r_{p,E0} = 0.65$ and $r_{p,E100} = 0.64$), isooctane spray has longer liquid penetration length, which can be proved by comparing the curves in Figure 3.10 and Figure 3.11. A result of the combined effects of vaporization inhibition caused by the HOV, the least trajectory change, and higher ambient pressure in E100 case can explain the shortened penetration.

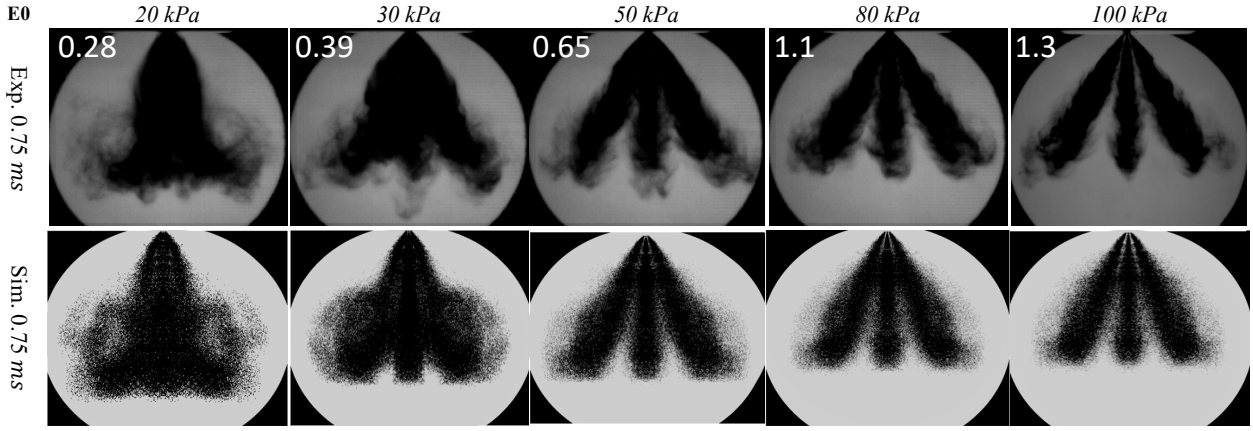


Figure 3.8: The synthetic droplet light blockage images for pure isooctane spray.

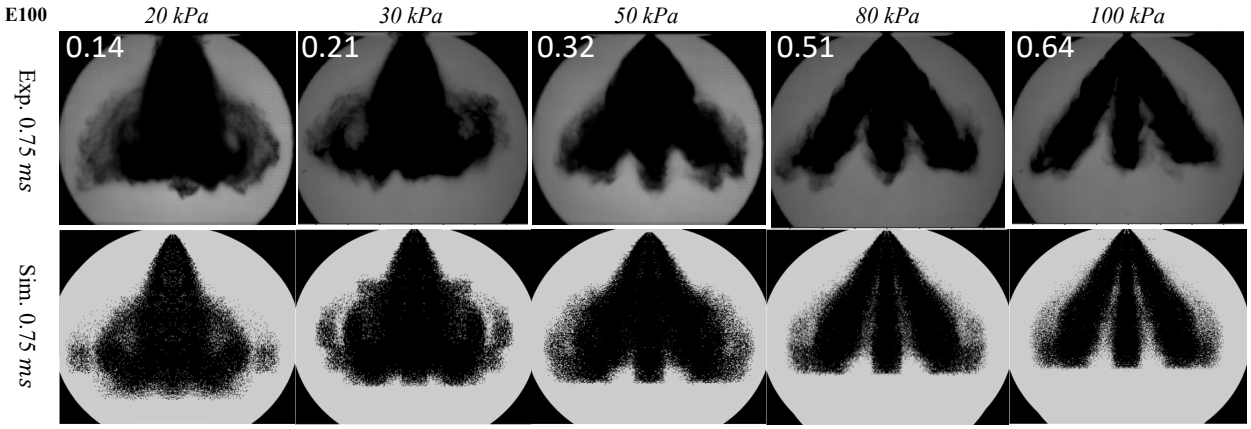


Figure 3.9: The synthetic droplet light blockage images for pure ethanol spray.

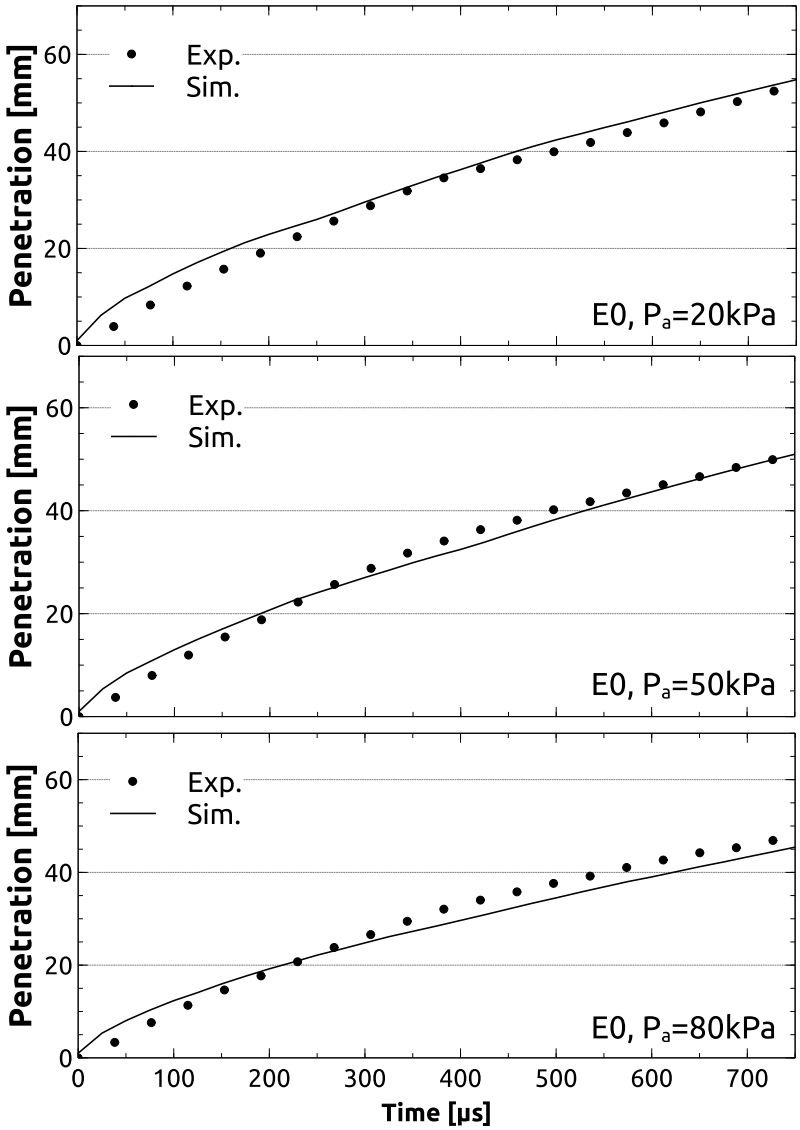


Figure 3.10: Liquid spray penetration for E0 at different ambient pressures.

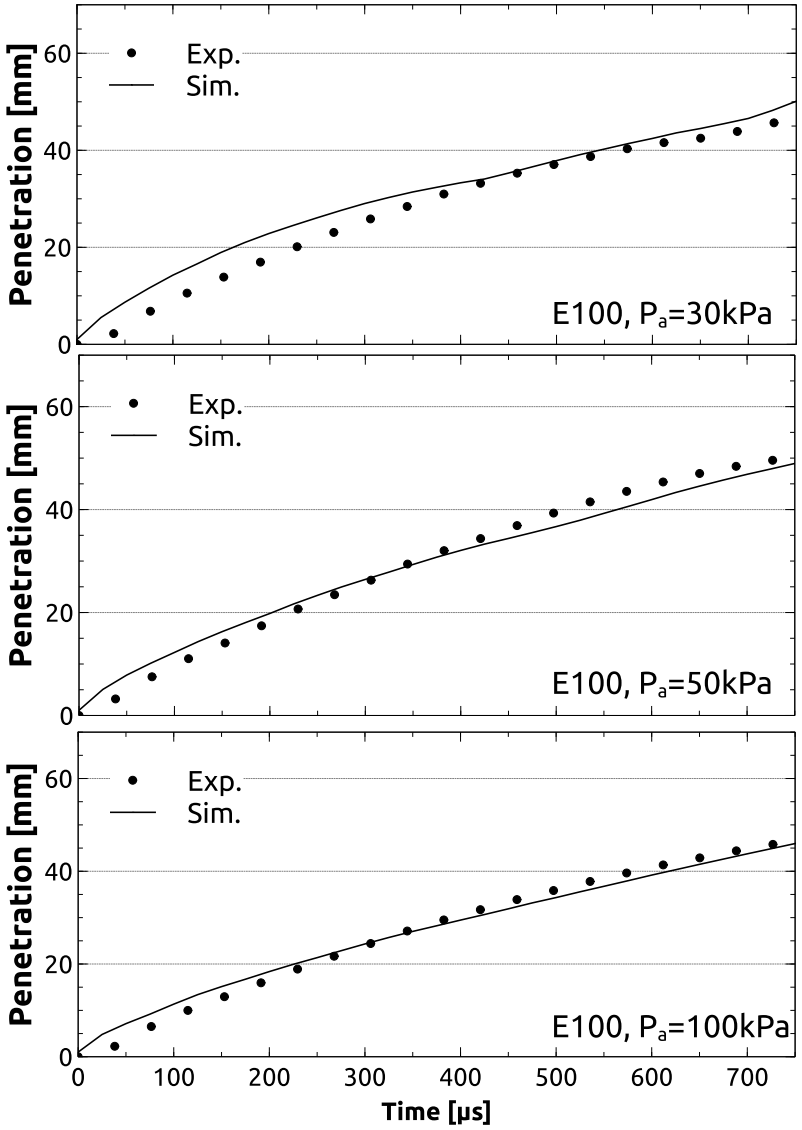


Figure 3.11: Liquid spray penetration for E100 at different ambient pressures.

From Figure 3.13 and Figure 3.14, simulation results prove that when superheated degree is high, most droplets at spray center are small, and the vapor concentration at spray center is relatively high during the injection process. Again, the measurements close to the spray center are inaccurate due to the PDA system's inability to gather data due to the high density of the sample population. Because of the plume widening effect, there exists a barrier that blocks the transfer from spray center to surrounding gases. As a result, the pressure difference between the spray

center and the ambient environment induced by condensation is built up, enhancing the spray collapsing behavior. At the 15mm downstream of injector tip, the dominate mechanism for changes in droplet size is vaporization rather than breakup. Compared to the ethanol sprays, SMD for isooctane sprays is smaller in spray center. High HOV of ethanol causes more local temperature drops and consequently inhibits vaporization rates. Then such low vaporization rates lead to low local vapor concentration and reduce the condensation induced pressure difference between the spray center and the ambient. On the other hand, larger droplets produced in E100 sprays have larger inertia, thus it is more difficult to manipulate the trajectory of these droplets due to such pressure differences. Therefore, ethanol sprays are more resistant to plume merging from microscopic point views.

Discrepancies for droplet SMD in Figure 3.13 and Figure 3.14 may be caused by the following reasons. First, the PDA data is obtained from multiple injections. In each injection, the spray structures would change marginally due to the uncertainty of the experiments. For simulations, the results stay the same in every calculation. Therefore, the SMD in experiments can be influenced by the outlying droplets. The second reason is due to the accuracy and spherical accuracy of the PDA setups as mentioned previously. Though 10000 droplets are taken during the measurements, only a portion of them are used to compute SMD. Despite these ineluctable uncertainties, simulations can predict droplet sizes relatively well under the various testing environments for E0 and E100 sprays.

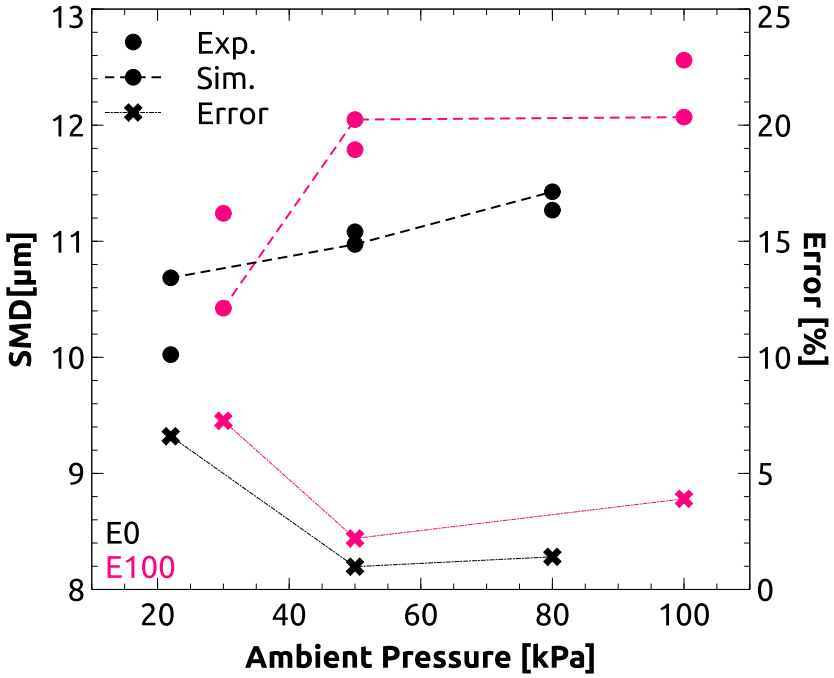


Figure 3.12: Comparisons of averaged SMD for single-component sprays.

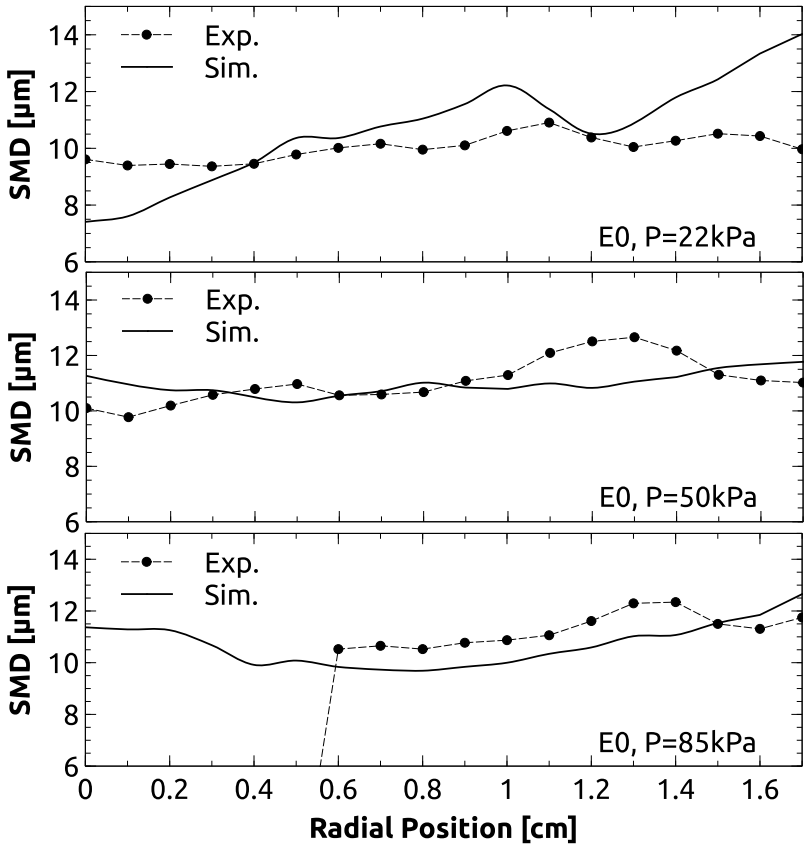


Figure 3.13: Droplet size distribution along the radial direction at 15mm downstream of the injector tip fueling with E0 at different ambient pressures.

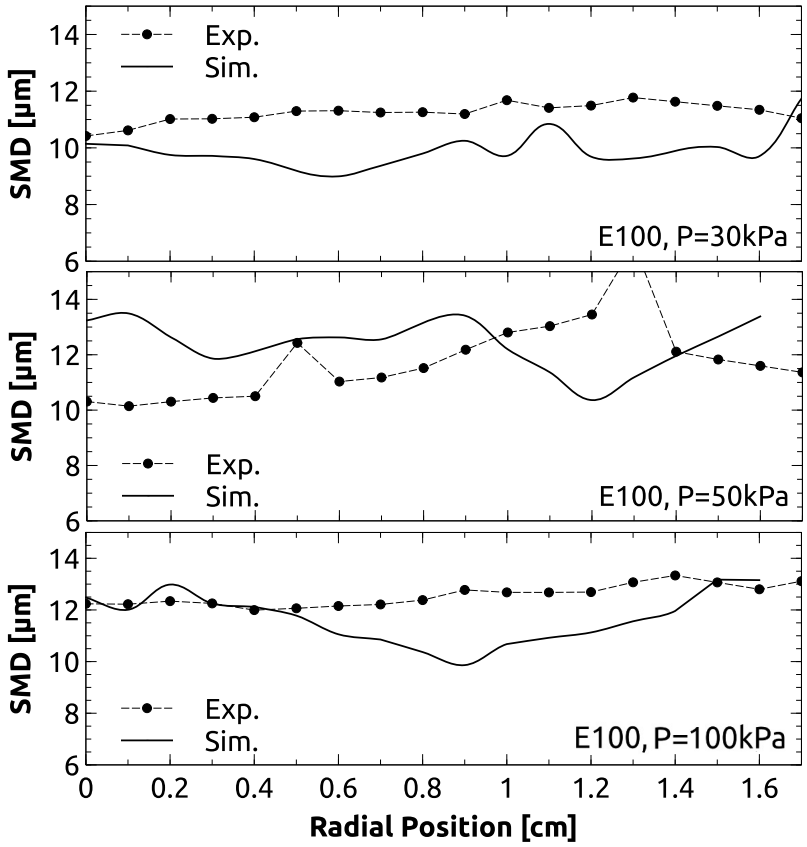


Figure 3.14: Droplet size distribution along the radial direction at 15mm downstream of the injector tip fueling with E100 at different ambient pressures.

3.5.2 Binary-Component Sprays

Macroscopic characterization for the sprays with different fuel blends are compared. Figure 3.15 shows the high-speed images and simulation results for E30 at five ambient conditions. At $100kPa$ ($r_{p,E30}$=0.6) and $80kPa$ ($r_{p,E30}$=0.48) ambient pressures, the sprays are at the non-collapsing regime, where the effect of flash boiling breakup is not significant. Though the current model restores the phenomenon of merging plumes near the injector tip to some degrees, sprays predicted by the model are similar and no significant differences. Further decreasing the ambient pressure, the r_p reduces, indicating the enhancement of flash boiling breakup. The current model accurately predicted the characteristics of spray behavior. Jet collapsing and tip recirculating are

well represented in the simulation results. Due to such strong recirculation, the liquid tip penetration reduces (see Figure 3.18). When the ambient pressures are very low (30 kPa and 20 kPa), an inward drifting motion of the droplets is developed and plumes are fully collapsed, and the liquid jet penetration increases again as the drag effect from ambient is reduced because of the lowered ambient density. Again, once the r_p values drop below 0.3, sprays enter the fully collapsing regime, and longer liquid penetration length indicates the high risk of fuel impingement on the wall or piston top, which would cause UHC emissions issues in engine applications.

Figure 3.16 compares the spray structures for various ethanol blend ratios at a fixed ambient pressure of 50 kPa. Predicted sprays for different fuel blends imply that the current spray model is capable of simulating either single- and multi- component sprays in which flash boiling breakup is dominant. As shown in Figure 3.16, Exx sprays undergo dramatically structural variation with increasing ethanol content until the blend ratio exceeds 30% in which the r_p value approaches to threshold of 0.3. Gaps between adjacent spray plumes vanish and collapse occurs for sprays with 30% to 85% ethanol content. However, for E100 spray, the collapsing of the spray plume is weakened, and individual jet tip can be identified easily. This can be explained by the spray droplet size and pressure difference across sprays due to condensation effect.

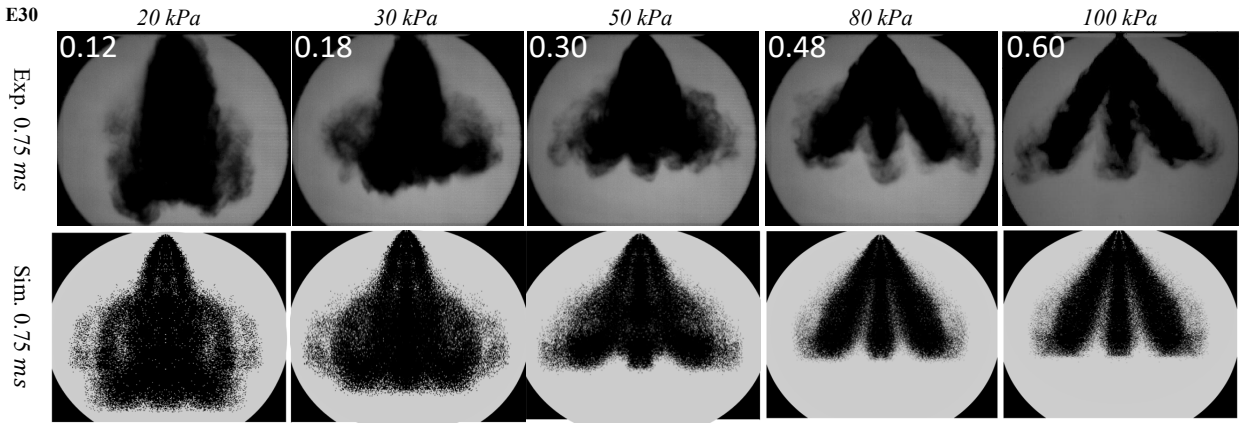


Figure 3.15: The synthetic droplet light blockage images for E30 spray at different pressure.

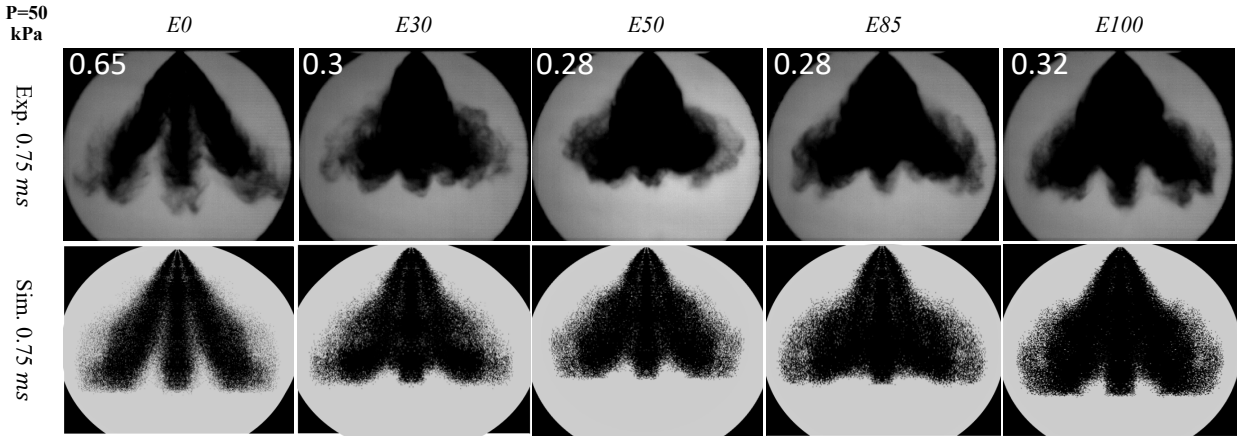


Figure 3.16: The synthetic droplet light blockage images for Exx spray at $P_a = 50kPa$.

At fixed ambient pressures, the liquid penetration lengths decrease with the increasing ethanol content and reach the minimum (~ 45 mm in experiments) at the 50% blend ratio as indicated in Figure 3.18. Further increasing the ethanol content, liquid penetration length increases. Adding ethanol to isooctane can raise the vapor pressure of Exx as plotted in Figure 3.4. At the fixed ambient pressure condition, the higher the vapor pressure of a mixture is, the smaller the r_p value becomes. However, the vapor pressure of the Exx mixture approaches a stable value at about 40% of ethanol additive, and later starts to drop after 80% of ethanol is added into isooctane. Thus, Exx sprays experience more intense flash boiling with medium ethanol content (40% to 80% approximately) due to lower r_p value. Flash boiling induced breakup enhances the atomization of liquid spray and produces smaller droplets that can benefit vaporization and reduce liquid penetration length. Though flash boiling intensity is similar when adding more than 30% of ethanol content to isooctane, the higher ethanol content can degrade the vaporization of droplets because of the increased HOV. Detailed temperature and vaporization analysis will be provided later.

Simulations for Hxx sprays are compared with experiments as well. Figure 3.17 shows spray images of H30 at five ambient pressures that cover wide range of flash boiling intensity. With increased superheated degrees, structures of H30 sprays evolve similarly as E30 sprays, i.e.,

plume becomes a spreading mist and merges together as reducing the ambient pressure. Once the r_p value passes 0.3, spray fully collapses and the recirculation movement at the jet tip is pronounced. Unlike the aforementioned trend of liquid penetration at increased superheated degree for Exx sprays, i.e., the liquid penetrates further into the downstream of injector; liquid penetration for H30 sprays remains nearly the same when lowering the ambient pressure from 68 kPa to 32 kPa, a wide span of superheated degree. HOV for hexane is comparable to isooctane, which are both much smaller than ethanol. Therefore, under the strong flash boiling condition where the atomization process is considerably enhanced, smaller droplets that scattered around the spray can evaporate faster, clearing the spreading mist of smaller droplets. Accordingly, the vertical penetration of liquid jets is shortened, and the resulting liquid plume is less dispersed.

At $r_p = 0.6$ and 0.45 (0.48 in E30 case), the spray is in non-collapsing regime for both H30 and E30, but the penetration length of H30 is higher than E30 at the same r_p because of the reduced ambient gas density in H30 cases. On the other hand, the low ambient density would depress the effect of aerodynamic breakup and potentially increase the breakup time of H30. However, the surface tension and liquid density of hexane are smaller when compared to ethanol. Adding hexane to isooctane can effectively promote the bubble growth process and lead to better flash boiling breakup and liquid dispersion. As a Consequence, comparing H30 and E30 sprays at the same superheated degree, contrasts in the spray structure are determined by the most competing breakup mechanism. Besides the breakup process, the vaporization rate for H30 is higher comparing to E30 at the same r_p value because of lower HOV and higher relative velocity between droplets and ambient for the H30 spray. As a result, the spray plume for H30 is narrower and resultant spray cone angle is smaller comparing to E30. Such observations are consistent with experimental measurements [148].

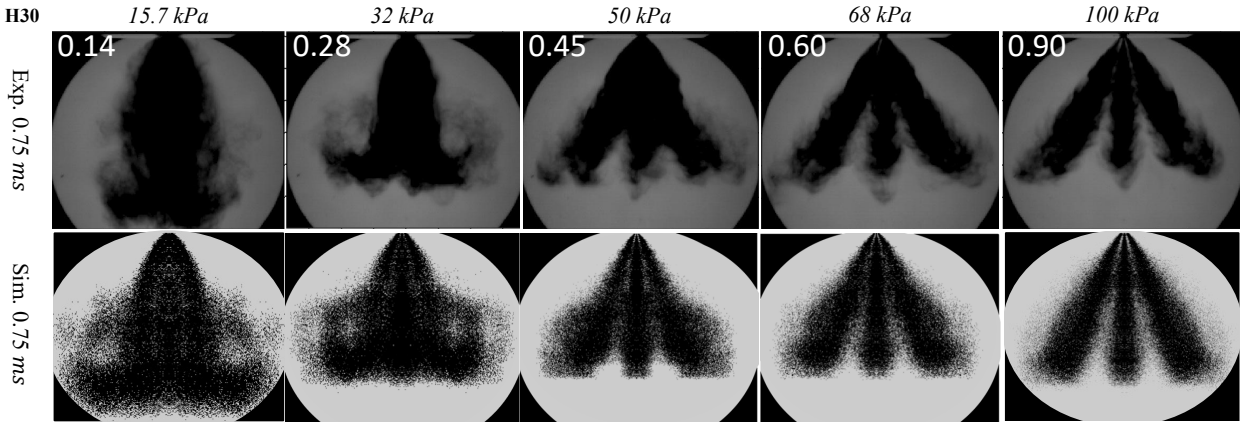


Figure 3.17: The synthetic droplet light blockage images for H30 spray at different pressure.

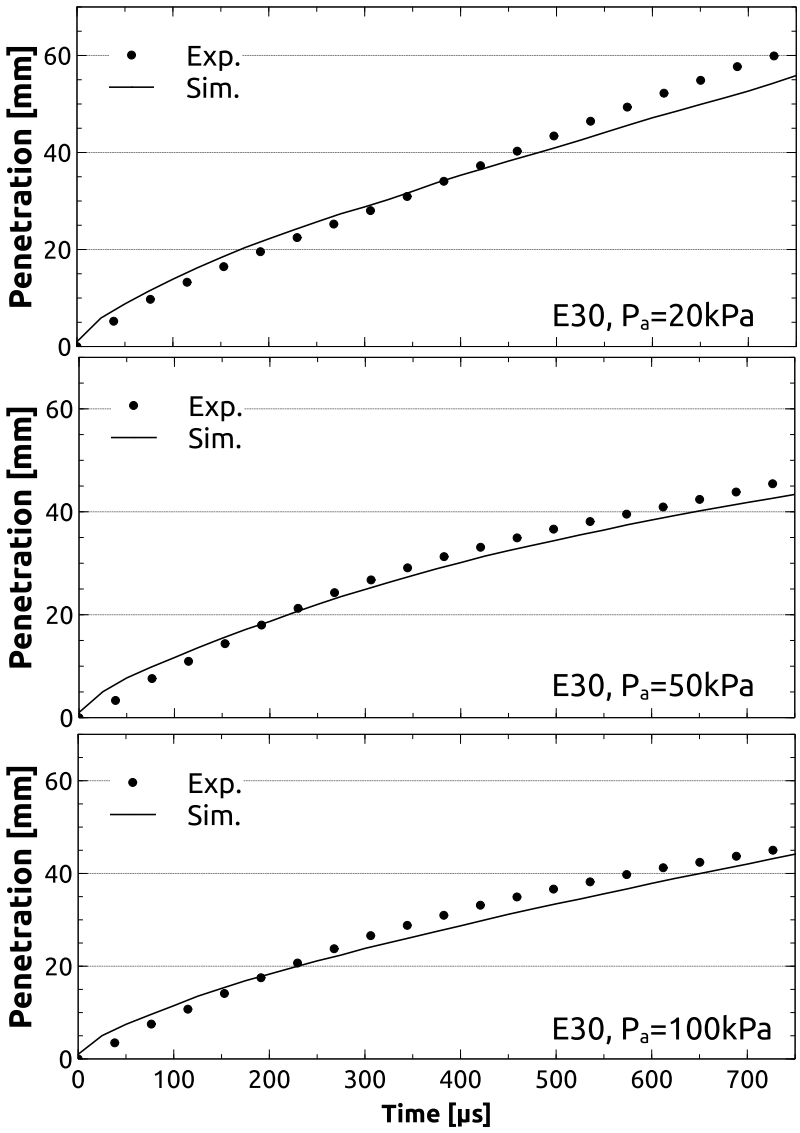


Figure 3.18: Liquid spray penetration for E30 at different ambient pressures.

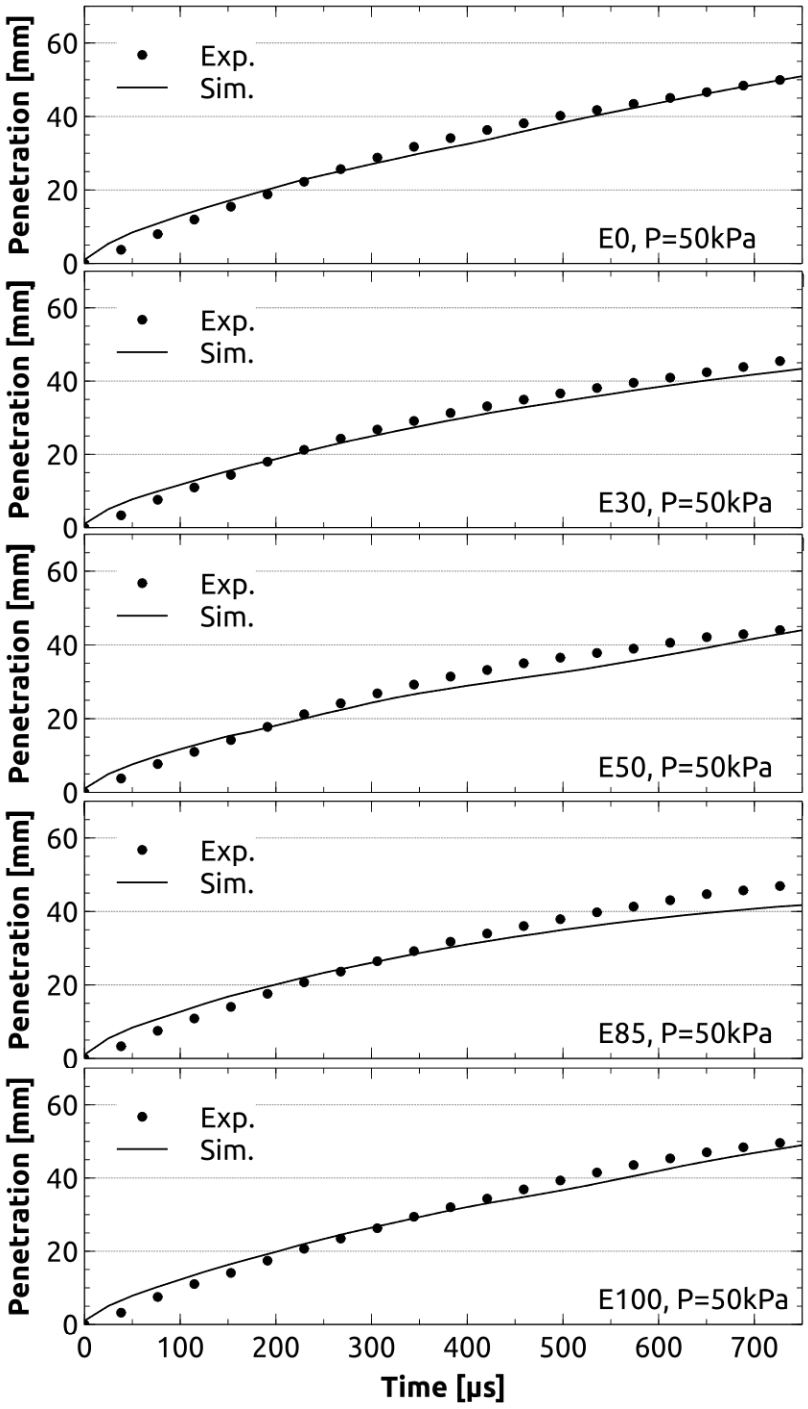


Figure 3.19: Liquid spray penetration for Exx at $P_a = 50kPa$.

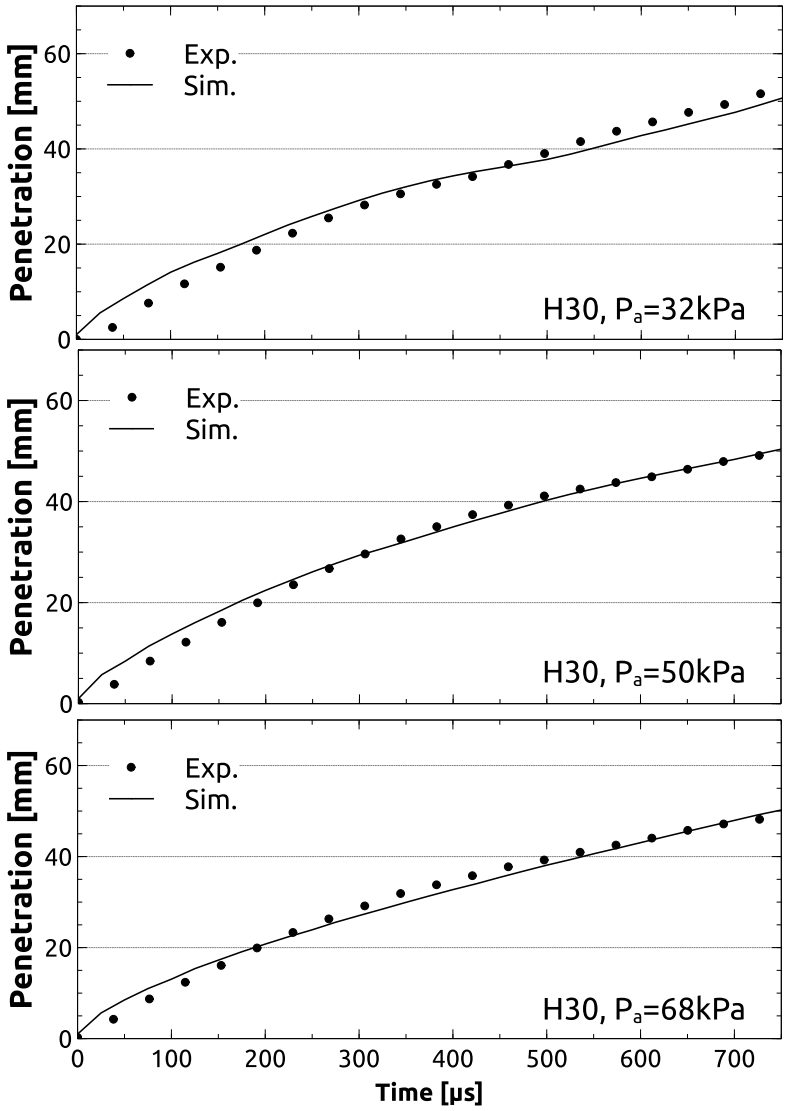


Figure 3.20: Liquid spray penetration for H30 at different ambient pressures.

In Figure 3.21, averaged droplet SMD increases with the increase of ambient pressure as can be seen from the experimental data. Such behavior is well captured by the model for different blends, and errors between the calculated and measured data are within 7% for all cases. The averaged SMD for H30 is smaller than Exx cases for all ambient pressure conditions. E30 and E50 have the similar averaged SMD at the same ambient from experimental measurements. In model calculations, E50 constantly has larger droplet size under all ambient conditions comparing to E30 at the testing location.

Near the spray center, the predicted droplet size is larger than the measured SMD for a majority of the cases (see Figure 3.22 to Figure 3.24); therefore, these droplets have larger momentum, thus the higher liquid penetration. Comparing to experimental results, calculated SMDs tend to be larger at the spray center and outer regime of the spray due to the PDA acquisition system has its limitation to collect droplets in a spray. During the injection period, PDA failed to collect data at the spray center due to the dense liquid presented at 15mm downstream. As for the reason that some larger SMD droplets appear at the outer spray region in simulations, one reason could be smaller spray angles predicted by the model. Due to the small spray angle, droplets are more concentrated within a certain range. Droplets at the outer spray region have insufficient kinetic energy to spread out, and larger droplets are trapped and travel with the mainstream of the spray. Analysis of droplet size distribution from vaporization point view will be provided in the following section. Overall, the droplet size distribution from the simulation matches reasonably well with the PDA data for different fuel blends at various superheated degrees.

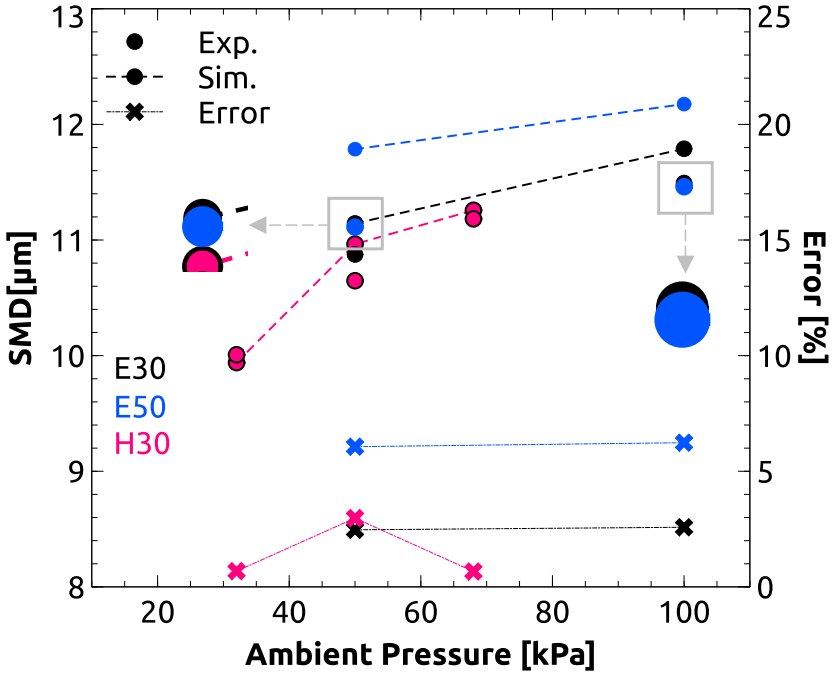


Figure 3.21: Comparisons of averaged SMD for binary-component sprays.

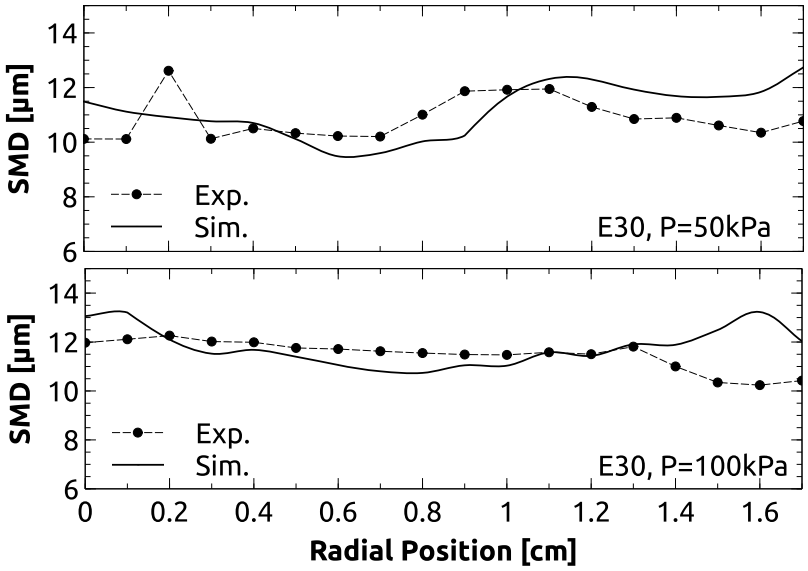


Figure 3.22: Droplet size distribution along the radial direction at 15mm downstream of the injector tip fueling with E30 at different ambient pressures.

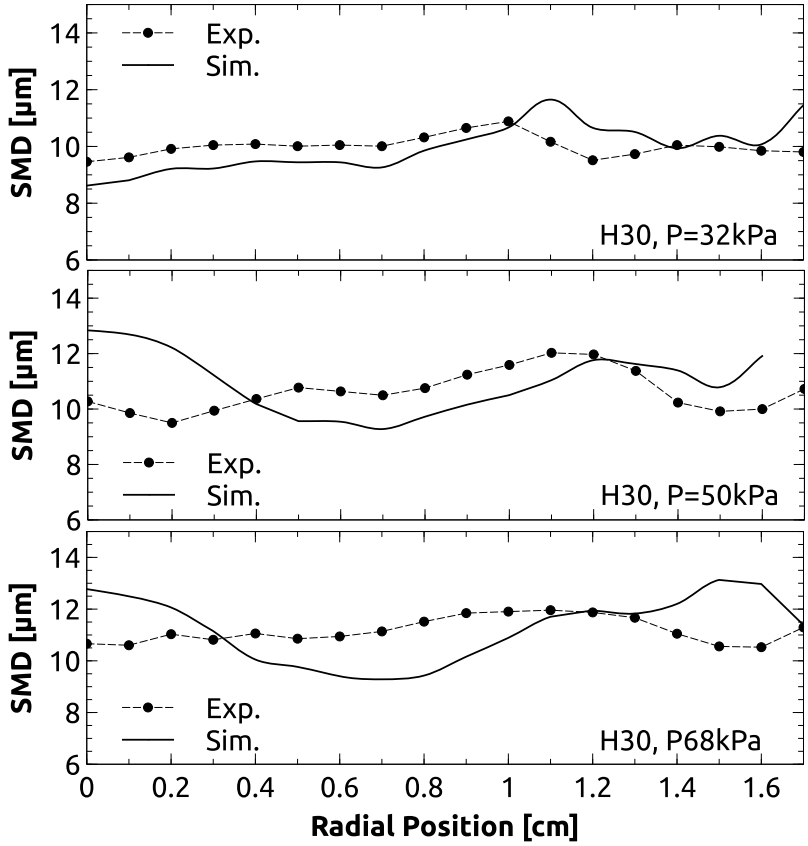


Figure 3.23: Droplet size distribution along the radial direction at 15mm downstream of the injector tip fueling with H30 at different ambient pressures.

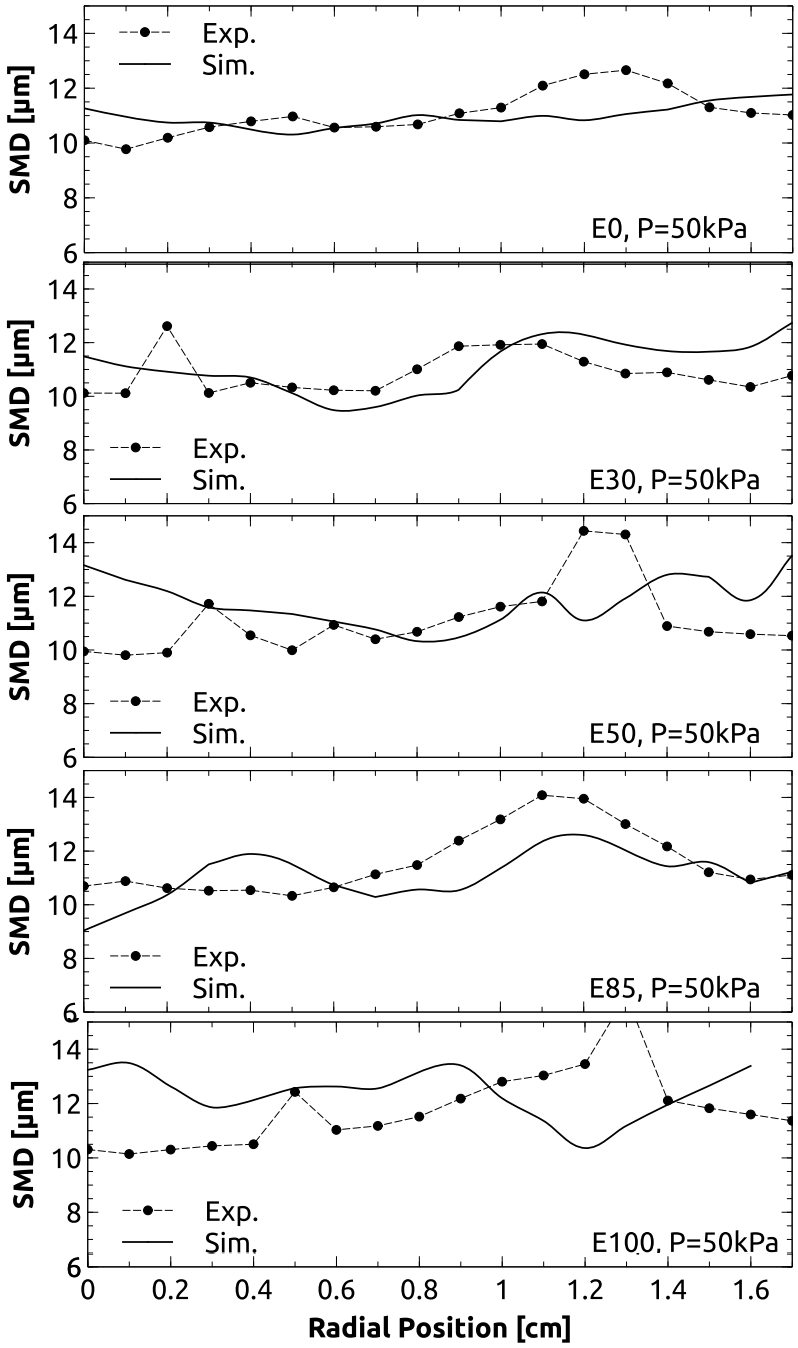


Figure 3.24: Droplet size distribution along the radial direction at 15mm downstream of the injector tip fueling with Exx at $P_a = 50kPa$.

3.6 Characteristics of Spray Vaporization and Mixing

To investigate both liquid and vapor phase characteristics during the injection process, 3-D rendering visualization is used. To best present the results, a 2-D slice from the 3-D simulation is used. The orientation for the 2D slice is indicted in Figure 3.25 which is along the same direction of the simulated spray jet. As shown in Figure 3.25, the parcels represent the liquid phase of the spray and indicate the skeleton of the spray. Vapor phase of the spray is indicated by the mass fraction of each component. To highlight the spray profile, contours of mass fraction of species with 0.05 are used: white contour represents isooctane and red contour is either ethanol or hexane.

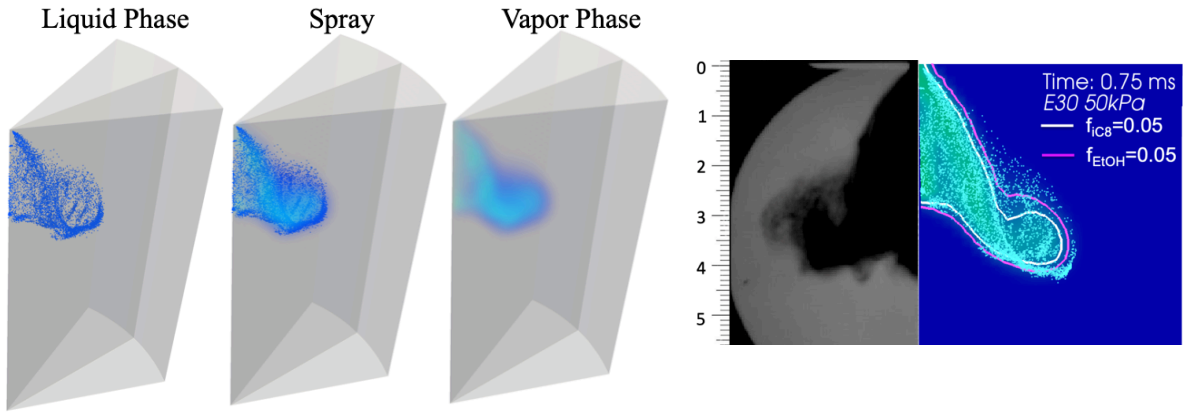


Figure 3.25: 3D rendering visualization.

3.6.1 Exx Blends at Various Superheated Degrees

Investigations on vapor and liquid distribution for Exx sprays at a fixed ambient pressure of 50 kPa are given in Figure 3.26. For a pure isooctane spray, the vaporization event is largely inhibited as the vapor concentration of isooctane is negligible during the entire injection process. E0 spray is in the non-collapsing flashing regime. Adding more ethanol content to isooctane, the spray collapsing phenomenon becomes significant and the liquid penetration is shortened, and it

reaches to the climax with 30% vol. of ethanol as indicated. When increasing the content of ethanol, the collapse among spray plumes is weakened and the liquid penetration increases. Stronger flash boiling intensity spreads the liquid uniformly in the space. More droplets are brought into the inner cone of the spray when the ethanol content is 30% due to the gas entrainment. When increasing the ethanol content, less droplets can be found at the spray inner cone. Higher ethanol content leads to the slower vaporization rate due to the high HOV of ethanol, thus larger droplet size, which have been justified in the PDA measurement. It is increasingly difficult to change the trajectory of these droplets with a larger radius, and consequently those droplets would keep their original path. Nevertheless, a considerable amount of ethanol is evaporated from the liquid fuel that contains more than 30% vol. of ethanol during the injection event.

Temperature distributions of vapor against the radial direction at 15 mm downstream of the injector tip fueling with Exx at $P_a = 50\ kPa$ are plotted in Figure 3.27 for selected cases. Visualization of the vapor temperature distribution for the entire spray is also displayed at the bottom of Figure 3.27. As mentioned in the simulation conditions, the temperature of liquid fuel is fixed at 90^oC $(363.15\ K)$ for all cases, and the ambient gas (nitrogen) temperature is controlled at 60^oC $(333.15\ K)$. Distinct variations in the temperature distribution can be observed. For E0, the gas-phase temperature along the radial direction increases sharply from the spray center to about $0.5\ cm$ away from the spray center. The temperature value at spray center is nearly the ambient gas temperature ($\sim 331\ K$) and the highest temperature is around $350\ K$ at $0.6\ cm$ away from spray center. The increased temperature is due to the heat transfer from liquid fuel to the ambient as it moves outwards. Even the E0 spray is under the flash boiling breakup regime, indicating a potential transport event (due to bubble growth and liquid vaporization from liquid droplet to inner bubble) inside droplets would occur and consequently lowering the temperature

of liquid fuel, the flash boiling intensity is not as strong as that in the fully collapsing regime and cannot guarantee that a substantial number of nucleation sites will be presented in the droplet or that inner bubble can grow to its critical size for later breakup. Therefore, for E0 sprays at $P_a = 50\ kPa$ a greater number of liquid fuel droplets continuously have a higher temperature than the environment and heat up the surrounding gas during the injection event. The plot of temperature distribution along the radial position of spray shows that the higher gas temperature can be obtained on the path of liquid jet, substantiating that heat is transferred from liquid fuel to surroundings. The temperature distribution of gas-phase in the testing domain also demonstrates that the highest temperature is detected at the center of the liquid stream owing to the heating effect from the hot liquid. Because of the poor vaporization, the droplet size along the radial position at 15 mm is nearly same (see Figure 3.24).

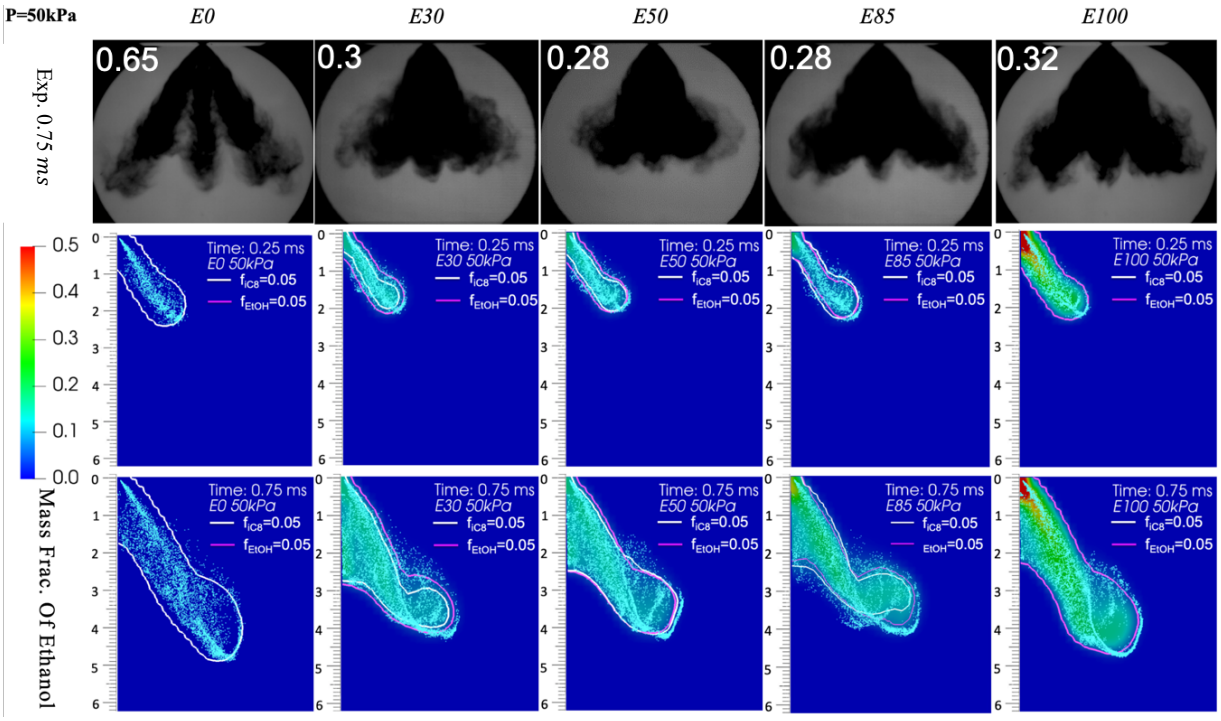


Figure 3.26: Gas/vapor and liquid phase distribution for Exx blends at the fix ambient pressure of $P_a = 50kPa$. DBI images (top) from experiments and corresponding r_p value is marked on the top left of each image; simulation results at 0.25 ms after SOI (middle); simulation results at EOI (bottom).

When there is a strong flash boiling intensity, temperature distribution becomes completely different. For E30 and E50 sprays, compared to the ambient temperature, higher temperature can be observed in the regions that are close to the injector at which the flash boiling occurs instantly. For droplets that experience the flashing breakup, thermal energy in the liquid droplet is consumed to proceed the inner bubble growth and the phase change from liquid droplet to vapor inside bubbles. Temperature of these droplets could reduce below the ambient temperature. However, there are still a portion of droplets that cannot initiate or proceed the flashing breakup. As a result, some droplets take thermal energy from the ambient surroundings, but some emit heat from themselves, and the local temperature is, subsequently, the resultant temperature of the two heat transfer events. Since the temperature of the near-injector region is generally higher than the ambient surroundings, the heat transferred from the liquid fuel to the ambient is more pronounced.

Temperature of the near-injector region for E50 spray is higher than that for E30 spray as indicated in Figure 3.27. Stronger flash boiling intensity further enhances heat transport from the liquid to both internal bubbles and surroundings once the liquid fuel exits the injector. For flash boiling occurs at the droplet-ambient gas interface, the temperature is assumed to be continuous across the interface (see formulation of VLE in chapter 2). Thus, higher vapor temperature can be observed near the injector with increased flash boiling intensity. Superheat in the E50 spray can be dramatically depleted due to the higher HOV. At the droplet-bubble interface, higher superheated degree for E50 indeed increases the nucleation rate and accelerates the bubble growth at the inertia-controlled stage, i.e., more droplets can initiate the nucleation site and the initial bubble growth rate is higher. However, research [157] shows that surface tension has significant instant effects on bubble growth during the later stage of bubble growth, i.e., thermal-controlled stage. Adding 50% vol. of ethanol to isooctane not only increases the surface tension and liquid

density of the mixture but also the HOV. Thus, the thermal-controlled bubble growth could be slowed for some bubble-in-droplet systems so that the internal bubble cannot reach to its critical sizes for breakup. At the same ambient conditions, E50 may produce some larger size droplets because of the aborted flash boiling breakup.

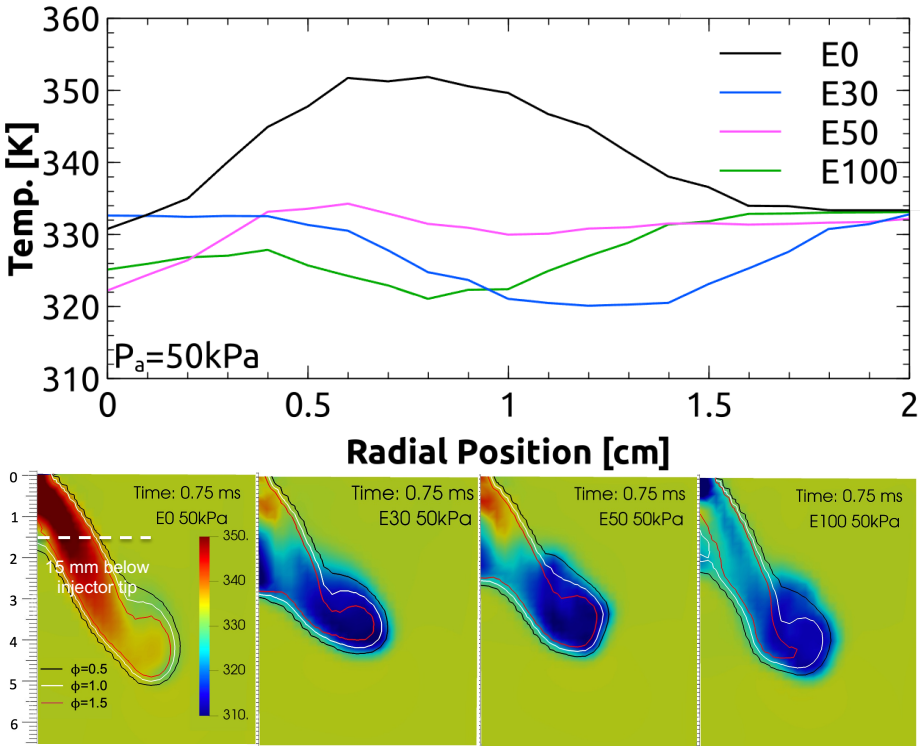


Figure 3.27: Temperature distributions of gas-phase for sprays fueling with Exx at $P_a = 50kPa$. Distribution along the radial direction at 15mm downstream of the injector tip (top); distribution for entire testing domain (bottom).

In the downstream of E30 and E50 sprays, vaporization of droplets plays a crucial role for spray evolutions. Flash boiling has been completed, and fuel droplets temperature can drop below the ambient gas temperature. Heat is transferred from the ambient surroundings to the liquid, and the vapor that has the same temperature as the droplet surface is formed during the vaporization process. This explains the temperature distribution in the field away from the injector tip is low compared to the flash boiling regime. In E30 and E50 cases, the spray center has a lower temperature region when comparing to E0 and E100 due to the vaporization. Such low temperature

region results in the collapsing of the plume as the pressure difference between the spray center and the ambient environment exerts an inward radial force on the droplet, eventually changing the path of the droplet. The extended low-temperature region in the center and smaller droplets presented in the downstream of E30 spray are the main reasons that more droplets are brought into the center of the E30 spray.

Pure ethanol sprays (E100) behave differently, and the lower temperature can be seen near the injector tip where a great amount of ethanol vapor is produced as shown in Figure 3.26. Superheated degree for E100 at $P_a = 50\ kPa$ is lower than E30 and E50, but r_p of 0.32 can still enable the flash boiling to produce hot ethanol vapor from the liquid to both the ambient gas and internal bubble. HOV of E100 is the highest among all fuel blends, so superheat in liquid droplet is consumed and impoverished rapidly compared to the other fuels, which causes the flash boiling to happen transitorily. Consequently, there is not enough hot vapor to raise the local temperature. The flash boiling breakup, on the other hand, is suppressed or aborted as discussed, and droplet size is not significantly reduced due to the lack of effective breakup. Energy from ambient gas is transferred to the liquid droplet for vaporization and relatively cool vapor can be produced and enveloped around the droplets. Since the droplet density near the injector tip is large, the cooling effect of vaporization from ethanol droplet is remarkable. For the far-field region where the plume is widened, and the droplets are dispersed in the space as shown in Figure 3.26. The cooling effect from vaporization is mitigated due to the less dense droplet distribution. Though E100 has the highest HOV, the mass fraction of ethanol vapor is high among the five Exx cases due to its high-volume content of ethanol.

At the spray tip, there are similarities to be seen for E30, E50, and E100 cases. Droplet size has been reduced by flash boiling and vaporization from the injector exit to the current location.

These liquid droplets can be easily carried by the recirculation motion and brought together for vaporization (see Lagrangian parcels in Figure 3.26). As a result, the cooling effect of vaporization is enhanced at this region.

Along the radial direction at 15 mm downstream of the injector tip, the highest temperature drop for all three cases (E30, E50, E100) is nearly 10 K. The spray center has higher temperature in E30 case, indicating the flash boiling is strong and smaller droplets are produced. This is consistent with the droplet SMD calculation in Figure 3.24. When moving horizontally away from the spray center, the temperature gradually decreases for E30. Droplets enter the evaporation regime after experiencing the flash boiling, and droplet size is further reduced. Beyond 1.5 cm, it approaches the outer edge of the spray, so temperature slowly increases to the ambient temperature. Droplets at this region are either the smaller droplet bursts from flash boiling breakup or larger size droplets with higher inertia. A similar trend is observed for E100, but flash boiling for E100 has completed at 15 mm downstream of the injector tip as discussed. Temperature drops when highly dense liquid jets pass through, and the cooling effect is strong at this region. Radial temperature distribution in E50 gradually increases and flattens out at the location of 0.5 cm. Beyond this point, the liquid droplets travel to the heating zone because of the flash boiling. Secondary, smaller droplets can be produced for parent droplets undergo the flash boiling breakup, lowering the SMD.

It is found that sprays with 30% vol. of ethanol have the superior performance than other ethanol-isooctane blend ratios at a fixed ambient pressure if considering the liquid penetration, droplet sizes and cooling effect. Next, it is important to conduct analysis for E30 sprays at different ambient conditions to ensure that E30 sprays can sustain these advantages and benefit the GDI engine operations.

Figure 3.28 shows the liquid parcels and fuel vapor distributions for E30 sprays at different superheated degrees. The spray structures are different even at the early stage of injection. Liquid dispersion is promoted as increasing the superheated degree. For sprays that under $r_p > 0.3$ conditions, the path of liquid parcels is less altered by the ambient, but small recirculation motions can be detected at the tip of spray. Limited ethanol is vaporized during the injection process. Once r_p is below 0.3, a significant amount of ethanol vapor is produced since the SOI. Near the injector tip, flash boiling breakup is energetic and plenty of secondary droplets are produced. Those droplets have an additional velocity component perpendicular to the original velocity. Because the ambient gas density is very low, droplets can travel faster and explode to form a wide-spreading

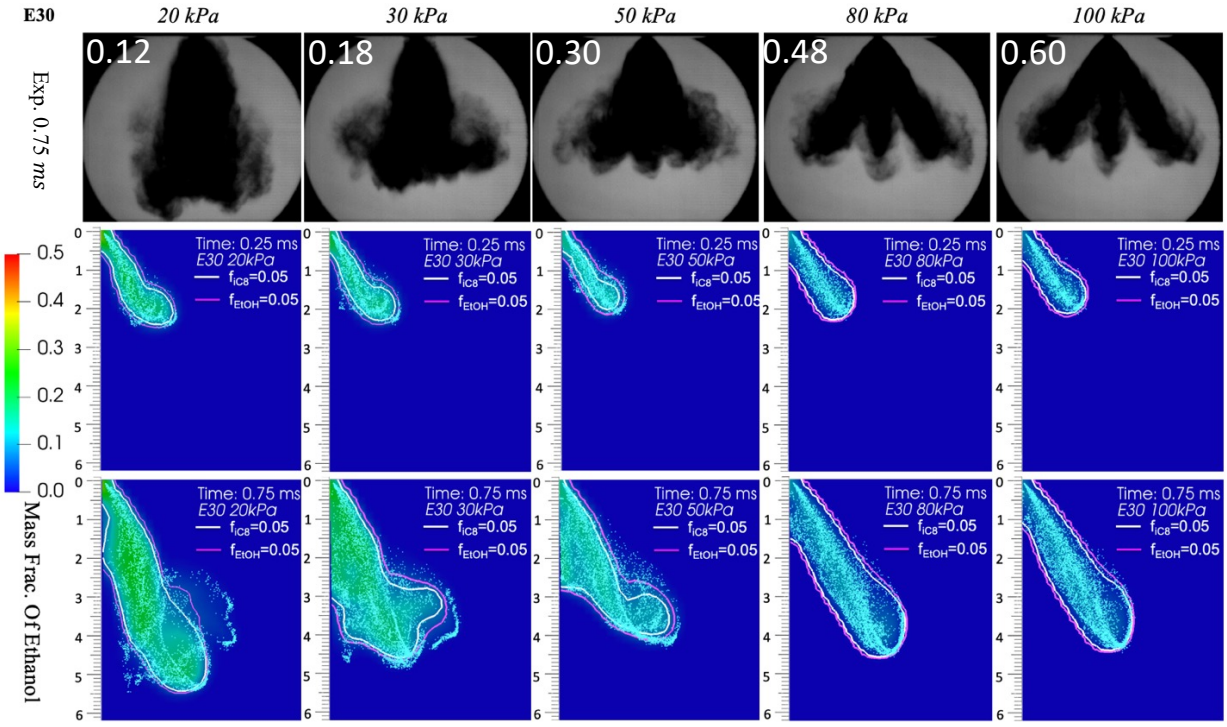


Figure 3.28: Gas/vapor and liquid phase distribution for E30 sprays at different ambient pressures. DBI images (top) from experiments and corresponding r_p value is marked on the top left of each image; simulation results at 0.25 ms after SOI (middle); simulation results at EOI (bottom).

mist, creating a larger near-field spray angle. Strong flash boiling intensity not only accelerates the phase change near the injector tip but also bursts smaller droplets that can improve the vaporization in the far field, thus the fuel vapor is distributed in a larger region.

Liquid jets are fully collapsed at $r_p = 0.18$, but a void is developed at the spray center if the ambient pressure is further reducing. When the ambient pressure is relatively low, the force in the radial direction exerted by the pressure difference between the spray center and the ambient environment is reduced. Trajectory of certain droplets can be altered due to such a pressure difference, but it has a finite effect in bringing those droplets to the spray center. Correspondingly, less droplets are presented at the spray center. The evolution of the spray structures with increased superheated degree, therefore, can be corrected as: the sprays are under a non-collapsing regime when $r_p > 0.3$; the sprays enter a fully collapsing regime for $r_{p,limit} < r_p < 0.3$, the sprays become non-collapsing again as $r_p < r_{p,limit}$. In this study, the potential value for $r_{p,limit}$ is 0.18, but careful testing is required to specify this value.

Radial vapor mass fraction and temperature at 15 mm downstream of the injector tip are presented in Figure 3.29. Ethanol and isooctane vapor mass fractions are shown at the top. Increasing superheated degree advances the production of fuel vapor as strong flash boiling and vaporization correlate together for faster phase change. Due to the high volatility of ethanol, phase change from liquid to vapor is more rapid for ethanol and ethanol vapor is predominant in the computational domain at EOI. Contrary to sprays at other ambient pressures, for E30 at $100\ kPa$ vapor mass distribution is highest at the spray center and falls gradually as moving to spray edge.

According to the temperature distributions, E30 sprays at various superheated degrees the temperature distributions in the entire domain look similar: the heating zone near the injector tip and low-temperature region at the spray tip. Flash boiling happens immediately when the liquid

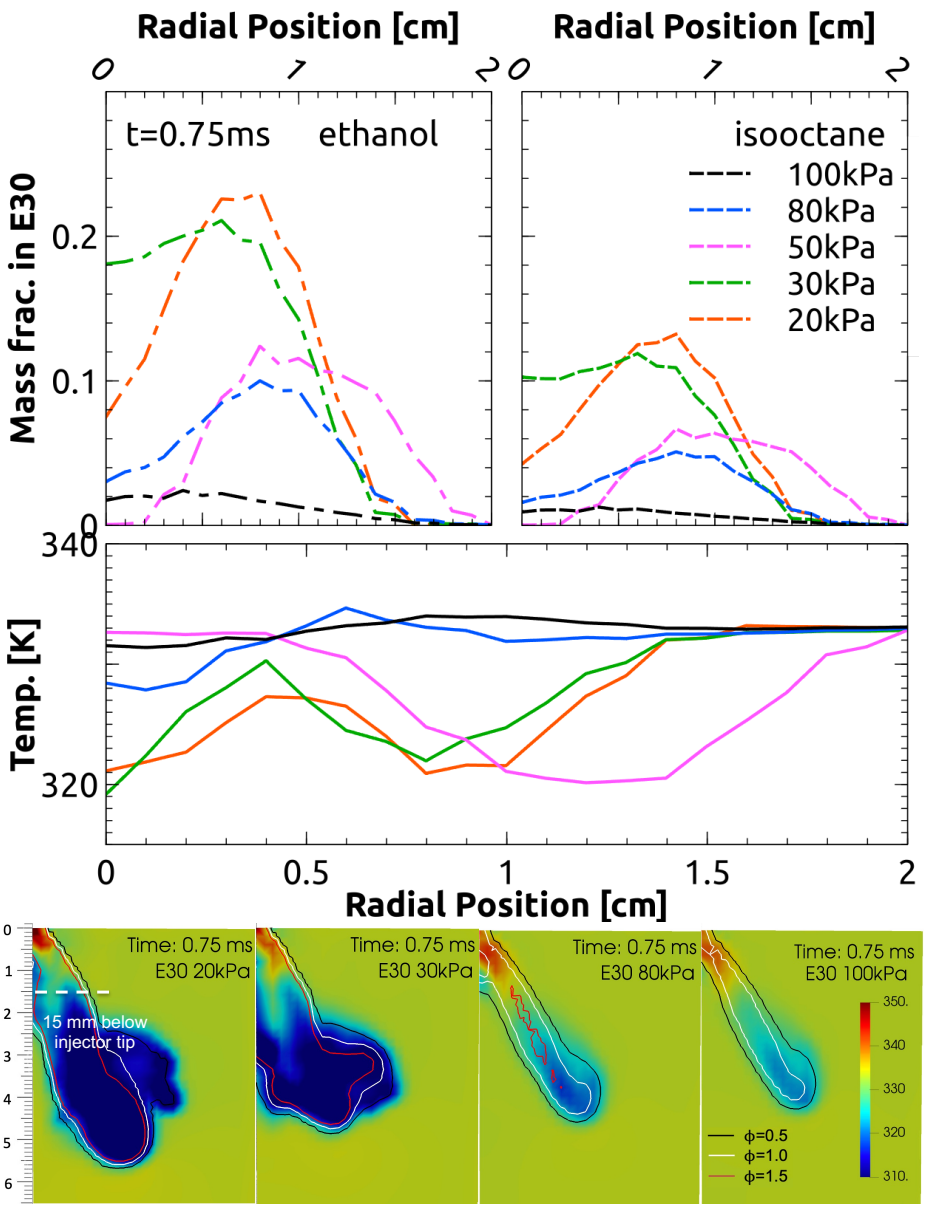


Figure 3.29: Mass fraction and temperature distributions of vapor-phase for E30 at different ambient pressures. Distributions along the radial direction are collected at 15 mm downstream of the injector.

exits injector nozzle. Hot vapor is quickly steamed from the superheated liquid droplets and raises the local temperature. As droplets travel away from the injector tip, vaporization starts to assist the phase transition which happens to droplets that have lower temperature than the ambient surroundings. Mixing effect of flash boiling and vaporization can be expected at this region. Near

the spray tip, flash boiling has completed, and the local absorption of heat is conspicuous due to intensive vaporization. The higher the superheated degree is presented, the greater the temperature spans.

At 15 mm downstream of the injector, the spray is in the mixing region. For sprays at high superheated degrees ($r_p < 0.3$), temperature distributions are similar and lower than the ambient temperature from the inside out. It signifies that a great number of droplets go through the flash boiling, effectively bringing down the liquid temperature. Some smaller, secondary droplets fly away from the main jet and evaporate faster. The majority of the larger size droplets remain in the main jet flow, proceeding to either flash boiling or evaporation and increasing the vapor concentration. This explains the increment of temperature around 0.5 cm from the spray center. The temperature variation for E30 at $r_p = 0.3$ has been analyzed in Exx at a fixed ambient pressure. When $r_p > 0.3$, the vapor/gas temperature at the spray center varies around the ambient temperature. Reduced flash boiling intensity extends the heating zone due to the mild, less effective phase transition. Moderate changes in the fuel vapor concentration at the same vertical location of the spray lead to a quasi-steady temperature distribution across the main spray jet.

Investigations on E30 sprays at different superheated degrees imply that an increased superheated degree can effectively enhance the phase transition and potentially is favorable to create homogeneous fuel-air mixture at the cost of elongated liquid penetration. The optimal operation condition for E30 needs to be carefully selected to maximize the benefits of adopting flash boiling in engine applications.

3.6.2 Hxx Blends at Various Superheated Degrees

In this section, the fuel vapor and liquid distribution of Hxx sprays are analyzed and compared with Exx at the same ambient pressure conditions, with the aim to find the advantages and disadvantages of using hexane as an additive.

With the increase of the hexane content (Figure 3.30), flash boiling is enhanced and spreads the liquid uniformly in the space. More droplets can be found in the spray center. Increasing the content of the hexane, the superheated degree of the fuel continuously increases but the HOV of Hxx blends does not change significantly comparing Exx blends. Therefore, the overall droplet size continuously decreases. Droplets with smaller radius are more easily to be brought into the spray center by following the gas entrainment motion. As shown in Figure 3.30, liquid dispersion is more pronounced when increasing the hexane content, and the production of fuel vapor is more efficient, resulting in larger region of fuel vapor distribution.

For the vapor temperature, the similar three-zone distribution can be observed. However, the heating and mixing zones are outspread, and the less significant cooling zone is presented at a small region of spray tip. This could be mainly due to lower HOV for hexane-isooctane blends at the same additive volume fraction. The effect of other properties on Hxx sprays have been studied in the previous sections. In the heating zone, less superheat in the droplet is expended for phase changes. One the other hand, in the cooling zone, less heat in the ambient is absorbed for vaporization. Due to the similarity in the temperature distributions, detailed results are not presented in this work.

Comparing Hxx and Exx blends, advantages of using Hxx are: 1) adding more hexane content can satisfactorily reduce the droplet size and the liquid penetration length; 2) fuel vapor production is enhanced and 3) the cooling effect of vaporization is less dramatic. Disadvantages

are also obvious as to achieve the same level of flash boiling intensity, higher hexane blend ratio is needed as the vapor pressure of Hxx is smaller than Exx at the same additive volume fraction. In real GDI applications, an alcohol additive can help to improve the engine efficiency and allow more stable combustion, and eventually reduce emissions, such as NOx, CO, and UHC.

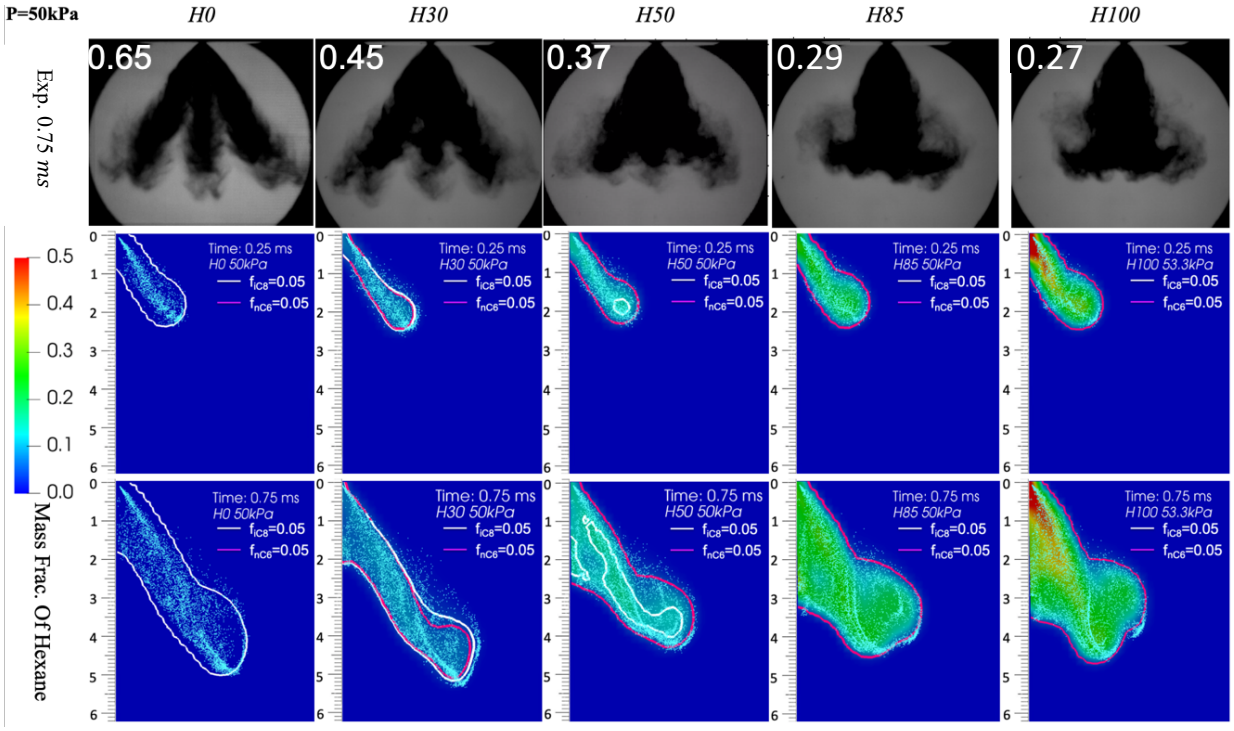


Figure 3.30: Gas/vapor and liquid phase distribution for Hxx blends at the fixed ambient pressure of $P_a = 50\ kPa$. DBI images (top) from experiments and corresponding r_p value is marked on the top left of each image; simulation results at 0.25 ms after SOI (middle); simulation results at EOI (bottom).

3.6.3 Fuel Vapor Mixing and Distribution

It is important to gain insights on the mixing process of the fuel vapors and ambient as well as the equivalence ratio distribution in the computational domain. Figure 3.31 shows vapor phase evolution during the injection for both isooctane and ethanol in E30 at two different ambient pressures. In both cases, ethanol vaporizes first and diffuses to the environment. As can be seen,

the highest mass fraction of ethanol appears right after exiting the injector tip for both cases, and the majority of isooctane in the liquid fuel is left and vaporizes at the tip of spray jet. This indicates the success of the droplet vaporization sub-model in predicting the preferential vaporization behavior.

When fixing the amount of ethanol content, decreasing the ambient pressure would enhance the flash boiling phenomenon, resulting overall smaller droplet thus a faster vaporization rate. Therefore, more fuel vapor can be observed at $P_a = 30\ kPa$ case. However, those vapors are trapped in the center region of the spray, and the collapsing phenomenon for vapor phase is more pronounced, compared to the liquid phase, because of the cooling-effect mentioned in the previous section. Such phenomenon causes a higher equivalence ratio at the spray center, inhibiting the mixing process and resulting in the over-rich region during the injection process. It should be noticed that the equivalence ratio computed in this section is based on the fuel vapor mass and nitrogen mass only. Though the mixture is concentrated around the spray, the overall mixture is nearly homogeneous. In engine applications, the ambient gas is no longer quiescent, and a strong flow motion would accelerate the mixing process and reduce the local equivalence ratio.

When adding 30% of hexane into isooctane at $50\ kPa$ ambient pressure, the superheated degree changes from 0.3 to 0.45. As indicated in Figure 3.32, a narrow fuel vapor region can be seen for H30, and the collapsing is not as significant as that in E30 case. However, preferential vaporization phenomenon is enhanced for H30 as observed from Figure 3.32. Hexane evaporates faster and diffuses uniformly in the chamber, and isooctane vaporizes slowly and concentrates at the jet center and tip. Such behavior is not observed during the E30 injections. The vapor distribution of isooctane and ethanol are nearly the same.

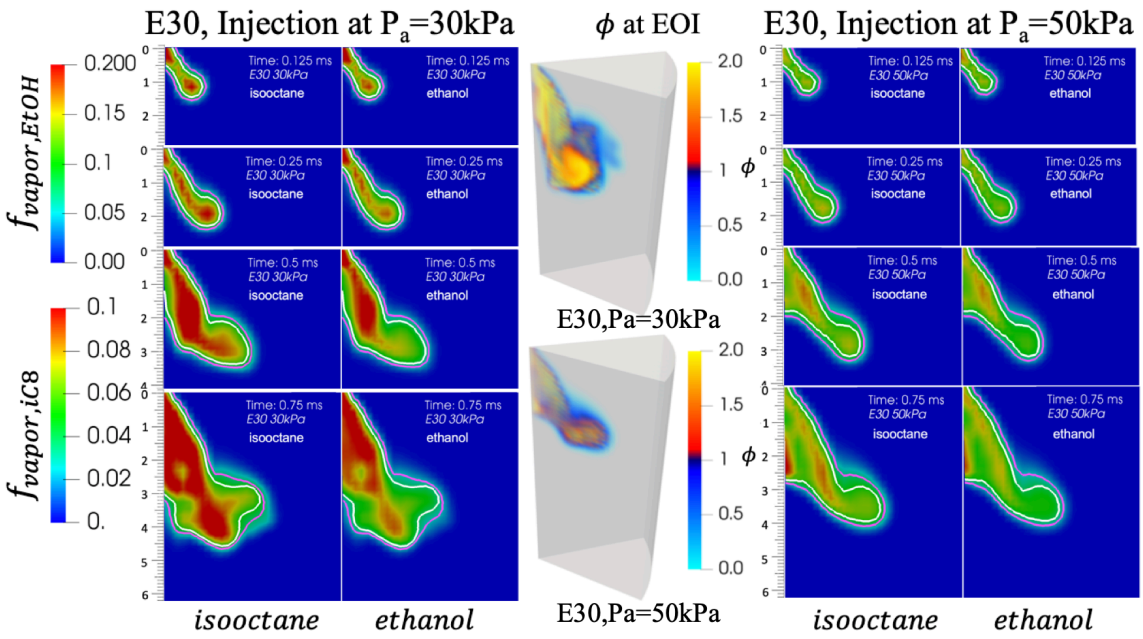


Figure 3.31: Evolutions of vapor phases for E30 at 30kPa and 50kPa ambient pressures during injection process.

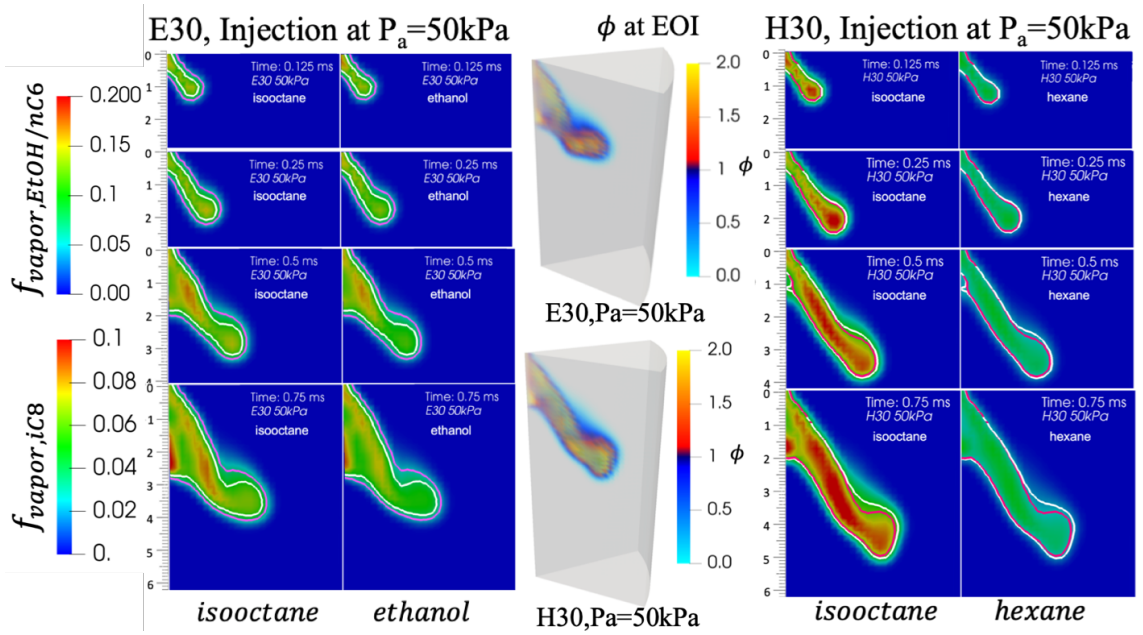


Figure 3.32: Evolutions of vapor phases for E30 and H30 at 50kPa ambient pressure during injection process.

Distinct vaporization behavior results in different mixing behavior of fuel vapor and ambient gas, thus the local equivalence ratio. As shown in Figure 3.33, at the same ethanol content, increasing the ambient pressure reduces the fuel rich region. This is due to the vaporization rate for high superheat case is slow, thus the vapor evaporated from the liquid fuel can diffuse into the ambient gas more uniformly. However, because of the slower vaporization rate, more liquid phase is left in the chamber, which increases the potential emission of UHC. Though at lower ambient pressure conditions, liquid droplets vaporize more violently and faster; the vapor cannot mix with ambient surroundings in time, forming the locally fuel-rich region. Those fuel regions are not able to dissipate immediately, increasing the potential of incomplete combustion. Therefore, there exists an optimal ambient pressure/superheat degree to enhance the vaporization process and meanwhile distribute the fuel vapor efficiently. Increasing the content of ethanol, superheated degree first reduces (0.65 for E0 and 0.28 for E50) then increases imperceptibly (to 0.32 with E100). Adding more ethanol, the local equivalence ratio decreases because of the slower vaporization process and more liquid would be left in the chamber. From the graphs, when the ethanol volume content is about 30%, the fuel vaporization process is enhanced but not too strong to create local fuel-rich region.

Simulations of sprays at different superheated degree demonstrate the capability of vaporization model and flash boiling model in predicting the phase change in an injection event. Droplets sizes and dynamic motion are well captured by models. Validated models are exploited to further investigate the temperature and fuel vapor distributions of sprays at different moments of injection. Better understandings of flash boiling sprays in terms of behaviors and characteristics are gained. Preliminary selections for fuels that can benefit engine performance by utilizing the flash boiling phenomenon are made.

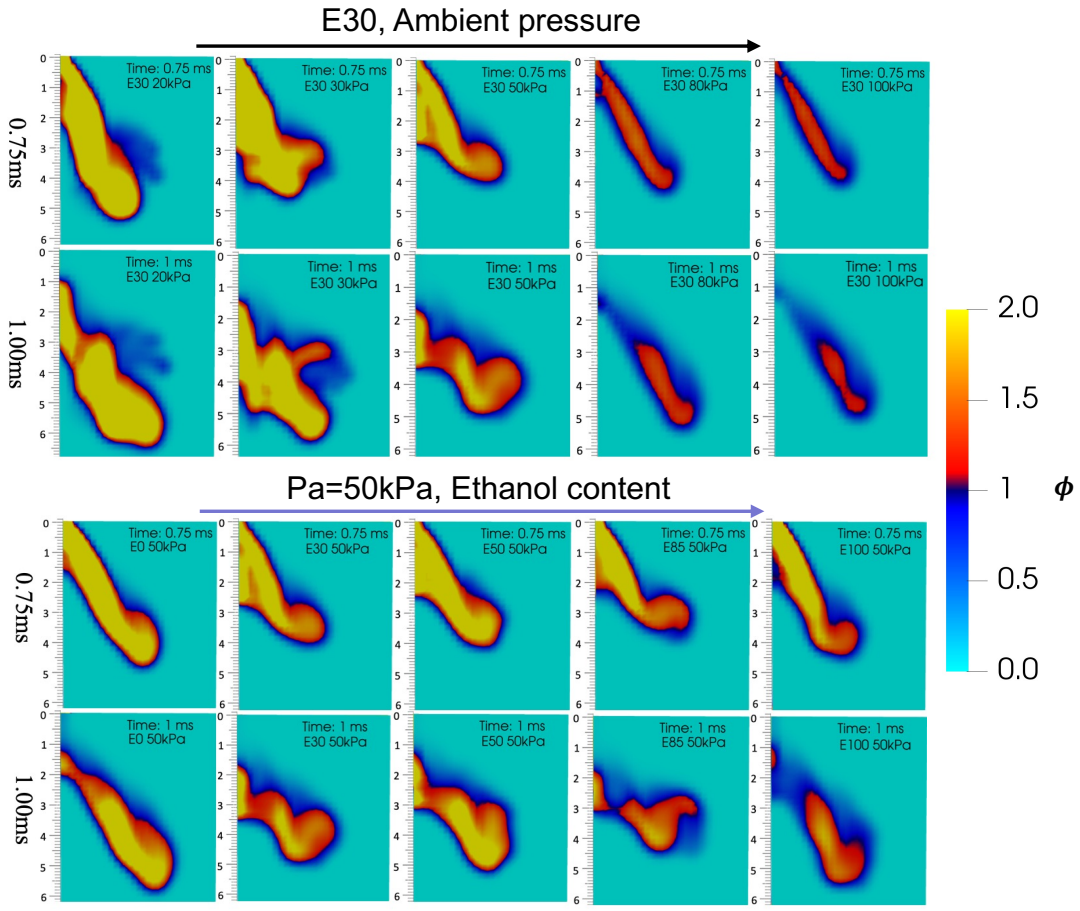


Figure 3.33: Local equivalence ratio comparisons for Exx sprays.

CHAPTER 4: EMISSIONS REDUCTION IN COMPRESSION-IGNITION ENGINES BY INVERTED IGNITION PHI-SENSITIVITY

A new method for CI engine in-cylinder NOx reduction is introduced. The method relies on the control of the burning sequence of the lean and near-stoichiometric region of the in-cylinder mixture. In typical CI engines, the near-stoichiometric region ignites faster, and is compressed after its local combustion due to the heat release in the rest of the combustion chamber. The high energy density as well as the burning-compression sequence of the near-stoichiometric region results in high local temperature, which favors NOx formation.

In this chapter, a method is introduced to invert the burning sequence such that the lean region ignites in prior of the near-stoichiometric region. By applying such method, the near-stoichiometric region undergoes a compression-burning process, which results in a lower final temperature comparing to the burning-compression process. Such an inverted ignition sequence is refereed as "inverted ϕ-sensitivity". In this study, a fuel that exhibits the "inverted ϕ-sensitivity" behavior is selected. Simulations of a small-bore diesel test engine operating with the selected fuel is conducted to demonstrate the usefulness of the proposed NOx reduction method.

It should be noted that the proposed NOx reduction method does not mean to provide a complete in-cylinder solution for regulation-complying NOx emission level. It is suggested that practical regulation-complying solution should still consider multiple in-cylinder methods as well as after-treatment.

4.1 Fuel Selection and 0-D Ignition Calculation

One of the major tasks of this study is to seek a fuel which exhibits inverted ϕ-sensitivity in the ignition process, i.e., the ignition delay increases with the equivalence ratio ϕ. No known fuel has such inverted ϕ-sensitivity as its inherent property. The inverted ϕ-sensitivity studied in this paper is due to the T-sensitivity of the ignition process. In the operation of a liquid-fueled direct-injection CI engine, the liquid fuel is often cooler than the gas in the combustion chamber at the moment of injection. The evaporation of the liquid fuel also absorbs heat from the surrounding gas. As the result, the rich region and the near-stoichiometric region in the combustion chamber have lower temperature comparing to the lean region before the ignition. In cases with high temperature drops and sufficiently strong T-sensitivity, the leaner region can ignite earlier than the rich region, hence exhibiting inverted ϕ-sensitivity. The fuel selection for inverted ϕ-sensitivity is based on two criteria: 1). High HOV; It contributes to a significant temperature difference inside the combustion chamber. 2). Strong ignition T-sensitivity without NTC (Negative Temperature Coefficient) behavior; it translates the large temperature drop into inverted ϕ-sensitivity.

Such criteria lead the fuel selection to an ideal candidate: ethanol (C_2H_5OH). Ethanol has a high HOV of 921 kJ/kg, while the HOV of diesel is 233 kJ/kg. Thus, the cooling effect by ethanol is much more significant when compared to that of diesel. Direct injection of ethanol into the combustion chamber creates stratified charge which presents a remarkable temperature gradient inside the chamber: leaner region absorbs less heat, resulting in a small temperature drop; richer region extracts more energy from the surrounding gas, leading to a more significant temperature decrease. Ethanol's strong T-sensitivity and lack of NTC behavior also make it an ideal fuel for this study. According to the study by Hass *et al*. [158], pure ethanol exhibits no

NTC behavior. In this perspective, owing to the lack of the chain branching decomposition, the low-temperature oxidation of ethanol is less important. As the result, the ignition delay decreases monotonically at a high rate with the increase of temperature, enabling the inverted ϕ-sensitivity.

Before conducting the detailed 3-D engine simulations, 0-D calculations are performed using an in-house-developed chemical kinetics solver [86] to illustrate the ignition characteristics of ethanol-air mixtures. Figure 4.1 presents the ignition delay of pure ethanol (E100) vs. the equivalence ratio at different temperatures and pressures. The 0-D calculation results are consistent with the previous study [159]. It is noticeable that pure ethanol is very sensitive to the change of temperature from 900 K to 1400 K. An ignition delay shortening of one order of magnitude is achieved by increasing the temperature by 100-200 K. While enriching the mixture from $\phi = 0.2$ to $\phi = 1$ reduces the ignition delay by only 50-80%. The ignition delay is lightly influenced by the pressure, increasing the pressure from 35 bar to 45 bar reduces the ignition delay by about 9%. Figure 4.2 shows the ignition delay vs. mixture temperature for different equivalence ratios. The result suggests that a temperature difference of approximately 100 K is adequate to counterbalance the inherent positive ϕ-sensitivity of ethanol: larger temperature difference results in inverted ϕ-sensitivity.

With the results of the 0-D simulations, it is concluded that E100, the fuel selected for present study, has the potential to exhibit an inverted ignition sequence. E100 is used in the 3-D engine simulation presented in the following sections.

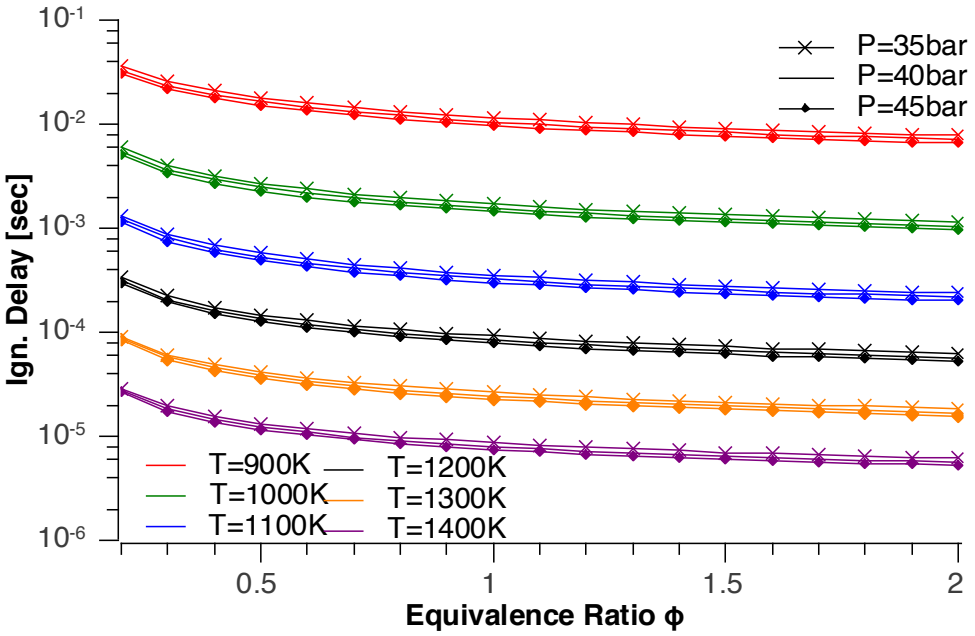


Figure 4.1: The result of 0-D calculation of ethanol ignition delay, ignition delay vs. equivalence ratio. Each curve is for a certain temperature and pressure.

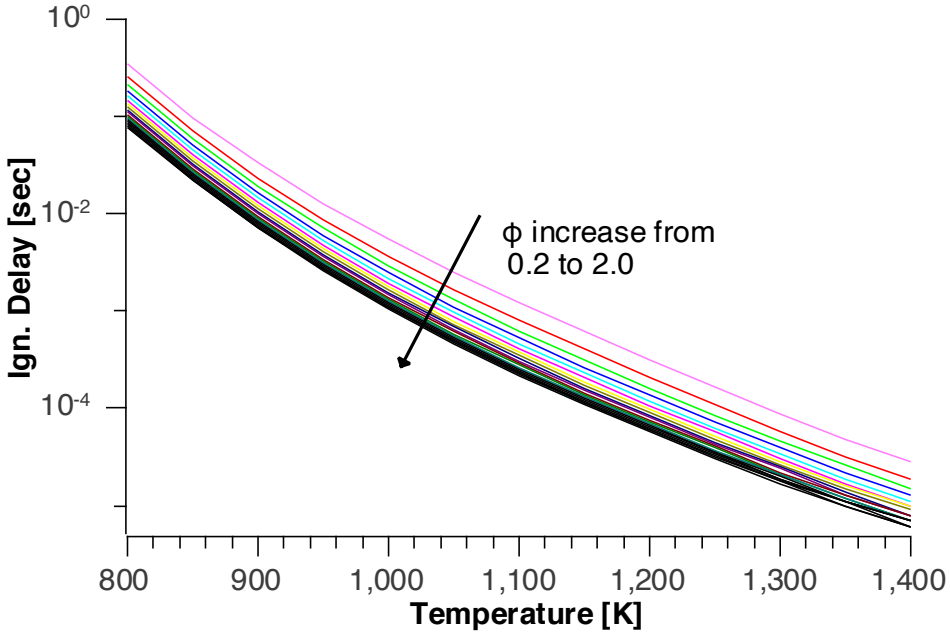


Figure 4.2: The result of 0-D calculation of ethanol ignition delay, ignition delay vs. temperature. ϕ increases from 0.2 to 2.0, and each curve is for a certain equivalence ratio.

4.2 Computation Method and Simulation Conditions for 3-D Calculations

In this study, a customized version of KIVA-3V release 2 program [106] is used. The CFD code uses an in-house-developed chemical solver [86] to solve the local chemical kinetics problem for each finite volume cell. The kinetic solver is based on an open-source thermal-chemical package, CANTERA [160]. A 40-specises skeletal mechanism [159] for HCCI combustion of ethanol and thermal NO formation is used in this research. For comparison purpose, 3-D simulations with PRF85 (primary reference fuel with 85% iso-octane by liquid volume) are also performed. PRF85 is chosen to represent the low-cost pump gasoline. Comparing to the straightforward PRF87, the PRF85 is a more accurate surrogate to the gasoline with AKI=87 in term of the MON, which is more relevant to the operation of modern high-energy-density engines. The reduced PRF mechanism is developed by Wang *et al*. [161]. In addition, a 12-step NOx model [162] is implemented into the PRF mechanism to predict the NOx emissions. The PRF85 is only used to model the chemical processes, while the liquid properties of the fuel use the values of gasoline. Other models used in the CFD simulation are summarized in Table 4.1.

The research engine used for this numerical study is derived from an AVL-5402 single cylinder diesel engine. The key parameters of the derived engine are listed in Table 4.2. The geometries for the derived and stock AVL-5402 engines are shown in Figure 4.3. One of the major differences between these two engines is the wider and deeper piston bowl geometry used in the derived configuration. The adjustment is made according to the suggestions by existing GDCI (gasoline direct-injection compression-ignition) studies [163-165]. The compression ratio is increased to 20.0, which is within the range of GDCI configurations found in literature, to promote the onset of ignition and mitigate the lower ignitability of ethanol and PRF85 comparing to diesel fuel. A lower rail pressure of 300 bar is used to estimate the fuel injection velocity throughout the

injector orifices as well as the injection duration. The flow inside the simulated engine is swirl-dominated and can be radially fitted by a function. Therefore, the simulations performed in this study are closed-chamber simulations with fitted initial swirl ratio (SR). Intake valve closing (IVC) timing, which is 226° (134° BTDC), and exhaust valve opening (EVO) timing, which is 480° (120° ATDC), are set to be the start and end of the simulations, respectively.

In this study, engine speed is fixed at 1200 rpm for all cases. Each engine operating cycle involves only one direct injection to simplify the analysis of the simulation result. As mentioned previously, the major task of this study is to test the ethanol's inverted ϕ-sensitivity and its effect on NOx formation. Therefore, a set of cases at different loads (i.e., fuel quantities, overall equivalence ratios) will be investigated. The injection timing of each case is varied such that the CA50 (the moment of 50% of heat released) is as close to 370° crank angle as possible. The tested cases for E100 and PRF85 are listed in Table 4.3. The IVC pressure is varied from 1.0 bar to 2.0 bar for both E100 and PRF85. E100 fuel quantities are set such that the overall equivalence ratio can roughly cover the range from 0.3 to 0.6. Then the fuel quantities of the corresponding PRF85 case is determined to have the same fuel energy. Due to the fact that the vaporization of E100 spray significantly lowers the in-cylinder temperature near the top dead center (TDC), elevating the IVC temperature for E100 cases is necessary to avoid misfire. Thus, the IVC temperatures for the E100 cases are chosen such that they are the lowest temperatures which enable the combustion to occur. For the PRF85 cases, the IVC temperature is fixed at 355 K, the baseline IVC temperature used in a recent study on GDCI with PRF85 [166]. It is also noticeable that under the conditions where the overall equivalence ratio is relatively higher (approximately above 0.45), the swirl ratio is also adjusted to reduce the mixing-controlled heat release.

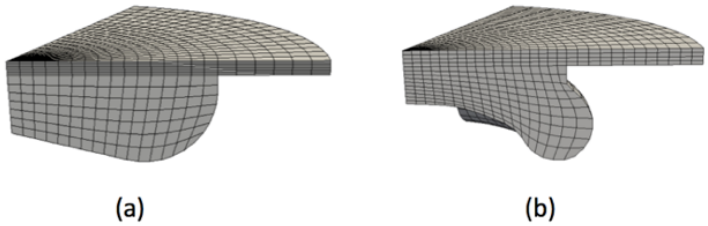


Figure 4.3: AVL-5402 single cylinder diesel engine (a) derived engine and (b) stock AVL-5402 engine.

Table 4.1: Models used in the simulation.

Phenomenon	**Model**
Drop Breakup	Taylor analogy breakup (TAB) [144]
Evaporation	Multi-component evaporation [110]
Turbulence	Renormalized k-ε [167]
Turbulence Combustion	Eddy dissipation concept (EDC) [168]

Table 4.2: Key parameters of the derived and stock AVL 5402 single cylinder test engine.

Stroke	90 mm
Bore	85 mm
Compression ratio	20.0/17.1 (derived/stock)
IVC angle	226°
Injector type	Multi-hole
Distribution cone angle	142°
Nozzle diameter	0.18 mm
Fuel delivery type	Common rail
Swirl Ratio	1.779 (otherwise specified)
Rail pressure	300/600 bar (derived/stock)
EGR type	Not mounted

Table 4.3: Tested cases with E100 and PRF85.

Case	***E100***				
P_i [bar]	Fuel Qty. [mg]	Overall ϕ	SOI [°]	T_i [K]	SR
1.0	15	0.33	342	421	1.779
1.2	20/25	0.38/0.48	350/345	420/426.5	1.779/3
1.5	30/40	0.45/0.61	349/346	420/423.5	3/3
2.0	30/40	0.33/0.44	350/348	400/405	1.779/3
	45/50	0.50/0.55	347/347	405.7/406.6	3/3
Case	***PRF85***				
P_i [bar]	Fuel Qty. [mg]	Overall ϕ	SOI [°]	T_i [K]	SR
1.0	9.1	0.29	354	355	1.779
1.2	12.2/15.2	0.33/0.41	356/356	355	1.779/3
1.5	18.2/24.3	0.39/0.52	359/358	355	3/3
2.0	18.2/24.3	0.29/0.39	360	355	1.779/3
	27/30	0.44/0.49			3/3

4.3 Impact of Inverted ϕ-Sensitivity on Engine-Out NOx Emissions

4.3.1 Influence of Inverted ϕ-Sensitivity on Ignition Events

The summarized results of the tested cases are listed in Table 4.4. The visualization of the early phase of the combustion is shown in Figure 4.4 for the E100 and PRF85 cases. The iso-surfaces are colored by temperature. In each case, two iso-surfaces are chosen to probe the lean region and the near-stoichiometric region. Note that the viewing angle for the E100 and PRF85 cases is different to highlight the features of the combustion event in each case, since the onset of ignition varies spatially. As can be seen in Figure 4.4, the behavior of the ignition for E100 cases is significantly different from the PRF85 cases. The lean region has higher temperature in the E100 cases while the near-stoichiometric region is heated to higher temperature first in the PRF85 cases. Right before the combustion, the temperature near the $\phi = 0.3$ iso-surface can reach above 1200 K and yet the highest temperature near the $\phi = 0.8$ iso-surface is approximately 1000 K. As

indicated in 0-D calculations (see Figure 4.1), the ignition delay of pure ethanol at 1200 K is about 0.18 ms, enabling the onset of ignition within two crank angles at 1200 rpm. The ignition delay at 1000 K, by contrast, is about one order of magnitude larger than the ignition delay at 1200 K. Therefore, the ignition first occurs near the $\phi = 0.3$ contour when using E100. Such an inverted ignition sequence is not observed in the PRF85 cases, where ignition first occurs near the $\phi = 0.8$ iso-surface. In conclusion, the compression-ignition behaviors using E100 and PRF85 are different: inverted ϕ-sensitivity brings E100 a distinct ignition sequence comparing to the ignition behavior of PRF85.

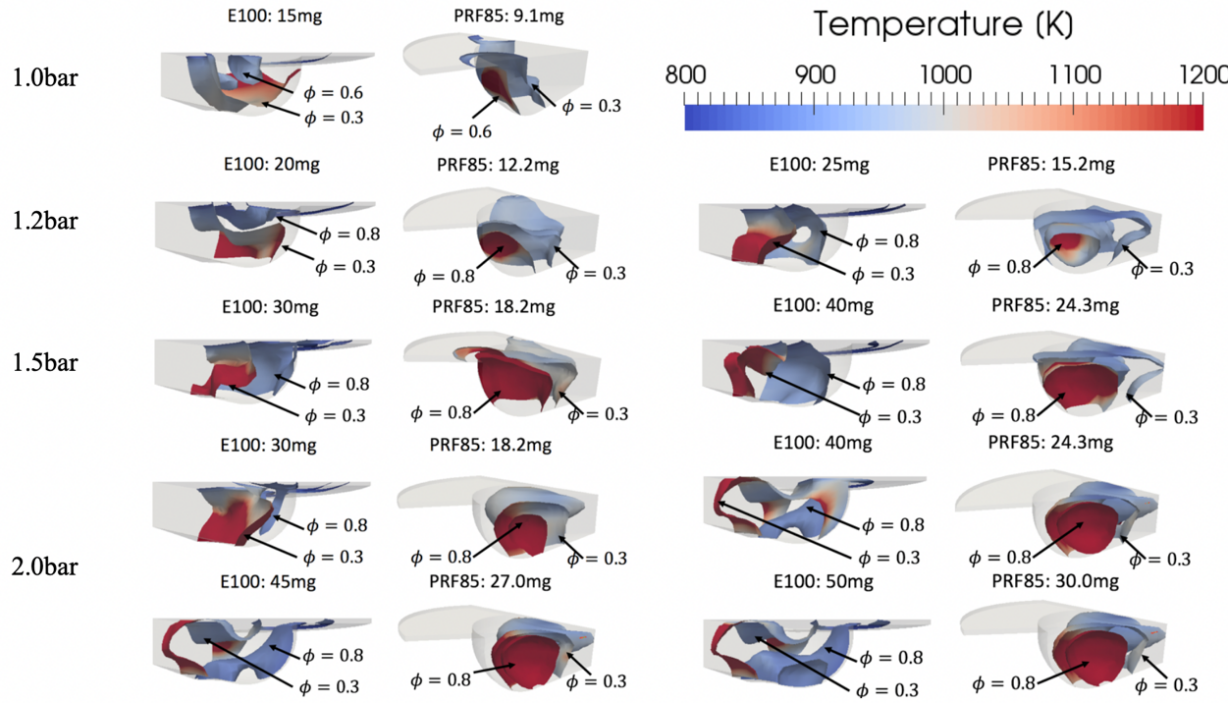


Figure 4.4: Onset of ignition of E100 and PRF85. The snapshot is taken at about 2° or 3° before CA10. Two sets of iso-surfaces, $\phi = 0.3$ and $\phi = 0.8$ (except the first at intake pressure of 1.0 bar where the overall equivalence ratio of this case is small so the representative iso-surface of $\phi = 0.8$ does not exist) are used to represent the fuel-lean and near-stoichiometric regions. Iso-surfaces are colored by temperature.

Table 4.4: Summary of the results for tested cases.

Case	***E100***			
P_i [bar]	Fuel Qty. [mg]	IMEP [bar]	Ign. Delay [CA]	Ign. Delay [ms]
1.0	15	3.0	27	3.75
1.2	20/25	4.1/5.2	19/24	2.64/3.33
1.5	30/40	6.1/7.9	19/22	2.64/3.06
2.0	30/40	6.1/8.6	18/20.5	2.50/2.85
	45/50	9.7/10.7	22.5/22.5	3.13/3.13
Case	***PRF85***			
P_i [bar]	Fuel Qty. [mg]	IMEP [bar]	Ign. Delay [CA]	Ign. Delay [ms]
1.0	9.1	2.9	15	2.08
1.2	12.2/15.2	4.2/5.5	12.5/13	1.74/1.81
1.5	18.2/24.3	6.5/8.8	10.5/11	1.46/1.53
2.0	18.2/24.3	6.5/8.9	8	1.11
	27/30	9.9/10.9		

4.3.2 Low and Medium Load Operations

To investigate the impact of such inverted ϕ-sensitivity on NOx emissions, the study is split into two parts, the effect under low-medium load conditions and under the high load conditions. In this subsection, the low-medium load operations are presented.

For the first case, $P_i = 1.0$ bar with default swirl ratio, the peak pressures in the pressure history curves of E100 and PRF85 (shown in Figure 4.5) are close to each other thanks to the tuning of the SOI timing. The cooling effect of the E100 is much more significant than that of PRF85 after injection. The instantaneous heat release rate (HRR) of PRF85 is marginally higher during the early combustion stage. While the peak overall temperature (Figure 4.6) of the E100 case is about 100 K higher than the PRF85 case due to the slightly higher pre-combustion temperature.

Figure 4.7 shows the local ϕ-T distribution before and after the combustion. E100 and PRF85 have different ignition sequence, and E100 exhibits inverted ϕ-sensitivity since the cells

with the lower ϕ is first to approach toward the equilibrium flame temperature. In the post-combustion plot, the slope of the E100 case (~$6.5 \cdot 10^{-3}\ K^{-1}$) in the scatter plot is slightly steeper comparing to that of the PRF85 case (~$5.7 \cdot 10^{-3}\ K^{-1}$). With such a difference between the ϕ-T slopes, the maximum local temperature is lower in the E100 case (see Figure 4.7) while its peak overall temperature is higher (see Figure 4.6), resulting in the lower NOx formation in the E100 case (see Figure 4.6). As noticed, all distributions are snapshots at 400° crank angle. The 400° is selected because: a) the combustion is finished; b) the NOx related reactions are near frozen; c) it is not too late that the dependency of emission on ϕ is smeared by diffusion.

Apart from the inverted ϕ-sensitivity, the mixture distribution also affects the NOx emissions. Where the ϕ is close to 0.8, the combination of high flame temperature and abundant oxygen supply is optimal for NOx formation. Deviating of local ϕ in both directions reduces NOx. The distribution of NOx and mass of mixture in the ϕ-space is visualized in Figure 4.8. The mixture in the E100 case is concentrated in the ϕ range of 0.3 to 0.5, while in the PRF85 case, more gas has leaner ϕ. Based on such mixture distribution, the E100 case is expected to generate more NOx. However, the effect of mixture distribution is overpowered by the inverted ϕ-sensitivity in this case.

For the mid-low load (corresponding Figures are visualized from Figure 4.9 to Figure 4.12), similar results are obtained. It should be noticed that the swirl ratio is increased from the default to 3 to reduce the combustion duration for the PRF85 case, such that it is comparable to the E100 case. As the result, the PRF85 case has slightly higher peak pressure, while the E100 case has slightly higher peak temperature. The trend of NOx distributions in ϕ-space is similar to the previous case. Nevertheless, the NOx emissions are both increased under the mid-low load condition for E100 and PRF85, NOx formation using E100 is apparently much less than using

PRF85, which can also be observed in Figure 4.10. Under this load condition, the distinct ignition sequences for E100 and PRF85 are indisputable, as shown in Figure 4.12. The slope of fitted line for E100 scatter plot at 400° is about $8.0 \cdot 10^{-3}\ K^{-1}$ compared to $5.7 \cdot 10^{-3}\ K^{-1}$ for PRF85 case resulting in the lower maximum local temperature and lower NOx emissions in the E100 case.

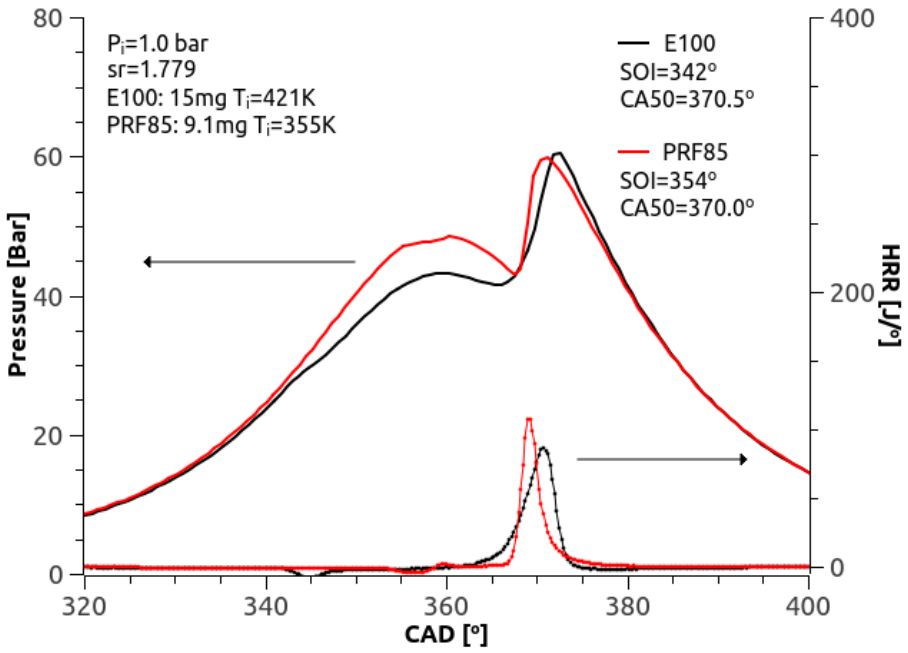


Figure 4.5: Pressure history and HRR at $P_i = 1.0\ bar$ with default swirl ratio.

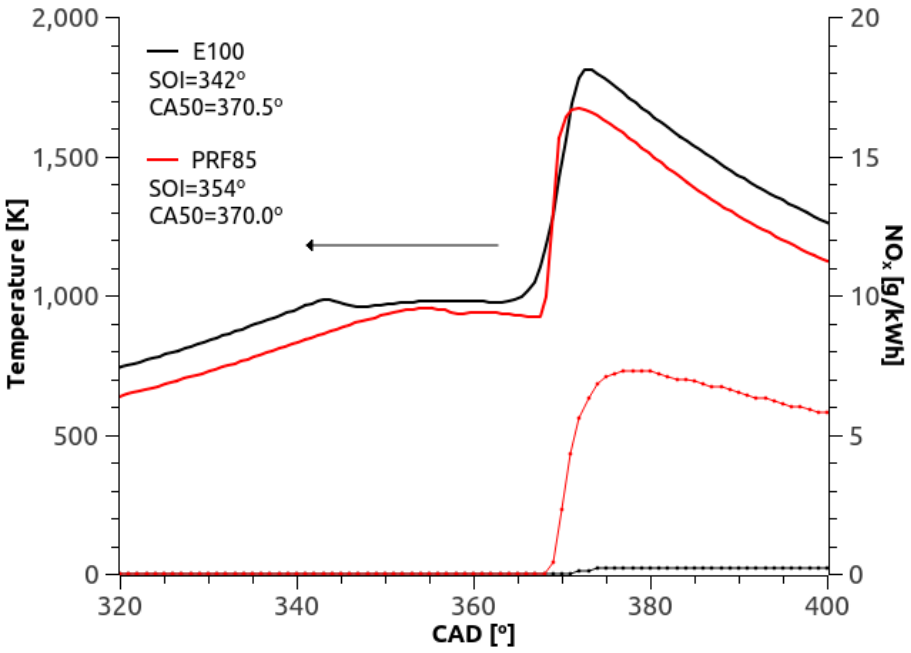


Figure 4.6: Average in-cylinder temperature and NOx emission in g/kWh at $P_i = 1.0\ bar$ with default swirl ratio.

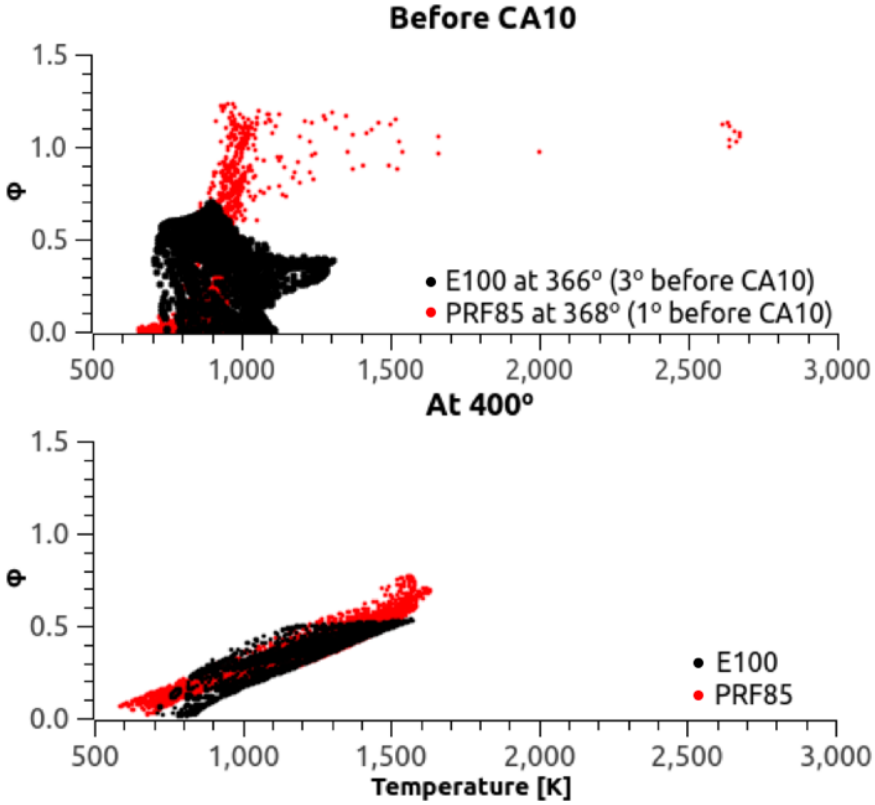


Figure 4.7: Local equivalence ratio distribution before and after combustion for $P_i = 1.0\ bar$ with default swirl ratio.

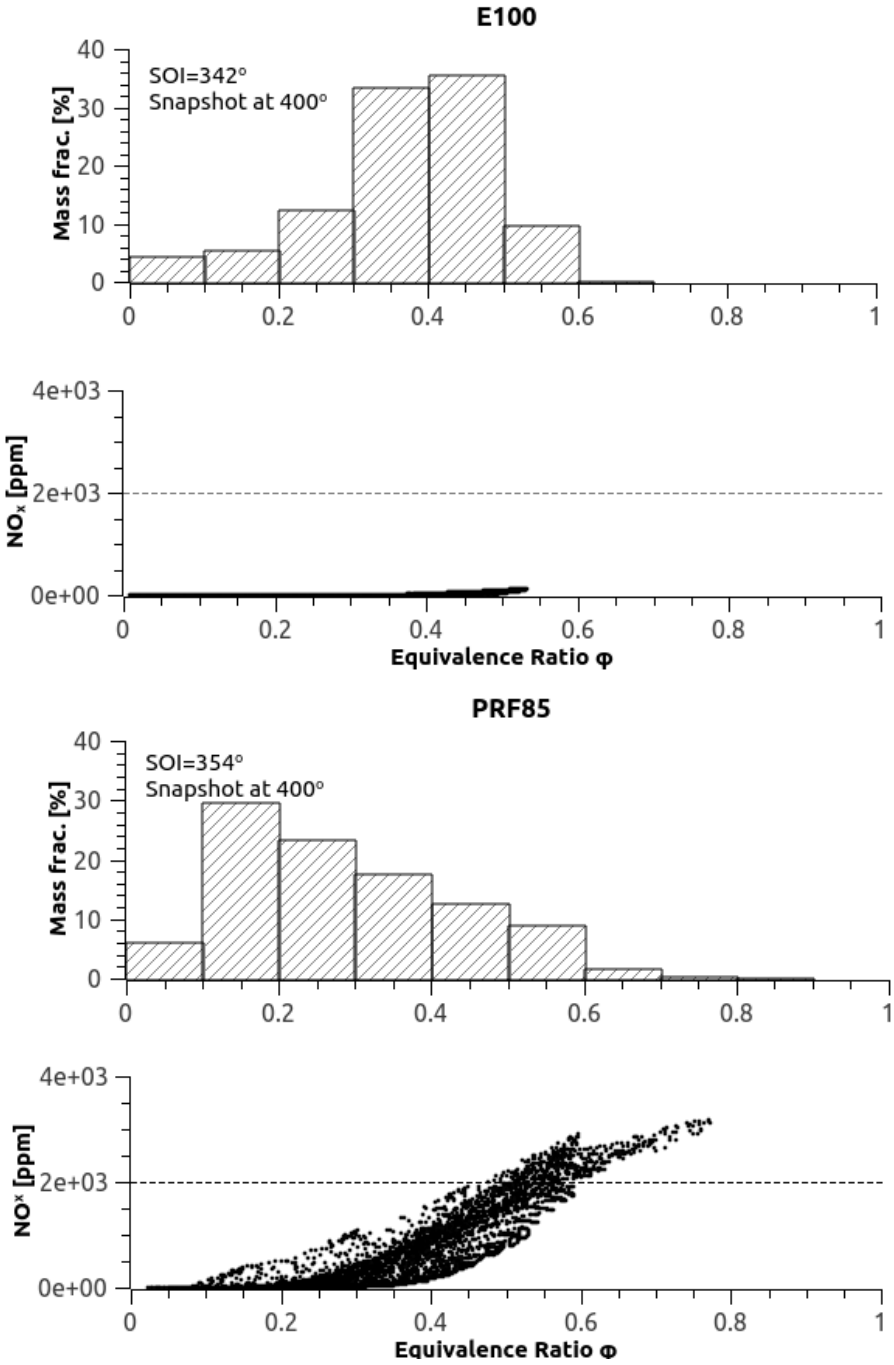


Figure 4.8: Snapshot of the E100 and PRF85 emissions, and the mixture distribution after combustion. $P_i = 1.0\ bar$ with default swirl ratio.

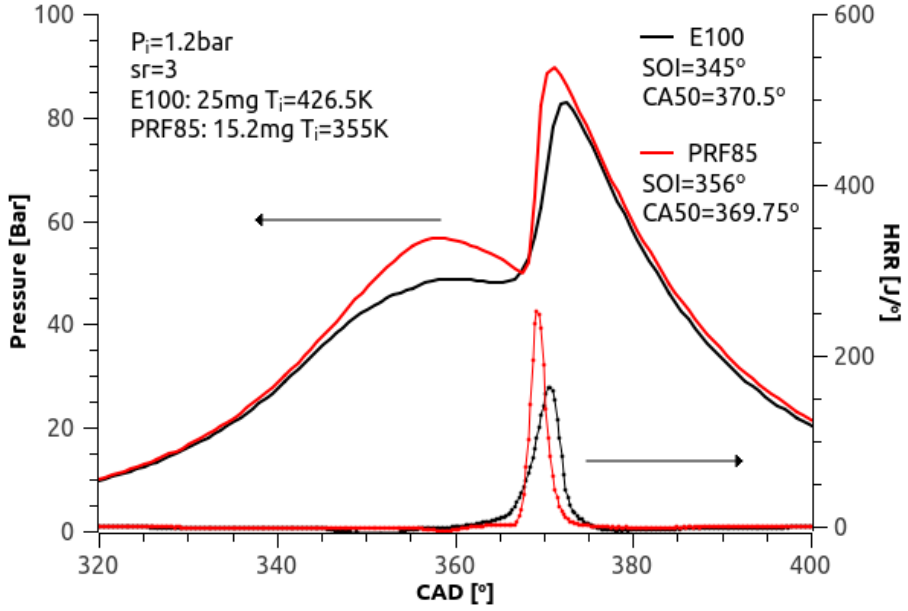


Figure 4.9: Pressure history and HRR at $P_i = 1.2\ bar$ with swirl ratio of 3.

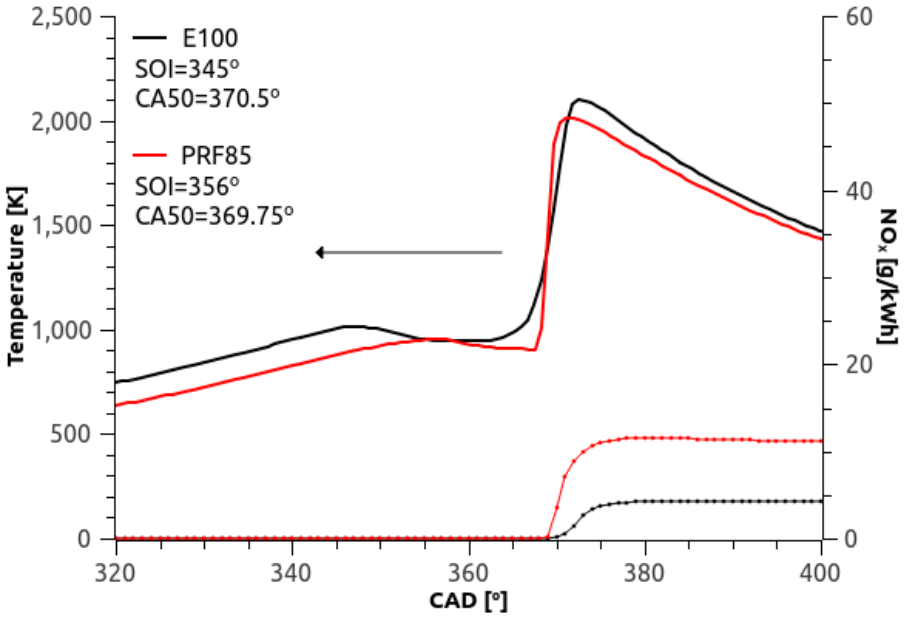


Figure 4.10: Average in-cylinder temperature and NOx emission in g/kWh at $P_i = 1.2\ bar$ with swirl ratio of 3.

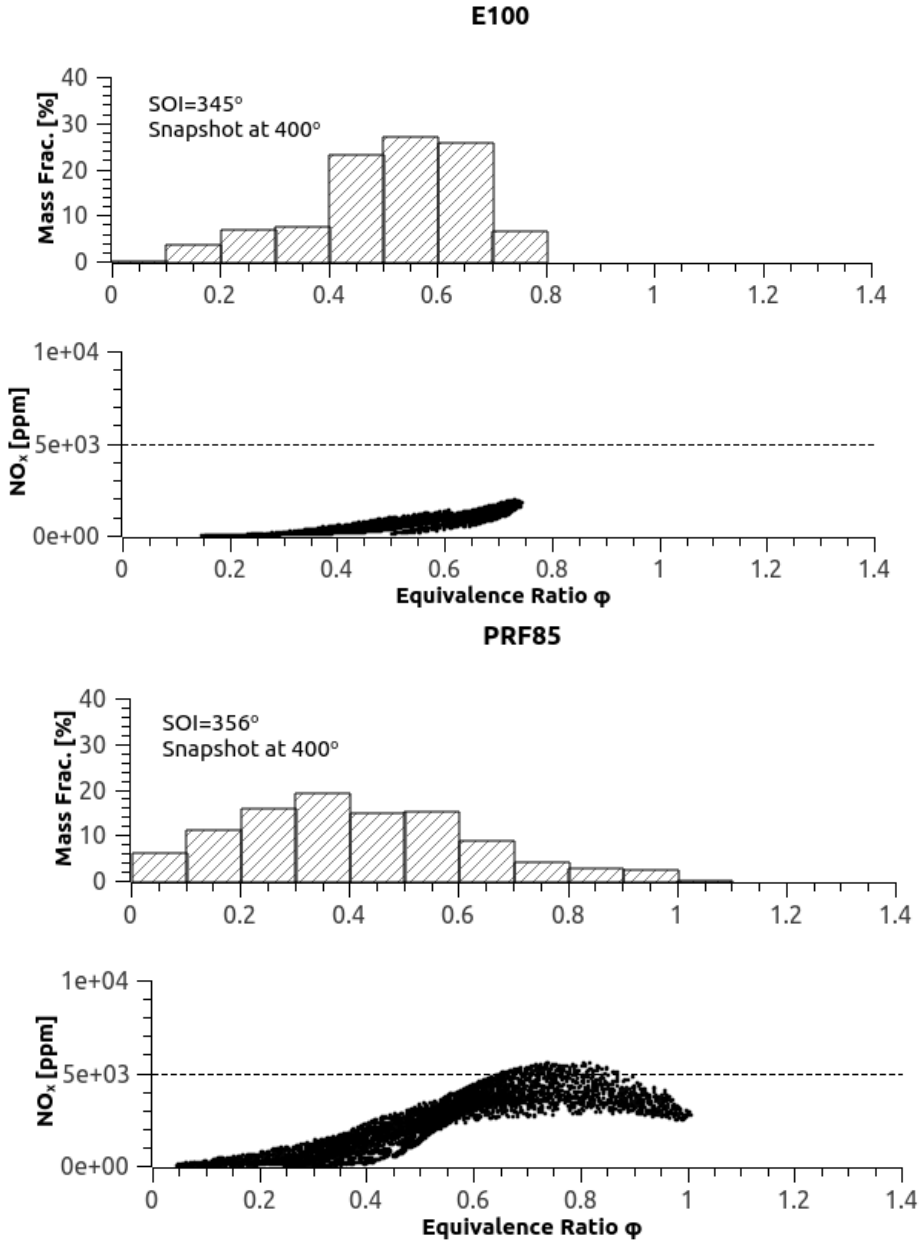


Figure 4.11: Snapshot of the E100 and PRF85 emissions, and the mixture distribution after combustion. $P_i = 1.2\ bar$ with swirl ratio of 3.

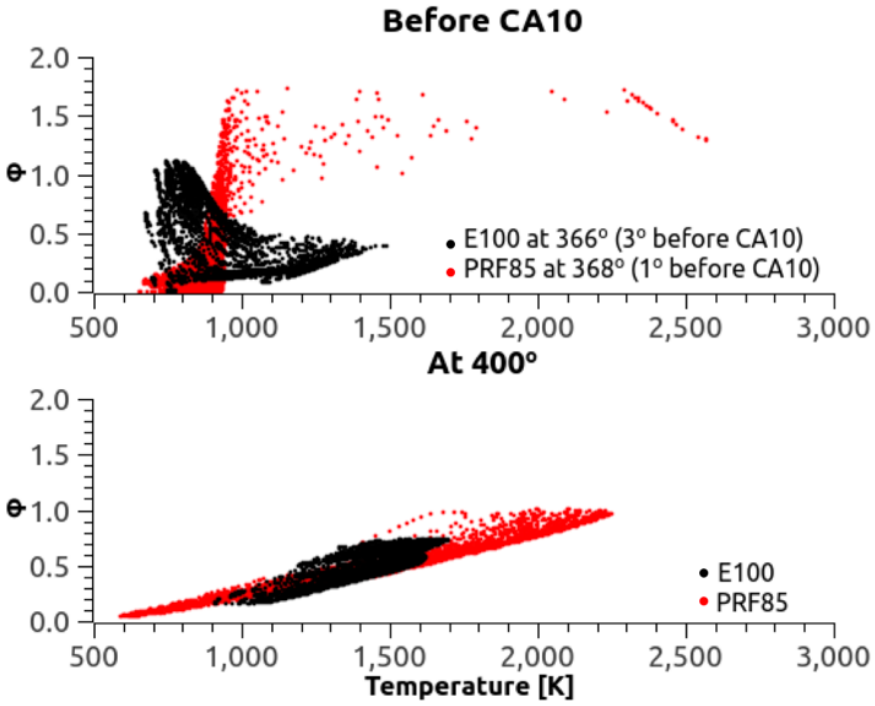


Figure 4.12: Local equivalence ratio distribution before and after combustion for $P_i = 1.2\ bar$ with swirl ratio of 3.

The results of the mid-high load condition are shown in Figure 4.13 to Figure 4.16. The fuel quantity of E100 is 30 mg, and the IVC pressure is 2.0 bar. In Figure 4.13, the pressure history is well matched excepted the small portion right after the injection. Furthermore, the rate of increase of the pressure caused by onset of combustion is nearly the same, resulting a comparative instantaneously HRR for E100 and PRF85. The engine-out NOx emissions fueling with E100 shown in Figure 4.14 is about five times less than the NOx emissions using PRF85. The influence of inverted ϕ-sensitivity on ignition events, NOx emissions and the mass distribution in the ϕ-space is visualized in Figure 4.15 and Figure 4.16. For both cases, the mass distribution is spread out in the ϕ-space. Again, high NOx formation is found at the region where the equivalence ratio is close to 0.8. Moreover, the distribution of the NOx in ϕ-space is dispersed even with the same

local equivalence ratio. The dispersion is also due to the inverted ϕ-sensitivity. The detailed analysis of such distribution can be found in the previous study [166].

The results in this subsection suggest that under the low and medium load conditions, the NOx emissions are effectively reduced by using a fuel which exhibits the inverted ϕ-sensitivity. As the load increases, the NOx emissions in $[g/kWh]$ does not change monotonically, and the results are consistent with the previous study done by and the results are consistent with the previous study done by Manente *et al.* [169].

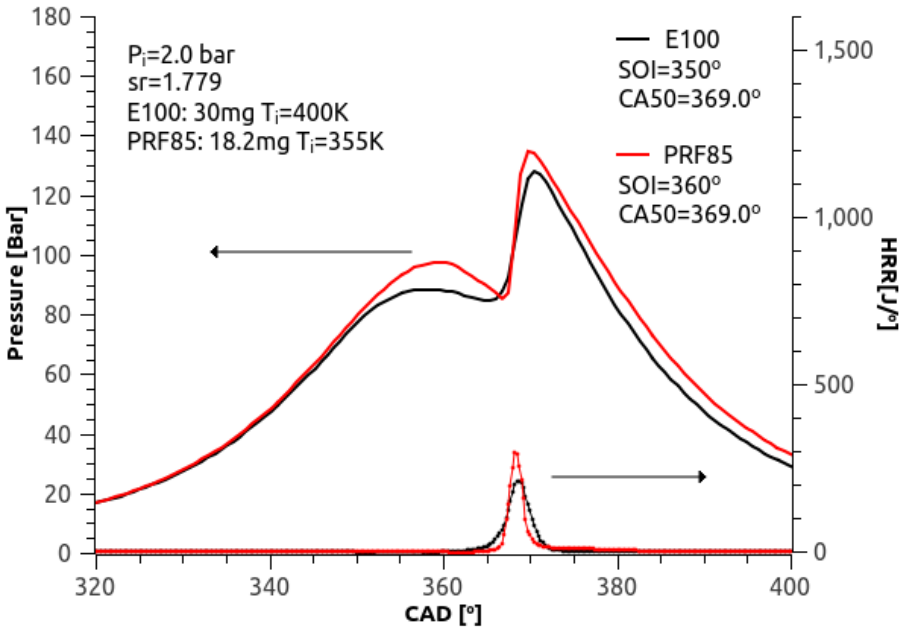


Figure 4.13: Pressure history and HRR at $P_i = 2.0\ bar$ with default swirl ratio.

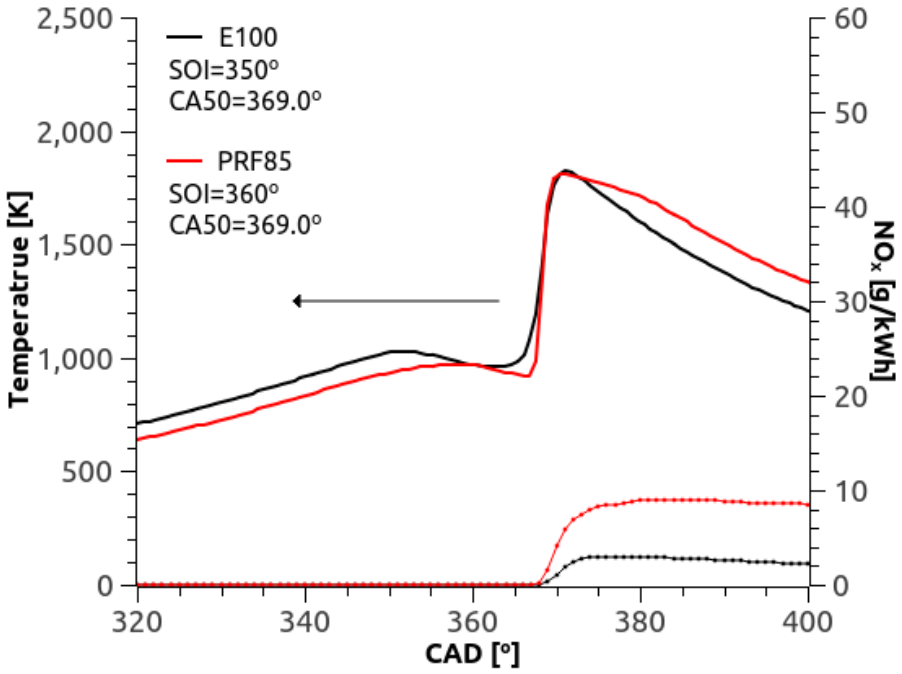


Figure 4.14: Average in-cylinder temperature and NOx emission in g/kWh at $P_i = 2.0\ bar$ with default swirl ratio.

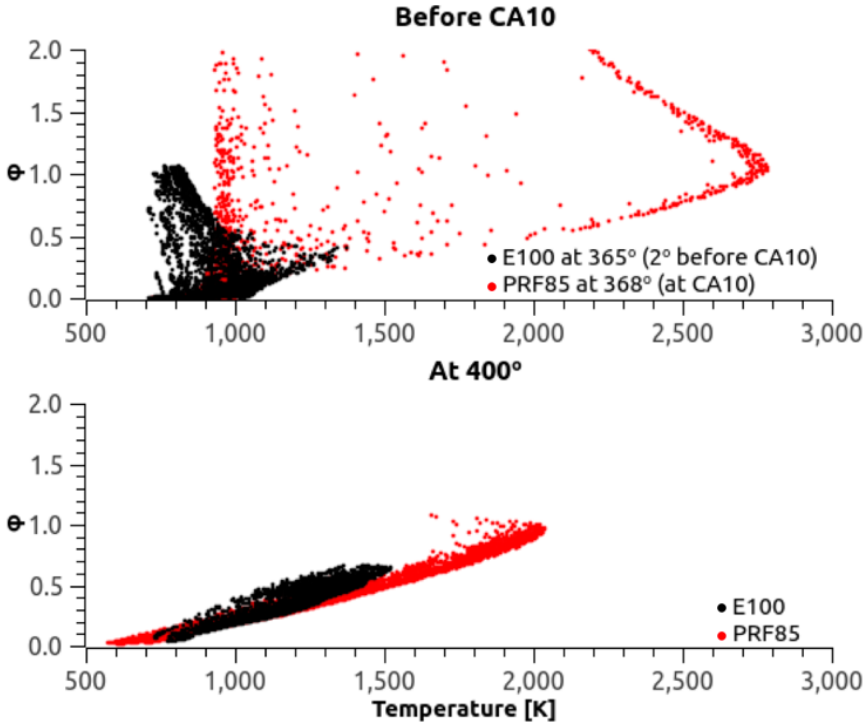


Figure 4.15: Local equivalence ratio distribution before and after combustion for $P_i = 2.0\ bar$ with default swirl ratio.

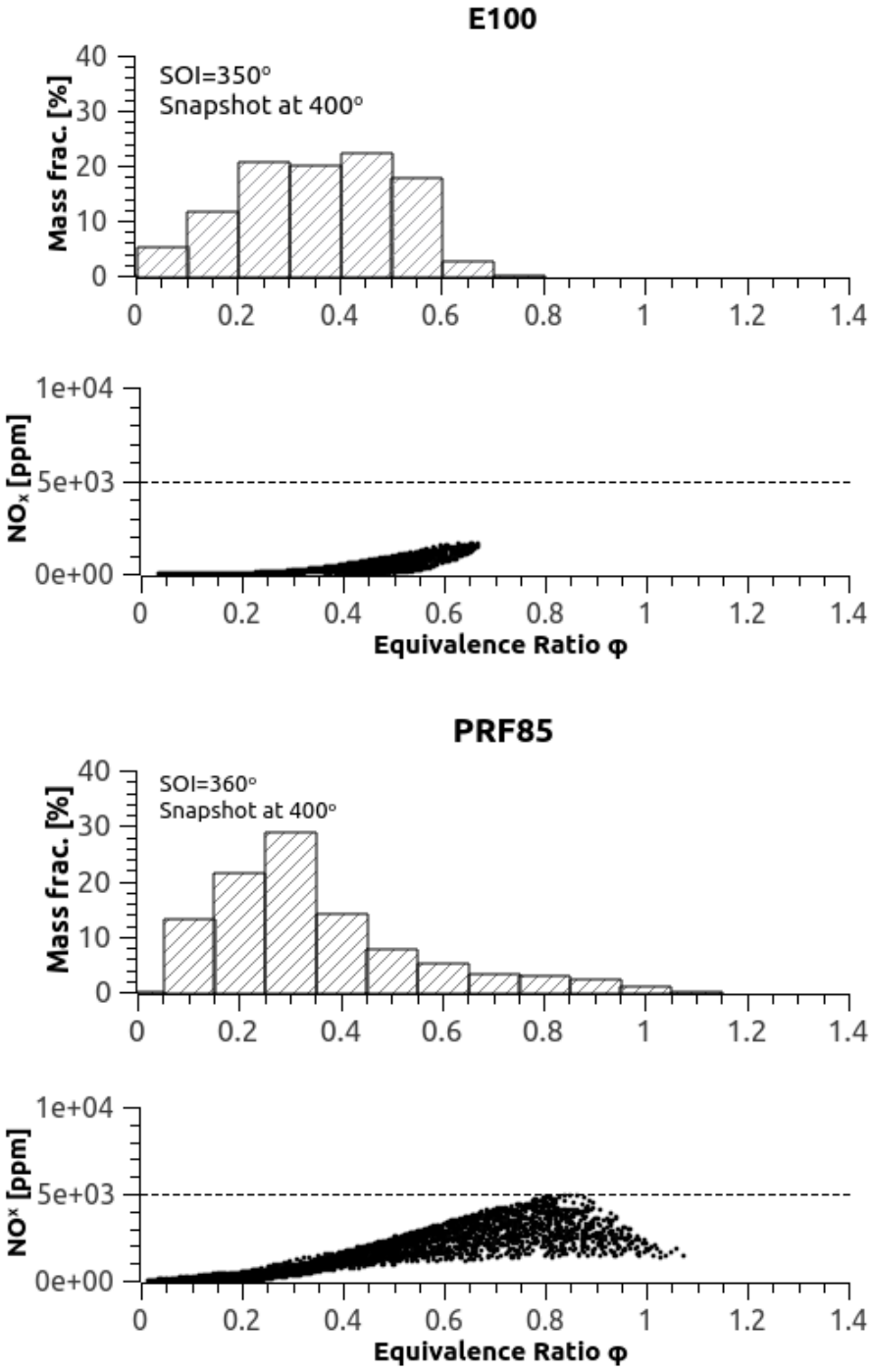


Figure 4.16: Snapshot of the E100 and PRE85 emissions, and the mixture distribution after combustion. $P_i = 2.0\ bar$ with default swirl ratio.

4.3.3 High Load Operations

In this subsection, the selected high load conditions are presented. The IVC pressure is at 2.0 bar and the fuel quantity is increased to 50 mg. Due to the high overall equivalence ratio, high swirl of 3 is used to reduce the diffusion-controlled heat release. As opposed to lower load conditions, it generated slightly more NOx emissions when fueling with E100 at high load. The pressure curves are shown in Figure 4.17. In this case, the in-cylinder peak pressure and temperature in the E100 case is higher compared to the case using PRF85 due to the faster instantaneously HRR. Such higher temperature eventually contributes to the formation of NOx, which can be seen from the accumulative NOx emissions curve indicated in Figure 4.18. As for the mixture distribution given in Figure 4.19, the highest local ϕ for the E100 case is close to 0.9, while in the PRF85 case, the mixture goes beyond local stoichiometric. At the same ϕ value, the NOx production level is high and not dispersed in ϕ-space as expected.

To explain the failure of E100 in reducing NOx, the evolution of the iso-surfaces, $\phi = 0.3$ and $\phi = 0.7$, in the E100 case are colored by the temperature, and are shown in Figure 4.20. Conceivably, the ignition event first occurs near the $\phi = 0.3$ iso-surface at 366° crank angle. However, only after two crank angles, the ignition can be seen also on the $\phi = 0.7$ iso-surface. Then the vigorous combustion occurs on both iso-surface, resulting in the drastic pressure and temperature increases. Although the lean regions ignite earlier, considerable amount of the near-stoichiometric region is still burned in the early phase of the overall combustion, removing the NOx reduction effect of the inverted ϕ-sensibility.

The study of the E100 inverted ϕ-sensitivity and its impact on the NOx emissions under the high load conditions suggests that when the overall equivalence ratio is beyond a certain value, say 0.55, the inverted ignition sequence will lose its effectiveness in reducing NOx emissions. For

a leaner overall equivalence ratio and lower load, using E100 which exhibits inverted ϕ-sensitivity is an effective method of in-cylinder NOx reduction.

By changing the fuel used in the compression-ignition engine, the engine operation is altered in many aspects besides the chemical kinetics and spray cooling that are responsible for the inverted ϕ-sensitivity studied in this paper. Maximum effort has been made to control the operation characteristics with different fuels while still be able to reveal the effects of the inverted ϕ-sensitivity. Due to the vast property differences between E100 and PRF85, identical operation characteristics cannot be achieved in spite of the effort in conducting valid comparisons, influencing the gaseous emissions inevitably [170].

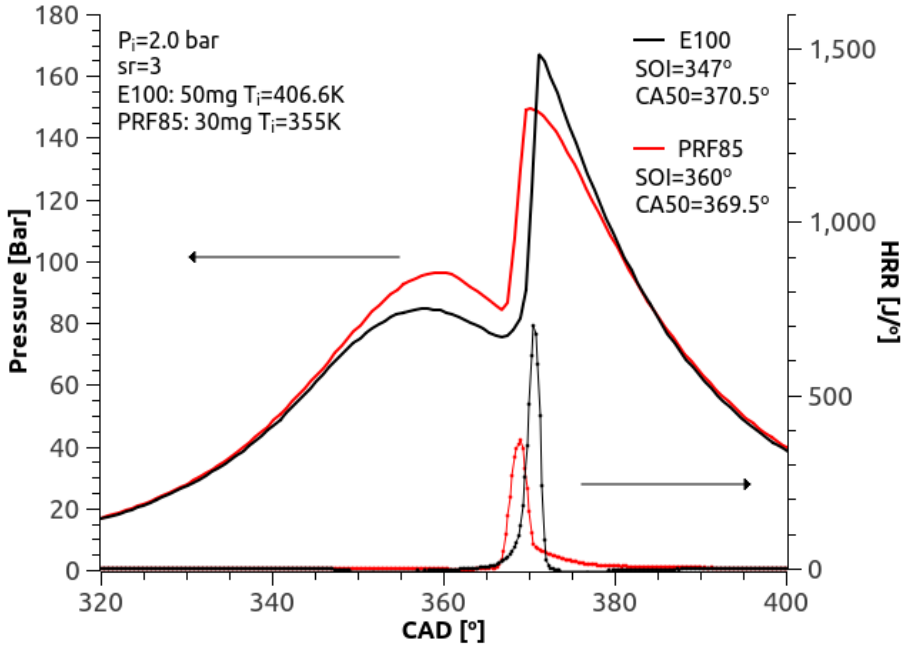


Figure 4.17: Pressure history and HRR at $P_i = 2.0\ bar$ with swirl ratio of 3.

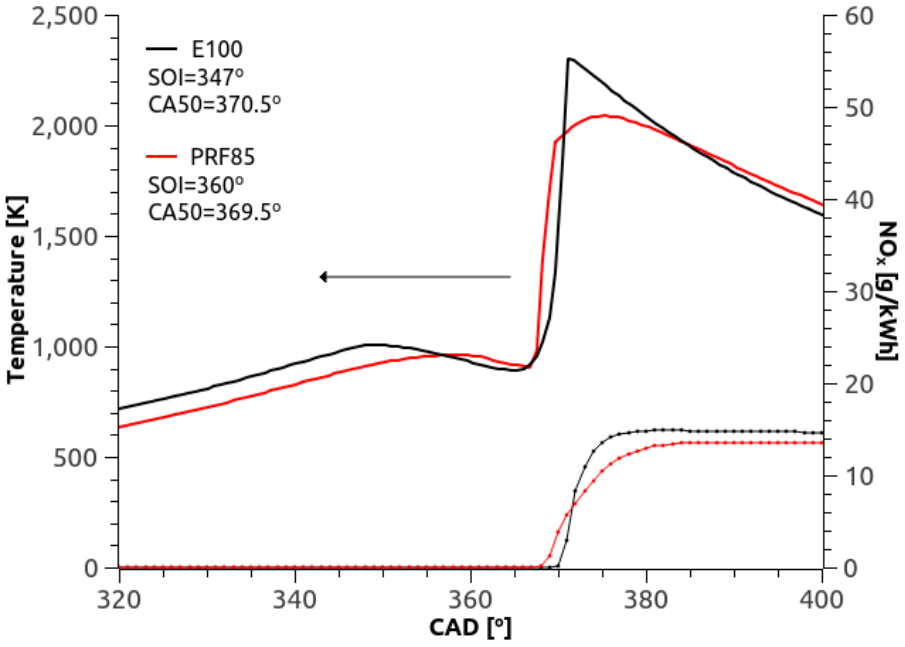


Figure 4.18: Average in-cylinder temperature and NOx emission in g/kWh at $P_i = 2.0\ bar$ with swirl ratio of 3.

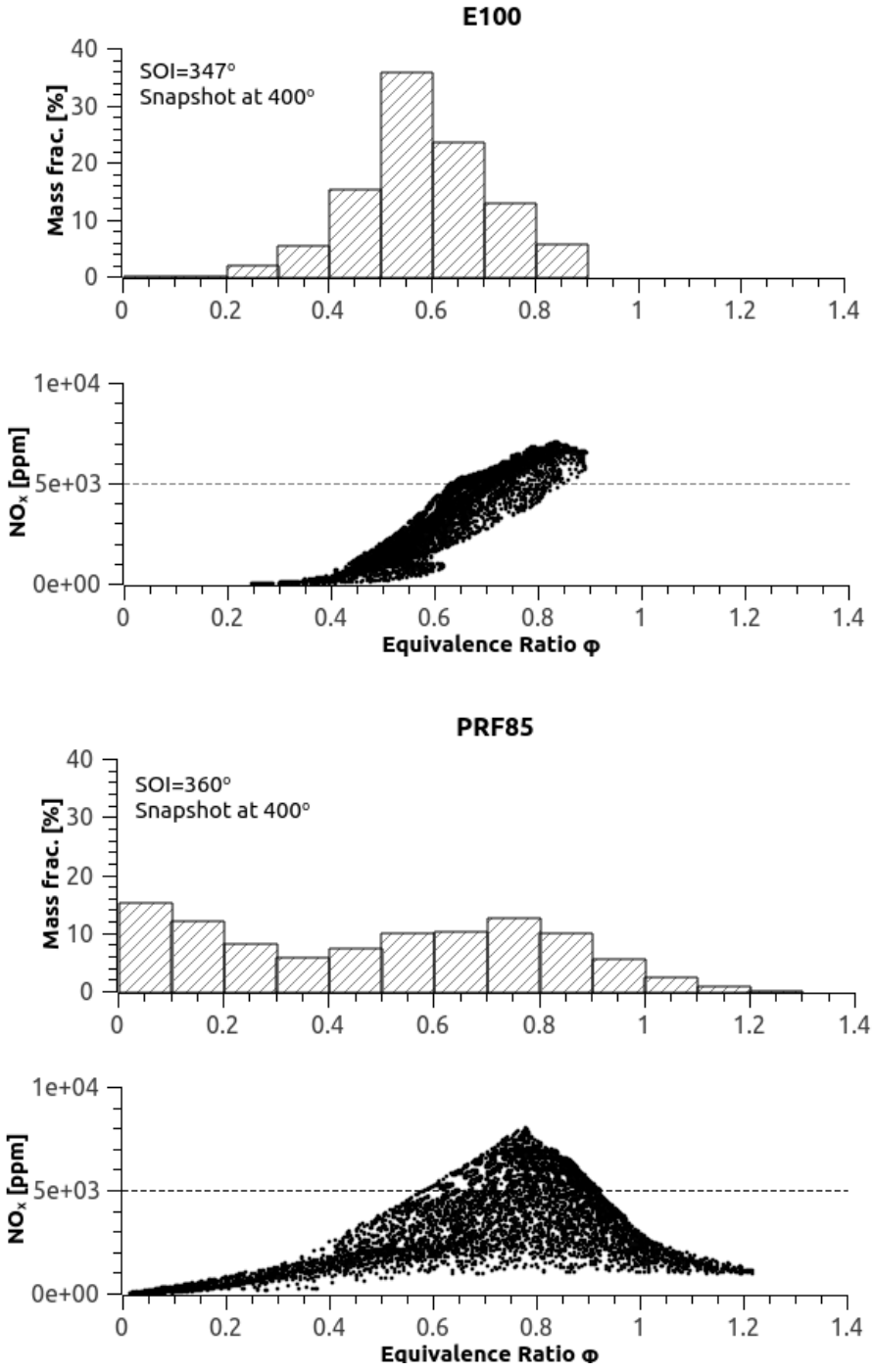


Figure 4.19: Snapshot of the E100 and PRE85 emissions, and the mixture distribution after combustion. $P_i = 2.0\ bar$ with swirl ratio of 3.

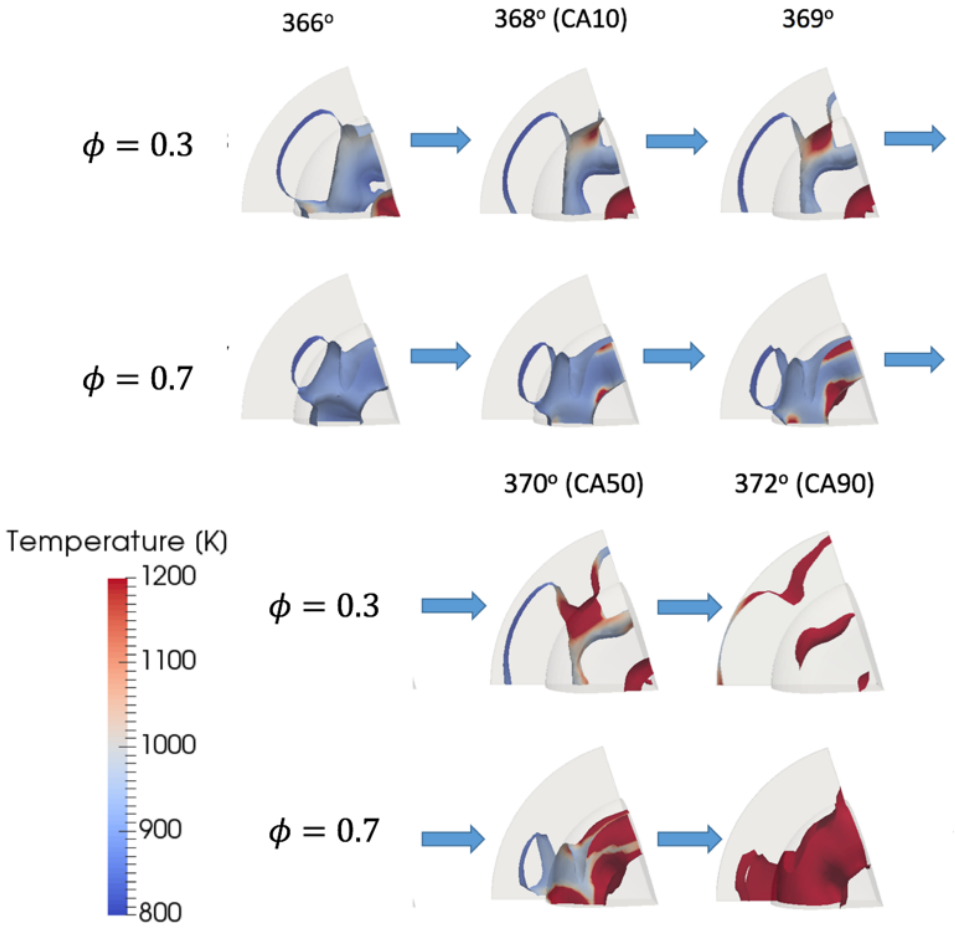


Figure 4.20: The evolution of the E100 iso-surfaces, $\phi = 0.3$ and $\phi = 0.7$, during the combustion stage.

CHAPTER 5: MULTI-INJECTION CONTROL PARAMETERS OPTIMIZATIONS FOR HIGH-LOAD C.I. ENGINE WITH INVERTED PHI-SENSITIVITY FUEL

The primary objective of in this section is to evaluate the proposed NOx reduction method for high load conditions in C.I. engines. This method relies on the control of the burning sequence of the lean and near-stoichiometric regions of the in-cylinder mixture [171]. If the lean region ignites earlier than the near-stoichiometric region, then the temperature rise of the near-stoichiometric region is inhibited, and consequently impedes the NOx formations. Such inverted ignition sequence is referred to as "inverted ϕ-sensitivity". As shown in previous section, the effect of inverted ϕ-sensitivity under low and medium loads in reducing the NOx emissions was pronounced. However, under high load conditions, the local equivalence ratio is stoichiometric, the vigorous combustion near the stoichiometric region occurs instantly once the lean region is ignited, removing the effectiveness of the inverted ϕ-sensitivity.

Therefore, it is desirable to recover the combustion sequence in the chamber such that the leaner region is burned before the near-stoichiometric region. When the combustion in near-stoichiometric region is inhibited, the temperature rise of that region is hindered and the formation of NOx is suppressed. To achieve the goal of homogenizing the mixture before combustion, thus switching ignition mode and lowering emissions when fueling with the target fuel, multiple injection strategies are applied to control the fuel distribution in the combustion chamber under high load conditions. The aim is to shift the local equivalence ratio to the leaner region before combustion occurs, hence recovering the inverted ϕ-sensitivity behavior. The control parameters of the test engine are optimized using the validated CFD models coupled with the GA code to preserve the better trade-off relations among emissions and engine performance. The simulation

environments are set to be the same as the single injection inverted ϕ-sensitivity studies in previous section, and the high load condition case with 50 mg ethanol directly-injection fuel from the previous study servers as the baseline in the current study. The total amount of fuel injected into the derived AVL-5402 single cylinder diesel engine and the engine operation speed are fixed to be 50 mg and 1200 rpm, respectively, for all cases.

5.1 Genetic Algorithm Optimization

GA is a method for solving optimization problems that is based on natural selection. It is capable to find an optimum solution even when the objective function has many local optimums. The GA is a process created to find a set of n parameters $(p_1, p_2, \dots, p_n)$ such that the value of a target function $f(p_1, p_2, \dots, p_n)$ is maximized or minimized, depending on selection of the application. The value of target function is determined by the parameters and computed via engine CFD simulation. Each combination of parameter set is an individual in a population and each individual has a chromosome representing as a binary string.

In the optimization process, GA randomly generates the parent control parameters in the 1st generation, allowing for the entire range of prescribed domain. The evolution cycle or iterations will be made by evaluating the fitness of all the individuals in the population, creating a new population by the following three mechanisms: 1) elite selection, surviving in the current generation due to best fitness values; 2) genetic recombination, combining pairs of parents in the current the generation; and 3) mutation, randomly change from a single parent, referring to Figure 5.1. The interactions between these mechanisms make optimization very complex. However, the role of the individual components remains the same. Old population will be replaced, and the iteration will be made again using the new population to minimize the target function for achieving

the highest efficient with lowest emissions. The probability that an individual will be selected for reproduction is based on its fitness scores. The algorithm terminates if the population has converged or if the user defined constrains has met. GA has been widely applied for optimization methodology in engine CFD simulation, and it uses function evaluations and does not require derivative form, which can be effective in finding a global optimum among the multi-modal optima frequently encountered in engine research.

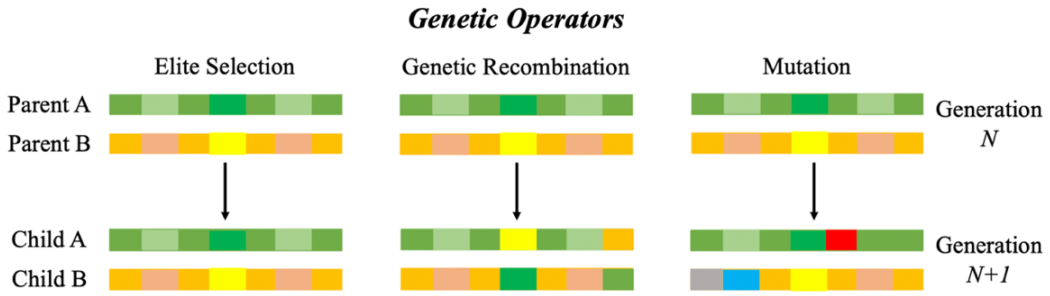


Figure 5.1: Main genetic operators for genetic algorithms.

An open-source python package, Playdoh, is utilized as the platform for the GA optimization [172]. Individuals in each generation are distributed and evolves independently across different computing nodes at which the target function is evaluated against a subset of the parameters. Later the nodes exchange the minimum information needed so that best individuals (or parameters) can be selected and migrate to the next generation. However, these computational tasks require some communication between subtasks and the introduction of synchronization points as they cannot be distributed using the independent parallel interface of Playdoh. A python package has been developed to enable the use of multiple CPUs on a single computer or across clusters and to provide the parallelism logic for the global optimization that runs in Playdoh. This package has been loosely coupled to programming interface provided in Playdoh, and then a standalone and lightweight inter-process communication (IPC) module can enable dynamic allocations in a network to provide an abundant supply for the computational resources.

For the sake of enhancing the inverted ϕ-sensitivity behavior under high load conditions and recovering the combustion mode to the premixed-dominated regime, the total directly injected fuel of 50 mg is divided and introduced separately into the cylinder. To achieve the peak engine performance under the consideration of the multi-injection strategy, the operation parameters of the AVL 5402 engine to be optimized are fuel split ratio (r) and start of injection (SOI) timings. In this study, r represents the ratio of fuel injected in the first injection (r_1) for double injection method, and that in the first and second injections (r_1, r_2) for triple injection method. The SOI_2 timing is confined within the injection timing range for the one direct-injection CI engine to avoid the very early first injection timing if given the dwell, the duration between the SOI_2 and end of the first injection (EOI_1). It should be noted that SOI_2 and the dwell in the triple injection strategy have narrower search space compared the double injection strategy to attain similar rates of convergence, since triple injection cases have two extra independent control parameters (r_2 and SOI_3). The variation for *SR* is also deliberate, and high *SR* may not require because the diffusion-controlled heat release phenomenon may be abated by fuel injection strategy. The specified ranges of variation for these control parameters are listed in Table 5.1.

The build-in solvers for global optimization in playdoh can be loosely coupled with the independent parallel tasks while enabling dynamic allocations in a network to provide an abundant supply for the computational resources. In this work, the *minimize* function in playdoh is called at the interface for KIVA and GA platform to minimize the target function $f(r_i, SOI_i, dwell, SR)$, which is evaluated for different combinations of control parameters in the CFD model and measures the quality of each combination constructed by the engine performance and emissions:

$$f = \frac{Y_{NO_X}}{Y_{NO_X}^{ref}} + \frac{Y_{soot}}{Y_{soot}^{ref}} + \frac{Y_{CO}}{Y_{CO}^{ref}} + \frac{Y_{UHC}}{Y_{UHC}^{ref}} + k_p \frac{w_i^{ref}}{w_i} \tag{5.1}$$

Included are the indicated work w_i from IVC to EVO, and engine-out emission mass fractions of NOx, soot, CO and UHC. Each term is normalized by its reference parameter. To balance the importance of engine performance versus emissions, a multiplier k_p is adopted and set to be 10 in this work. The reference emissions are taken from previous computational studies and are set such that each term of emission retains palpable contribution to the final value of target function, i.e., $Y_{NO_x}^{ref} = 250\ ppm$, $Y_{soot}^{ref} = 20\ ppm$, $Y_{CO}^{ref} = 150\ ppm$, $Y_{UHC}^{ref} = 100\ ppm$. The target indicated work is 50% of the total fuel energy. It should be noted that the emphasis in this work is the NOx emission, as it is one of the indicators for inverted-ϕ dominated ignition. Therefore, the chosen references for CO, soot, and UHC emissions are set to be higher than that from the simulation results of the baseline case. The influence of such bias in the target function is discussed in the optimization results section.

In this study, 3-D CFD simulations are performed for 1800 combinations of $(r_i, SOI_i, dwell, SR)$ in 30 generations. To initialize the evolution, GA randomly generates the parent control parameters in the 1st generation, allowing for the entire range of prescribed domain. The children that make up the successive generations are created by aforementioned mechanisms.

Table 5.1: Independent control parameters and their prescribed ranges.

Control Parameter	***Search Space***	
	Double	*Triple*
r_1	0.1~0.9	0~0.4
r_2	-	0~0.6
SOI_2	350°-380°	330°-350°
Dwell (SOI_2- EOI_1)	0-70°	0-50°
SOI_3	-	360°-380°
SR	1.5-3.5	1.5-3.5

5.2 Optimal Strategy

5.2.1 Multiple Injection Optimization

To illustrate the use of the genetic algorithm and to evaluate the optimization performance, the evolutions of control parameters in 30 generations are plotted in Figure 5.2 - Figure 5.6. The variations of SOI_is for the double injection scheme is shown in Figure 5.2. GA methodology finds the approximate optimum SOI_2 timing around the 9th generation, and then it quickly evolves toward a convergent value. SOI_1 is directly acquired from SOI_2 and dwell; roughly only three more generations later the SOI_1 timing draws to its optimal value near 295°. It is observed that the first injection timing swings markedly in the search space before the convergence of SOI_2 and narrows down to a confined range afterward. This can be disclosed by the sensitivity of NOx formation to the injection timings and will be elaborated in the following section. The convergent amount of injected fuel quantity in each injection for double injection scheme, indicated in Figure 5.3, is obtained near the 14th generation, and the majority of the E100 is fueled to the chamber during the first injection. The deferred convergence of the injected fuel quantity in each injection indicates that the correlation between the engine behavior and the fuel split ratio is emphasized after deciding the injection timing. The SOI timing and fuel-split ratio determine the fuel vapor distribution inside the cylinder, thus the combustion mode.

Compared to Figure 5.2, the rate of convergence for triple injection GA optimization, plotted in Figure 5.4, is similar to that for the double injection scheme. That is, the main and post injection timings, SOI_2 and SOI_3, converge quickly to their optimal values after about 10-generations, and the conspicuous attraction to the optimal SOI_1 can be clearly observed after the 10th generation. The spray mass designated to each injection is shown in Figure 5.5 for the triple injection scheme. *GA* arrives at a comparable fuel supply during the 1st and 2nd injection events

and a trace amount of ethanol, about 20%, to be introduced in the post injection. All three injected fuel amounts converge nearly at the same time around the 10th generation again. This implies that SOI_i and r_i both indisputably affect the evolutionary process of optimization.

In Figure 5.6, the swirl ratio applied to these two optimization cases develops rapidly over the initial 13 generations, and its value only perturbs slightly in the vicinity of the optimal SR in the successive generations. It is noteworthy that the optimal SR in the double injection strategy (~2.0) is a little bit smaller than that in the triple injection strategy (~2.3). Comparing the two strategies, approximately 10% more E100 is injected into the chamber before the onset of ignition for in the triple injection scheme, thus a higher swirl ratio is desired to reduce the mixing-controlled heat release. The optimal control parameters are listed in Table 5.2.

Table 5.2: Operation conditions for baseline and optimized cases.

Control Parameter	*Baseline*	*Double Injection*	*Triple Injection*
r_1	1	0.694	0.388
r_2	-	-	0.408
SOI_1	347°	316.6°	318.6°
SOI_2	-	376.2°	339.9°
SOI_3	-	-	379.9°
SR	3	2.03	2.3

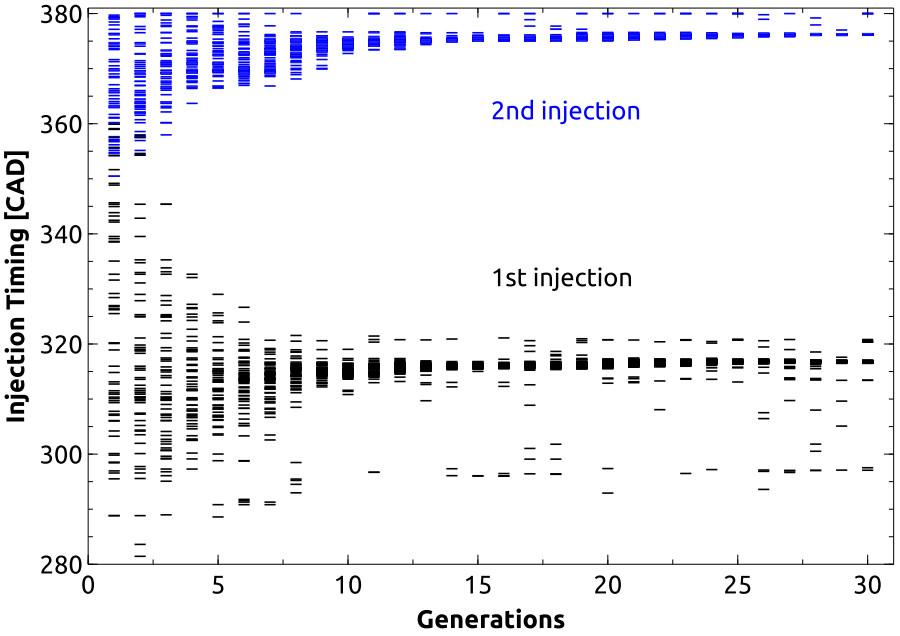


Figure 5.2: Evolution of SOI through generations for double injection strategy.

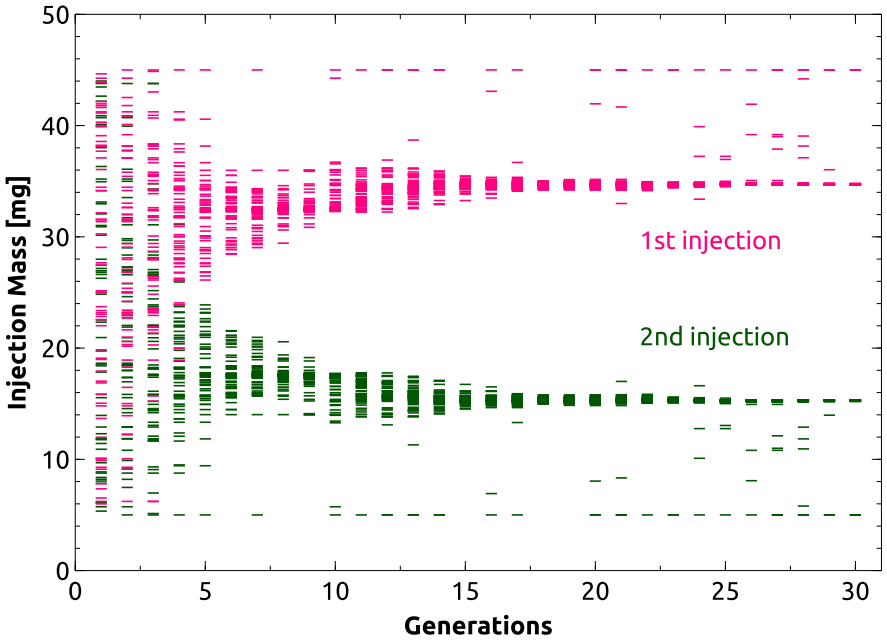


Figure 5.3: Convergence of the injected fuel quantity in each injection through generations for double injection strategy.

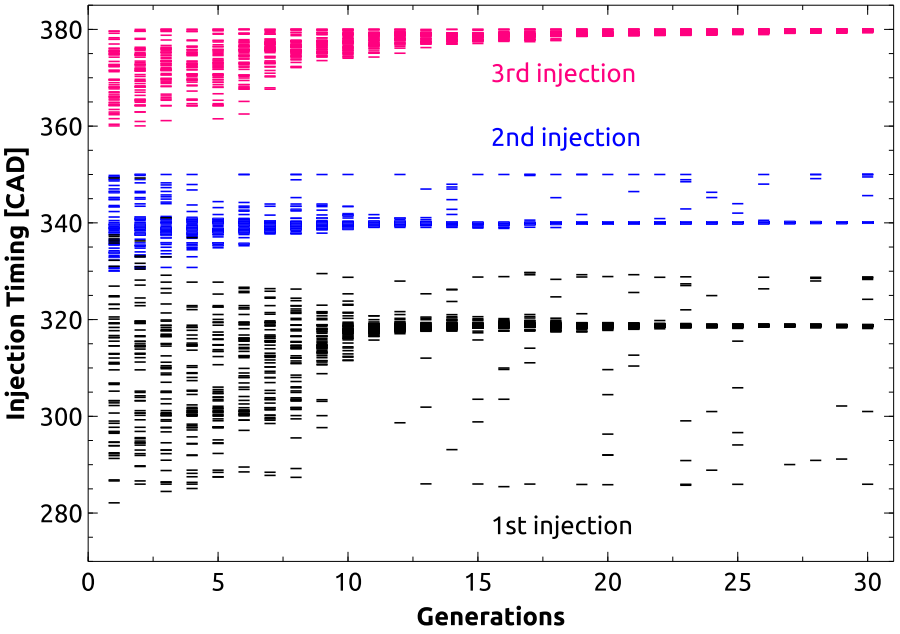


Figure 5.4: Evolution of SOI through generations for triple injection strategy.

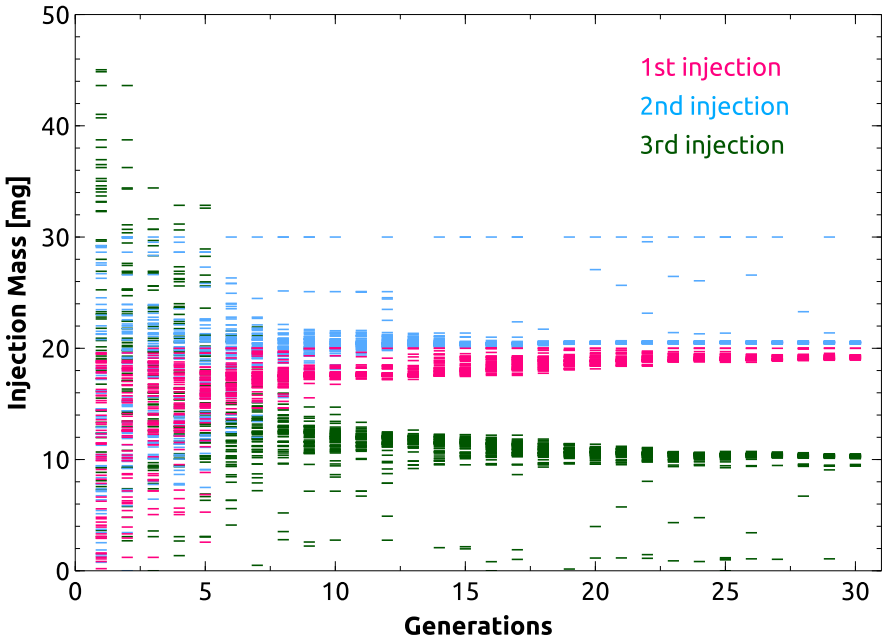


Figure 5.5: Convergence of the injected fuel quantity in each injection through generations for triple injection strategy.

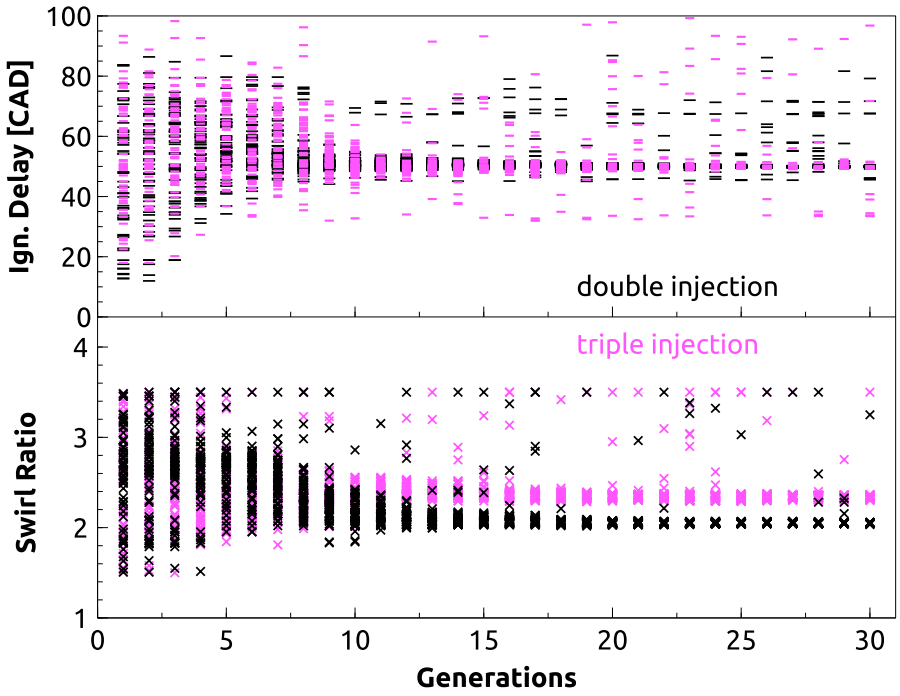


Figure 5.6: Convergences of ignition delay and swirl ratio in 30 generations for double and triple injection schemes.

The predicted optimum SOI_1 timing is very advanced for both schemes, suggesting that HCCI-like combustion is useful for improving engine performance at the prescribed operating condition (1200 rpm, 50 mg load). The present optimization for both schemes shows that the resulting long ignition delay (~50°) allows enough time for fuel-air mixing and reduces the extent of fuel rich regions. It should be noted that after the convergence of each parameter, the optimization program keeps mutating the parameters within the prescribed range to discover potential improvement.

Figure 5.7 shows the minimum target function value, f_{min}, achieved in each generation. The trend of the curves is consistent with the sensitivity analysis for control parameter convergence. Initial values of f_{min} are high due to the random selection of the individual parameters and the unestablished correlations between these parameters and the optimization target. f_{min} value drops

dramatically and approaches to its minimum within 7-generations, signifying the effectiveness of obtaining optimal control parameters. For the triple injection scheme, f_{min} decreases smoothly in each successive generation after 7th generation and eventually reaches its minimal value. As for the double injection scheme, a small hump comes forth around the 14th generation, stressing the fact that sensitivity weighting of the control parameter is different for GA optimization within this scheme. The overall performance of the triple injection scheme is more superior to that of the double injection since a lower f_{min} spans over the generations is achieved.

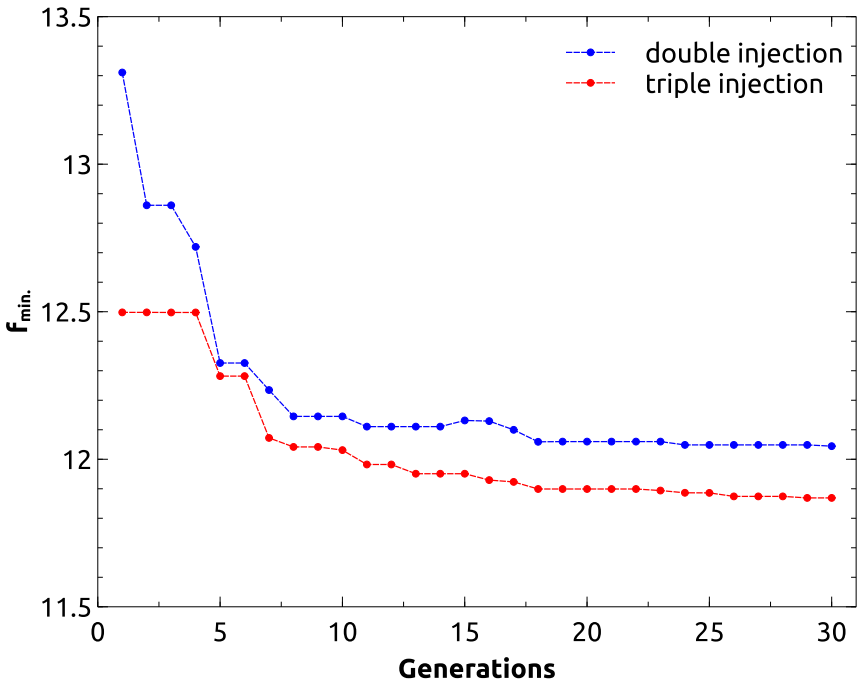


Figure 5.7: Variation of minimum target function values with generations.

5.2.2 Optimized Engine Performance

The present GA methodology has found a set of engine parameters that significantly reduces engine-out emissions while simultaneously increases the indicated work, compared to the initial baseline case under the operating conditions listed in Table 5.2. The evolution of combustion phasing is plotted in Figure 5.8. Overall, a similar combustion phase can be recognized after

convergence for both the double and triple injection schemes; that is, a short, premixed combustion period followed by a mixing-controlled combustion due to the post injection. However, a wider band of variations for CA50 and CA90 emerges when approaching the last 6 generations, and their values are no longer close to a single optimal value.

Figure 5.9 and Figure 5.10 show the improvement of the indicated work and emissions through the generations. As expected, GA balances each term in the target function to approach the global optimum. In Figure 5.9, the optimal IMEPs in both injection schemes gradually converge in the successive generations after approximately the 10th generation. Though the NOx and CO emissions converge rapidly with each subsequent generation, as seen in Figure 5.10, small perturbations in finding the optimum value can still be perceived during the optimization process. Therefore, compromises must be made between the indicated work and emissions. What can also be observed is that there is a trade-off among different emissions, but not as prominent in this study due to the selection of the reference emissions in the target function.

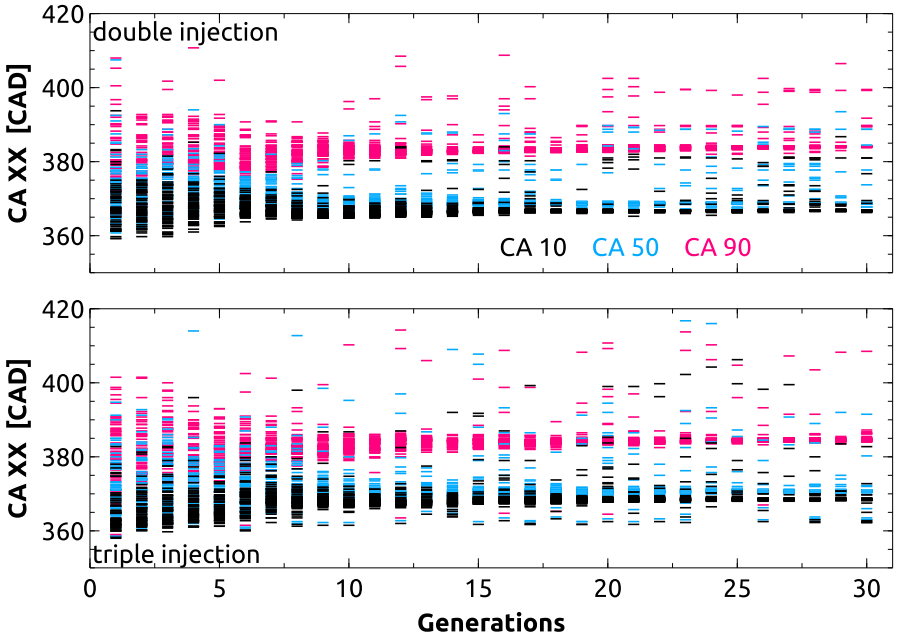


Figure 5.8: Changes of combustion phasing through generations for double and triple injection strategy; CA XX represents the moment of XX% of heat released, and CA 10 usually refers to the timing that combustion just gets started.

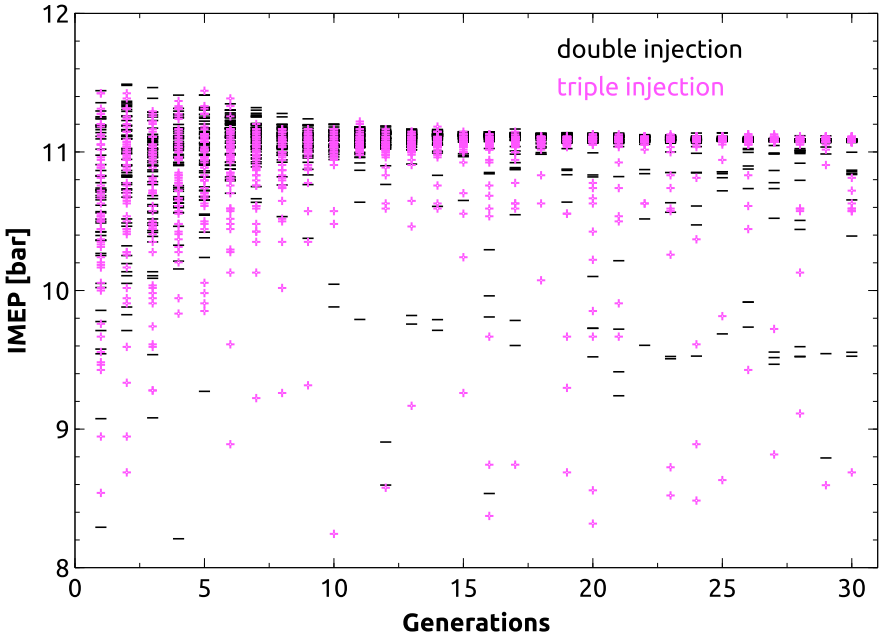


Figure 5.9: Engine performance through generations for double and triple injection strategy.

Comparing the NOx and CO emissions in Figure 5.10, widely spread CO emissions after the convergence reveals that the sensitivity of CO in the target function is not significant, i.e., the target function value is insensitive to CO emissions in CFD calculations. Similar results are observed for the soot and UHC emissions over the generations. On the contrary, the merit value tends to be more sensitive to changes in the NOx emissions. Though the GA optimization does not intentionally find the control parameters to suppress the formation of CO, soot and UHC, the optimized multi-injection strategy provides prominent advantages over the baseline case in the CO and UHC emissions due to the more complete combustion. The optimal double injection scheme, on the other hand, tends to have higher soot emissions. The detailed CFD results will be used to clarify the reasons in the next section. The summary for engine performance is given in Table 5.3. GA slightly increases the IMEPs but prominently reduces NOx emissions, leading the optimization to a NOx driven process.

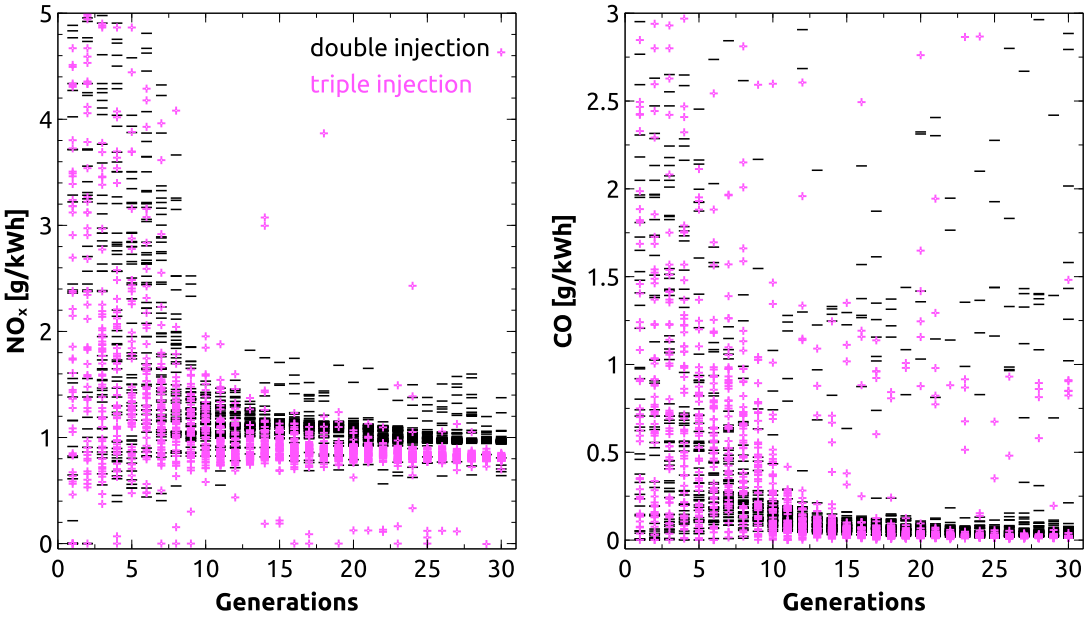


Figure 5.10: Improvements of NOx and CO emissions through generations. Values are in g/kWh, which are calculated from amount of emission of each species in PPM and indicated work, to eliminate the influence of incomplete combustion.

Table 5.3: Engine performance for baseline and optimized cases.

Performance	*Baseline*	*Double Injection*	*Triple Injection*
$IMEP[bar]$	10.69	11.08	11.07
NOx	14.4	0.97	0.78
CO	1.34	0.057	0.024
$Soot$	$7.27 \cdot 10^{-3}$	$9.12 \cdot 10^{-3}$	$5.42 \cdot 10^{-4}$
UHC	$1.83 \cdot 10^{-2}$	$3.82 \cdot 10^{-4}$	$4.17 \cdot 10^{-4}$

**Unit for emissions is* $[g/kWh]$

As mentioned previously, the NOx formation is closely related the post injection timing for both injection schemes, i.e., the high sensitivity of NOx emissions to the value of SOI_2 in double injection scheme, for example. Investigation has been made by varying the SOI_2 timing while keeping all other parameters the same. An individual from the 5th generation of the double injection scheme is selected. The selected SOI_2 timing is 375.4°, less than 1° advanced injection timing comparing to that in optimal double injection scheme, and all other control parameters are comparable to each other. Early SOI_2 maintains a higher in-cylinder peak temperature (1901 K for $SOI_2 = 375.4^O$ and 1871 K for optimum), consequently increasing the NOx emissions by almost 51%. The relationship between the post injection timing and NOx emission is indicated in Figure 5.11. Such strong correlation is not observed in other NOx-control parameter pairs.

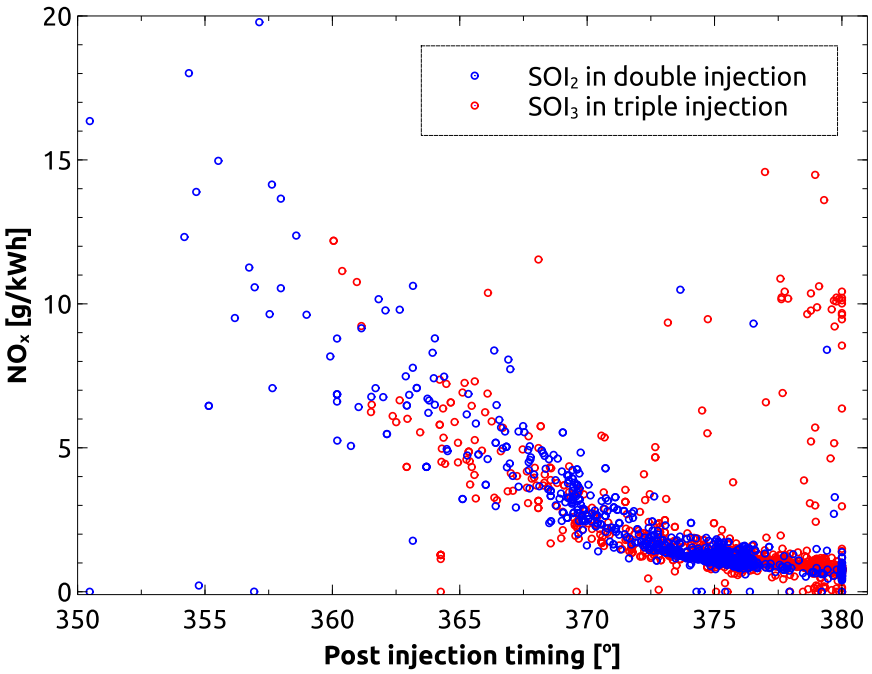


Figure 5.11: Correlation between the NOx formation and the post injection timing; the scatter plot is made by the results from all 1800 simulation cases.

5.3 Realization of Inverted ϕ-Sensitivity Under High Load Condition

The optimal combinations of control parameters are used in KIVA CFD simulations, and the corresponding results are shown in Figure 5.12 - Figure 5.15. For the baseline and optimized cases, the CA50s are comparable and close to 370° crank angle, confirming the similar combustion phasing. In Figure 5.12 and Figure 5.13, the instantaneous heat release rate and averaged temperature are both sufficiently high for the baseline. Under high load conditions, the elongated fuel vaporization process deteriorates the mixing process, so the air-fuel mixture before the ignition (CA10) is extremely stratified, as shown in Figure 5.14. The vigorous combustion occurs simultaneously in both lean and near-stoichiometric regions [171], leading to the tremendous pressure and temperature increases and thus the NOx formation. In Figure 5.14, the local ϕ distribution at CA50 clearly displays that a large number of scatters are found in the high temperature NOx formation regime.

With the multi-injection strategies, advanced pilot injections well benefit the mixture preparation before the combustion. Even though a very advanced pilot injection increases the risk of fuel impingement, the fuel film on the piston head would completely vaporize and mix with ambient gas because of the increased in-cylinder temperature and the squish effect as the piston moves toward TDC. As seen in Figure 5.14, partially premixed mixture can be attained before CA10 for both multi-injection schemes, and the cells with low equivalence ratios are the first to approach the equilibrium flame temperature. Ignition in the lean regime is more pronounced, revealing the familiar behavior of inverted ϕ-sensitivity. Such inverted ignition sequence retards the combustion event near the stoichiometric region, leading the near-stoichiometric region to a compression-ignition burning process rather than the typical ignition-compression sequence. A lightened heat releasing process is observed in Figure 5.12, mitigating the pressure rising rate. The

in-cylinder temperature drops conspicuously and suppresses the NOx formation during the combustion (indicated in Figure 5.14).

The lower in-cylinder temperature of the double injection scheme compared to the triple injection scheme (Figure 5.14) is supposed to generate less engine-out NOx emissions, but the double injection strategy ends up with higher NOx emissions (Figure 5.13). This is consistent with the analysis that NOx emissions are vastly sensitive to the post injection timing. Though a lower NOx formation can be achieved in the initial stage of combustion, once the post injection is triggered, the NOx emissions are reversed because the post injection timing in the triple injection scheme is more retarded.

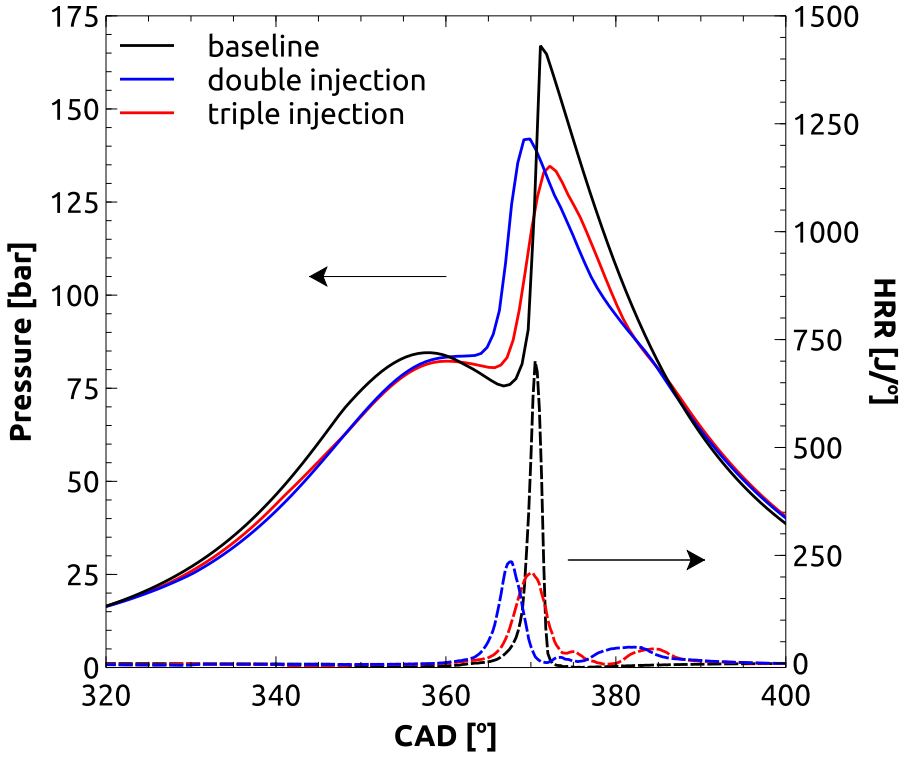


Figure 5.12: Comparisons of pressure history and heat release rate for optimal multi-injection strategies and the baseline fueling with 50mg E100.

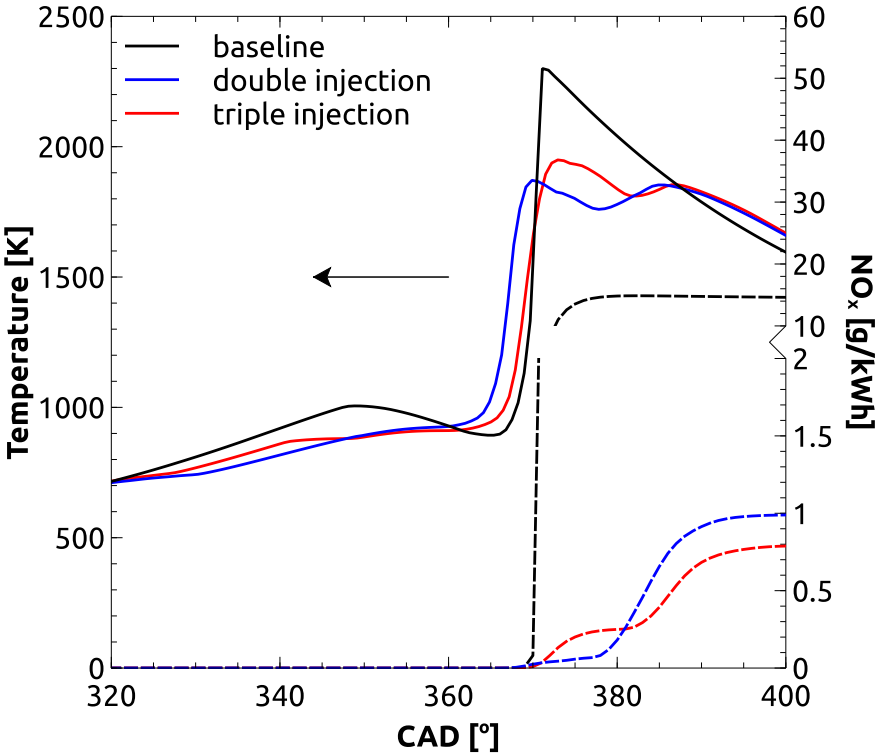


Figure 5.13: Comparisons of averaged in-cylinder temperature and engine-out NOx emissions for optimal multi-injection strategies and the baseline fueling with 50mg E100.

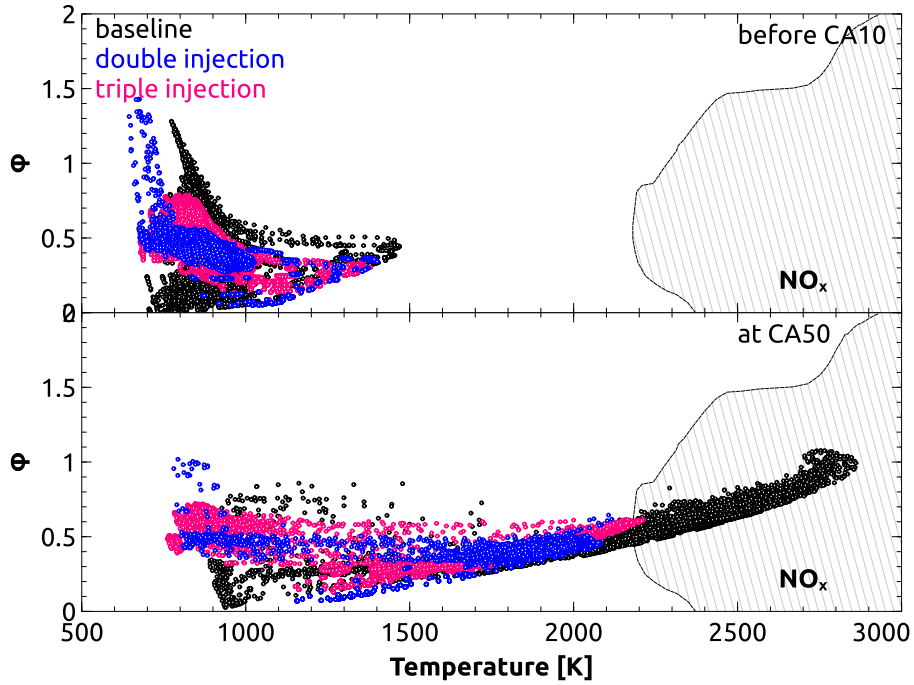


Figure 5.14: Local equivalence ratio distribution before CA10 (top) and at CA50 (bottom). The NOx region definition is from [173].

The cell mass and NOx distribution in the ϕ-space at 400° crank angle is visualized in Figure 5.15. For the majority of the cells, combustion is finished at this moment, and the NOx related reactions are nearly frozen. The dependency of emission on ϕ has not been smeared by diffusion yet. With the single direct-injection scheme, the mixture is concentrated around ϕ=0.6. The maximum NOx formation is settled near the stoichiometric region where the high flame temperature and plentiful oxygen suffice the NOx production. Deviating in either direction reduces NOx. The desired NOx dispersion in the ϕ-space is not observed. Distinct ignition sequence on a ϕ iso-surface also helps to reduce NOx as the early burnt gas is compressed due to the heat release from the rest of combustion chamber, which leads to higher local temperature. The NOx-ϕ dispersion is remedied in the multi-injection schemes due to the realization of inverted ϕ-sensitivity under such high load condition. Over 40% of the cell mass is concentrated at ϕ=0.6 for triple injection scheme. Compared to the baseline, the triple injection scheme is expected to generate more NOx. However, recovered inverted ϕ-sensitivity overpowers the effect of the mixture distribution and leads to a considerably less NOx production. The NOx-ϕ distributions for the double and triple injection schemes are almost identical. In the double injection scheme, the cell mass concentration is left skewed, illustrating the comparable effects of the inverted ϕ-sensitivity and the advanced post injection timing.

From Figure 5.14, the upper portion of the scatters reaches above ϕ=1 in the double injection scheme, which suggests a stratified distribution inside the chamber. Due to the early pilot injection, the evaporated fuel film at the squish forms a locally rich region. The in-cylinder ϕ distribution is shown in Figure 5.16. The stratified mixture is expected for the baseline; and for the multi-injection schemes, the E100 inside the piston bowl is already mixed with air, and a distinct ignition sequence spurred by inverted ϕ-sensitivity is forthcoming. The locally rich region has

inconspicuous effect on the NOx formation, while the soot formation tends to slightly increase in the double injection scheme for favorable soot formation environment in the low temperature (near the wall) fuel rich zone (see Table 5.3).

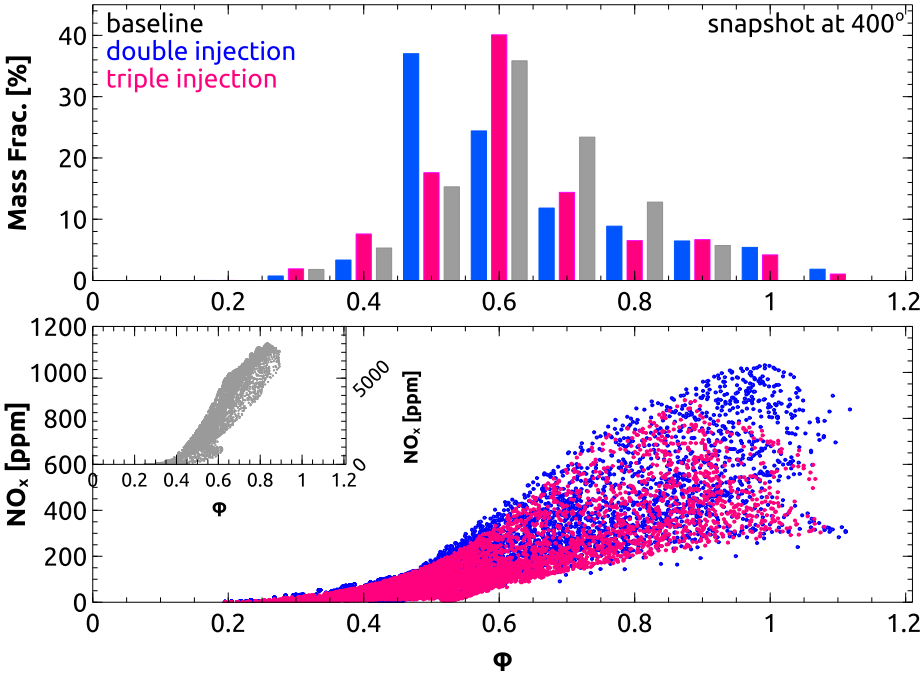


Figure 5.15: Snapshot of mixture distribution and NOx emissions after combustion.

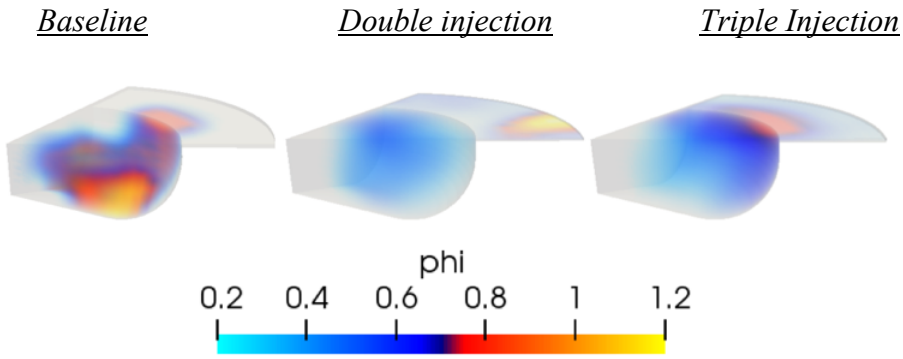


Figure 5.16: In-cylinder equivalence ratio distribution before CA10 for optimal multi-injection strategies and the baseline fueling with 50mg E100.

CHAPTER 6: APPLICATIONS OF MACHINE LEARNING IN ENGINE MODELING AND OPTIMIZATION

Machine learning (ML) is one of today's most rapidly growing technical fields, lying at the intersection of computer science and statistics, and at the core of AI and data science. The AI index annual report [174] shows that over 50% of AI researches fell into the ML category in 2017, and fruitful ML algorithms have been developed by engineers and data scientists. Massive amounts of data are today widespread across scientific disciplines. Gaining insight and actionable information from them have become a new mode of scientific inquiry as well as a commercial opportunity. In this section, model development with the state-of-the-art technique is presented. Data-driven surrogate models are constructed which can easily consume unlimited amounts of data with timely analysis and assessment.

The technique used to develop the data-driven model is called ML that can train the algorithm to mimic the human brain and to learn by observing. In this way, real-time data and predictions can be "quickly" produced comparing to CFD simulations. With the well-trained ML models, the engine design process for better performance can be accomplished by utilizing the ML-GA framework. The ML-GA will be applied to the optimization problems for multiple injections mentioned in Chapter 5, and detailed discussions will be yielded in terms of framework implementations and the computational results comparisons. To highlight the results, ML-GA accelerates the optimization process and shortens the engine design period to meet the industrial interests comparing to CFD-GA methodology.

6.1 Supervised Machine Learning

As with any method, ways to train ML algorithms are different, each with their own advantages and disadvantages. Regardless of the ways to frame these methods, there are three main types of ML: supervised learning, unsupervised learning, and reinforcement learning. In supervised ML, sample data containing various independent features as input and the desired output is provided to algorithms that decipher patterns exist between the input and output values and map a function from the input to the output. This function will be stored as a model that later can be used to predict an outcome with new dataset. For unsupervised learning, the combination of features and targets is unknown, and it emphasizes to create new labels by analyzing the relationship between features and uncovering hidden patterns regarding possible targets. Consequently, the training process for unsupervised learning is based on unlabeled data without any guidance. In reinforcement learning, the prediction model is built by gaining feedbacks from random trial-and-error method.

Considering the applications for substituting IC engine CFD simulations, supervised learning techniques is the optimal option to correlate the complex thermodynamic, chemical kinetic, and fluid dynamic processes that go on in an engine into a compact information process. Supervised learning uses classification algorithms and regression techniques to develop predictive models, but only the regression analysis will be performed in this study to predict numerical responses, such as work delivered, or emission produced over an engine cycle. Figure 6.1 provides the concise workflow for training and prediction of a ML model. The training dataset is basically a matrix: the rows are called "samples" and represents the inputs to and output from the each CFD simulation. The columns X_i's represent the inputs, i.e., design features that to be optimized in GA process, like injection timing, fuel split ratio, etc. The last column, Y, represents the output from

the CFD simulation. There are multiple outputs or objectives to be inspected, for example engine-out emissions, fuel consumption, and efficiency, so Y is essentially a sort of merit value combining these outputs in some manner.

It is still necessary to perform the certain numbers of CFD simulations to generate training data for ML models. However, all these CFD simulations can be conducted simultaneously to generate the training data in short order as the optimization process is not iteratively performed using CFD simulations. After preprocessing the raw data from CFD simulations, the training process can be proceeded with the structured dataset, and a tentative data-driven model can be created after training the ML algorithm selected for a specific task. The trained ML model needs to be evaluated against an unused control dataset, and possible modifications may be required to improve the model performance. The well-trained ML model is capable to make predictions given arbitrary input parameters, and it will very quickly evaluate the merit of that design.

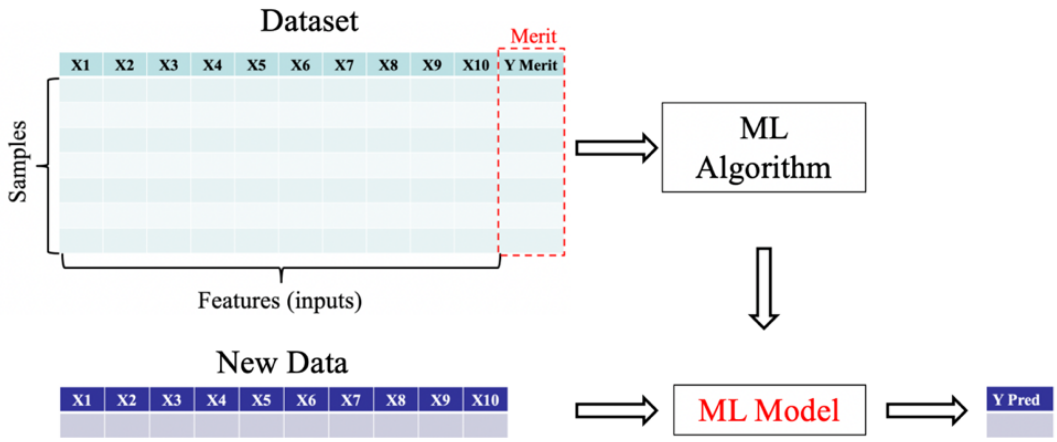


Figure 6.1: General procedures for ML model development.

6.2 Data Preparation

Raw data collected from experiments or obtained from theoretical analysis needs upfront clean and manipulation before feeding it to ML algorithms, and the data points that are incomplete, incorrectly formatted, irrelevant or duplicated need to be removed or modified to make the raw data more applicable and structured. Though it is tedious, preprocessing data is essential to achieve better results from the applied model in ML to lower the risk of "garbage in, garbage out". There are many featured data preprocessing techniques, such as handling the categorical variables, standardizing raw data, one-hot encoding for Boolean variables, or binarizing data according to a threshold, and in this study the most employed one is standardization.

Standardization of engine datasets is a common requirement for machine learning algorithms to improve the numerical stability and to speed up the training process. Raw dataset often is comprised different attributes $(x_1, x_2, \dots, x_n)$ with varying ranges, for example injection timing of spray alters from 300^oCA to 380^oCA and fuel split ratio for multi-injection cases varies from 0 to 1; features with higher attribute will intrinsically influence the result more due to their larger value. The algorithm makes giant leaps toward the very close target while tiny steps are needed. Overshooting will make algorithms to oscillate or explode. Standardization can be realized by transforming attributes with a Gaussian distribution and differing means and standard deviations to a standard Gaussian distribution with a mean of 0 and a standard deviation of 1. Standardized features $(z_1, z_2, \dots, z_i)$ are given in Eq. (6.1). The mean and standard deviation are computed with training sets, and later same transformation is reapplied on the testing set or new dataset that is fed into the trained ML model.

$$z_i = \frac{x_i - \mu_i}{\sigma_i} \tag{6.1}$$

$$x_i \sim \mathcal{N}(\mu_i, \sigma_i^2) \qquad z_i \sim \mathcal{N}(\mu = 0, \sigma^2 = 1)$$

The modified dataset is randomized and split in two parts: the first part, used in training model, will be the majority of the dataset (about 70-80%). The second part will be used for evaluating trained model's performance. Additionally, cross validation (CV) is adopted to maximize the availability of training data by splitting data into different combinations and testing each specific combination, avoiding methodological mistakes due to the overfitting. A commonly used CV approach, known as k-fold, is employed to divide the training set into k assigned small sets, and a model is trained with (k-1) sets. One set is reserved to measure and evaluate the performance of the trained model. Above process is repeated k number of times such that all sets have been utilized as both training and test set. Schematic of CV process is shown in Figure 6.2. Clearly, this approach can be computationally expensive, but the prediction error can be significantly minimized [175]. Details for ML related errors are elaborated in section 6.5.

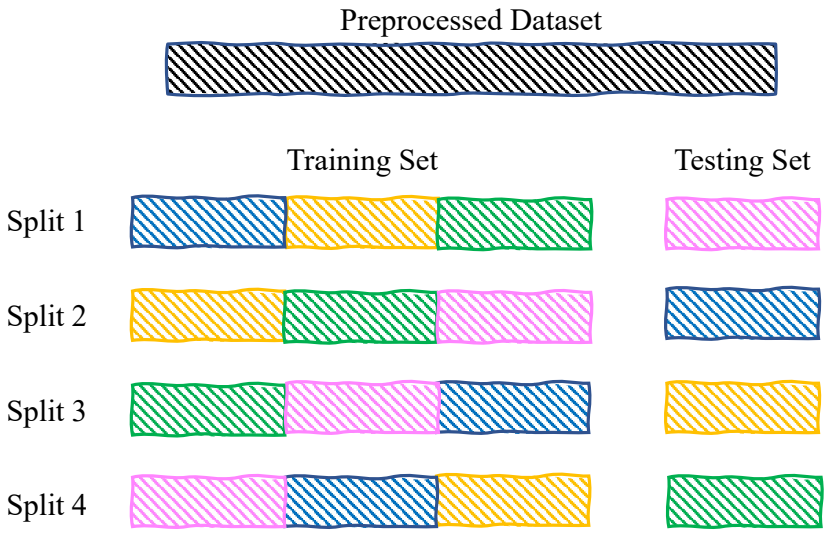


Figure 6.2: k-fold ($k = 4$ in this example) cross validation process.

6.3 Machine Learning Algorithms

There are many well-established open-source ML libraries that supports a variety of applications, such as Scikit-Learn [175], TensorFlow [176], LightGBM [177], and SuperLearner [178], and they have been widely used in ML-related studies. Algorithm selection is an essential step in understanding hidden patterns in the data, and each algorithm produces vastly different prediction as mathematical formulations are different in each algorithm and the hyperparameters, will be discussed later, provided can also change the outcomes. Algorithms conducted in this study are well understood ones with moderate sample size requirement.

In this research, Scikit-Learn, a Python-based package integrating a wide range of machine learning algorithms for medium-scale supervised and unsupervised problems, is adopted as one of the ML platforms for preliminary investigations in IC engine simulations. Algorithms, i.e., Linear Regression (LR), K-nearest Neighbors (KNN) Regression, Random Forest (RF) Regression, and Support Vector Regression (SVR), are imported from Scikit-Learn package. Light Gradient Boosting Machine, a.k.a. LightGBM, is a decision tree-based learning package. It emphasizes the gradient boosting framework for faster training speed and higher efficiency, but lower memory usage. LightGBM is adopted as the gradient boosting libraries for the purpose of yielding an extraordinarily powerful ensemble of trees learnings. The last algorithm tested in this study is the Artificial Neural Network (ANN), and TensorFlow which is a ML platform specialized on training and inference neural networks is used for this purpose. Different supervised ML algorithms will be tested for accuracy and robustness for given IC engine problems.

6.3.1 Linear Regression

Linear regression, a simplest regression technique, is a model that assumes a linear relationship between the n input variables ($\boldsymbol{x_i}$) and the output variables ($\boldsymbol{y_i}$). The representation of such relationship is a linear equation $f(\boldsymbol{x}) = b + \boldsymbol{w}^T\boldsymbol{x}$, and weight variables, known as coefficient w_i, are assigned to the features. An additional coefficient b, called the intercept or the bias coefficient, is also added to provide the regression line an additional degree of freedom. This regression line is called hyperplane. The constraint for estimating the intercept and slope is to minimize the squared distance (hence the "least squares") that is determined by minimizing the residual sum of squares between the observations themselves and the predicted values (see Eq. (6.2)), and this method is called the Least Square Estimation Method. The coefficient w_i that gives the minimum sum of the squared differences can be found by taking the derivative of Eq. (6.2) and then setting it to zero.

$$residuals = \frac{1}{n}\sum_{i}^{n}(f(x_i) - y_i)^2 \tag{6.2}$$

When applying linear regression to the dataset, a few cautions need to be noted. The dataset to be trained by linear regression must be continuous variables. Relations between independent and dependent variables should be linear and the dependent variable is distributed normally at each value of independent. It may require additional tests for normality of dataset, for example Kolmogorov-Smirnov test and Shapiro-Wilk test. Linear regression requires that there is no or little multicollinearity among the independent variables.

6.3.2 Support Vector Regression

Support Vector Regression (SVR) [179] is an advanced regression technique and works on similar principles as Support Vector Machine (SVM) for classification problem. Unlike linear regression, SVR can manage both discrete and continuous dataset. For a regression problem, a hyperplane $f(x)$ with two boundaries $f(x) \pm \varepsilon$ are defined in SVR such that there exist maximum number of data points closest to the hyperplane and within that boundary lines, see Figure 6.3. The decision boundary is fully specified by a small subset of training samples, called support vectors.

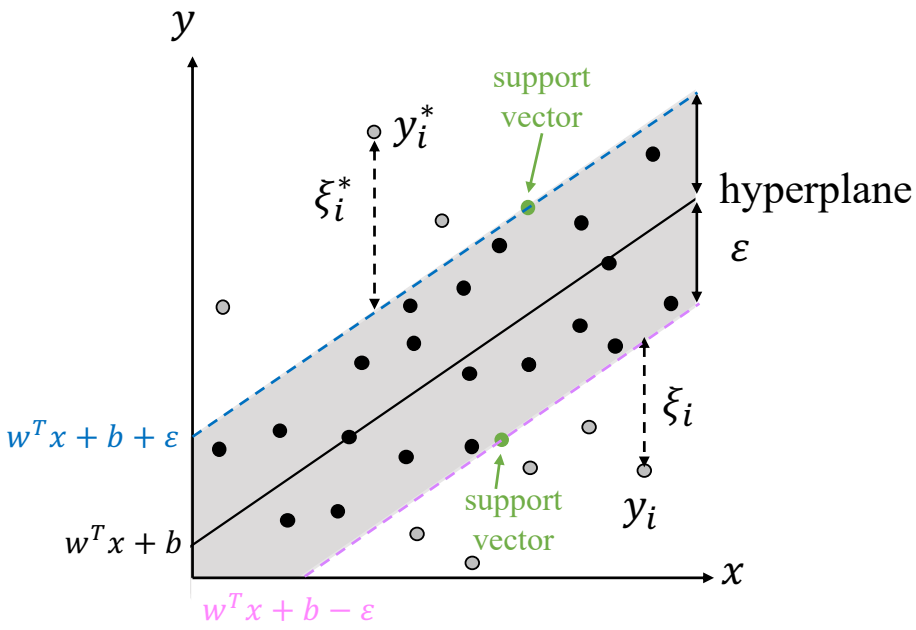


Figure 6.3: SVM for a simple 2D regression problem.

Therefore, SVR problems become a convex optimization problem with an object function in Eq. (6.3) and subjected to the following constrains in Eq. (6.4) [179]:

$$\min_{\boldsymbol{w}\in\mathbb{R}^d} \|\boldsymbol{w}\|^2 \; + C \sum_{i}^{n} (\xi_i^* + \xi_i) \tag{6.3}$$

$$\begin{cases} y_i - w^T x - b \le \varepsilon + \xi_i^* \\ w^T x + b - y_i \le \varepsilon + \xi_i \end{cases}, \qquad \xi_i^*, \xi_i > 0, i = 1, \dots, n \tag{6.4}$$

Slack variable ξ is introduced for the purpose of soft margin to measure the error that occurs when the training data on the wrong side of the marginal hyperplanes, and a constant C, a positive numeric value, controls the penalty imposed on observations that lie outside the boundaries and helps to prevent overfitting. A Lagrangian function is constructed from (6.3) to obtain a linear combination of the training variables in terms of Lagrange multipliers, $w = \sum(\alpha_i - \alpha_i^*)x_i$, and the interception b is evaluated from Karush–Kuhn–Tucker (KKT) conditions [180, 181]. So far, analysis is based on the linear assumptions, regression problems in reality always become complex and cannot adequately be described using a linear model. A nonlinear kernel function, extended from the previously described Lagrangian formulation, is used to map solution from low-dimensional to a high-dimensional space. More details on the theory and mathematical formulation can be found in previous works [182, 183]. Therefore, the generalized hyperplane $f(x)$ yields:

$$f(x) = \sum_{i}^{n} (\alpha_i - \alpha_i^*) G\langle x_i, x\rangle + b \tag{6.5}$$

The accuracy of SVR algorithm depends on a good setting of hyperparameters, such as the regularization parameter C mentioned in Eq. (6.3), ε in Eq.(6.4) for the loss function that associated with points predicted within a distance (ε) from the actual value in the training process, and the kernel parameters (type of kernel functions and coefficient). Kernel functions in SVR enable the use of linear regression techniques to produce a regression that has non-linear characteristics, and effectively deal the high-dimensional dataset. Kernel acts in the way that taking data as input and transforming it into the required form, such that the new boundary in the transformed space is linear. In this study, two types of kernels are tested: linear kernel and Radial Basis Function (RBF) kernel based on the anticipation of the dataset. The optimal kernel function will be selected according to the hyperparameter optimization results. RBF is the commonly used

nonlinear SVR kernel to gain linearly separation by mapping the data to a higher dimensional space, and the corresponding formula for RBF mapping is given in Eq. (6.6). γ is related to the variance σ^2 and will be specified in the hyperparameter tunning process.

$$K(\boldsymbol{x_i}, \boldsymbol{x_j}) = \exp\left(-\gamma \left\| \boldsymbol{x_i} - \boldsymbol{x_j} \right\|^2\right), \qquad \gamma = \frac{1}{2\sigma^2} \tag{6.6}$$

Compared to other ML methods, SVR is less sensitive to the outliers in data, and thus can be a good choice when the variance is high and superior when the data pattern is complex. However, it is not suitable for large data sets due to the higher processing time to train a model.

6.3.3 K-Nearest Neighbors

The third regression algorithm adopted in this study is neighbors-based learnings. Though this type of algorithm was originally derived for classification problems [184] to label new data points based on their position to nearby data points, many studies have been successfully applied neighbors-based learning for regression problems in different disciplines [185-187]. Among all neighbors-based learnings, K-nearest neighbors (KNN) algorithm is an, generally, accurate and simple technique that stores all existing cases and predicts the numerical target based on a similarity measure, e.g., distance functions.

The scatterplot in Figure 6.4 illustrates the KNN approach in regression to make predictions. The first step for KNN is to set number of k to determine how many points needed to assess the new data point. As indicated in Figure 6.4, k equals 3, and it means that the three nearest data points or neighbors are used for the analysis. There are several distance functions used to identify these neighbors, e.g., Euclidean and Manhattan, and in this study the Euclidean formulation is employed as shown in Eq. (6.7),

$$\varepsilon(x_i, x_m) = \sqrt{\sum_{m=1}^{k} (x_i - x_m)^2} \tag{6.7}$$

Given a value for k and a prediction point x_i, KNN algorithm first identifies the k training observations (N_o) that are closest to x_i, marking with black dots with pink filling. Then the estimation for continuous target $y_i(x_i)$ is evaluated by taking the contributions of these k values. When computing the contributions of these k neighbors, each data point can have equal/different contributions. In Scikit Learn package, there are two weighting methods: uniform and inverse distance weighting. With uniform weighting, all k values have equal influence, and the simple average of the labels are computed sequentially as the prediction. With inverse distance weighting, the higher weights, based on the inverse of its distance from the new data point, are assigned to the closer training points. Then the weighted average of the training labels is calculated.

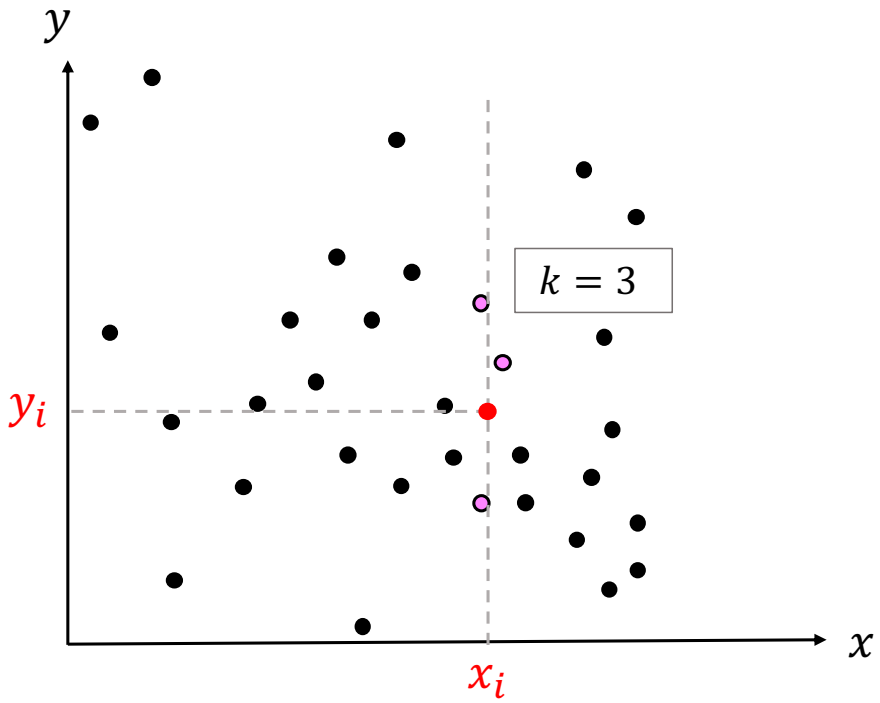


Figure 6.4: KNN learning for $k = 3$. Scatter plot of x versus y with predicted y_i for an arbitrary value of x_i based on 3 nearest neighbors. The prediction is represented as a red dot, and 3 nearest neighbors are black dots with pink filling.

When there is little a priori knowledge about the shape of the true regression function of the dataset, KNN is a decent choice since it is considered as non-parametric method, approximating the connection between independent variables and the outcome by averaging the observations in the same neighborhood. However, the selection for value of k can be crucial in determining the results for KNN method and requires hyperparameter tuning to obtain its value. The tuning process for k is relatively simple, and it is discussed in this section rather in a separated section for hyperparameter optimization (see Section 6.6). To get the optimal value for k to avoid under/over-fitting, the elbow plot is generated to help the selection of k. In Figure 6.5, the Root Mean Square Errors (RMSEs) in KNN models with different k values are plotted for different targets. The best value of k is 5 for NOx emissions datasets and 4 for IMEP results as the RMSEs reach the minimum at these k values.

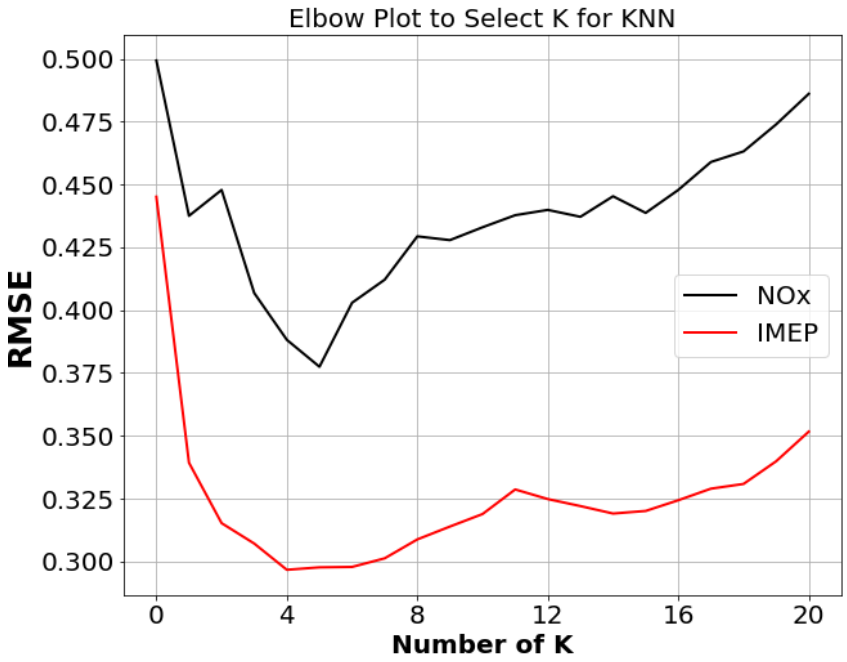


Figure 6.5: Selection of k using elbow method. For demonstration purpose, two targets (NOx and IMEP) from double-injection scheme are plotted. The optimal values of k are 5 for NOx and 4 for IMEP.

Despite many strengths of using KNN, some drawbacks need to be aware when choosing KNN as ML algorithm. When the dataset is large, KNN is not recommended as heavy calculations for distance functions of new and existing data points could result in the demand of large computational resources. Besides, there is a high risk of curse of dimensionality associated with KNN if the dimension of dataset is high [188].

6.3.4 Tree-Based Algorithms

Random Forest [189] is an ensemble of supervised learning technique, namely decision tree, and is applicable for both regression and classification problems. Decision trees analyze data by performing a recursive binary partitioning of the feature space and selecting the best split from a set of possible splits at which the maximum information gain (Δ) is yielded. Split θ at node m partition sample of N_m in two subsets, $S_L(\theta)$ and $S_R(\theta)$, by a threshold t_m. Information gain can be represented with the impurity criterion entropy H, a measure of the homogeneity of the labels. In regression problems information gain is:

$$\Delta(\mathrm{S}, \theta) = H(S) - [f_L H(S_L) + f_R H(S_R)] \tag{6.8}$$

$$S_L = (\boldsymbol{x}, y) \,|(\, x_i < t_m) \qquad S_R = S_L^c = Q \backslash S_L$$

$$f_L = \frac{N_L}{N_m} \qquad f_R = 1 - f_L \qquad H_k = \frac{1}{N_k} \sum_i^{N_k} (y_i - \mu_k)^2$$

At node m, solving the best split θ^* is equivalent to

$$\theta^* = min(f_L H(S_L) + f_R H(S_R)) \tag{6.9}$$

Compared to other algorithms, preprocessing data is less demand for decision tree. However, ML models trained with decision tree algorithm are unstable and susceptible to the input dataset. To address these weaknesses, bootstrap aggregating technique, also called bagging, is adopted to reduce the variance of prediction while retaining low bias. In random forest algorithm,

referring to Figure 6.6, each individual decision tree runs independently and draws random samples from dataset with replacement (bootstrapping). Predictions collected from individual decision tree undergo aggregation for the final prediction, circumventing the problem of overfitting and making more accurate predictions than any individual model.

The third tree-based algorithm applied in this study is in the category of boosting. Like random forest machine learning, Gradient-Boosted Decision Trees (GBDT) is a set of decision trees, but there are some distinguished differences between these two algorithms. In boosting algorithm, only one single tree is built at a time. It randomly draws a subset of dataset without the replacement. The subsequent subset in the second tree is taken in the manner of mixing the unplaced dataset in and mistakes from the previous tree. Therefore, gradient boosting method is a stage-wise additive model that combines "weak" learner into one "strong" model [177] and minimizes the loss function of the model by adding weak learners using gradient descent. The final prediction is then obtained from the average of all weak learners.

Compared to random forest, boosting can result in better performance as it can mitigate the issue of overfitting with fewer trees. However, boosting can be time-consuming because trees in boosting algorithms are trained sequentially and tend to be harder to tune than random forests. Hence, in this study the package LightGBM is implemented for boosting. The tree growth strategy is in the leaf-wise pattern (refer Figure 6.7), and the splitting rule is known as the histogram-based algorithms [190, 191]. The continuous feature values are bucketed into discrete bins which fasten the training procedure and reduce memory usage. The summarized comparisons for different tree-based algorithms are given in Table 6.1.

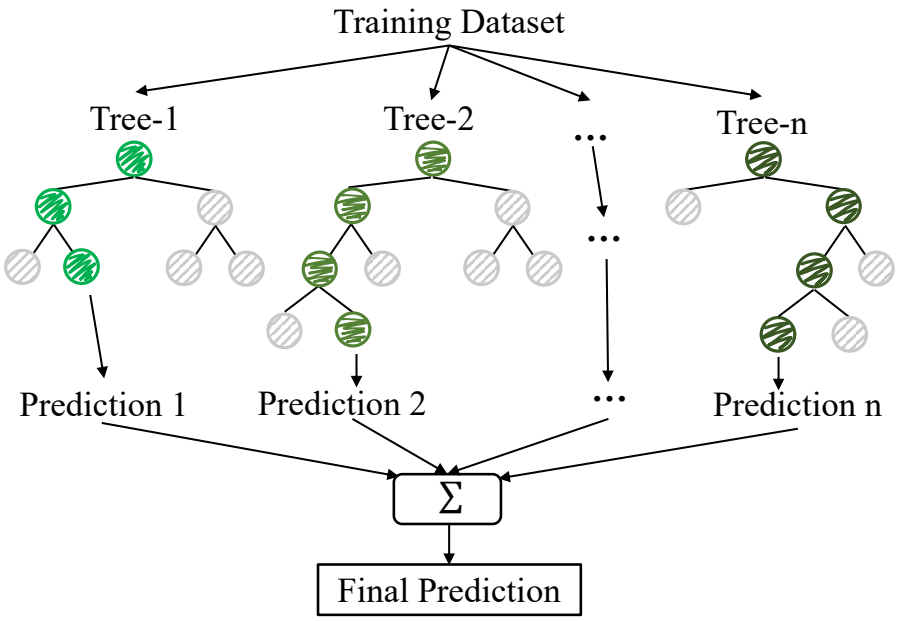


Figure 6.6: Random Forest Regression structure.

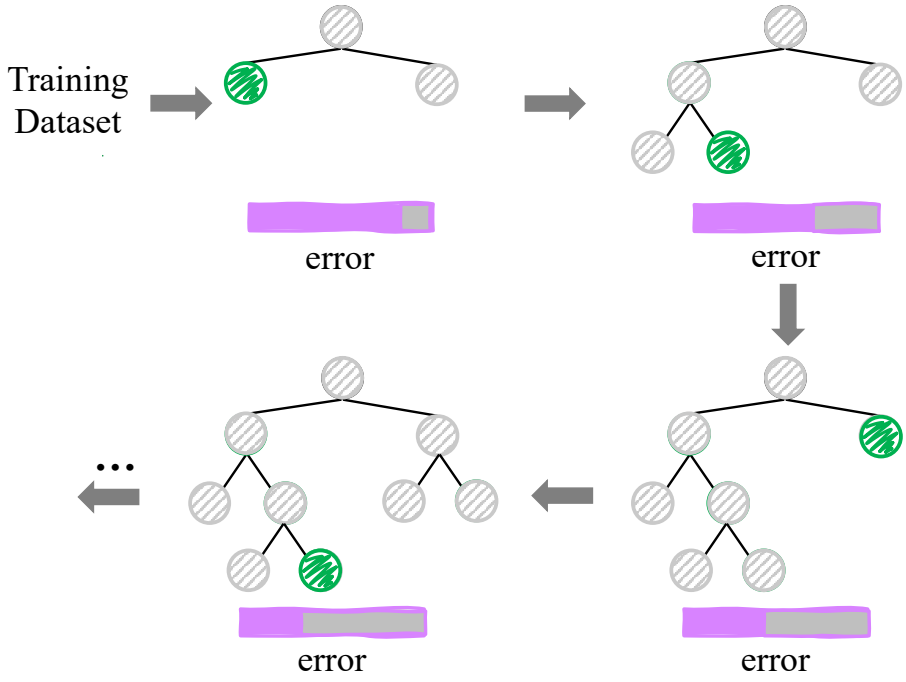


Figure 6.7: Gradient Boosted Decision Tree in leaf-wise pattern [177].

Table 6.1: Comparisons for tree-based ML algorithms.

	Decision Tree	**Bagging**	**Random Forest**	**Boosting**
# of trees	Single	Multiple	Multiple	Multiple
Dataset	Entire data	Random subset of data for each tree	Random subset of data for each tree	Subsets of the original data, grow sequentially
Dimensions for picking splitting rule	All dimensions considered at each node	All dimensions considered at each node	Random subset of dimensions considered at each node	All dimensions considered at each node
Output	Decision of tree	Average of the predictions produced by the trees in the forest.	Average of the predictions produced by the trees in the forest.	Weight predictions produced by the trees

**For Boosting, the selection of subsets is not random and depends upon the performance of the previous models*

6.3.5 Artificial Neural Network

Artificial neural network (ANN), also known as neural network [192], is inspired by biological neural network that constitutes animal brain and designed to learn and perform a variety of task generally without being programmed with any task-specific rules. An advanced library, TensorFlow, that constructs and focuses on training and inference on neural networks is used. The implementation of TensorFlow also provides the possibilities of utilizing GPU for workload and improving the computational performance effectively.

In Figure 6.8, a neural network is built with numbers of neurons or perceptron. Like nodes in decision trees, each neuron can make simple decisions and feeds those decisions to other neurons from next layer. The connection between neurons in adjacent layers (black arrow) has particular weight to measure the impact of the neuron has on the neuron from the next layer. Neurons are organized in the form of layers, and there are three kinds of layers in an ANNs: 1) input layer loads features from dataset for the network; 2) hidden layers apply functions from previous layers and

transform processed information to next layers; 3) output layer produces predictions. Messages in the presented ANN flow in one direction through multiple hidden layers, and such ANN is called the multilayer feedforward network.

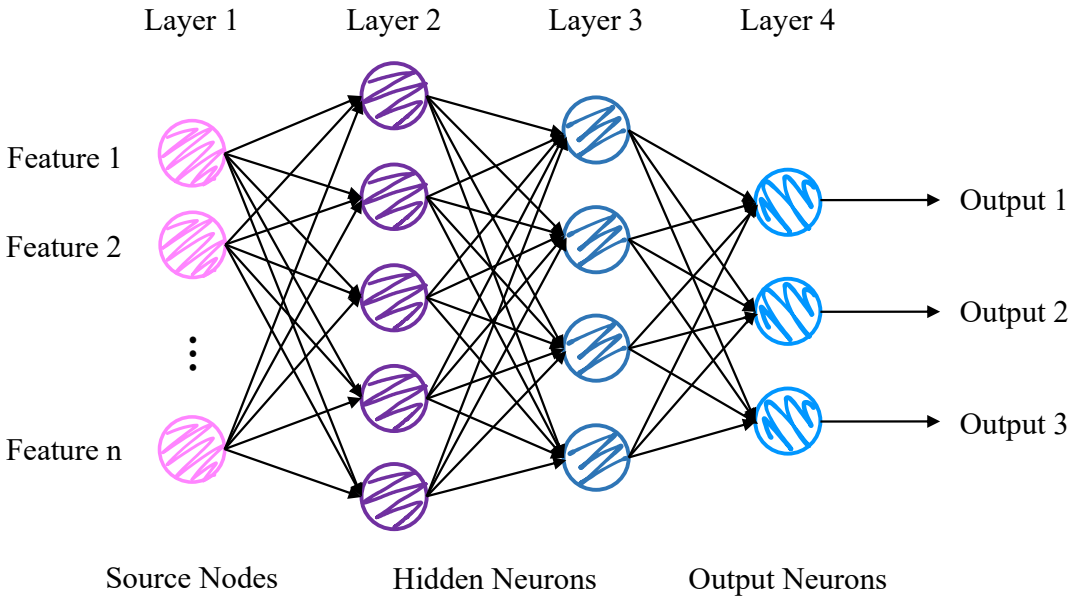


Figure 6.8: ANN with three layers of neurons.

In a neural network, inputs are fed into the neurons in the network, and the algorithm learns a function $f(\boldsymbol{x})$ to predict output $\mathcal{R}^o$ from input features $\mathcal{R}^i$. Each neuron has a weight, and the inputs are multiplied by the weight and fed into the activation function $\mathcal{S}$ which defines if given neuron should be "activated" or not. Most widely used activation functions are sigmoid function (Eq. (6.10)) and ReLU (Eq. (6.13)), and two non-linear functions enable flexibility to absorb small changes in edge weights without triggering inverse results.

$$\text{Sigmoid: } \sigma(z) = \left(1 + e^{-f_w(\boldsymbol{x})}\right)^{-1} \tag{6.10}$$

$$\text{ReLU: } R(x) = \max\left(0, f_{\boldsymbol{w}}(\boldsymbol{x})\right) \tag{6.11}$$

The activation function has a significant impact on the learning speed. If a neuron is activated, a bias value, b, is added to the result thus shifts the activation function and enables better

fit for the data. Figure 6.9 shows a portion of learning procedure for a neural network, and $f_w(\boldsymbol{x})$ is defined in the following equation.

$$f_w(\boldsymbol{x_j}) = \boldsymbol{w}'\, \mathcal{S}\left(\boldsymbol{w}^T \boldsymbol{x}_j + b\right) + b' \tag{6.12}$$

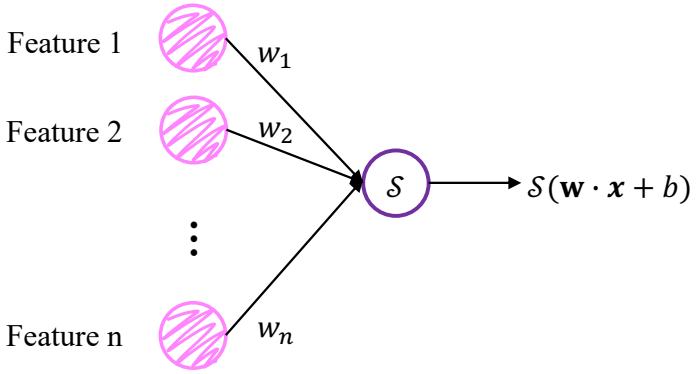


Figure 6.9: ANN learning algorithm with an activation function.

In the training process, the weights are updated using Eq. (6.13) by gradient descent, and α is the learning rate which controls the step-size in the parameter space search. It should be noted that gradients are computed in the direction from output to input layers and combined using chain rule (backpropagation), providing each weight parameter with an updated value meants to decrease the loss. The loss function is expressed in Eq. (6.14), and N is the number of samples. The training of a network is to find network weights to minimize the error between true and estimated labels. Similar procedures are used to update the bias value, b, in ANN. Detailed derivations can be referred to previous works [175, 192].

$$\boldsymbol{w} \leftarrow \boldsymbol{w} - \alpha \frac{\partial E}{\partial \boldsymbol{w}} \tag{6.13}$$

$$E(\boldsymbol{w}) = \frac{1}{N} \sum_{j=1}^{N} \left(y_j - f_w(\boldsymbol{x}_j)\right)^2 \tag{6.14}$$

Neural Networks derive features of the dataset automatically as a constrained optimization problem. It is, therefore, an ideal option to interpret complex and large datasets with no time or

computational constraints. ANN can properly deal with outliers and incomplete information in the dataset. However, unlike other graphic models or decision trees that can be explicitly described with domain knowledge, ANN is less interpretable as tracking the decision-making process at each node and explaining how the solution is arrived at are limited. The major downside of ANN is such black-box dilemma.

6.4 General Procedures for ML-GA Modeling

The trained ML models are coupled with GA for faster but reliable design process for ICEs. The flow chart in Figure 6.10 displays the general procedures for ML-GA. In this approach, first the training data is produced by running a limited number of CFD simulations to sample the design space. Note that all these CFD simulations can be independent of each other, as the optimization process is not iteratively running via CFD. Therefore, all these CFD simulations can be performed at the same time. In this study, the training data can be directly obtained from the CFD simulations completed in Chapter 5, and thus two datasets are available, double-injection and triple-injection schemes, for CI engine designs fueling with ethanol.

Raw data collected from experiments or obtained from theoretical analysis needs upfront clean and manipulation before feeding it to ML algorithms to make the raw data more applicable and structured (refer to section 6.2 Data Preparation). The size of raw data for each injection scheme is 1800. Number of features for double- and triple-injection schemes are 4 and 6, respectively. There are 5 targets (4 emissions + 1 performance) from CFD calculations for each dataset. Once the data is ready and fed into the algorithm, 5 tentative, data-driven models can be created after training the ML algorithm selected for each target.

When building machine learning models, a challenging task is to keep error as low as possible and to design a generalized model that can accurately predict unseen data points. There are two major sources of error: bias and variance [193]. Errors appear when using a ML model to run assessment on both training and testing datasets. It is desired to lower errors, thus both bias and variance need to be kept at their minimum. However, that is quite impossible, and there is a trade-off relationship between bias and variance. Hence, the learning curve is introduced next to characterize the ML model. If a ML model spits out poor results using k-fold cross-validation, the modifications or tuning for hyperparameters of the model may be needed to ensure the ML model can fit both training and testing data sufficiently. Elaborations on bias and variance trade-off will be provided in the next section. Until the reliable prediction can be made with ML models, the next step of ML-GA methodology proceeds.

Though it is plausible to build a ML model that can directly predict the merit value from features, i.e., to construct a stand-alone ML model. The better approach for the scenarios in this study is to separately train and tune the ML models for each target as base models, and then construct an ensemble ML model using base models in the effort of increasing the robustness and performance. This step is called stacked generalization [194, 195]. The stacking of base models can be accomplished using simple linear combinations. Predictions from base models are concatenated to form a vector that is afterward fed to the ensemble ML model as input. Therefore, this generalized ML model is fitted on the out-of-fold predictions. The output of the ensemble ML model is the merit value after considering the individual output which constitutes the merit function. Subsequently, a stochastic global optimization GA is used with the ensemble ML model as an objective function to perform optimization of the merit value.

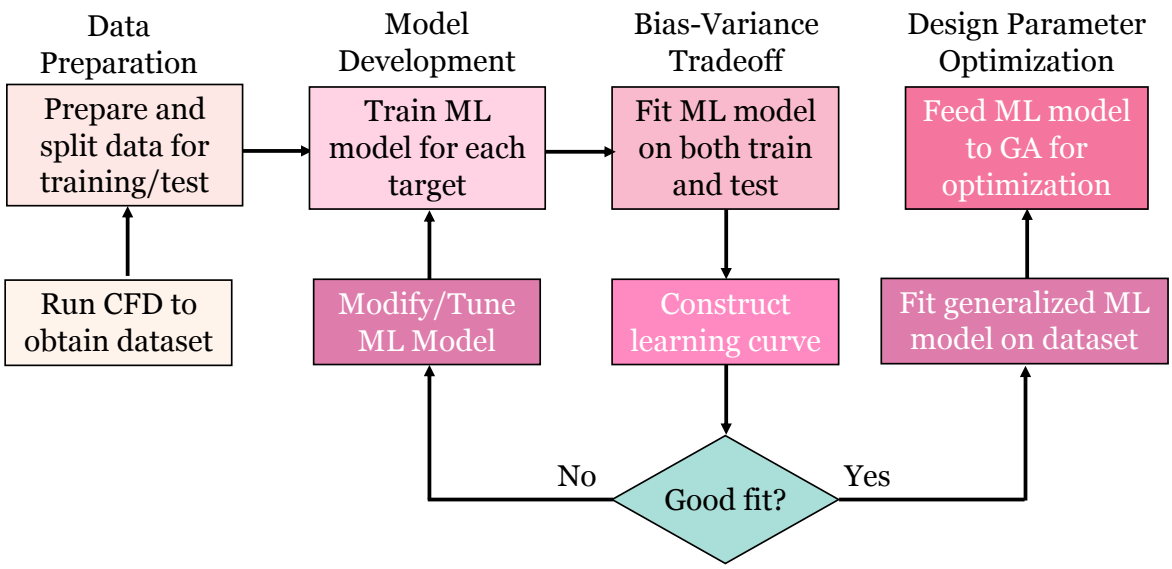


Figure 6.10: Flow chart of the general procedure for ML-GA process. The dataset used in the generalized ML model is out-of-fold predictions from the base models.

6.5 Bias and Variance Trade-offs

Evaluating results from ML models is essential to produce better predictions. Three scenarios, generally, can be used to describe the outcome of a ML model: underfitting, overfitting and optimal balance. Bias and variance are two types of errors associated with model performance. Bias specifies the disagreement between the predicted value from a ML model and the true value in the dataset. High bias indicates that the predictions and actual values are greatly discrepant. Variance, on the other hand, measures the variability of model prediction for a given data point in relation to each other.

Underfitting occurs when a ML model cannot capture the underlying pattern in the data. Overly simple models or insufficient sample size could lead to this issue. If the training and testing sets are not randomly drawn from the dataset, it could also be the cause of underfitting as the ML model is unable to learn all possible combinations through the training process. Prediction errors that exist in underfitting ML models are primarily caused by the high bias and low variance. To

remedy underfitting, it is desirable to make the model complex so that it captures all the important interactions in the input-output space. In this work, hyperparameters optimization is applied to increase the model complexity and thus avoid underfitting.

However, if a ML model is excessively complex and unable to generalize the data adequately, it can exhibit large changes in output predictions as the inputs change. High variance would lead to overfitting issue. Bagging or boosting algorithms, known as the ensemble method, are good examples of remedying the overfitting issue for single decision tree. Cross-validation can help to reduce the variance as well, and it allows all data to be eventually used during the training process. Choosing right amount of sample size can mitigate both underfitting and overfitting issues as there exists an optimal balance of bias and variance when changing the sample sizes.

To understand and assess the model behaviors, the bias-variance trade-offs via learning curves are conducted. For each learning curve, the total dataset size is increased from a minimum sample size to maximum of 80% of the total CFD samples, increasing at 100 samples for every dataset. In each dataset, 80% of the data is randomly sampled to generate a training set and the remaining 20% of the data is used as the test set. A ML model with default hyperparameters is then trained on each of the outputs using 10-fold cross-validation. Next, for each output prediction, the trained models are tested on both the training and testing datasets to generate learning curves and mean squared errors (MSEs) are calculated at each of these training stages.

Figure 6.11 displays examples of three learning curves with the default tree-based model from triple-injection scheme. High bias can be observed when the sample size is small (< 400). For CO and IMEP cases, the prediction errors are both relatively high, thus variances between the training score and testing score are relatively low. Poor results are produced by ML models because of the underfitting. As moving toward to the larger sample size, bias starts to drop in most cases.

Oppositely, variance increases as the prediction error declines in training set but grows in testing set, leading to overfitting. It is possible to find the optimal number of samples to minimize the total prediction errors. For example, in the CO case the optimal balance of prediction error between training and testing sets occurs when sample size is 400 using default tree-based algorithm, illustrating that the ML would never be underfitted or overfitted at this point. Whereas the optimal sample size can be identified so far, the overall MSEs are still high. Future tuning on hyperparameters is needed to reduce the overall prediction errors.

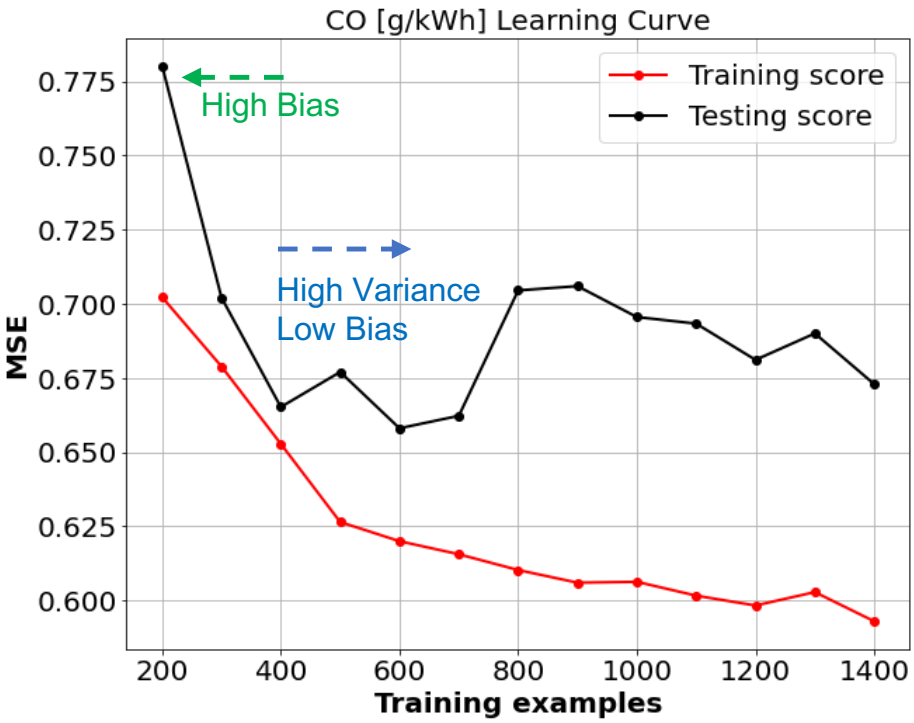


Figure 6.11: Learning curves of different outputs (triple-injection scheme) with default hyperparameters for tree-based algorithm.

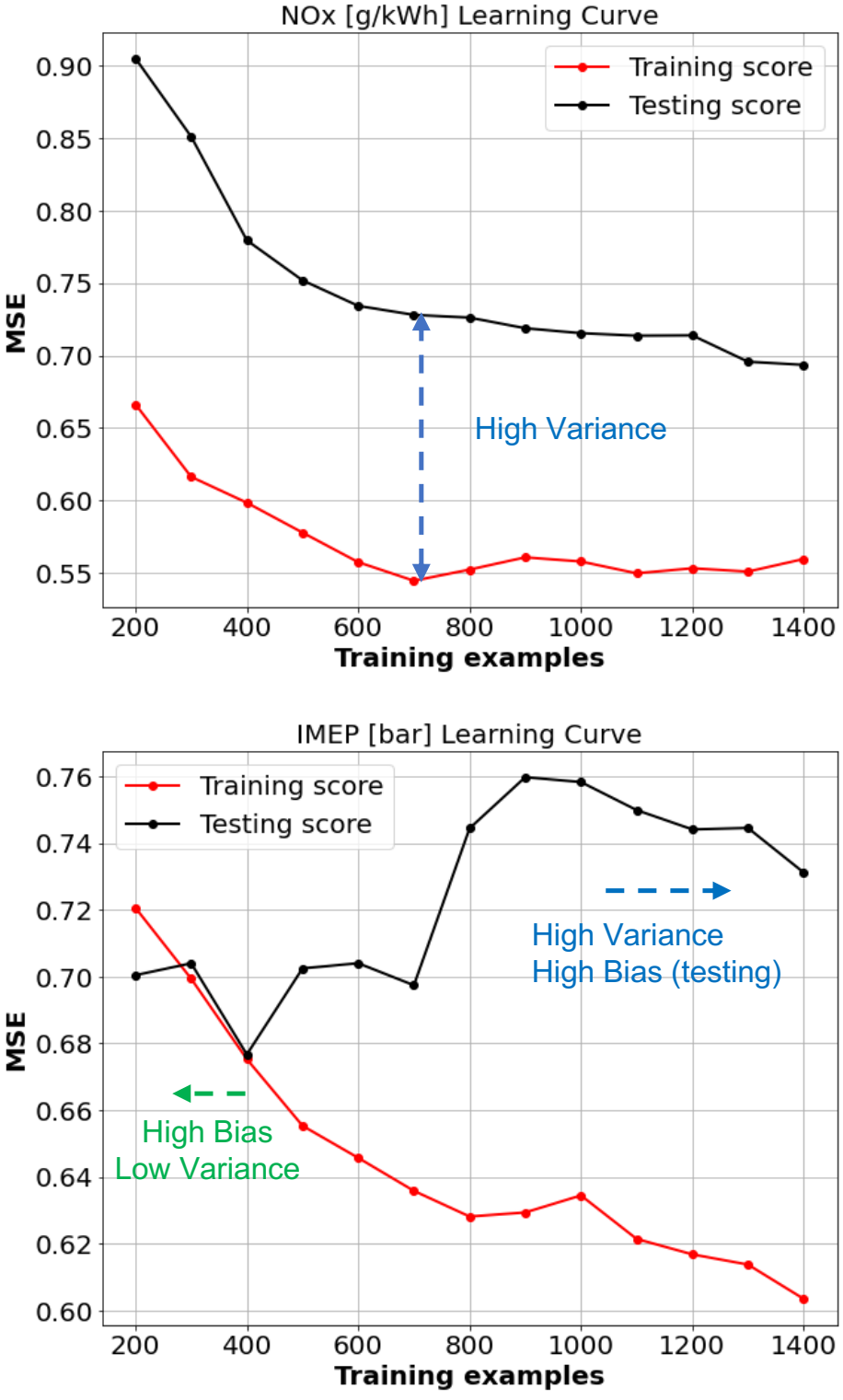


Figure 6.11 (Continued).

6.6 Hyperparameters Optimization

Hyperparameters are external parameters of a ML model that is set before the learning process begins to configure the model. Parameters, for example the margin ε or types of kernel functions used in SVR, number of trees in random forest, and number of hidden layers in ANN, can be tuned thus help the model to achieve maximal performance. Tuning hyperparameters is a trial-and-error based, time-consuming process, and many different combinations need to be tested to find the optimal model settings. In this work, hyperparameter optimization strategy is applied to boost ML model performance. Also, potentials to accelerate the tuning process will be investigated.

Tuning the hyperparameters to achieve the best performance of ML models is an optimization problem with an unknown target function, and it has been reported that Bayesian optimization (BayeOpt) is a superior technique to solve such expensive, black-box problems [196-198]. In this work, an open-source python library, HyperOpt [199], that based on a Bayesian optimization and supported by the SMBO (Sequential Model-Based Global Optimization) methodology is used. SMBO is an automated approach for algorithm configuration with abilities to evaluate performance of observed parameter settings and to hypothesize unseen regions of parameter space [200].

In BayeOpt, the objective function (f) is evaluated in a derivative-free, probabilistic model, and most popular surrogate model used for approximating the objective function is Gaussian process (GP). If given gaussian random variables $\boldsymbol{X} \sim N(\mu, \Sigma), X \in \mathbb{R}^d$, where μ is the mean and Σ is the covariance matrix. For observations $D = (\boldsymbol{X}, f)$, GP can be expressed as:

$$p(f|D) = \mathcal{GP}(f; \mu_{f|D}, \Sigma_{f|D}) \propto P(D|f)P(f) \tag{6.15}$$

In Eq. (6.15), $P(D|f)$ is the likelihood function and $P(f)$ is the prior. The initial value of prior is randomly assumed, and the likelihood can be characterized by μ and Σ and computed from the normal density function. The determination of covariance functions and associated kernels can be found in literatures [201, 202]. Such statistical model provides a posterior probability distribution that describes potential values for f at a candidate point $P(score|configuration)$ which is updated through an iterative process of querying a history "H" of (score, configuration) whose objective is the maximization of the score given a configuration "c" [199].

In t iteration, the surrogate model is fitted to all observations of the target function made so far. Then the acquisition function (a), which uses the predictive distribution of the probabilistic model, determines the utility of different candidate points, trading off exploration where the objective function is very uncertain and exploitation where the objective function is expected to be high. There are different approaches to interpret acquisition functions in the framework of BayeOpt, for example, probability of improvement (PI), expected improvement (EI), entropy search or upper confidence bound (UCB) [201]. The goal at this step is to maximize the acquisition function for selecting the location $(\boldsymbol{x}_{t+1})$ of the next observation, and optimization follows the principle of maximum expected utility [202].

$$\boldsymbol{x_{t+1}} \leftarrow argmax_{\boldsymbol{x}} a(\boldsymbol{x}; D_{1:t}) \tag{6.16}$$

Next the objective function is sampled $\boldsymbol{x}_{t+1}$, and the prior distribution in GP with the new data $D_{1:t+1}$ can be updated for $t+1$ to produce a posterior. The BayeOpt terminates after a finite number of iterations.

To compare the time consumption and accuracy, random search [203] is applied as well for function optimization. The implementation of random search is relatively simple than BayeOpt. In random search, the algorithm independently and randomly draws parameters from the prescribed

range of values. There are, generally, no requirements for random search other than that the next values are selected at random. One major drawback of random search for hyperparameter optimization is the accuracy and computational time are highly dependent on the size of the random subsets drawn from the parameter space; the smaller this subset the faster but less accurate the optimization and vice versa. It is also likely that random sampling cannot fully cover parameter space.

In this work, both random search and BayeOpt are operated for each individual target over 50 iterations. The optimal hyperparameters for each target are selected from either random search or BayeOpt, whichever has the highest testing scores. To demonstrate the hyperparameter tuning history, results from BayeOpt and random search over 50 iterations for GBDT in double-injection scheme are provided in Figure 6.12. For listed four targets, the performance of BayeOpt is superior to random search. Higher averaged r^2 scores in 5-fold CVs can be observed in BayeOpt trails for different targets except IMEP. Random search is less time-consuming, and the average time elapsed for each target during the optimization is about 6.5 sec., in GBDT for example, nearly 4 sec. less than that in BayeOpt. Figure 6.13 summarizes the PDF for number of leaves distribution in GBDT algorithm. Dataset used in this figure is form NOx target in double-injection scheme. In BayeOpt, the PDF is almost a normal distribution with a mean value around 240 leaves. Random search has similar results, bimodal distribution as indicated in Figure 6.13, comparing the sampling results, verifying the randomness in random search algorithm. Lists of hyperparameter settings for each target in various ML algorithms are stated from Table 6.2 and Table 6.5. LR is not tested as no hyperparameters need to be tuned for this algorithm.

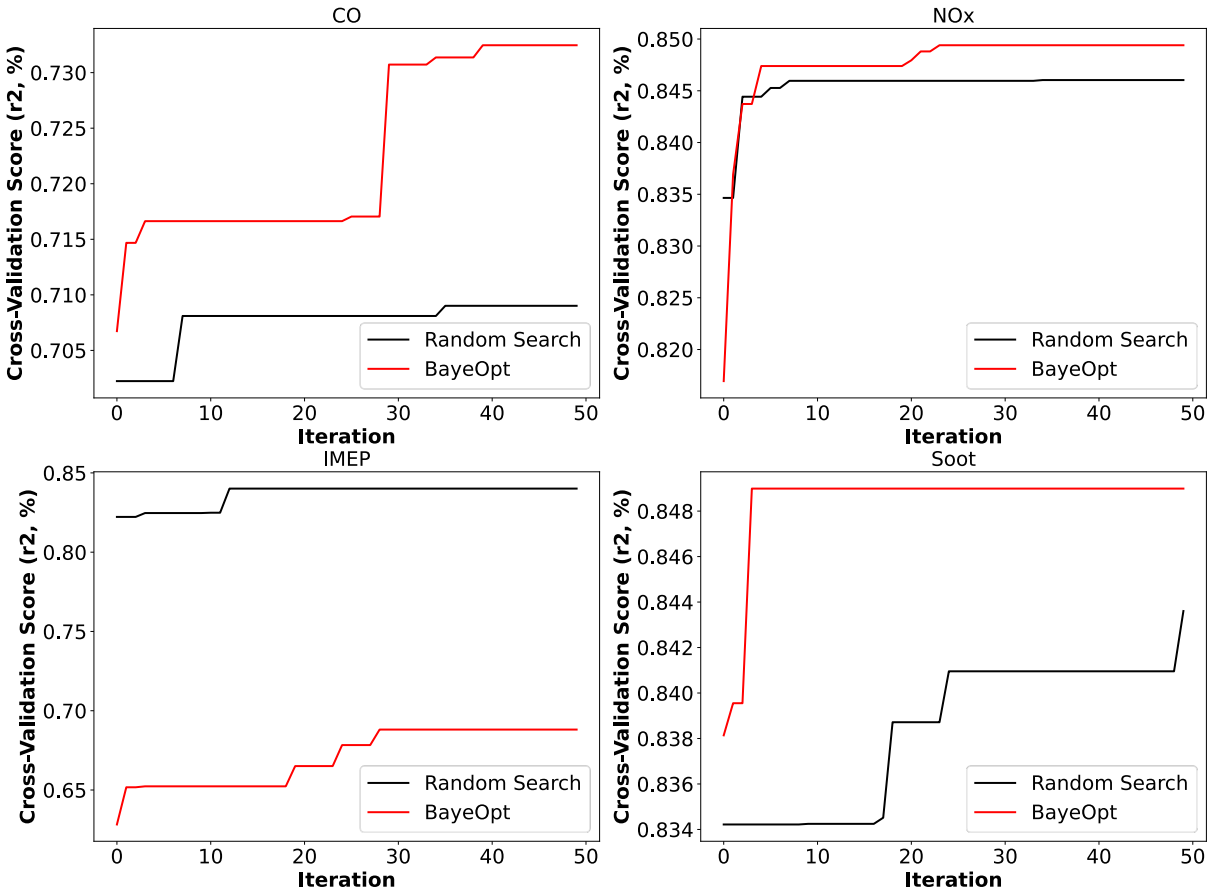


Figure 6.12: Hyperparameter optimization results for GBDT algorithm (double injections).

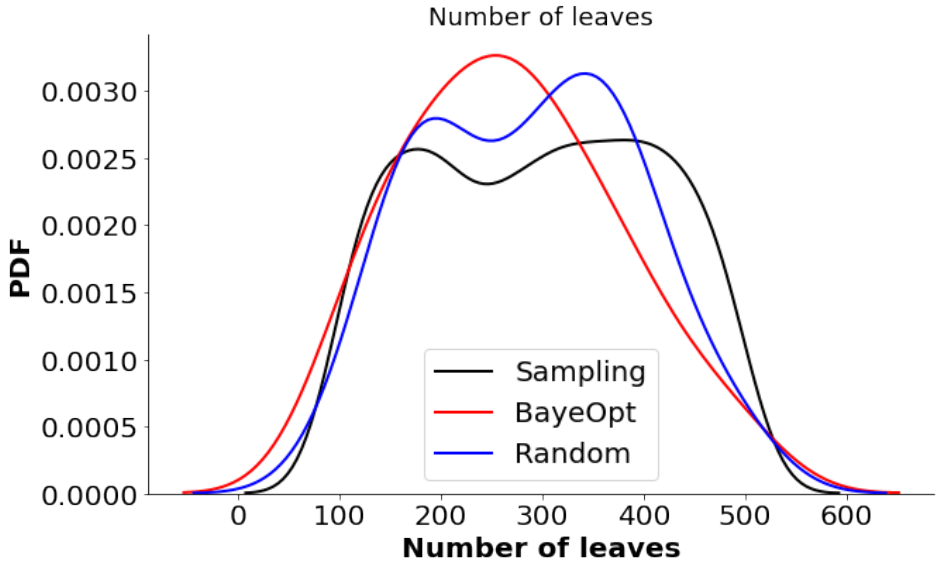


Figure 6.13: Number of leaves distribution for GBDT for NOx (double injections).

Table 6.2: Optimal hyperparameters for GBDT algorithm in double-injection scheme.

Targets	*learning rate*	*max depth*	*estimators*	*leaves*	*colsample bytree*	*L2 regularization*
CO	0.0555	11	545	143	0.9370	0.5031
NOx	0.0398	15	256	238	0.9908	0.3614
UHC	0.0125	13	141	433	0.9481	0.7641
$Soot$	0.0787	8	600	104	0.8759	0.8304
$IMEP$	0.2120	7	637	387	0.7964	0.2265

**Colsample bytree is the fraction of features (randomly selected) that will be used to train each tree.*

Table 6.3: Optimal hyperparameters for ANN algorithm in double-injection scheme.

Targets	*learning rate*	*hidden layers*	*input layer nodes*	*hidden layer nodes*	*activation function*	*batch size*	*adam learning rate decay*
CO	0.00091	4	223	619	ReLU	334	0.00824
NOx	0.00815	3	268	490	ReLU	149	0.00936
UHC	0.00094	4	192	290	ReLU	487	0.00807
$Soot$	0.00578	1	307	452	ReLU	92	0.00274
$IMEP$	0.00032	4	314	800	Sigmoid	291	0.00751

Table 6.4: Optimal hyperparameters for SVM algorithm in double-injection scheme.

Targets	*kernel*	*C*	*gamma*	*epsilon*
CO	RBF	32	1.71633	0.08255
NOx	RBF	21	1.51429	0.02139
UHC	RBF	40	9.59592	0.20488
$Soot$	RBF	40	7.97959	0.40876
$IMEP$	RBF	32	1.71633	0.08255

Table 6.5: Optimal hyperparameters for RF algorithm in double-injection scheme.

Targets	*estimators*	*leaf nodes*	*max depth*
CO	347	379	14
NOx	584	240	10
UHC	706	451	7
$Soot$	283	444	14
$IMEP$	450	180	13

With the optimal hyperparameter settings, learning curves are plotted to visualize the changes in bias-variance trade-off relations after tuning. Figure 6.14 and Figure 6.15 exhibit the improvements of bias-variance trade-off relations for NOx target with tree-based algorithm. Bias has been reduced prominently, and variances between the training and testing scores continuously diminish as increasing the sample size and become stable around 800 samples. Such trends are observed in other tuned ML learning curves, and thus 800 samples are taken from dataset for ML model constructions from this point.

For each target, the scores from tuned ML models are plotted in Figure 6.16 for double-injection scheme and in Figure 6.17 for triple-injection scheme. Based on the histograms, the ML with the best performance is selected for a target. For example, ANN is picked as the ML model to establish the relation between design features and NOx emissions in double-injection scheme.

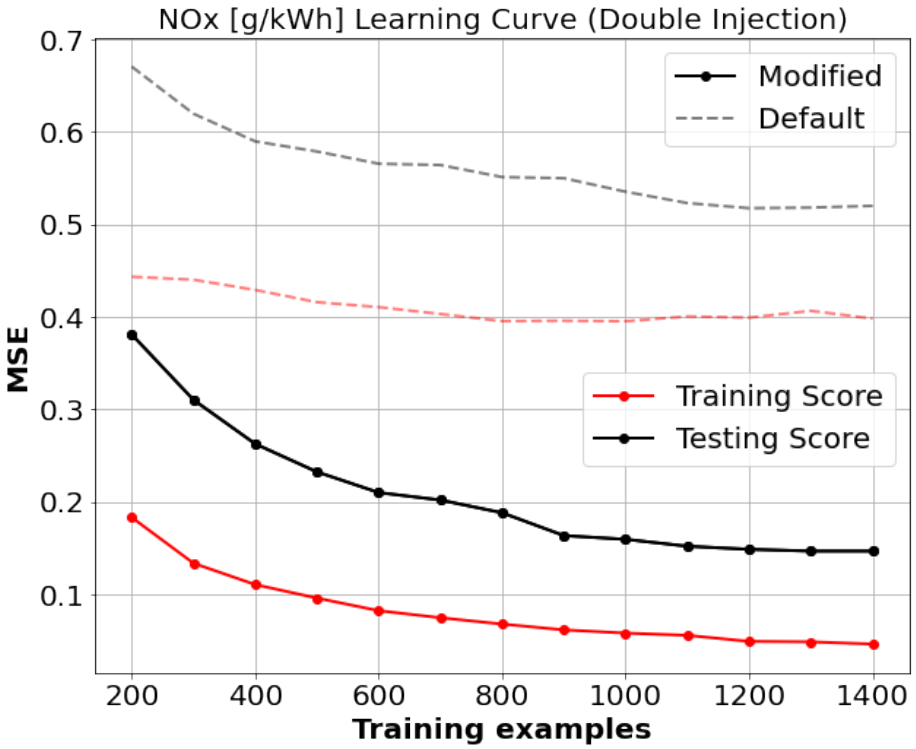


Figure 6.14: Learning curve comparisons between default and tuned tree-based ML algorithm for double injection scheme.

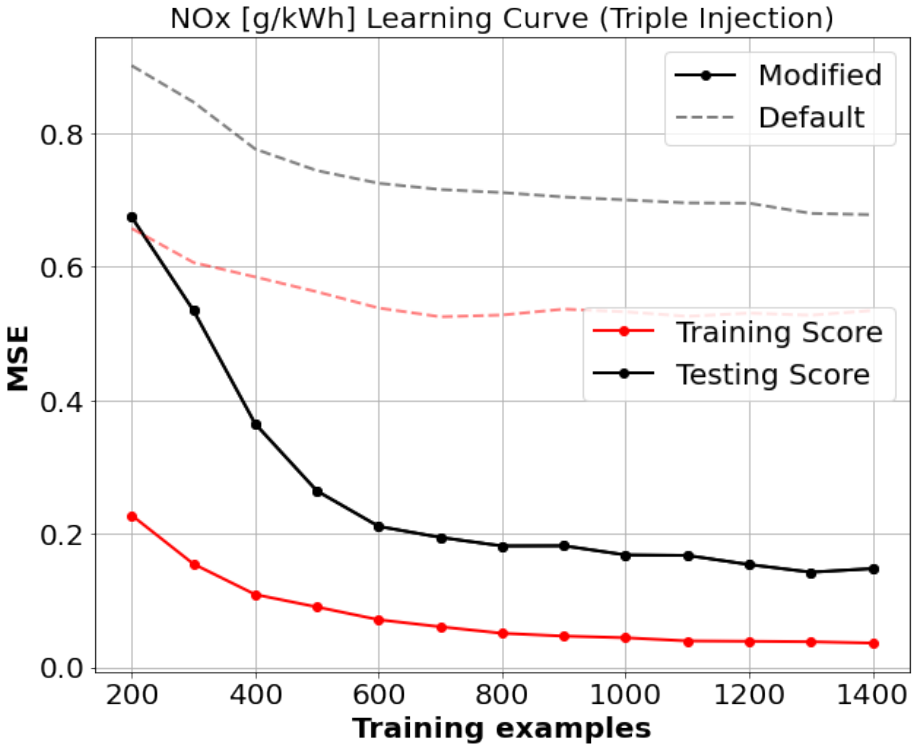


Figure 6.15: Learning curve comparisons between default and tuned tree-based ML algorithm for triple injection scheme.

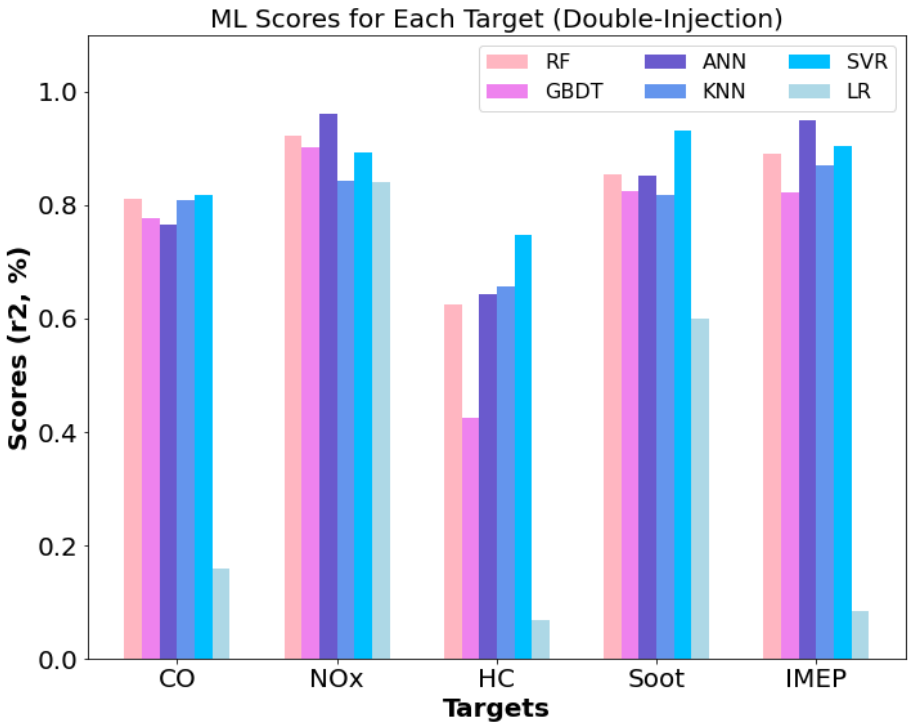


Figure 6.16: ML scores for different algorithms (double-injection scheme).

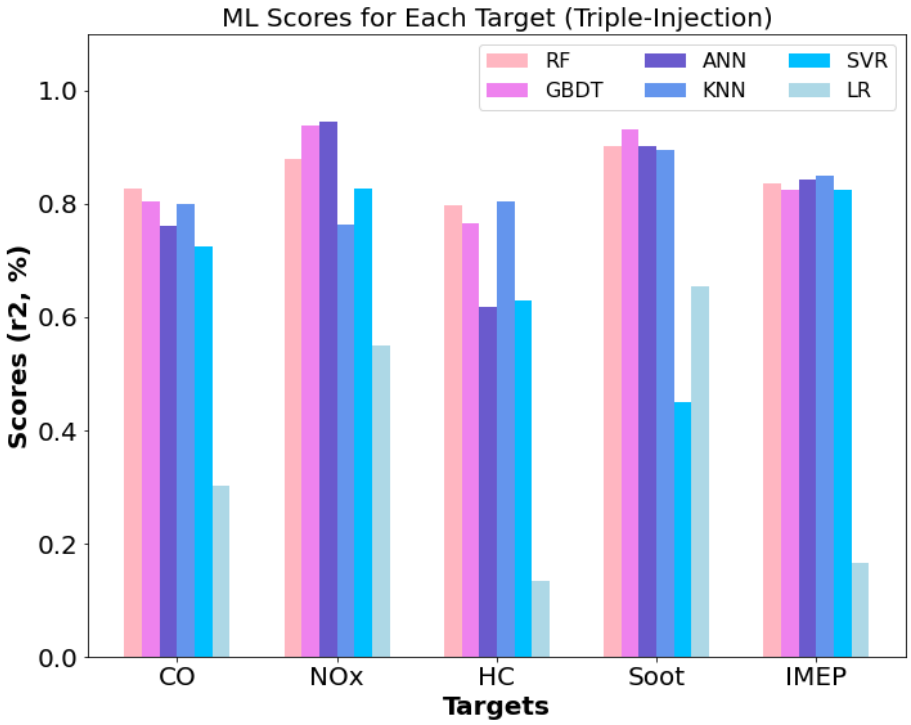


Figure 6.17: ML scores for different algorithms (triple-injection scheme).

6.7 Optimization for Engine Control Parameters with Stacked ML Models

Five fast-running, compact ML models have been selected to build the key relationships between the design features and the outcome, i.e., one ML model for predicting each output parameter. A stacked ML model is assembled using the five base models for generalization (a schematic of stacking is shown in Figure 6.18) and later fed to GA for optimization, aiming to reduce the spread or dispersion of the predictions. Since the relation between the five targets and merit value is clear from Eq. (5.1), a simple linear algorithm can be used for stacking. Details for stacking generalization can be found in section 6.4. The optimization process for ML-GA strategy is nearly the same as that for CFD-GA. At the interface of ML and GA platform, the *minimize* function is called to minimize the merit value. Same optimization strategies are used in ML-GA implementation, and ML simulations are performed for 1800 combinations of features $(r_i, SOI_i, dwell, SR)$ in 30 generations. For each injection scheme, ten trails of ML-GA are conducted to test the robustness and accuracy of data-driven optimization.

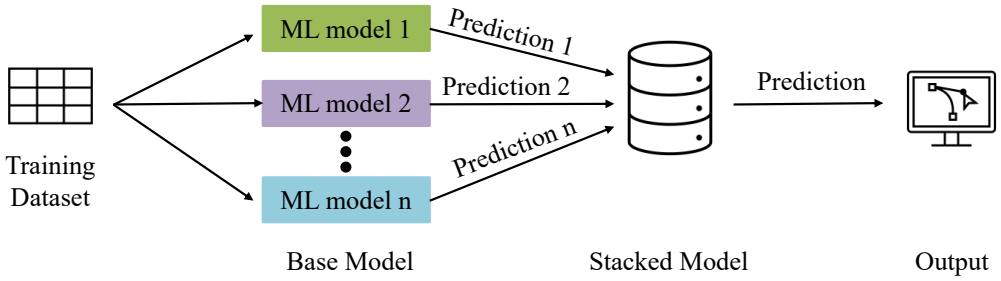


Figure 6.18: Schematic of stacked generalization.

Optimization evolutions for the minimum merit value in each generation are plotted in Figure 6.19 and Figure 6.20. The convergence of merit value in ML-GA approach agrees satisfactorily with that in CFD-GA approach for both injection schemes. Though noticeable variations among ten ML-GA trails appear ineluctably in first 15 generations, they all converge to the minimal value afterwards. The initialization of 1st generation is different in each individual GA

trail as GA randomly assigns control parameters within the prescribed domain. As the evolution proceeds, the optimal combination of control parameters that is associated with the minimum merit value is revealed. Since GA is a global optimization algorithm, it eventually returns an absolute minimum regardless of the initial parent combinations. This explains the convergence of f_{min} for all GA trails, and yet there is slightly difference of f_{min} can be seen at the 30th generation.

A standalone ML model is also tested in the optimization process and is used to compare the differences between the two learning approaches, and results are shown in Figure 6.20 as an example. A standalone ML model is trained with the dataset in which the target only includes the merit value. Same steps are applied for model selection mentioned in previous section, and tree-based algorithm emerges and is selected to create the standalone ML model. From Figure 6.20, the standalone ML model exhibits the stability issues. Evolutionary processes are diverse in ten ML-GA trails, and the value of f_{min} even exceeds the lower boundary presented in the dataset. Even though there exists the relation between features and the merit value, the underlying patterns in the data are deeply tangled and highly implicit. Single ML model is inadequately to depict these patterns thoroughly, and the model performance and robustness are deteriorated ultimately. Stacked generalization uses base ML models that designed for each output and combines individual models, in other words, the strengths, to produce stronger results.

Optimal control parameters are yielded from optimization with stacked ML models, and results are given in Figure 6.21 and Figure 6.22. Values of optimal control parameters vary in ten ML-GA trails, but they closely distribute around the optimal values obtained from CFD-GA. In contrast, optimization results from standalone ML trails are deviated from the values received in CFD simulations and disperses in the prediction space. Admitting that using ensemble ML methods could increase computational cost and complexity, it is inevitable that benefits outweigh its

disadvantages after applying the ensemble learnings. Table 6.6 lists the numeric comparisons for optimal control parameters with the computed percentage of difference. The averaged values from ten stacked ML-GA trails are used for better analysis. As indicated, all differences between CFD-GA and stacked ML-GA optimization approaches are within 1%, which implies that the relations of design features to engine performance are well established through data-driven models.

Table 6.6: Optimal control parameters obtained from CFD-GA and ML-GA.

Control Parameter	*Double Injection*			*Triple Injection*		
	CFD-GA	ML-GA	Diff. %	CFD-GA	ML-GA	Diff. %
r_1	0.694	0.689	0.181	0.388	0.398	0.636
r_2	-	-	-	0.408	0.414	0.365
SOI_1	316.6°	317.2°	0.047	318.6°	318.5°	0.008
SOI_2	376.23°	376.21°	0.001	339.9°	340.0°	0.007
SOI_3	-	-	-	379.9°	379.4°	0.033
SR	2.034	2.033	0.012	2.32	2.29	0.325



Figure 6.19: Double-injection scheme ML-GA optimization history: variation of minimum target function values with generations for ten trails.

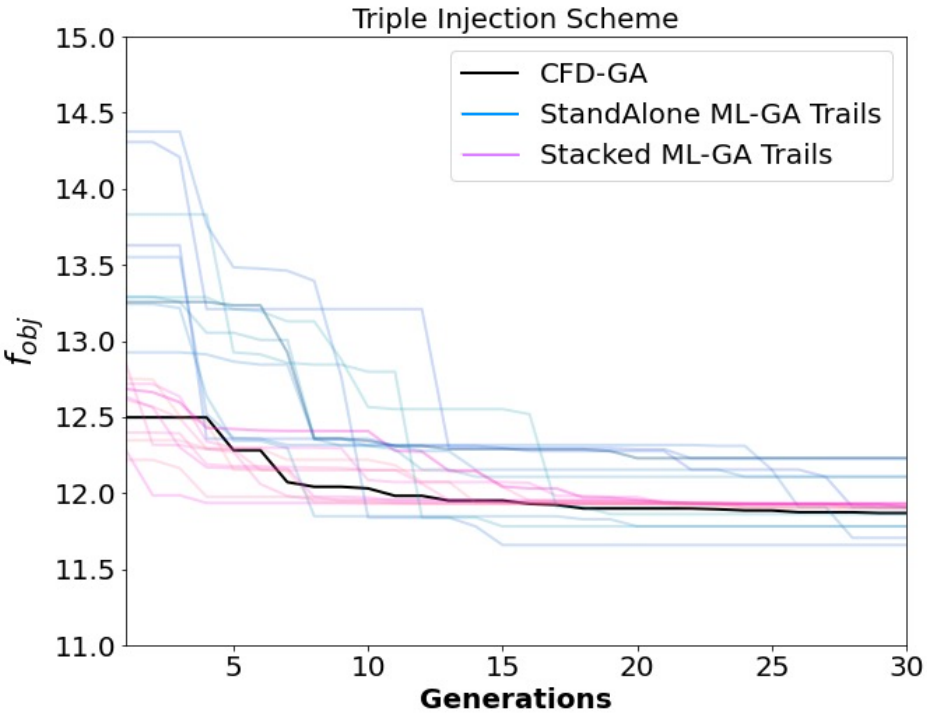


Figure 6.20: Triple-injection scheme ML-GA optimization history: variation of minimum target function values with generations for ten trails.

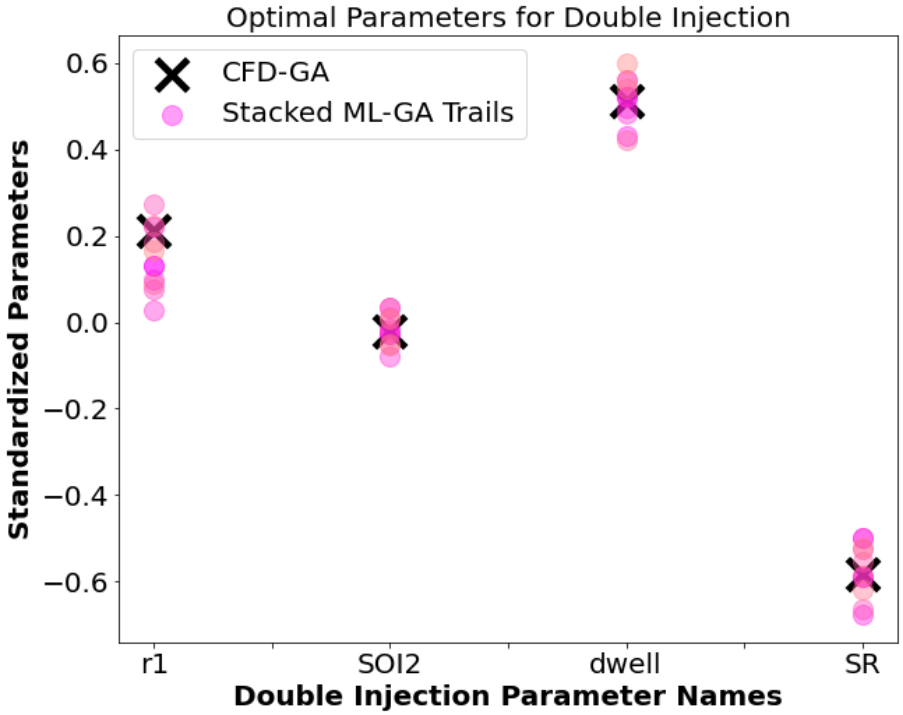


Figure 6.21: Optimal control parameters comparisons between ML-GA and CFD-GA methodologies in double-injection scheme.

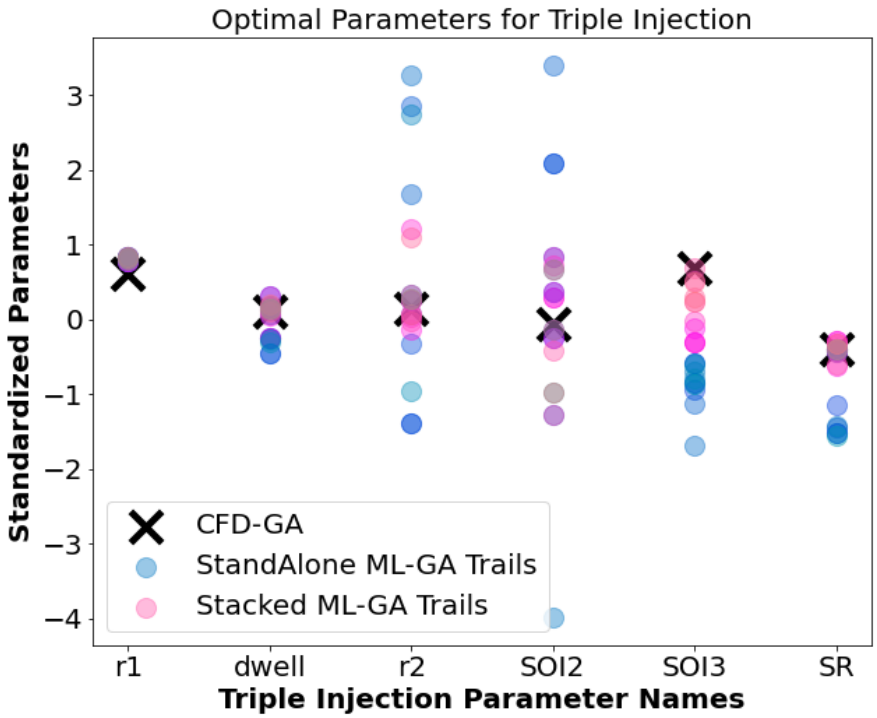


Figure 6.22: Optimal control parameters comparisons between ML-GA and CFD-GA methodologies in triple injection scheme.

The ultimate goals of applying ML-GA are to accelerate the engine design with acceptable accuracy. Therefore, comparisons are made in terms of the computation cost and model accuracy. Table 6.7 summarizes the computational cost for CFD-GA and ML-GA methodologies. CFD-GA simulations that used in Chapter 5 are performed over a computational cluster that consists of 128 processors. The overall CFD-driven optimization campaign takes about 2.5 months for each design scheme. On the contrary, data-driven optimization process with ML models prominently reduces the computational time scale from month to second. Thus, the promising design can be obtained in a fraction of the time.

Engine performances from CFD simulations and ML models using optimal control parameters under the columns of CFD and ML (given in Table 6.6) for double-injection and triple-injection schemes are provided in Table 6.8 and Table 6.9, respectively. For the validation purposes,

CFD simulations with the optimal control parameters collected from the ML-GA process are also performed and related outputs are given in Table 6.8 and Table 6.9 as well under the column of CFD_{optML}. The difference between CFD and ML outputs indicates the accuracy of ML-GA process in predicting the optimal parameters. The difference between the ML and CFD_{optML} results implies the precision of ML models to represent the complex physics-based models as they have the same input parameters. Variations between CFD and CFD_{optML} results provide the evidence that how significant it could change the results when altering the control parameters.

Comparing results from CFD and ML models, target outputs from ML models' prediction match the CFD results well for two injection schemes. Though there are about a 5% difference that can be seen for CO and UHC emission predictions, they have negligible influence on the GA process for finding optimal control parameters as the setup for objective function is primarily driven by the NOx emissions as discussed in previous chapters. Therefore, a good prediction for NOx results is important for GA process, and it turns out that the NOx predictions from the ML model are close to the result from CFD calculation with only 0.026% and 0.318% difference for double-injection and triple-injection schemes, respectively. There are a few minor differences, up to around 3% and 0.35% can be noticed for soot emissions and IMEP, respectively. The CFD-GA process, therefore, can be replaced by the fast-running ML-GA process with similar NOx-driven orientation and proper merit values.

Considering the comparison of CFD results that run with ML-GA optimized control parameters (third column with name CFD_{optML}) and with CFD-GA optimized feature combinations (first column with name CFD), most of the predicted values of the outputs are within 5%. With the optimal control parameters obtained from ML-GA processes, NOx emissions from either ML predictions or CFD simulations increase slightly in both injection schemes, and the reason for

higher NOx values could be due to the changes in post injection timings. There is a strong correlation between NOx emissions and the post injection timing as discussed in Chapter 5, and 0.001% (SOI_2 in double-injection scheme) and 0.033% (SOI_3 in triple-injection scheme) changes in post injection timing could increase the NOx emissions, and the NOx production is higher with the greater changes in post injection timings. There is a noteworthy reduction for soot emissions in triple-injection scheme. The difference in predictions of soot form the CFD and CFD_{optML} simulations could be due to the undiscovered correlation between soot emissions and control parameters. For example, the 14% difference in the soot prediction could be resulted from the changes in amount of fuel injected in first or second injections, or swirl ratio, as the predicted values of these three parameters are above 3% of CFD-GA predicted values, and soot emissions could be sensitive to the changes in these three parameters. The accuracy of soot emissions can be increased by modifying the reference values in objective function and enhancing the influence of soot values on the merit value. Because the inverted ϕ-sensitivity studies are the primary objective to reduce the NOx emissions, soot-control parameters sensitivity analysis will be investigated and addressed in future studies.

Results of CFD_{optML} simulations are closer to values predicted by ML models if comparing the percentage of difference values in the last columns from Table 6.8 and Table 6.9, and almost all of values are below 3%. To be noted, for triple-injection scheme there is a ~8% discrepancy can be seen in soot prediction. Though it has a negligible impact on the overall process for optimizing inputs and outputs from ML-GA, soot prediction can be improved in the future by improving the ML models and discovering the inherent correlation of a higher degree in the soot output with respect to the 6 inputs. Considering the hyperparameters tuning has been done to improve the ML model accuracy for soot, one possible solution could be building an ensemble ML

model for soot prediction to combine the strength from several ML models thus enhance the model performance. Nevertheless, the input parameters for ML models and CFD_{optML} simulations are same, from the ML-GA optimized inputs. This signifies that the ML models selected in this study can well interpret the underlying relations between the input features and individual target. The results for difference between CFD and ML calculations shown in Table 6.8 and Table 6.9 also agrees with the outcomes from the model accuracy studies in previous section (Figure 6.16 and Figure 6.17), i.e., the model with a higher accuracy score is able to produce the more precise estimation.

When comparing results from the two injection strategies, it is noticeable that for double-injection scheme, the predicted outputs from ML models and CFD_{optML} simulations are closer, and less deviated from CFD simulations using the CFD-GA optimized set of inputs. The feature dimension for double-injection scheme is lower than that for triple-injection scheme, and consequently ML models can capture the inherent patterns in the dataset more effectively. In general, optimizations using ML-GA for both injection schemes show promising results with merit values and the optimized control parameters being consistent with CFD-GA but at low cost of computational resources.

Table 6.7: Computational cost comparisons between CFD-GA and ML-GA.

Methodology	**NO. of Processors**	**Computational Time**	
CFD-GA	128	~ 2.5 months	
ML-GA	1	double inj.	triple inj.
		63.31 sec.	67.38 sec.

**Computational time in ML-GAs is the averaged time for ten trails*

Table 6.8: Optimal simulation results comparison for double injection scheme.

Targets	CFD	ML	CFD_{optML}	*% Diff* $_{CFD-ML}$	*% Diff* $_{CFD-CFD_{optML}}$	*% Diff* $_{ML-CFD_{optML}}$
CO	0.0578	0.0480	0.0476	4.631	4.839	0.209
NOx	0.972	0.973	0.997	-0.026	-0.635	-0.609
UHC	$3.82\cdot10^{-4}$	$4.35\cdot10^{-4}$	$4.10\cdot10^{-4}$	-3.244	-1.768	1.479
$Soot$	$9.12\cdot10^{-3}$	$9.19\cdot10^{-3}$	$8.43\cdot10^{-3}$	-0.191	1.966	2.156
$IMEP\ [bar]$	11.079	11.077	11.078	0.005	0.002	-0.002

**Unit for emissions is $[g/kWh]$; CFD(ML) is the CFD simulations using the parameters obtained from ML-GA approach for validation purposes*

Table 6.9: Optimal simulation results comparison for triple injection scheme.

Targets	CFD	ML	CFD_{optML}	*% Diff* $_{CFD-ML}$	*% Diff* $_{CFD-CFD_{optML}}$	*% Diff* $_{ML-CFD_{optML}}$
CO	0.0243	0.0275	0.0308	-3.089	-5.898	-2.830
NOx	0.78	0. 790	0.814	-0.318	-1.066	-0.748
UHC	$4.17\cdot10^{-4}$	$4.93\cdot10^{-4}$	$5.21\cdot10^{-4}$	-4.176	-5.544	-1.381
$Soot$	$5.\ 42\cdot10^{-4}$	$4.16\cdot10^{-4}$	$3.02\cdot10^{-4}$	2.724	14.218	7.939
$IMEP\ [bar]$	11.073	10.92	10.95	0.349	0.279	-0.069

**Unit for emissions is $[g/kWh]$; CFD(ML) is the CFD simulations using the parameters obtained from ML-GA approach for validation purposes*

CHAPTER 7: SUMMARY AND FUTURE WORK

7.1 Development of Spray Models in IC Engines

An efficient multi-component fuel droplet vaporization model has been developed in this work using a discrete approach. The precise modeling of the droplet vaporization process is divided into two parts: vapor-phase and liquid-phase sub-models. Temporal evolution of the flow inside the droplet is considered to describe the transient behavior introduced by the slow diffusion process. In order to account for the internal circulation motion, surface regression and finite diffusion without actually resolving the spatial governing equations within the liquid phase, a set of ordinary differential equations is applied to describe the evolution of the non-uniform distributions of universal diffusional variables, i.e., temperature and species mass fraction.

The differences between the droplet surface and bulk mean states are modeled by constructing a quasi-1D frame; the effect of the internal circulations is taken into consideration by using the effective diffusivity rather than physical diffusivity. The Peng-Robinson (PR) Equation of State (EOS) is utilized to deliberate the non-ideal behavior in a high-pressure environment and to compute the vapor-liquid equilibrium (VLE) at the droplet surface. The quasi-steady assumption is made for the gaseous flow in determining the vaporization rate and heat flux to the droplet.

The model results are compared with the measured data from fuel droplet evaporation experiments using a suspending silica filament technique in a constant volume chamber (CVC). The support filament has a 100-μm diameter to minimize the effect of thermal conduction. The experiments are carried out with different ambient temperatures. Droplet lifetime and vaporization rate are determined from the data recorded by a high-speed CCD camera. Droplet temperature is acquired by a thermocouple with 50 μm diameter. The present model is also compared with

measured data from literature resources. The comparison demonstrates the capability of the droplet model in predicating the droplet size and temperature change under the various conditions.

The present vaporization model is capable of accurately estimating the temporal history of the droplet vaporization at atmospheric ambient pressures. The preferential vaporization behavior for multi-component droplets is realized by the present model as well; the lighter component in the fuel would evaporate first and the heavier component that remains evaporates toward the end of the vaporization process. The droplet vaporization characteristics are also conducted under the convective flow environment. The relative velocity between the ambient gas and droplet can enhance the circulation motion of the liquid droplet, and hence the mixing process of species and temperature within the droplet.

The second model developed in this work is for the atomization and focuses on the process of droplet breakup under the flash-boiling condition. For GDI engines, heated fuel can be rapidly introduced to an environment that has an ambient pressure to be lower than its saturation pressure, and the flash-boiling would occur within the liquid fuel. The flash boiling phenomenon is very complex, involving complicated analysis of thermodynamics, instabilities, dynamics etc. To develop a comprehensive multi-component fuel flash boiling model, three main processes: bubble nucleation, bubble growth, and breakup, are considered.

For the nucleation process, under high injection pressure conditions, small amount of air can dissolve into the liquid fuel and later become nucleation sites during the injection process. An empirical relation is adopted to describe the steady-state rate of formation of bubble nuclei at different superheated degree. The nucleation site would expand during the injection process, and three stages are considered for the bubble growth. Initially the growth rate is controlled by the momentum interaction between the bubble and liquid fuel. Proceeding to the end of the bubble

growth, the dominant mechanism switches from the inertia to heat-transfer. At the intermediate times the mixing effect of the inertia and heat transfer on bubble growth is established.

The superheated liquid droplet may experience either flash-boiling breakup or aerodynamic breakup, or both. In the case of flash-boiling breakup, the expansion of the internal bubbles is the direct cause of the breakup; and in the case of aerodynamic breakup, the expansion of the internal bubbles also promotes the aerodynamic-load-induced droplet distortion, hence the aerodynamic breakup process. A unified model based on an analogy between the oscillating and distorting droplet and a spring-mass system is proposed which can handle the breakup under either non-flashing or flashing breakup conditions.

The new breakup model and vaporization model are integrated into an open source CFD program, KIVA, for further evaluation of the spray superheating effects. Two fuel blends are tested at different ambient pressure conditions. The vaporization and breakup models well predicted the characteristics of spray behavior, for example, the jet collapse and tip recirculation when flash boiling phenomenon is very strong at low ambient pressures. The averaged SMD calculations match the measurement sufficiently well. Stronger flash boiling can significantly reduce the droplet size, but higher ethanol content, for example by comparing E30, and E50, retards the vaporization rate due to the high heat of vaporization of ethanol, thus resulting in a larger droplet size.

To investigate spray vaporization behaviors and liquid droplet distributions, 3D rendering visualization is used. Such visualization techniques can help in the understanding of the distribution of both liquid and vapor phase distributions during the injection, which cannot be measured by experiments. It also can help to predict the fuel vapor and air mixing process for better management of engine operation strategies.

7.2 Novel Investigations on Engine Emission Reduction

A new approach to reduce the engine-out NOx emissions in the compression-ignition engine is introduced. In the proposed method, the lean mixture ignites faster than the near-stoichiometric mixture, i.e., exhibits inverted ϕ-sensitivity. While no known fuel has inverted ϕ-sensitivity as its inherent property, the inverted ignition sequence can be achieved when the fuel has strong spray cooling effect and strong T-sensitivity. Ethanol is selected for this study because it has the potential to exhibit inverted ϕ-sensitivity during the combustion in the operation of compression-ignition engines. 0-D ignition simulation shows that a temperature difference of approximately 100 K is sufficient to counterbalance the inherent positive ϕ-sensitivity of ethanol-air mixture: a larger temperature difference results in inverted ϕ-sensitivity. In the 3-D simulation of a compression-ignition engine, a primary reference fuel (PRF85) is chosen for comparison. The 3-D simulation covers a wide range of load conditions. Detailed analysis of the representative cases is conducted for both low-medium load and high load conditions.

It is found that the inverted ϕ-sensitivity is possible with careful fuel selection, and it is effective in reducing NOx emissions. Under low and medium load where the overall equivalence ratio is low, the effect of inverted ϕ-sensitivity in reducing the NOx emissions is more pronounced. However, when increasing the load and the overall equivalence ratio, the NOx reduction effect vanishes because a considerable amount of near-stoichiometric mixture is still consumed in the early phase of combustion. Therefore, it is desirable to recover the combustion sequence in the chamber such that the leaner region is burned before the near-stoichiometric region. When the combustion in near-stoichiometric region is inhibited, the temperature rise of that region is hindered and the formation of NOx is suppressed. To achieve the goal of homogenizing the mixture

before combustion, switching the ignition mode, and lowering emissions when fueling with the target fuel, multiple direct-injection strategies are applied to this study.

7.3 Applications of Advanced Techniques and Innovations

KIVA-GA simulations are performed in a compression-ignition engine with a multi-injection strategy to promote the pronounced inverted ϕ-sensitiviy using E100, a fuel that exhibits an inverted ignition sequence in compression-ignition engines. The purpose of adopting the multi-injection strategy is to create a partially premixed fuel-air mixture before the ignition under the desired high load condition. With the GA methodology, the optimized multi-injection strategies can be utilized for CFD simulations, providing the results that are able to restore and enhance the effect of inverted ϕ-sensitivity on engine performance. Simulation results are compared with the previously conducted single-injection operation study. Detailed analysis for the GA optimization and CFD simulations is conducted.

With the GA methodology, a set of optimized control parameters can be obtained for the sake of reducing engine-out emissions while keeping a high engine efficiency. The target function for this study is set to be NOx-driven on purpose to guide the optimization process to get an optimized strategy that can exhibit inverted ϕ-sensitivity behavior during the combustion. The control parameters display various sensitivities to the merit value. The post injection timing is confirmed to have a strong correlation to the merit value as well as the NOx emissions. With the optimal combinations for the double and triple injection schemes, the desired inverted ignition sequence is attained at the prescribed engine condition, disclosing the possibility of the inverted ϕ-sensitivity behavior under high load conditions. The distribution of ϕ over the in-cylinder

temperature and NOx distributions using multi-injection schemes reveals the success of realizing the pronounced inverted ϕ-sensitivity that significantly reduces the engine-out NOx emissions.

To accelerate the optimization process for engine design process, in this work data-driven models are development to substitute the complex and expensive CFD simulations. Optimizing using CFD simulations can still be quite time consuming and expensive. Based on the fidelity of the CFD, each simulation can take several hours running on anywhere between ten to a hundred processors, and the overall CFD-driven optimization campaign can take several months.

By developing the ML model as a compact representation of our CFD model, the higher-fidelity CFD model can be replaced by a reduced-order model that correlates inputs to outputs that need to be minimized. The raw data collected from CFD simulations are used as "synthetic" training data to teach a fast-running, compact ML model the key relationships between the design features and the individual target. ML models are evaluated using bias-variance trade-off to ensure the model is at its optimal balance to avoid overfitting and underfitting. For each target, different ML models are trained and tested, hyperparameter tuning is conducted, and the ML model with the best performance is selected to build a stacked generalization ML model for the merit value prediction in the GA process. The training process itself is quite fast, as is the optimization process to give the promising design.

This work demonstrates the essential steps for implementation of ML and GA methodologies for engine research. Comparisons between CFD-GA and ML-GA approaches shows that the ML-GA methodology can reduce the computational cost prominently. In addition, similar design features can be secured from the ML-GA process and merit optimization accuracy is close to the CFD-GA approach. Adopting the advanced techniques in ICE study is essential and beneficial for prototyping the designs that meet the emission regulations and performance

requirements. When designing a new engine configuration, many control parameters or geometry of piston need to be considered. It becomes even more complicated to meet customers' requirement or budgets. With the available datasets, ML algorithms can help to construct the data-driven models that can very quickly evaluate the merit of any design and to provide the promising design configurations after the optimization process.

7.4 Recommendations for Future Works

Fuel spray control has been an important part of IC engine designs, and recent research efforts have demonstrated how precisely controlled operation parameters and fuel compositions can generate spray phenomena such as flash boiling that optimize fuel atomization. The design process requires numerical models that can accurately replicate physical observation, and the development of spray models has been primarily focused on the steady state injection process while. However, the transient behavior of a spray event, such as end-of-injection processes, has non-trivial impact on IC engine performance and key emissions. Fuel dribble generation following an injection event is another example of spray characteristic not considered by model spray models. Recent high-resolution in-nozzle flow simulations revealed the importance of transient flow behaviors from needle valve lifts and on orifice geometries, but the high computational costs of these LES models impedes the widespread application in engine simulation models.

Recommendations are provided to develop a computationally efficient numerical model that considers the complete spray event from start- to end-of-injection and is capable of simulating flash boiling response to complex properties of fuel mixture. In-nozzle simulations output coupled with experimental data can be used to identify key parameters to be included in the new model, which may include needle sealing rate, pressure changing rate and injector tip temperature. The

state-of-the-art artificial intelligence methodology, ML, can be employed to optimize the transient spray sub-model, reducing the complexity of the sub-model. The new model can incorporate a unified breakup sub-model that considers both aerodynamic breakup and flash boiling breakup. The goal is to establish correlations between these two breakup mechanisms, which are lacking in current models. Experiments will be performed to verify and validate all numerical results. The dynamics of the in-nozzle flow and the spray behavior near the injector exit can be investigated using the high-speed microscopic imaging technology. Various laser diagnostics (PIV, LIEF, etc.) can also be applied to provide a better understanding of spray characteristics, flow field and liquid/vapor distribution.

The implementation of the new spray model into engine simulations can lead to more efficient and accurate IC engine designs with shorter cycles. The comprehensive transient spray model will help the development of injection strategies that improve overall spray evolution, thus the subsequent fuel-air mixing and combustion processes. A better air-fuel mixing can be achieved through model identification of fuels mixing, coupled with carefully designed control parameters, to promote flash boiling that optimizes fuel spray atomization. These new engine designs may help to further downsize engines, relieve negative environmental impacts, and secure long-term sustainable energy source development via the utilization of renewable sources.

REFERENCES

1. Daw, C.S., et al., *Summary Report on the Transportation Combustion Engine Efficiency Colloquium Held at USCAR, March 3 and 4, 2010*. 2010, Oak Ridge National Laboratory (ORNL).
2. Reitz, R., et al., *IJER editorial: the future of the internal combustion engine*. 2020, SAGE Publications Sage UK: London, England.
3. Dudley, B., *BP statistical review of world energy 2016.* London, UK, 2015.
4. Cavallo, A.J., *Predicting the peak in world oil production.* Natural Resources Research, 2002. **11**(3): p. 187-195.
5. Cavallo, A.J., *Hubbert's petroleum production model: an evaluation and implications for world oil production forecasts.* Natural Resources Research, 2004. **13**(4): p. 211-221.
6. Ward, B., *Unburnable Carbon 2013: Wasted capital and stranded assets*. 2013: Carbon Tracker.
7. Ritchie, H. and M. Roser, *CO_2 and greenhouse gas emissions.* Our world in data, 2020.
8. Regner, G., et al., *The achates power opposed-piston two-stroke engine: performance and emissions results in a medium-duty application.* SAE International Journal of Engines, 2011. **4**(2011-01-2221): p. 2726-2735.
9. Shkolnik, A., et al., *High Power Density and Efficiency Epitrochoidal Rotary Engine*. 2018, Google Patents.
10. Petitjean, D., et al., *Advanced Gasoline Engine Turbocharging Technology for Fuel Economy Improvements*. 2004, SAE International.

11. Kasseris, E., et al., *Real World Performance of an Onboard Gasoline/Ethanol Separation System to Enable Knock Suppression Using an Octane-On-Demand Fuel System*. 2018, SAE International.

12. Mizuno, K., et al., *Study of Alcohol-Gasoline Separation Technology to Suppress Knock and Enable Higher Efficiency Engines*. 2018, SAE International.

13. Morganti, K., et al., *Leveraging the benefits of ethanol in advanced engine-fuel systems.* Energy Conversion and Management, 2018. **157**: p. 480-497.

14. Kim, Y., et al., *Improvement of alcohol engine performance by flash boiling injection*. 1980.

15. Pierpont, D., D. Montgomery, and R.D. Reitz, *Reducing particulate and NOx using multiple injections and EGR in a DI diesel*. 1995, SAE Technical Paper.

16. Mazda, M.C. *NEXT-GENERATION SKYACTIV-X GASOLINE ENGINE*. 2018; Available from: http://www2.mazda.com/en/next-generation/technology/.

17. Epping, K., et al., *The potential of HCCI combustion for high efficiency and low emissions*. 2002, SAE Technical Paper.

18. Alkemade, U.G. and B. Schumann, *Engines and exhaust after treatment systems for future automotive applications.* Solid State Ionics, 2006. **177**(26): p. 2291-2296.

19. Koebel, M., M. Elsener, and M. Kleemann, *Urea-SCR: a promising technique to reduce NOx emissions from automotive diesel engines.* Catalysis Today, 2000. **59**(3): p. 335-345.

20. Johnson, T.V., *Review of diesel emissions and control.* International Journal of Engine Research, 2009. **10**(5): p. 275-285.

21. Lefebvre, A.H., *The Role of Fuel Preparation in Low-Emission Combustion.* Journal of Engineering for Gas Turbines and Power, 1995. **117**(4): p. 617-654.

22. KADOTA, T. and H. HIROYASU, *Evaporation of a single droplet at elevated pressures and temperatures: 2nd report, theoretical study.* Bulletin of JSME, 1976. **19**(138): p. 1515-1521.

23. Faeth, G., *Current status of droplet and liquid combustion.* Progress in Energy and Combustion Science, 1977. **3**(4): p. 191-224.

24. Sirignano, W. and C. Law, *Transient heating and liquid-phase mass diffusion in fuel droplet vaporization.* Adv. Chem. Ser, 1978. **166**(3).

25. Sirignano, W.A., *Fuel droplet vaporization and spray combustion theory.* Progress in Energy and Combustion Science, 1983. **9**(4): p. 291-322.

26. Ra, Y. and R.D. Reitz, *A vaporization model for discrete multi-component fuel sprays.* International Journal of Multiphase Flow, 2009. **35**(2): p. 101-117.

27. Zeng, Y., *Modeling of multicomponent fuel vaporization in internal combustion engines*. 2000, University of Illinois at Urbana-Champaign.

28. Wang, M., *Modeling of droplet evaporation, flash-boiling, and mixture preparation in intenal combustion engines*. 2018, University of Illinois at Urbana-Champaign.

29. Tamim, J. and W.L. Hallett, *A continuous thermodynamics model for multicomponent droplet vaporization.* Chemical Engineering Science, 1995. **50**(18): p. 2933-2942.

30. Lippert, A.M. and R.D. Reitz, *Modeling of multicomponent fuels using continuous distributions with application to droplet evaporation and sprays*. 1997, SAE Technical Paper.

31. Shen, C., W. Cheng, and C. Lee, *Finite Diffusion Multi-Components Fuel Droplet Vaporization Modeling Using Continuous Thermodynamics for Fuels with Distinct Composition Distributions.* 2012.

32. Yi, P., et al., *Development of an improved hybrid multi-component vaporization model for realistic multi-component fuels.* International Journal of Heat and Mass Transfer, 2014. **77**(Supplement C): p. 173-184.

33. Sazhin, S., et al., *A quasi-discrete model for heating and evaporation of complex multicomponent hydrocarbon fuel droplets.* International Journal of Heat and Mass Transfer, 2011. **54**(19): p. 4325-4332.

34. Sazhin, S.S., et al., *A multi-dimensional quasi-discrete model for the analysis of Diesel fuel droplet heating and evaporation.* Fuel, 2014. **129**(Supplement C): p. 238-266.

35. Law, C.K., *Multicomponent droplet combustion with rapid internal mixing.* Combustion and Flame, 1976. **26**: p. 219-233.

36. Law, C.K., S. Prakash, and W.A. Sirignano, *Theory of convective, transient, multicomponent droplet vaporization.* Symposium (International) on Combustion, 1977. **16**(1): p. 605-617.

37. Wang, C., X. Liu, and C. Law, *Combustion and microexplosion of freely falling multicomponent droplets.* Combustion and Flame, 1984. **56**(2): p. 175-197.

38. Chung, S.S. and O. Kawaguchi, *An experimental study on the evaporation of freely falling droplet under high temperature and high pressure gas stream.* Journal of Mechanical Science and Technology, 1990. **4**(2): p. 172-177.

39. Randolph, A., A. Makino, and C. Law. *Liquid-phase diffusional resistance in multicomponent droplet gasification*. in *Symposium (International) on Combustion*. 1988. Elsevier.

40. Kumagai, S., T. Sakai, and S. Okajima. *Combustion of free fuel droplets in a freely falling chamber*. in *Symposium (International) on Combustion*. 1971. Elsevier.

41. Nomura, H., et al. *Experimental study on high-pressure droplet evaporation using microgravity conditions*. in *Symposium (International) on Combustion*. 1996. Elsevier.

42. Ghassemi, H., S.W. Baek, and Q.S. Khan, *Experimental study on binary droplet evaporation at elevated pressures and temperatures.* Combustion science and technology, 2006. **178**(6): p. 1031-1053.

43. Chauveau, C., et al. *An experimental study on the droplet vaporization: effects of heat conduction through the support fiber*. in *Proc. of 22 nd Annual Conference on Liquid Atomization and Spray Systems (ILASS Europe 2008)*. 2008.

44. Javed, I., S.W. Baek, and K. Waheed, *Evaporation characteristics of heptane droplets with the addition of aluminum nanoparticles at elevated temperatures.* Combustion and Flame, 2013. **160**(1): p. 170-183.

45. Wong, S.-C. and A.-C. Lin, *Internal temperature distributions of droplets vaporizing in high-temperature convective flows.* Journal of fluid mechanics, 1992. **237**: p. 671-687.

46. Shih, A.T. and C.M. Megaridis, *Suspended droplet evaporation modeling in a laminar convective environment.* Combustion and flame, 1995. **102**(3): p. 256-270.

47. Heywood, J.B., *Combustion engine fundamentals.* 1ª Edição. Estados Unidos, 1988.

48. Malaguti, S., et al., *Modelling of primary breakup process of a gasoline direct engine multi-hole spray.* Atomization and Sprays, 2013. **23**(10).

49. Som, S. and S. Aggarwal, *Effects of primary breakup modeling on spray and combustion characteristics of compression ignition engines.* Combustion and Flame, 2010. **157**(6): p. 1179-1193.

50. Lee, C.S. and S.W. Park, *An experimental and numerical study on fuel atomization characteristics of high-pressure diesel injection sprays.* Fuel, 2002. **81**(18): p. 2417-2423.

51. Beale, J.C. and R.D. Reitz, *Modeling spray atomization with the Kelvin-Helmholtz/Rayleigh-Taylor hybrid model.* Atomization and sprays, 1999. **9**(6): p. 623-650.

52. Zhao, H., *Overview of gasoline direct injection engines*, in *Advanced direct injection combustion engine technologies and development*. 2010, Elsevier. p. 1-19.

53. Sher, E., T. Bar-Kohany, and A. Rashkovan, *Flash-boiling atomization.* Progress in energy and combustion science, 2008. **34**(4): p. 417-439.

54. Neroorkar, K., et al., *Simulation of flash boiling in pressure swirl injectors.* Atomization and Sprays, 2011. **21**(2).

55. Saha, K., M. Battistoni, and S. Som, *Modeling of Flash Boiling Phenomenon in Internal and Near-Nozzle Flow of Fuel Injectors*, in *Droplets and Sprays*. 2018, Springer. p. 167-181.

56. Zuo, B., A. Gomes, and C. Rutland, *Modelling superheated fuel sprays and vaproization.* International Journal of Engine Research, 2000. **1**(4): p. 321-336.

57. Price, C., et al., *Numerical modelling of fuel spray formation and collapse from multi-hole injectors under flash-boiling conditions.* Fuel, 2018. **221**: p. 518-541.

58. Chang, D.-L. and C.-F.F. Lee, *Development of a simplified bubble growth model for flash boiling sprays in direct injection spark ignition engines.* Proceedings of the Combustion Institute, 2005. **30**(2): p. 2737-2744.

59. Wang, M., *Modeling of droplet evaporation, flash-boiling, and mixture preparation in internal combustion engines*. 2018, University of Illinois at Urbana-Champaign.

60. Zeng, Y. and C.-F.F. Lee, *An atomization model for flash boiling sprays.* Combustion Science and Technology, 2001. **169**(1): p. 45-67.

61. Khan, M.M., et al., *Experimental and numerical study of flash boiling in gasoline direct injection sprays.* Applied Thermal Engineering, 2017. **123**: p. 377-389.

62. Alriksson, M., T. Rente, and I. Denbratt, *Low soot, low NOx in a heavy duty diesel engine using high levels of EGR*. 2005, SAE Technical Paper.

63. Ogawa, H., et al., *Characteristics of diesel combustion in low oxygen mixtures with ultra-high EGR*. 2006, SAE Technical Paper.

64. Takeda, Y., N. Keiichi, and N. Keiichi, *Emission characteristics of premixed lean diesel combustion with extremely early staged fuel injection*. 1996, SAE Technical Paper.

65. Stanglmaier, R.H. and C.E. Roberts, *Homogeneous charge compression ignition (HCCI): benefits, compromises, and future engine applications*. 1999, SAE Technical Paper.

66. Noehre, C., et al., *Characterization of Partially Premixed Combustion*. 2006, SAE International.

67. Upatnieks, A. and C.J. Mueller, *Clean, controlled DI diesel combustion using dilute, cool charge gas and a short-ignition-delay, oxygenated fuel*. 2005, SAE Technical Paper.

68. Ishida, M., H. Ueki, and D. Sakaguchi, *Prediction of NOx reduction rate due to port water injection in a DI diesel engine*. 1997, SAE Technical Paper.

69. Kohketsu, S., et al., *Reduction of exhaust emission with new water injection system in a Diesel engine*. 1996, SAE Technical Paper.

70. Bedford, F., et al., *Effects of direct water injection on DI diesel engine combustion*. 2000, SAE Technical Paper.

71. Kook, S., et al., *The Influence of Charge Dilution and Injection Timing on Low-Temperature Diesel Combustion and Emissions*. 2005, SAE International.

72. Mohan, B., W. Yang, and S. kiang Chou, *Fuel injection strategies for performance improvement and emissions reduction in compression ignition engines—A review.* Renewable and Sustainable Energy Reviews, 2013. **28**: p. 664-676.

73. Montgomery, D. and R.D. Reitz, *Six-mode cycle evaluation of the effect of EGR and multiple injections on particulate and NOx emissions from a DI diesel engine*. 1996, SAE Technical paper.

74. Tow, T., D. Pierpont, and R.D. Reitz, *Reducing particulate and NOx emissions by using multiple injections in a heavy duty DI diesel engine*. 1994, SAE Technical Paper.

75. Ra, Y., et al., *Gasoline DICI engine operation in the LTC regime using triple-pulse injection.* SAE International Journal of Engines, 2012. **5**(2012-01-1131): p. 1109-1132.

76. Ricaud, J. and F. Lavoisier, *Optimizing the multiple injection settings on an HSDI diesel engine*, in *Thermo-and Fluid Dynamic Processes in Diesel Engines 2*. 2004, Springer. p. 199-234.

77. Mallamo, F., M. Badami, and F. Millo, *Application of the design of experiments and objective functions for the optimization of multiple injection strategies for low emissions in CR diesel engines*. 2004, SAE Technical Paper.

78. Montgomery, D.T. and R.D. Reitz, *Optimization of Heavy-Duty Diesel Engine Operating Parameters Using A Response Surface Method*. 2000, SAE International.

79. Lee, A., et al., *A flexible framework and model library for process simulation, optimization and control*, in *Computer Aided Chemical Engineering*. 2018, Elsevier. p. 937-942.

80. Forum, M.P., *MPI: A message-passing interface standard*. 1994, University of Tennessee.

81. Barney, B., *Introduction to parallel computing.* Lawrence Livermore National Laboratory, 2010. **6**(13): p. 10.

82. Dagum, L. and R. Menon, *OpenMP: an industry standard API for shared-memory programming.* IEEE computational science and engineering, 1998. **5**(1): p. 46-55.

83. Chandra, R., et al., *Parallel programming in OpenMP*. 2001: Morgan kaufmann.

84. Ali, A., et al. *Improvement in computational efficiency for HCCI engine modeling by using reduced mechanisms and parallel computing*. in *Central State Section Meeting*. 2003.

85. Velghe, A., N. Gillet, and J. Bohbot, *A high efficiency parallel unstructured solver dedicated to internal combustion engine simulation.* Computers & Fluids, 2011. **45**(1): p. 116-121.

86. Wang, M. and F.L. Chia-fon. *Efficient computation methods for combustion reaction kinetics*. in *ASME 2014 Internal Combustion Engine Division Fall Technical Conference*. 2014. American Society of Mechanical Engineers.

87. De Jong, K.A., *Analysis of the behavior of a class of genetic adaptive systems*. 1975.

88. Holland, J.H., *Adaptation in natural and artificial systems: an introductory analysis with applications to biology, control, and artificial intelligence*. 1992: MIT press.

89. Yang, X.-S., *Nature-inspired optimization algorithms*. 2014: Elsevier.

90. Hiroyasu, H., et al., *Genetic algorithms optimization of diesel engine emissions and fuel efficiency with air swirl, EGR, injection timing and multiple injections*. 2003, SAE Technical Paper.

91. Kim, M., M.P. Liechty, and R.D. Reitz, *Application of micro-genetic algorithms for the optimization of injection strategies in a heavy-duty diesel engine*. 2005, SAE Technical Paper.

92. Zhang, Q., R.M. Ogren, and S.-C. Kong, *A comparative study of biodiesel engine performance optimization using enhanced hybrid PSO–GA and basic GA.* Applied energy, 2016. **165**: p. 676-684.

93. Wang, M., et al., *Numerical Study and Parameter Optimization on a Diesel-Natural Gas Dual Fuel Engine*. 2016, SAE Technical Paper.

94. Gao, S. and C.-F. Lee, *High-Load Compression-Ignition Engine Emissions Reduction with Inverted Phi-Sensitivity Fuel Using Multiple Injection Strategies*. 2019, SAE Technical Paper.

95. Liu, Y. and R.D. Reitz, *Optimizing HSDI diesel combustion and emissions using multiple injection strategies*. 2005, SAE Technical Paper.

96. Shi, Y. and R.D. Reitz, *Assessment of optimization methodologies to study the effects of bowl geometry, spray targeting and swirl ratio for a heavy-duty diesel engine operated at high-load.* SAE International Journal of Engines, 2008. **1**(2008-01-0949): p. 537-557.

97. Dempsey, A.B. and R.D. Reitz, *Computational optimization of a heavy-duty compression ignition engine fueled with conventional gasoline.* SAE International Journal of Engines, 2011. **4**(2011-01-0356): p. 338-359.

98. Moiz, A.A., et al., *A machine learning-genetic algorithm (ML-GA) approach for rapid optimization using high-performance computing.* SAE International Journal of Commercial Vehicles, 2018. **11**(2018-01-0190): p. 291-306.

99. Kalogirou, S.A., *Artificial intelligence for the modeling and control of combustion processes: a review.* Progress in energy and combustion science, 2003. **29**(6): p. 515-566.

100. Kodavasal, J., et al. *Machine learning analysis of factors impacting cycle-to-cycle variation in a gasoline spark-ignited engine*. in *ASME 2017 Internal Combustion Engine Division Fall Technical Conference*. 2017. American Society of Mechanical Engineers Digital Collection.

101. Hanuschkin, A., et al., *Machine learning–based analysis of in-cylinder flow fields to predict combustion engine performance.* International Journal of Engine Research, 2019: p. 1468087419833269.

102. Billa, K.K., G.R.K. Sastry, and M. Deb, *Artificial Intelligence Based Artificial Neural Network Model to Predict Performance and Emission Paradigm of a Compression Ignition Direct Injection Engine Under Diesel-Biodiesel Strategies*, in *Energy Recovery*

Processes from Wastes, S.K. Ghosh, Editor. 2020, Springer Singapore: Singapore. p. 65-83.

103. Pulga, L., et al., *A machine learning methodology for improving the accuracy of laminar flame simulations with reduced chemical kinetics mechanisms.* Combustion and Flame, 2020. **216**: p. 72-81.

104. Alonso, J.M., et al., *Combining neural networks and genetic algorithms to predict and reduce diesel engine emissions.* IEEE transactions on evolutionary computation, 2007. **11**(1): p. 46-55.

105. Bertram, A.M. and S.-C. Kong, *Computational Optimization of a Diesel Engine Calibration Using a Novel SVM-PSO Method*. 2019, SAE Technical Paper.

106. Amsden, A.A., *KIVA-3V, release 2, improvements to KIVA-3V.* Los Alamos National Laboratory, Los Alamos, NM, Report No. LA-UR-99-915, 1999.

107. Reitz, R.D. and R. Diwakar, *Structure of High-Pressure Fuel Sprays*. 1987, SAE International.

108. Miyasaka, K. and C.K. Law. *Combustion of strongly-interacting linear droplet arrays*. in *Symposium (International) on Combustion*. 1981. Elsevier.

109. Yang, J.-R. and S.-C. Wong, *An experimental and theoretical study of the effects of heat conduction through the support fiber on the evaporation of a droplet in a weakly convective flow.* International journal of heat and mass transfer, 2002. **45**(23): p. 4589-4598.

110. Zeng, Y. and C.-F. Lee, *A preferential vaporization model for multicomponent droplets and sprays.* Atomization and Sprays, 2002. **12**(1-3).

111. Jin, J.D. and G.L. Borman, *A Model for Multicomponent Droplet Vaporization at High Ambient Pressures*. 1985, SAE International.

112. Ranz, W.E., *Evaporation from drops, Parts I & II.* Chem Eng Prog., 1952. **48**: p. 141-146.

113. Peng, D.-Y. and D.B. Robinson, *A new two-constant equation of state.* Industrial & Engineering Chemistry Fundamentals, 1976. **15**(1): p. 59-64.

114. Chueh, P. and J. Prausnitz, *Vapor-liquid equilibria at high pressures: Calculation of partial molar volumes in nonpolar liquid mixtures.* AIChE journal, 1967. **13**(6): p. 1099-1107.

115. Linstrom, P.J. and W.G. Mallard, *The NIST Chemistry WebBook: A chemical data resource on the internet.* Journal of Chemical & Engineering Data, 2001. **46**(5): p. 1059-1063.

116. Thermal Fluid Central. *Thermophysical Properties*. 2010; Available from: https://www.thermalfluidscentral.org/encyclopedia/index.php/Thermophysical_Properties:_Ethanol.

117. Yaws, C., et al., *PHYSICAL AND THERMODYNAMIC PROPERTIES. 24. CORRELATION CONSTANTS FOR CHEMICAL COMPOUNDS.* Chemical Engineering, 1976. **83**(25): p. 153-162.

118. Dubey, G.P., M. Sharma, and N. Dubey, *Study of densities, viscosities, and speeds of sound of binary liquid mixtures of butan-1-ol with n-alkanes (C 6, C 8, and C 10) at T=(298.15, 303.15, and 308.15) K.* The Journal of Chemical Thermodynamics, 2008. **40**(2): p. 309-320.

119. Poling, B.E., J.M. Prausnitz, and J.P. O'connell, *The properties of gases and liquids*. Vol. 5. 2001: Mcgraw-hill New York.

120. Cummings, L.W.T., F. Stones, and M. Volante, *High-Pressure Rectification.* Industrial & Engineering Chemistry, 1933. **25**(7): p. 728-732.

121. Knapp, H., *" Vapor-Liguid Equilibria for Mixtures of Low Boiling Substances" Part1-4.* DECHEMA Chemistry Data Series, 1982.

122. Malewski, M.K. and S.I. Sandler, *High-pressure vapor-liquid equilibria of the binary mixtures nitrogen+ n-butane and argon+ n-butane.* Journal of Chemical and Engineering Data, 1989. **34**(4): p. 424-426.

123. Yucelen, B. and A.J. Kidnay, *Vapor− liquid equilibria in the nitrogen+ carbon dioxide+ propane system from 240 to 330 K at pressures to 15 MPa.* Journal of Chemical & Engineering Data, 1999. **44**(5): p. 926-931.

124. García-Sánchez, F., et al., *Vapor–liquid equilibria of nitrogen–hydrocarbon systems using the PC-SAFT equation of state.* Fluid phase equilibria, 2004. **217**(2): p. 241-253.

125. Sage, R., B. Hicks, and W. Lacey, *Phase equilibria in hydrocarbon systems.* Industrial & Engineering Chemistry, 1940. **32**(8): p. 1085-1092.

126. Chung, T.H., L.L. Lee, and K.E. Starling, *Applications of kinetic gas theories and multiparameter correlation for prediction of dilute gas viscosity and thermal conductivity.* Industrial & engineering chemistry fundamentals, 1984. **23**(1): p. 8-13.

127. Chung, T.H., et al., *Generalized multiparameter correlation for nonpolar and polar fluid transport properties.* Industrial & engineering chemistry research, 1988. **27**(4): p. 671-679.

128. Riazi, M.R. and C.H. Whitson, *Estimating diffusion coefficients of dense fluids.* Industrial & engineering chemistry research, 1993. **32**(12): p. 3081-3088.

129. Laboratory, N.N.P. *Kaye & Laby Tables of Physical & Chemical Constants, National Physical Laboratory.* . 2015; Available from: http://www.kayelaby.npl.co.uk/atomic_and_nuclear_physics/4_5/4_5_4.html.

130. Moore, J.W. and R.M. Wellek, *Diffusion Coefficients of n-Heptane and n-Decane in n-Alkanes and n-Alcohols at Several Temperatures.* Journal of Chemical and Engineering Data, 1974. **19**(2): p. 136-140.

131. Thek, R.E. and L.I. Stiel, *A new reduced vapor pressure equation.* AIChE Journal, 1966. **12**(3): p. 599-602.

132. Riedel, L., *Kritischer Koeffizient, Dichte des gesättigten dampfes und verdampfungswärme. untersuchungen über eine erweiterung des theorems der übereinstimmenden zustände. Teil III.* Chemie Ingenieur Technik, 1954. **26**(12): p. 679-683.

133. Curtis, E., A. Uludogan, and R.D. Reitz, *A new high pressure droplet vaporization model for diesel engine modeling*. 1995, SAE Technical Paper.

134. Daıf, A., et al., *Comparison of multicomponent fuel droplet vaporization experiments in forced convection with the Sirignano model.* Experimental Thermal and Fluid Science, 1998. **18**(4): p. 282-290.

135. Wilms, J., *Evaporation of multicomponent droplets*. 2005.

136. Rehman, H.L.-u., J. Weiss, and P. Seers, *Effect of heat conduction on droplet life time and evaporation rate under forced convection at low temperatures.* Experimental Thermal and Fluid Science, 2016. **72**: p. 59-66.

137. Zhang, H., *Evaporation of a suspended droplet in forced convective high-pressure environments.* Combustion Science and Technology, 2003. **175**(12): p. 2237-2268.

138. Kalikmanov, V.I., *Classical nucleation theory*, in *Nucleation theory*. 2013, Springer. p. 17-41.

139. Senda, J., Y. Hojyo, and H. Fujimoto, *Modeling on atomization and vaporization process in flash boiling spray.* JSAE Review, 1994. **15**(4): p. 291-296.

140. Kawano, D., et al., *Numerical study on flash-boiling spray of multicomponent fuel.* Heat Transfer—Asian Research, 2006. **35**(5): p. 369-385.

141. Plesset, M. and S.A. Zwick, *The growth of vapor bubbles in superheated liquids.* Journal of Applied Physics, 1954. **25**(4): p. 493-500.

142. Mikic, B., W. Rohsenow, and P. Griffith, *On bubble growth rates.* International Journal of Heat and Mass Transfer, 1970. **13**(4): p. 657-666.

143. Faeth, G., *Dynamics of secondary drop breakup rate controlling processes in dense sprays.* Zaragoza, 2002. **9**: p. 11.

144. O'Rourke, P.J. and A.A. Amsden, *The Tab Method for Numerical Calculation of Spray Droplet Breakup*. 1987, SAE International.

145. Taylor, G., *The shape and acceleration of a drop in a high speed air stream.* The scientific papers of GI Taylor, 1963. **3**: p. 457-464.

146. Yan, J., et al., *Macroscopic and Microscopic Characteristics of Flash Boiling Spray with Binary Fuel Mixtures*. 2019, SAE Technical Paper.

147. Yan, J., et al., *Experimental study of sprays with isooctane, hexane, ethanol and their binary mixtures under different flash boiling intensities.* International Journal of Heat and Mass Transfer, 2021. **179**: p. 121715.

148. Yan, J., et al., *Experimental study of flash boiling spray with isooctane, hexane, ethanol and their binary mixtures.* Fuel, 2021. **292**: p. 120415.

149. Oktavian, R., et al., *Vapor pressure measurements of ethanol–isooctane and 1-butanol–isooctane systems using a new ebulliometer.* Fuel, 2013. **107**: p. 47-51.

150. Golubkov, I., et al., *Alternative fuel for conventional spark ignition engines based on a standard gasoline, ethanol and other oxygenates*. 2006, IJER.

151. ECN, *Engine combustion network.*

152. Duke, D.J., et al., *Internal and near nozzle measurements of Engine Combustion Network "Spray G" gasoline direct injectors.* Experimental Thermal and Fluid Science, 2017. **88**: p. 608-621.

153. Li, Y., et al., *Morphology analysis on multi-jet flash-boiling sprays under wide ambient pressures.* Fuel, 2018. **211**: p. 38-47.

154. Zeng, W., et al., *Atomization and vaporization for flash-boiling multi-hole sprays with alcohol fuels.* Fuel, 2012. **95**: p. 287-297.

155. Plesset, M.S. and S.A. Zwick, *The growth of vapor bubbles in superheated liquids.* Journal of applied physics, 1954. **25**(4): p. 493-500.

156. Li, Y., et al., *Spray morphology transformation of propane, n-hexane and iso-octane under flash-boiling conditions.* Fuel, 2019. **236**: p. 677-685.

157. Zhang, X., et al., *Effects of surface tension on bubble growth in an extensive uniformly superheated liquid.* Chinese Science Bulletin, 2011. **56**(30): p. 3191-3198.

158. Haas, F.M., M. Chaos, and F.L. Dryer, *Low and intermediate temperature oxidation of ethanol and ethanol–PRF blends: An experimental and modeling study.* Combustion and Flame, 2009. **156**(12): p. 2346-2350.

159. Bhagatwala, A., J.H. Chen, and T. Lu, *Direct numerical simulations of HCCI/SACI with ethanol.* Combustion and Flame, 2014. **161**(7): p. 1826-1841.

160. Goodwin, D., *An open-source, extensible software suite for CVD process simulation.* Chemical Vapor Deposition XVI and EUROCVD, 2003. **14**(40): p. 2003-08.

161. Wang, H., M. Yao, and R.D. Reitz, *Development of a reduced primary reference fuel mechanism for internal combustion engine combustion simulations.* Energy & Fuels, 2013. **27**(12): p. 7843-7853.

162. Sun, Y., *Diesel combustion optimization and emissions reduction using adaptive injection strategies (AIS) with improved numerical models*. 2007: ProQuest.

163. Sellnau, M.C., et al., *Full-Time Gasoline Direct-Injection Compression Ignition (GDCI) for High Efficiency and Low NOx and PM.* SAE International Journal of Engines, 2012. **5**(2012-01-0384): p. 300-314.

164. Sellnau, M., et al., *GDCI Multi-Cylinder Engine for High Fuel Efficiency and Low Emissions.* 2015.

165. Wang, M., et al. *Different Diesel Engine Ignition Regimes With a Single Injection*. in *ASME 2015 Internal Combustion Engine Division Fall Technical Conference*. 2015. American Society of Mechanical Engineers.

166. Wang, M., S. Gao, and C.-F. Lee, *Private Communications.* TBD.

167. Han, Z. and R.D. Reitz, *Turbulence modeling of internal combustion engines using RNG κ-ε models.* Combustion science and technology, 1995. **106**(4-6): p. 267-295.

168. Magnussen, B.F. and B.H. Hjertager. *On mathematical modeling of turbulent combustion with special emphasis on soot formation and combustion*. in *Symposium (International) on Combustion*. 1977. Elsevier.

169. Manente, V., et al., *Effects of ethanol and different type of gasoline fuels on partially premixed combustion from low to high load*. 2010, SAE Technical Paper.

170. Tsang, K., et al., *Reducing emissions of a diesel engine using fumigation ethanol and a diesel oxidation catalyst.* Energy & Fuels, 2010. **24**(11): p. 6156-6165.

171. Gao, S., M. Wang, and C.-F. Lee, *NOx Reduction in Compression-Ignition Engine by Inverted Ignition Phi-Sensitivity*. 2017, SAE Technical Paper.

172. Rossant, C., B. Fontaine, and D.F. Goodman, *Playdoh: a lightweight Python library for distributed computing and optimisation.* Journal of Computational Science, 2013. **4**(5): p. 352-359.

173. Dempsey, A.B., S.J. Curran, and R.M. Wagner, *A perspective on the range of gasoline compression ignition combustion strategies for high engine efficiency and low NOx and soot emissions: Effects of in-cylinder fuel stratification.* International Journal of Engine Research, 2016. **17**(8): p. 897-917.

174. Shoham, Y., et al., *The AI Index 2018 annual report.* AI Index Steering Committee, Human-Centered AI Initiative, Stanford University, Stanford, CA, 2018.

175. Pedregosa, F., et al., *Scikit-learn: Machine learning in Python.* Journal of machine learning research, 2011. **12**(Oct): p. 2825-2830.

176. Abadi, M., et al. *Tensorflow: A system for large-scale machine learning*. in *12th {USENIX} Symposium on Operating Systems Design and Implementation ({OSDI} 16)*. 2016.

177. Ke, G., et al., *Lightgbm: A highly efficient gradient boosting decision tree.* Advances in neural information processing systems, 2017. **30**: p. 3146-3154.

178. Polley, E., et al., *Package 'SuperLearner'*. 2019, CRAN.

179. Vapnik, V.N., *The nature of statistical learning.* Theory, 1995.

180. Karush, W., *Minima of functions of several variables with inequalities as side constraints.* M. Sc. Dissertation. Dept. of Mathematics, Univ. of Chicago, 1939.

181. Kuhn, H.W. and A.W. Tucker. *Nonlinear Programming*. in *Proceedings of the Second Berkeley Symposium on Mathematical Statistics and Probability*. 1951. Berkeley, Calif.: University of California Press.

182. Smola, A.J. and B. Schölkopf, *A tutorial on support vector regression.* Statistics and computing, 2004. **14**(3): p. 199-222.

183. Vapnik, V., *The nature of statistical learning theory*. 2013: Springer science & business media.

184. Fix, E. and J.L. Hodges, *Discriminatory analysis. Nonparametric discrimination: Consistency properties.* International Statistical Review/Revue Internationale de Statistique, 1989. **57**(3): p. 238-247.

185. Altman, N.S., *An introduction to kernel and nearest-neighbor nonparametric regression.* The American Statistician, 1992. **46**(3): p. 175-185.

186. Imandoust, S.B. and M. Bolandraftar, *Application of k-nearest neighbor (knn) approach for predicting economic events: Theoretical background.* International Journal of Engineering Research and Applications, 2013. **3**(5): p. 605-610.

187. Farahnakian, F., et al. *Energy aware consolidation algorithm based on k-nearest neighbor regression for cloud data centers*. in *2013 IEEE/ACM 6th International Conference on Utility and Cloud Computing*. 2013. IEEE.

188. Ray, S. *A quick review of machine learning algorithms*. in *2019 International conference on machine learning, big data, cloud and parallel computing (COMITCon)*. 2019. IEEE.

189. Liaw, A. and M. Wiener, *Classification and regression by randomForest.* R news, 2002. **2**(3): p. 18-22.

190. Ranka, S. and V. Singh. *CLOUDS: A decision tree classifier for large datasets*. in *Proceedings of the 4th knowledge discovery and data mining conference*. 1998.

191. Jin, R. and G. Agrawal. *Communication and memory efficient parallel decision tree construction*. in *Proceedings of the 2003 SIAM international conference on data mining*. 2003. SIAM.

192. Haykin, S., *Neural Networks and Learning Machines, 3/E*. 2010: Pearson Education India.

193. Goodfellow, I., Y. Bengio, and A. Courville, *Machine learning basics.* Deep learning, 2016. **1**: p. 98-164.

194. Wolpert, D.H., *Stacked generalization.* Neural networks, 1992. **5**(2): p. 241-259.

195. Breiman, L., *Stacked regressions.* Machine learning, 1996. **24**(1): p. 49-64.

196. Jones, D.R., M. Schonlau, and W.J. Welch, *Efficient global optimization of expensive black-box functions.* Journal of Global optimization, 1998. **13**(4): p. 455-492.

197. Bergstra, J.S., et al. *Algorithms for hyper-parameter optimization*. in *Advances in neural information processing systems*. 2011.

198. Snoek, J., H. Larochelle, and R.P. Adams. *Practical bayesian optimization of machine learning algorithms*. in *Advances in neural information processing systems*. 2012.

199. Bergstra, J., D. Yamins, and D. Cox. *Making a science of model search: Hyperparameter optimization in hundreds of dimensions for vision architectures*. in *International conference on machine learning*. 2013. PMLR.

200. Hutter, F., H.H. Hoos, and K. Leyton-Brown. *Sequential model-based optimization for general algorithm configuration*. in *International conference on learning and intelligent optimization*. 2011. Springer.

201. Shahriari, B., et al., *Taking the human out of the loop: A review of Bayesian optimization.* Proceedings of the IEEE, 2015. **104**(1): p. 148-175.

202. Brochu, E., V.M. Cora, and N. De Freitas, *A tutorial on Bayesian optimization of expensive cost functions, with application to active user modeling and hierarchical reinforcement learning.* arXiv preprint arXiv:1012.2599, 2010.

203. Bergstra, J. and Y. Bengio, *Random search for hyper-parameter optimization.* Journal of machine learning research, 2012. **13**(2).